Remote sensing, numerical modelling and ground truthing for analysis of lake water quality and temperature

A thesis

submitted in fulfilment

of the requirements for the degree

of

Doctor of Philosophy in Biological Sciences

at

The University of Waikato

by

MATHEW GRANT ALLAN

KO TE TANGATA

THE UNIVERSITY OF
WAIKATO
Te Whare Wānanga o Waikato

2014

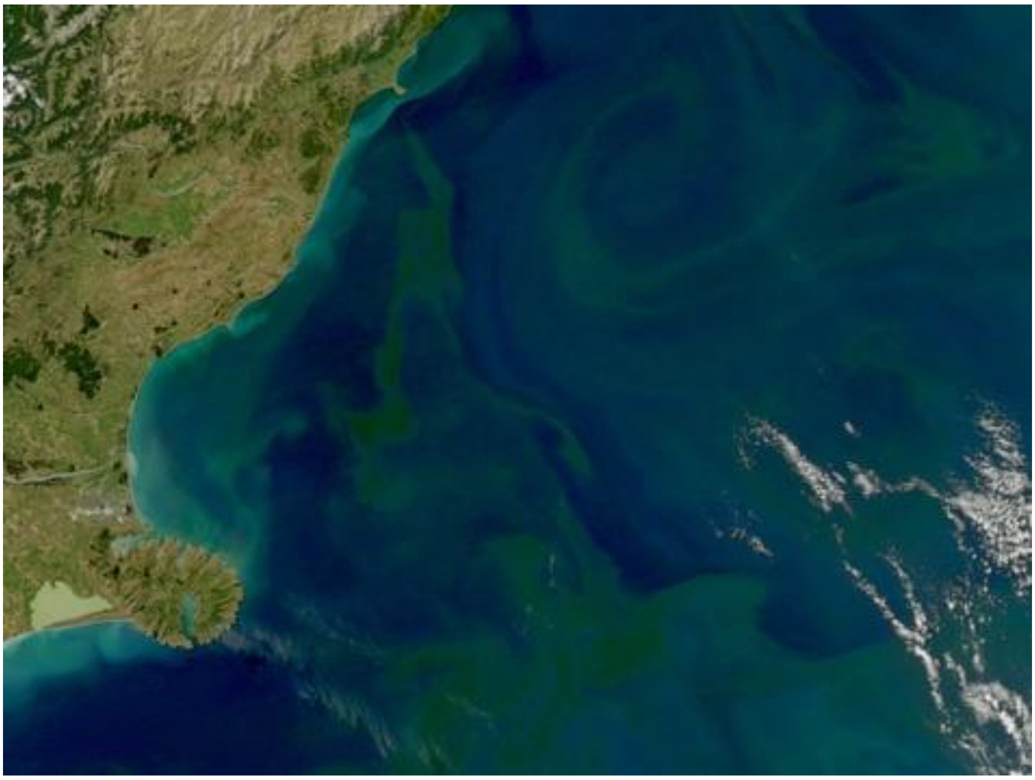

MODIS image captured in February 2011 by NASA's Aqua satellite. Lake Ellesmere (Te Waihora) is visible in the bottom left coastal land area of the image.

Abstract

Freshwater accounts for just 2.5% of the earth's water resources, and its quality and availability are becoming an issue of global concern in the 21st century. Growing human population, over-exploitation of water sources and pressures of global warming mean that both water quantity and quality are affected. In order to effectively manage water quality there is a need for increased monitoring and predictive modelling of freshwater resources. To address these concerns in New Zealand inland waters, an approach which integrates biological and physical sciences is needed. Remote sensing has the potential to allow this integration and vastly increase the temporal and spatial resolution of current monitoring techniques, which typically involve collecting grab-samples. In a complementary way, lake modelling has the potential to enable more effective management of water resources by testing the effectiveness of a range of possible management scenarios prior to implementation. Together, the combination of remote sensing and modelling data allows for improved model initialisation, calibration and validation, which ultimately aid in understanding of complex lake ecosystem processes.

This study investigated the use of remote sensing using empirical and semi-analytical algorithms for the retrieval of chlorophyll *a* (chl *a*), tripton, suspended minerals (SM), total suspended sediment (SS) and water surface temperature. It demonstrated the use of spatially resolved statistical techniques for comparing satellite estimated and 3-D simulated water quality and temperature.

An automated procedure was developed for retrieval of chl *a* from Landsat Enhanced Thematic Mapper (ETM+) imagery, using 106 satellite images captured from 1999 to 2011. Radiative transfer-based atmospheric correction was applied to images using the Second Simulation of the Satellite in the Solar Spectrum model (6sv). For the estimation of chl *a* over a time series of images, the use of symbolic regression resulted in a significant improvement in the precision of chl *a* hindcasts compared with traditional regression equations. Results from this investigation suggest that remote sensing provides a valuable tool to assess temporal and spatial distributions of chl *a*. Bio-optical models were applied to quantify the physical processes responsible for the relationship between chl *a* concentrations and subsurface irradiance reflectance used in regression algorithms, allowing the identification of possible sources of error in chl *a* estimation. While the symbolic regression model was more accurate than traditional empirical models, it was still susceptible to errors in optically complex waters such as Lake Rotorua, due to the effect of variations of SS and CDOM on reflectance.

Atmospheric correction of Landsat 7 ETM+ thermal data was carried out for the purpose of retrieval of lake water surface temperature in Rotorua lakes, and Lake Taupo, North Island, New Zealand. Atmospheric correction was repeated using four sources of atmospheric profile data as input to a radiative transfer model, MODerate resolution atmospheric TRANsmission (MODTRAN) v.3.7. The retrieved water temperatures from 14 images between 2007 and 2009 were validated using a high-frequency temperature sensor deployed from a mid-lake monitoring buoy at the water surface of Lake Rotorua. The most accurate temperature estimation for Lake Rotorua was with radiosonde data as an input into MODTRAN, followed by Moderate Resolution Imaging Spectroradiometer (MODIS) Level 2, Atmospheric Infrared Sounder (AIRS) Level 3, and NASA data. Retrieved surface water temperature was used for assessing spatial heterogeneity of surface water temperature simulated with a three-dimensional (3-D) hydrodynamic model (ELCOM) of Lake Rotoehu, located approximately 20 km east of Lake Rotorua. This comparison demonstrated that simulations reproduced the dominant horizontal variations in surface water temperature in the lake. The transport and mixing of a geothermal inflow and basin-scale circulation patterns were inferred from thermal distributions from satellite and model estimations of surface water temperature and a spatially resolved statistical evaluation was used to validate simulations. This study has demonstrated the potential of accurate satellite-based thermal monitoring to validate water surface temperature simulated by 3-D hydrodynamic models.

Semi-analytical and empirical algorithms were derived to determine spatial and temporal variations in SS in Lake Ellesmere, South Island, New Zealand, using MODIS band 1. The semi-analytical model and empirical model had a similar level of precision in SS estimation, however, the semi-analytical model has the advantage of being applicable to different satellite sensors, spatial locations, and SS concentration ranges. The estimations of SS concentration (and estimated SM concentration) from the semi-analytical model were used for a spatially resolved validation of simulations of SM derived from ELCOM-CAEDYM. Visual comparisons were compared with spatially-resolved statistical techniques. The spatial statistics derived from the Map Comparison Kit allowed a non-subjective and quantitative method to rank simulation performance on different dates. The visual and statistical comparison between satellite estimated and model simulated SM showed that the model did not perform well in reproducing both basin-scale and fine-scale spatial variation in SM derived from MODIS satellite imagery. Application of the semi-analytical model to estimate SS over the lifetime of the MODIS sensor will greatly extend its spatial and temporal coverage for historical monitoring purposes, and provide a tool to validate SM simulated by 1-D and 3-D models on a daily basis.

A bio-optical model was developed to derive chl *a*, SS concentrations, and coloured dissolved organic matter /detritus absorption at 443 nm, from MODIS Aqua subsurface remote sensing reflectance of Lake Taupo, a large, deep, oligotrophic lake in North Island, New Zealand. The model was optimised using in situ inherent optical properties (IOPs) from the literature. Images were atmospherically corrected using the radiative transfer model 6sv. Application of the bio-optical model using a single chl *a*-specific absorption spectrum ($a^*_\phi(\lambda)$) resulted in low correlation between estimated and observed values. Therefore, two different absorption curves were used, based on the seasonal dominance of phytoplankton phyla with differing absorption properties. The application of this model resulted in reasonable agreement between modelled and in situ chl *a* concentrations. Highest concentrations were observed during winter when Bacillariophytes (diatoms) dominated the phytoplankton assemblage. On 4 and 5

March 2004 an unusually large turbidity current was observed originating from the Tongariro River inflow in the south-east of the lake. In order to resolve fine details of the plume, empirical relationships were developed between MODIS band 1 reflectance (250 m resolution) and SS estimated from MODIS bio-optical features (1 km resolution) were used estimate SS at 250 m resolution. Complex lake circulation patterns were observed including a large clockwise gyre. With the development of this bio-optical model MODIS can potentially be used to remotely sense water quality in near real time, and the relationship developed for B1 SS allows for resolution of fine-scale features such turbidity currents.

Table of Contents

List of Figures

List of Tables

List of acronyms

3-D	Three-dimensional
6sv	Second Simulation of a Satellite Signal in the Solar Spectrum
AC	Atmospheric Correction
AIRS	Atmospheric InfraRed Sounder
AOD	Aerosol Optical Depth
AOPs	Apparent Optical Properties
BIOPTI	Bio-optical model for inland waters
BOPRC	Bay of Plenty Regional Council
BRDF	Bi-directional Reflectance Distribution Function
CAEDYM	Computational Aquatic Ecosystem Dynamics Model
CDOM	Coloured Dissolved Organic Matter
CZCS	Coastal Zone Colour Scanner
DN	Digital Number
DYRESM	DYnamic REservoir Simulation Model
ELCOM	Estuary Lake and Coastal Ocean Model
ESA	European Space Agency
ETM+	Enhanced Thematic Mapper Plus
GIS	Geographic Information System
GloVis	GloVis
GWR	Geographically Weighted Regression
IDL	Interactive Data Language
IOPs	Inherent Optical Properties
IR	Infrared
LDCM	Landsat Data Continuity Mission
LMM	Linear Mixture Modelling
LOWTRAN	LOW Resolution TRANsmission model
MCK	Map Comparison Kit
MERIS	MEdium Resolution Imaging Spectrometer
MNF	Minimum Noise Function
MODIS	MODerate Resolution Imaging Spectroradiometer
MODTRAN	MODerate resolution atmospheric TRANsmission
NAP	Non-Algal Particles
NASA	National Aeronautics and Space Administration
NAVSS	Non-Algal Volatile Suspended Sediment
NIR	Near Infrared
NIWA	National Institute of Water and Atmospheric Research
NN	Neural Network

NZST	New Zealand Standard Time
OACs	Optically Active Constituents
PAR	Photosynthetically Active Radiation
RH	Relative Humidity
RMSE	Root Mean Squared Error
SM	Suspended Minerals
SNR	Signal-to-Noise Ratio
SPOT	Système Probatoire d’Observation de la Terre
SS	Total Suspended Sediment or particles
TLTMP	Taupo Long Term Monitoring Programme
TM	Thematic Mapper
TOA	Top Of Atmosphere
VSS	Volatile Suspended Sediment
WRC	Waikato Regional Council

List of symbols

$a(\lambda)$	Spectral absorption coefficient (m^{-1})
$a^*_{TR}(\lambda)$	Specific absorption coefficient of tripton ($\mathrm{m}^2\ \mathrm{g}^{-1}$)
$a^*_{\phi}(\lambda)$	Chlorophyll-specific absorption coefficient ($\mathrm{m}^2\ \mathrm{mg}^{-1}$)
$a_{\mathrm{CDOM}}(\lambda)$	CDOM absorption coefficient (m^{-1})
$a_{CDOMD}(\lambda)$	CDOM and detritus absorption coefficient (m^{-1})
$a_w(\lambda)$	Pure water absorption coefficient (m^{-1})
$b(\lambda)$	Spectral scattering coefficient (m^{-1})
$b^*_{SS}(\lambda)$	Specific scattering coefficient of SS ($\mathrm{m}^2\ \mathrm{g}^{-1}$)
$b^*_{TR}(\lambda)$	Specific scattering coefficient of tripton ($\mathrm{m}^2\ \mathrm{g}^{-1}$)
$b^*_{\phi}(\lambda)$	Specific scattering coefficient of phytoplankton ($\mathrm{m}^2\ \mathrm{mg}^{-1}$)
$b_b(\lambda)$	Spectral backscattering coefficient (m^{-1})
B_{bSS}	Backscattering ratio of suspended sediment
B_{bTR}	Backscattering ratio of tripton
$b_{bw}(\lambda)$	Backscattering coefficient of pure water (m^{-1})
$B_{b\phi}$	Backscattering ratio of phytoplankton
B_r	Landsat bias ($\mathrm{W\ m^{-2}\ sr^{-1}\ \mu m^{-1}}$)
C_{SM}	Concentration of suspended minerals ($\mathrm{mg\ L^{-1}}$)
C_{TR}	Concentration of tripton ($\mathrm{mg\ L^{-1}}$)
C_{ϕ}	Concentration of chl *a* ($\mathrm{\mu g\ L^{-1}}$)
$E(\lambda)$	Irradiance ($\mathrm{W\ m^{-2}\ nm^{-1}}$)
$E_d(\lambda)$	Downwelling irradiance ($\mathrm{W\ m^{-2}\ nm^{-1}}$)
$E_{\mathrm{u}}(\lambda)$	Upwelling irradiance ($\mathrm{W\ m^{-2}\ nm^{-1}}$)
g_0, g_1, r_1	Factors relating $r_{rs}(\lambda)$ and $R(0\text{-})$ to a and b_b (sr^{-1})
G_r	Landsat rescaled gain ($\mathrm{W\ m^{-2}\ sr^{-1}\ \mu m^{-1}/DN}$)
$L(\lambda)$	Spectral radiance ($\mathrm{W\ m^{-2}\ nm^{-1}\ sr^{-1}}$)
$L_a(\lambda)$	Atmospheric or upwelling radiance emitted/scattered by the atmosphere ($\mathrm{W\ m^{-2}\ sr^{-1}\ \mu m^{-1}}$)
$L_r(\lambda)$	Radiance due to multiple scattering by air molecules (Rayleigh) ($\mathrm{W\ m^{-2}\ nm^{-1}\ sr^{-1}}$)
$L_t(\lambda)$	At-sensor radiance ($\mathrm{W\ m^{-2}\ sr^{-1}\ \mu m^{-1}}$)
$L_s(\lambda)$	Surface leaving radiance ($\mathrm{W\ m^{-2}\ nm^{-1}\ sr^{-1}}$)

L_{sky}	Downwelling or sky radiance reflected from the surface ($W\ m^{-2}\ sr^{-1}\ \mu m^{-1}$)
$L_u(\lambda,z)$, $L_w(\lambda)$	Upwelling radiance ($W\ m^{-2}\ nm^{-1}\ sr^{-1}$)
$L_w(\lambda)$	Water leaving radiance ($W\ m^{-2}\ nm^{-1}\ sr^{-1}$)
n	Scattering exponent of tripton or SS
ʊ	Elevation angle (°)
σ_L	Fresnel reflectance (sr^{-1})
ω	Azimuth angle (°)
$R(0-)(\lambda)$	Subsurface irradiance reflectance
$R(0+)(\lambda)$	Above water surface irradiance reflectance
$R_{rs}(\lambda)$, $r_{rs}(\lambda)$	Above, below water surface remote sensing reflectance (sr^{-1})
R_v	gas constant for moist air = 461.5 $J\ kg^{-1}$
S	Spectral slope coefficient of CDOM (nm^{-1})
$\tau(\lambda)$	Atmospheric transmittance
z	Depth (m)
$\beta(\theta)$	volume scattering function ($m^{-1}\ sr^{-1}$)
$\beta(\theta)$	Volume scattering function ($m^{-1}\ sr^{-1}$), where θ is forward scattering angle
ε	Emissivity of the water surface
θ	Zenith angle (°)
θ	forward scattering angle (°)
λ, λ_0	Wavelength, reference wavelength (nm)
Q	The amount of energy held by a photon (J)
h	Plank's constant ($J\ s^{-1}$)
v	Frequency (Hz)
$\tau_{atm}(\lambda)$	Atmospheric transmittance from water to sensor

Acknowledgments

First and foremost I would like to thank my chief supervisor Professor David Hamilton for his constant enthusiasm and tireless effort in supervising this project. Thanks to my lovely partner Tineke Webley for your support and patience. I thank my co-supervisors Associate Professor Brendan Hicks and Dr Lars Brabyn. I also thank the following collaborators; Dr Dennis Trolle in chapters 3 and 4, Kohji Muraoka in Chapter 3, and Dr Max Gibbs in Chapter 5. Dr Deniz Özkundakci provided valuable technical advice on many aspects of this thesis. Jonathan Abell provided feedback on drafts and technical advice.

Funding was provided by the Bay of Plenty Regional Council (BOPRC) and the Ministry of Science and Innovation (contract UOWX0505). This work benefited from participation in the Global Lakes Ecological Observatory Network (GLEON).

I thank BOPRC for providing the measured data for water quality variables, in particular Glenn Ellery, Paul Scholes, and Gareth Evans. Dr Salman Ashraf, Dr Kevin Collier (Environment Waikato) and Associate Professor Lex Chalmers (University of Waikato), who provided valuable advice on data analysis. Dr Matt Pinkerton (National Institute of Water and Atmospheric Research, New Zealand) provided technical guidance on satellite platforms and capability. Julia Barsi (NASA) provided the Interactive Data Language (IDL) code to apply spectral response functions to MODTRAN output and created the NASA atmospheric correction tool used in this study. Chris McBride (University of Waikato) provided data from a monitoring buoy on Lake Rotorua. Dr Hirokazu Yamamoto (Advanced Industrial Science and Technology, Japan) gave valuable feedback on atmospheric correction calculations. Graeme Plank (University of Canterbury Physics Department) provided weather station data from Birdlings Flat under difficult circumstances soon after the Canterbury earthquake. Dr Stéphane Maritorena (University of California Santa Barbara) provided valuable advice in

adapting the bio-optical model for image applications and provided a MODIS Aqua version of the bio-optical model code. Jonathan King provided the aerial image of Lake Taupo. Associate Professor Hiroshi Yajima provided valuable technical assistance in 3-D modelling.

This thesis is dedicated to my late father James Grant Allan, who I know was proud at seeing this Ph.D. near its completion.

Preface

This thesis is comprised of six chapters which present the results relating to this study, relevant literature and discussion. Chapters 2-5 have been written for publication in peer-reviewed scientific journals. Except where referenced, I conceived the work presented in this thesis, including data analysis, interpretation and writing, undertaken while under the supervision of Professor David P. Hamilton (University of Waikato).

Chapter 2 is in preparation for submission to a peer reviewed journal under the title 'Remote sensing of chlorophyll *a* concentrations in Rotorua lakes of New Zealand' by Mathew Allan, David P. Hamilton, Brendan Hicks and Lars Brabyn.

Chapter 3 has been submitted to Remote Sensing of Environment under the title 'Atmospheric correction of Landsat thermal imagery for surface water temperature retrieval and three-dimensional hydrodynamic model validation of spatial heterogeneity in geothermally-influenced lakes' by Mathew Allan, David P. Hamilton, Dennis Trolle, Kohji Muraoaka and Chris McBride. David Hamilton assisted with planning and editing, Dennis Trolle assisted with model creation, Kohji Muraoaka created the 3-D visualisation, and Chris McBride manufactured the buoy.

Chapter 4 is in preparation for submission to a peer reviewed journal under the title 'MODIS-based estimates of suspended minerals to evaluate performance of a three-dimensional hydrodynamic-ecological model application to a large, shallow coastal lagoon' by Mathew Allan, David P. Hamilton and Dennis Trolle. David Hamilton assisted with planning and editing, Dennis Trolle provided the original 1-D model which was modified, and with my help, set up the 3-D model, which was then modified.

Chapter 5 is in preparation for submission to a peer reviewed journal under the title ‘Optimization of a semi-analytical model for remote sensing of Chlorophyll *a* in a large oligotrophic lake using MODIS’ by Mathew Allan, David P. Hamilton and Max M. Gibbs. Daivd Hamilton assisted with planning/editing, and Max Gibbs provided in situ data and assisted with editing.

1 General introduction

1.1 Motivation

Eutrophication

Eutrophication is generally defined as an increase in nutrients such as phosphorus and nitrogen which enhance algal growth (Wetzel 2001), leading to a decrease in water quality. It is a natural process whereby with age lakes gradually infill with sediment, nutrients, and organic matter. Human induced changes within catchments can speed up this natural process, which is then termed cultural eutrophication. Cultural eutrophication can result in decreased water clarity, harmful algal blooms, increased suspended sediment, hypoxia and anoxia, losses or increased growth of submerged macrophytes and lake biota, and, ultimately, risks to human health (Williamson et al. 2008). Lakes can be thought of as integrators of environmental change which has occurred within their catchments (Williamson et al. 2008).

Remote sensing and modelling solutions

Methods to assess water quality may be categorised into three main types; in situ sampling, numerical modelling and remote sensing (Dekker et al. 1996). In situ methods using grab-samples are generally suited to monitoring at low temporal resolution. By contrast autonomous water quality sensors allow for monitoring at high frequency and potentially in real time. However, neither of these methods is well suited to effectively capturing horizontal heterogeneity of water quality and temperature.

Remote sensing can provide synoptic monitoring of optically active water constituents (e.g., Kloiber et al. 2002) and may therefore allow monitoring of temperature and optically active water quality variables at high spatial resolution (e.g., Dekker et al. 2002; Binding et al. 2007). Furthermore it can be accomplished at near real time in cases where satellite overpasses occur daily.

Three-dimensional (3-D) and one-dimensional (1-D) hydrodynamic and thermodynamic modelling of lake water temperature offers an opportunity to interpolate temporal gaps in data derived from satellite and traditional monitoring of water quality and temperature, and to extend the analysis to the vertical domain (Hedger et al. 2002). When coupled to ecological models, this modelling may also provide insights into the spatial variability of biogeochemical processes (Jorgensen 2008).

The synthesis of data derived from remote sensing, modelling and in situ sampling provides an unparalleled opportunity for understanding ecosystem structure and function. Horizontal validation of 3-D models with traditional point-based monitoring is often limited by the synoptic coverage and quantity of field data. Remote sensing therefore has the potential to provide a cost effective method for synoptic validation. Modelling provides an opportunity for interpretation of remotely sensed imagery through the quantification of the physical and biological fluxes that redistribute variables and lead to the spatial distributions observed through remote sensing.

However, there are some inherent limitations of remote sensing. Use of visible and infrared (IR) radiation of from lakes is not possible during periods of cloud cover, which is a frequent occurrence in New Zealand. Remote sensing is unable to derive estimates of non-optically active water constituents, such as nutrient concentrations. Measurements of total radiance from satellites may comprise up to 90% atmospheric path radiance, making it difficult to quantify radiance from optically active constituents (OACs) of water (Vidot and Santer 2005), therefore atmospheric correction is essential for the standardisation of a time series of images. In optically complex Case 2 waters found in lakes, at least three optically active constituents influence reflectance, and these constituents can vary independently from each other (Bukata et al. 1995). The retrieval of water constituent concentrations from Case 2 waters is therefore more demanding in terms of algorithm complexity and the required level of satellite sensor spectral resolution (Matthews 2011).

Water quality monitoring in New Zealand

Of the 3820 lakes larger than one hectare in New Zealand, only 3% (117) are monitored as part of a long-term programme. Forty-four percent of the monitored lakes were recently found to be eutrophic and 33% oligotrophic (Verburg et al. 2010). In past and present monitoring programmes, lake trophic state is reported for 134 lakes (Hamill 2006). Water quality monitoring in New Zealand currently uses traditional monitoring techniques involving collection of a water grab-sample from one site in a lake or occasionally from multiple sites in larger lakes, and subsequent laboratory analysis. Other measurements may be made in situ, such as Secchi depth and profiles of temperature, turbidity, light or dissolved oxygen. Laboratory sampling methods are time-consuming and expensive, with results often not available for considerable time periods after the sample is taken. The small percentage of lakes monitored in New Zealand is indicative of the high cost associated with traditional point sample collection and subsequent analysis.

Remote sensing theory

Remote sensing is the science of obtaining information about an object using a device that is not in contact with that object (Bukata et al. 1995). According to this definition, remote sensing was practiced by the pioneers of astronomy such as Galileo and Copernicus. Modern environmental remote sensing has its roots in the military reconnaissance of World War I (Bukata et al. 1995). Remote sensing has subsequently benefited from technological advances emerging from space exploration programs (Bukata et al. 1995).

Passive remote sensing involves sensors that record electromagnetic (EM) energy reflected or emitted by the earth. The energy can be modelled either as a wave or as a particle which travels at the speed of light. The most important characteristic of EM for the purpose of remote sensing is the wavelength (λ). Longer wavelengths are associated with lower frequency and energy according to Equation 1.1 which defines Q, the amount of energy held by a photon (measured in joules), as:

$$Q = h\,v = h\,\frac{c}{\lambda} \tag{1.1}$$

where h is Planck's constant, v is frequency, and c = 2.998 × 108 m s^{-1}.

Remote sensors record EM in the form of radiance, $L(\theta, \varphi, \lambda)$, which is defined as the radiant flux per unit solid angle per unit area at right angles to the direction of EM propagation (W m^{-2} sr^{-1}), with a specified azimuth (θ) and zenith (φ) angle. Radiance is a subset of irradiance $E(\lambda)$, which is defined as the total radiative flux incident upon a point on a surface from all directions above the surface. The geometry associated with a remote sensing instrument is shown in Figure 1.2.

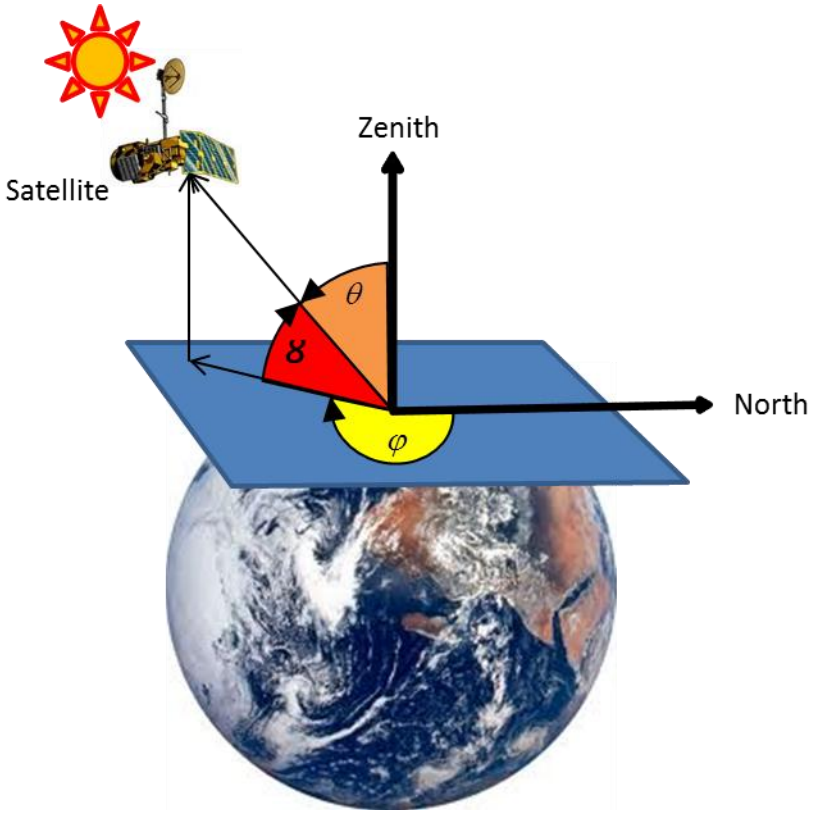

Figure 1.1. Satellite and solar geometry. θ is azimuth angle, ɤ is elevation angle and φ is zenith angle, which can be apply to either solar or sensor (view) geometry.

The simplified radiance recorded by a remote sensor can be expressed as (assuming no adjacency effects or bottom reflection):

$$L_t(\theta_v, \varphi_v, \theta_s, \lambda) = L_r(\theta_v, \varphi_v, \theta_s, \lambda) + L_a(\theta_v, \varphi_v, \theta_s, \lambda) + T_{atm}(\theta_v, \theta_s, \lambda)L_s(\theta_v, \varphi_v, \theta_s, \lambda) \quad (1.2)$$

where:

$L_r(\lambda)$ = radiance due to multiple scattering by air molecules (Rayleigh scattering)
$L_a(\lambda)$ = radiance from multiple scattering of aerosols
$T_{atm}(\lambda)$ = atmospheric transmittance from water to sensor
$L_s(\lambda)$ = surface leaving radiance
λ = wavelength
θ_v = view or observation zenith angle
φ_v = view azimuth angle
θ_s = solar zenith angle

Adjacency effects are caused by reflection from a non-target area (e.g. land) being scattered into the field of view by the atmosphere. If the non-target area is brighter than the target, there will be an increase in the apparent brightness of the target area, and a reduction of image contrast (Santer and Schmechtig 2000).

Surface-leaving radiance, $L_s(\theta_v, \varphi_v, \theta_s, \lambda)$, is estimated through applying an atmospheric correction, described below. Water-leaving radiance is estimated from (Kallio 2012):

$$L_w(\theta_v, \varphi_v, \theta_s, \lambda) = L_s(\theta_v, \varphi_v, \theta_s, \lambda) - \sigma_L L_{sky}(\theta_v, \varphi_v, \theta_s, \lambda) \quad (1.3)$$

where:
$L_{sky}(\theta_v, \varphi_v, \theta_s, \lambda)$ = sky specular reflectance at sensor
σ_L = Fresnel reflectance

Water surface remote sensing reflectance (sr^{-1}) is given as:

$$R_{rs}(\theta_v, \varphi_v, \theta_s, \lambda) \equiv \frac{L_w(\theta_v, \varphi_v, \theta_s, \lambda)}{E_d(\lambda)} \qquad (1.4)$$

where E_d is downwelling irradiance immediately above the water surface. Subsurface remotely sensed reflectance $r_{rs}(\lambda)$ can be estimated from $R_{rs}(\lambda)$ by correcting for air-water interface effects, assuming a nadir viewing sensor and optically deep waters (Lee et al. 2002):

$$r_{rs}(\lambda) \approx \frac{R_{rs}(\lambda)}{0.52 + 1.7R_{rs}(\lambda)} \qquad (1.5)$$

The general term reflectance used in this thesis refers to $r_{rs}(\lambda)$. Subsurface irradiance reflectance $R(0\text{-})(\lambda)$ is given as (depth=0, spectrally dependant):

$$R(0-) = \frac{E_d}{E_u} \qquad (1.6)$$

where E_u is upwelling radiance.

Atmospheric correction of remote sensing data

Atmospheric correction is a crucial step in any time series analysis of satellite imagery as a satellite only captures a fraction of radiation coming from a target. Radiance recorded by remote sensing can be comprised of greater than 90% path radiance, which originates from scattering of solar radiation by air molecules and aerosols (suspended liquid and particles such as salt, dust, ash, pollen and sulphuric acid) (Vidot and Santer 2005). These molecules and particles can also attenuate radiation through absorption. Scattering can occur multiple times and there is variability of aerosol particulate distributions (Bukata et al. 1995), resulting in complex photon paths.

There are various methods of atmospheric correction, including radiative transfer modelling correction, image based correction and vicarious calibration correction.

Vicarious calibration involves measuring solar irradiance and reflectance concurrently with satellite overpass. The most common image-based atmospheric correction to estimate L_s involves dark object subtraction (DOS), in which the darkest pixel in each band is used as an estimate of path radiance, and is subtracted from radiance at the top of the atmosphere (Chavez 1996).

The application of radiative transfer models offers the flexibility to address the complexities of atmospheric correction over inland waters (e.g., Campbell et al. 2011). Such complexities include variations in elevation, which affect molecular calculations due to changes in air pressure, and adjacency effects. In addition, heterogeneous concentrations of aerosols and aerosol content at coastal and inland locations needs to be considered, although it is often assumed that aerosol optical depth (AOD) is homogenous at spatial scales of 50 to 100 km (Vidot and Santer 2005). There is also interaction of absorption and scattering, and the radiative transfer model must provide a complete description to provide accurate simulation. Gaseous absorption is therefore calculated for each scattering path whilst absorption is computed as a simple multiplicative factor. The principal absorbing gases are oxygen, ozone, water vapour, carbon dioxide, methane, and nitrous oxide, of which ozone and water vapour are assumed to vary most in time and space (Kotchenova et al. 2008). The calculation of scattering is much more complex, and includes contributions from Rayleigh and aerosols. Second Simulation of a Satellite Signal in the Solar Spectrum (6sv) (Kotchenova et al. 2008) is a radiative transfer atmospheric correction code accounting for radiation polarization, which enables accurate simulations of satellite and airborne observations, accounting for a molecular and aerosol mixed atmosphere.

An alternative approach to atmospheric correction of ocean colour data is the use of the SeaDAS range of atmospheric correction procedures (Ruddick et al. 2000; Wang et al. 2009; Bailey et al. 2010), which preserve the near infra-red (NIR) reflectance peak (Odermatt et al. 2012a). However, this procedure can return negative reflectance at blue wavelengths over turbid or inland waters (Goyens et al. 2013). A promising alternative, which obviates negative reflectance, is a neural network (NN) based inversion approach (Schroeder et al. 2007), which has been shown to outperform SeaDAS atmospheric correction algorithms over turbid waters (Goyens et al. 2013).

Water colour theory

The colour and clarity of water depend on its optical character, and relate to the bulk optical processes of absorption and scattering (Davies-Colley et al. 1993). Absorption and scattering characteristics of water are determined by inherent optical properties (IOPs). Absorption refers to the transfer of light energy into another form of energy (e.g., heat) and is quantified by the spectral absorption coefficient, $a(\lambda)$ (m^{-1}), which is the fraction of incident light absorbed divided by the thickness of the layer. Scattering is defined as deflection of light photons from their original path (Davies-Colley et al. 1993), and can be quantified by the spectral scattering coefficient, $b(\lambda)$ (m^{-1}), which is the fraction of the incident light which is scattered divided by the thickness of the layer (Kirk 2010). Light scattering is also quantified by the volume scattering function ($\beta(\theta)$), where θ is the forward scattering angle (Mobley 1994). The integral of $\beta(\theta)$ for angles from 0 to π yields b:

$$b = 2\pi \int_{0}^{\pi} \beta(\theta)\sin(\theta)d\theta \qquad (1.7)$$

The backscattering coefficient is a subset of the angle used to define b:

$$b_b = 2\pi \int_{\pi/2}^{\pi} \beta(\theta)\sin(\theta)d\theta \qquad (1.8)$$

The backscattering ratio B_b is defined as $b_b(\lambda)/b(\lambda)$.

Apparent optical properties (AOPs) are determined by the combined effects of the geometric structure of the light field and water constituents (Kirk 2010). They are therefore partly determined by the solar zenith angle and local atmospheric conditions (Bukata et al. 1995). The underwater vertical attenuation coefficient, Secchi depth and irradiance reflectance are considered to be AOPs (Preisendorfer

1976; Mobley 1994). In contrast IOPs are affected only be the medium, and radiative transfer theory describes the connection of IOPs and AOPs (Mobley 1994). The IOPs of a water body are completely quantified by the $\beta(\theta)$ and $a(\lambda)$ (Mobley 1994).

Clear water in natural ecosystems contains low concentrations of optically active constituents. Consequently the spectral reflectance is low and the spectral shape is similar to that for pure water molecules. It shows an exponential increase in absorption towards longer wavelengths and an increase in scattering at shorter wavelengths of the visible range of the electromagnetic spectrum (Rudorff et al. 2006).

Algae-laden water exhibits a reflectance peak in the green region, which represents an aggregate chl absorption minimum, and another reflectance peak at 700 nm. Absorption troughs occur in the blue and red/ IR wavelength range (Han 1997), with the exact location and width of these troughs dependent on phytoplankton species' assemblages and their physiological state (Kirk 2010). Fluorescence is an optical process which involves the absorption of part of the energy of a photon and re-radiation of a lower energy photon in an arbitrary direction, which can sometimes influence the colour of natural waters (Davies-Colley et al. 1993). Phytoplankton displays a fluorescence peak centred at 685 nm, meaning concentrations can be measured using fluorometers when photoreaction centres are not saturated (Yentsch and Yentsch 1979).

Tripton includes sand, silt, clay and other inorganic material such as atmospheric dust (Koponen 2006), as well as non-living organic matter. The optical properties of tripton are affected by the shape and size distribution of particles, which have a major effect on their absorption and scattering properties (Bukata et al. 1995). In clear water, increasing concentrations of tripton result in a linear increase in reflectance in the IR, with a coefficient of variation near to one. In this area of the electromagnetic spectrum the effect of chlorophyll (chl) *a* is negligible (Han 1997). In algae-laden water, additive effects of tripton on reflectance occur at all wavelengths (Bukata et al. 1995).

The absorption spectrum of coloured dissolved organic matter (CDOM) increases exponentially at shorter wavelengths of the visible spectrum and there is little absorption above 700 nm (Bricaud et al. 2009). The effect of CDOM on light scattering is minimal and can be ignored (Koponen 2006).

Methods of remote sensing of water quality

In Case 1 waters where variation in $r_{rs}(\lambda)$ is primarily due to phytoplankton, simple empirical band ratio models can be used to determine chl *a* (Gordon and Morel 1983). Case 2 waters are optically complex and $r_{rs}(\lambda)$ varies with differing IOPs and concentrations of optically active constituents, namely chl *a*, tripton and CDOM.

There are three general approaches of retrieving water quality parameters via remote sensing, including empirical, and analytical methods, with the term semi-empirical/analytical applied to approaches somewhere between the two (Carder et al. 1999). Empirical methods use statistical techniques to directly relate in situ samples to concurrently acquired satellite data. These models offer a simpler approach but have limited spatio-temporal applicability. Analytical methods are based on bio-optical models which use radiative transfer modelling or simplifications of radiative transfer models. Bio-optical models can be developed independently of in situ data, however, they require knowledge of, or assumptions about inherent optical properties. The spatio-temporal applicability of empirical and analytical models depends on variations in IOPs of the target water, and how these affect the water quality retrieval of the parameter of interest.

Bio-optical models and IOPs

Bio-optical models are generally used in two forms: complex radiative transfer models such as Hydrolight (Mobley 1994), and simplifications such as the analytical model of Gordon et al. (1988). In the latter model $r_{rs}(\lambda)$ is given by:

$$r_{rs}(\lambda) = g_0 u(\lambda) + g_1 [u(\lambda)]^2 \tag{1.9}$$

where:

$$u(\lambda) = \frac{b_b(\lambda)}{a(\lambda) + b_b(\lambda)} \qquad (1.10)$$

b_b(m^{-1}) is the total backscattering coefficient, a(m^{-1}) is the total absorption coefficient and g_o and g_1 are empirical constants that depend on the anisotropy of the downwelling light field and scattering processes within the water.

The model of Gordon et al. (1988) was successfully applied to eutrophic inland waters (Dekker et al. 1997) as (spectral dependence not shown):

$$R(0-) = r_1\left[\frac{b_b}{b_b + a}\right] \qquad (1.11)$$

where R(0-) is subsurface irradiance reflectance and r_1 depends on the anisotropy of the downwelling light field and scattering processes within the water.

The absorption and backscattering coefficients comprise the sum of individual optically active components;

$$b_b(\lambda) = b_{bw}(\lambda) + B_{bTR}\, b^*_{TR}(\lambda)\, C_{TR} + B_{b\phi}\, b^*_{\phi}(\lambda)\, C_{\phi} \qquad (1.12)$$

$$a(\lambda) = a_w(\lambda) + a^*_{\phi}(\lambda)\, \mathrm{C}_{\phi} + a^*_{TR}(\lambda)\, C_{TR} + a_{CDOM}(\lambda) \qquad (1.13)$$

$$a_{CDOM}(\lambda) = a_{CDOM}(\lambda_0)\, \exp[-S(\lambda-\lambda_0)] \qquad (1.14)$$

$$b^*_{TR}(\lambda) = b^*_{TR}(\lambda_0)\left(\frac{\lambda}{\lambda_0}\right)^n \qquad (1.15)$$

where:

(λ) = wavelength

(λ_0) = reference wavelength

$b_{bw}(\lambda)$ = backscattering coefficient of water

B_{pTR} = backscattering ratio of tripton

$b^*_{TR}(\lambda)$ = specific scattering coefficient of tripton

C_{TR} = concentration of tripton

$B_{p\phi}$= backscattering ratio of phytoplankton

$b^*_{\phi}(\lambda)$ = specific scattering coefficient of phytoplankton

$a_w(\lambda)$ = absorption coefficient of pure water

C_{ϕ} = concentration of chl *a*

$a^*_{\phi}(\lambda)$ = specific absorption coefficient of phytoplankton

a^*_{TR} = specific absorption coefficient of tripton

$a_{CDOM}(\lambda)$ = absorption by coloured dissolved organic matter (CDOM)

S = the spectral slope coefficient for $a_{CDOM}(\lambda)$

n = the exponent for tripton scattering

Inherent optical properties vary temporally and spatially (Kostadinov et al. 2010; Moisan et al. 2011; Devred et al. 2011), which presents a potential source of error when inverting bio-optical models in the estimation of optically active constituent concentrations. Variance in the phytoplankton pigment specific absorption coefficient ($a^*_{\phi}(\lambda)$) is a result of several factors such as phytoplankton pigment composition, cell size, packaging effect, light accumulation and nutrient limitation (Babin et al. 1993; Babin 2003; Bricaud 2004; Blondeau-Patissier et al. 2009). Variation of $a^*_{\phi}(\lambda)$ causes non-linearity between light absorption and chl *a* concentration (Bricaud and Morel 1981).

The backscattering ratio $B_{p\phi}$ and the specific scattering coefficient $b^*_{\phi}(\lambda)$ of phytoplankton are determined by the size, physical structure, and the outer coating of cells (Stramski et al. 2004). With increasing phytoplankton biomass there is greater cell wall surface area which causes increased scattering (Yacobi et al. 1995). The presence of gas vacuoles in some cyanobacteria has been found to substantially increase the value of $b^*_{\phi}(\lambda)$ (Dubelaar et al. 1987; Volten et al. 1998).

The specific scattering coefficient of tripton, $b^*_{TR}(\lambda)$, varies in time and space, mostly due to variations in particle size distribution and the bulk refractive index of the particles (Tzortziou et al. 2006). The refractive index of inorganic tripton is generally higher than that of organic particles (including phytoplankton) due to the high water content of organic material (Twardowski et al. 2001). The slope of the tripton backscattering coefficient is related to the particle size distribution and, in combination with angular scattering, can be used to estimate the refractive index of particles (Twardowski et al. 2001).

The spectral slope coefficient of CDOM, *S,* is known to vary with the proportion of fulvic and humic acids (Carder et al. 1989). Autochthonous sources of CDOM include decay products from phytoplankton, for example, which can lead to covariance of CDOM with chl *a* in open ocean waters (Carder et al. 1989). Allochthonous sources include decaying organic matter such as that derived from leaf litter, and are often associated with river inputs.

Bio-optical models have generally been applied to satellite imagery with high spectral resolution, and to hyperspectral data, both of which can be used to derive precise measurement of spectral slopes of reflectance. Various methods of solving (or inverting) these models are used including Monte Carlo simulation (Gordon & Brown 1973; Morel & Prieur 1977; Kirk 1981), invariant embedding (Preisendorfer 1976; Mobley 1994), matrix operator method (Fischer and Grassl 1984; Fell and Fischer 2001), and finite-element method (Kisselev et al. 1995; Bulgarelli et al. 1999). Bio-optical models have also been inverted efficiently using the Levenberg-Marquardt nonlinear least squares procedure (Maritorena et al. 2002; van der Woerd and Pasterkamp 2008) and neural networks (Doerffer and Schiller 2007).

Spaceborne earth observation sensors

There are three general categories of sensors for spaceborne remote sensing, including hyperspectral sensors such as Hyperion, broadband high spatial resolution terrestrial remote sensing sensors such as Landsat’s Enhanced Thematic Mapper (ETM+), and narrow band medium saptial resolution satellite sensors such as MOderate Resolution Imaging Spectroradiometer (MODIS) and MEdium Resolution Imaging Spectrometer (MERIS). Satellite Sensors vary in temporal, spatial, radiometric and spectral resolution. The spatial resolution will determine the minimum lake size that can be monitored via remote sensing, while the radiometric and spectral resolution will determine the complexity of any derived algorithms and the ability of the sensor to differentiate optically active constituents (Matthews 2011).

The MODIS sensor developed by NASA has been fitted to the Terra (data available from February 2000) and Aqua (data available from July 2002) satellite platforms, and enables twice-daily global coverage. NASA now has a policy of full and open sharing of imagery for Earth observing satellites spanning more than 40 years. This policy has contributed to increased use of remote sensing for many applications including monitoring quality of inland waters. The high spatial resolution of NASA Landsat series of sensors, and free availability of the data archive has in the past made Landsat the sensor of choice for monitoring inland water quality in small lakes. The Landsat satellite sensor has relatively high spatial resolution (30 m) compared with ocean colour sensors such as MODIS (250 - 1000 m resolution), and is therefore able to resolve finer-scale features within lakes, as well as to record data from small lakes where there would otherwise be inadequate resolution. Landsat Multispectral Scanner (MSS) imagery is available from 1972 to 1981, Landsat 5 Thematic Mapper (TM) was launched in 1984 and is still operating, and Landsat 7 ETM+ was launched in 1999. The repeat cycle of image capture is 16 days, and each scene is 185 km wide and 120 km high.

Ocean colour applications of remote sensing for optically active constituent retrieval of Case 2 waters

Remote sensing of Case 2 waters using ocean colour sensors has been applied using various algorithms to estimate optically active constituents, including traditional ocean colour band ratios, and empirical, semi-analytical, and analytical algorithms (Odermatt et al. 2012a). There has been a large body of research on remote sensing of the Laurentian Great Lakes (e.g., Budd et al. 2004, Binding et al. 2007; Witter et al. 2009; Binding et al. 2011; Mouw et al. 2013), and comparisons can be drawn with remote sensing of other environments. The trophic status of the Great Lakes ranges from oligotrophic in Lake Superior, to eutrophic (and higher) in the western basin of Lake Erie. In a recent review of satellite ocean colour algorithms applied to the Great Lakes (Lesht et al. 2011), it was shown that no single retrieval method produced consistent results due to the unpredictable nature of the IOPs. The review by Lesht et al. (2011) highlighted the complexities of remote sensing of Case 2 waters, and demonstrated the complicated and often conflicting information that has been presented in the literature. As with the Great lakes, universally applicable algorithms for the remote sensing of optically active constituents have not yet been established (Odermatt et al. 2012a). Band ratio ocean colour algorithms have been applied with various degrees of success. In some instances, there are strong linear relationships between retrieved and in situ chl *a*, however, the slope of the relationships often deviates significantly from one, requiring some regional parameterisation. Budd and Warrington (2004) applied the OC2-V2 algorithm in oligotrophic Lake Superior, and found strong co-variance between estimated chl *a* with in situ samples, but there was a three-fold overestimate of chl *a* concentration. Witter et al. (2009) compared 12 empirical ocean colour algorithms for assessment of chl *a* concentration in Lake Erie, and found reasonable relationships between in situ and satellite-derived chl *a*, but with significant bias at high and low chl *a* concentrations. These authors then developed a regional empirical algorithm specific to the western, eastern and central basins of Lake Erie and concluded that the eastern and central basin algorithms produced promising results, however, regional algorithms were not applicable to the western basin.

Empirical ocean colour algorithms have been applied assuming Case 1 conditions in inland waters (e.g., Heim 2005; Horion et al. 2010), however, in a review paper of remote sensing of Case 2 waters, inaccuracies in chl *a* retrieval were considered to result from independently varying CDOM concentrations, especially at short wavelengths (Odermatt et al. 2012a). Using a bio-optical model based on that of Bukata et al. (1985), Lesht et al. (2011) demonstrated that traditional empirical and band ratio algorithms for chl *a* retrieval are susceptible to error due to varying concentrations of CDOM and tripton. Modifications have been applied to ocean colour algorithms in order to minimise the influence of CDOM using MERIS data, with some success in oligotrophic waters of Lake Superior (Gons et al 2008).

However, their retrieval approached an asymptote at chl *a* concentrations above 2.7 μg L^{-1}, and is therefore not applicable to meso and eutrophic waters.

Fluorescence line height (FLH) algorithms use a relative measure of reflectance at chlorophyll fluorescence emission wavelengths (which is not necessarily derived solely from fluorescence). Gons et al (2008) demonstrated that FLH algorithms were promising at estimating chl *a* in oligotrophic waters but in practice produced noisy retrievals of chl *a*, likely due to the low chl *a* (0.4-0.8 μg L^{-1}).

Semi-analytical algorithms have been applied to remote sensing of optically active constituents in the Great Lakes. They can be used to estimations total suspended sediment (SS) by inversion of field-measured subsurface irradiance reflectance (Bukata et al. 1985); and inversion of MODIS volume reflectance (Binding et al. 2010) and CDOM (Bukata et al. 1985; Mouw et al. 2013). The success of bio-optical models for the estimation of chl *a* ranged from complete failure (e.g., Bukata et al. 1985; Mouw et al. 2013) to algorithms with poor accuracy (e.g. Li et al. 2004; Shuchman et al. 2006). Mouw et al. (2013) attributed the failure of the bio-optical algorithm in retrieving chl *a* in Lake Superior to the dominant influence of CDOM on the absorption budget. Bukata et al. (1985) attributed the chl *a* retrieval failure to varying IOPs, and the dominance of non-algal particles (NAP) and CDOM on reflection. Shuchman et al. (2006) applied a version of the Bukata et al. (1985) algorithm using updated IOPs from Bukata et al (1991), however, chl *a* retrievals were underestimated by an order of magnitude (Lesht et al. 2006).

In addition to the complexities of remote sensing of water quality caused by independently varying concentrations of optically active constituents in Case 2 waters, there may be atmospheric correction errors resulting from incorrect assumptions such as the use of fixed aerosol models (Odermatt et al. 2008). Accurate atmospheric correction is critical for remote sensing of oligotrophic lakes, as the reflectance of surface water is small compared to the atmospheric path radiance (Guanter et al. 2010). Adjacency effects also tend to be more pronounced for oligotrophic waters with low reflectivity (Odermatt et al. 2008).

For the estimation of chl *a* concentrations for oligotrophic inland waters, it has been suggested that more complex, physically based inversion models are needed (Odermatt et al. 2010). The Modular Inversion and Processing System (MIP) is a set of processing tools for the retrieval of water and atmosphere (look up table approach) constituents from hyperspectral and multispectral satellite data (Heege and Fischer 2004). Odermatt et al. (2008) used MIP for the retrieval of chl *a* from MERIS imagery in oligotrophic to mesotrophic Lake Constance, Germany. The authors stated that the correlation between retrieved and in situ chl *a* was “sufficient” considering that the time differences between in situ and satellite image acquisition were up to three days (and in some instances longer). Odermatt et al. (2008) considered that atmospheric correction was the greatest potential source of error (including adjacency effects) but did not state the level of error, however, the method may not provide sufficient resolution for determining small changes in chl *a* (c. 1 μg L^{-1}) in oligotrophic waters.

While remote sensing of water quality by NASA has been focused on coastal and oceanic waters, the European Space Agency (ESA) has also funded research on development of Case 2 coastal water quality algorithms (including the MERIS algal_2 product), and MERIS lake water quality algorithms including Case-2 Regional (C2R), Boreal Lakes and Eutrophic Lakes water quality retrieval algorithms (Doerffer and Schiller 2007, 2008). The MERIS Case 2 water quality algorithm uses a neural network (NN) inversion technique to retrieve chl *a*, SS and a_{CDOM} (λ). The NN construction is based on 550 000 simulated entries from a forward model built using HYDROLIGHT radiative transfer code and a bio-optical model which relates IOPs to optically active constituent concentrations (Doerffer and Schiller 2007). The Case 2 Boreal processor NN was trained using IOPs from Finnish lakes, and the Eutrophic Lakes was trained using IOPs from Spanish lakes (Doerffer and Schiller 2008).

Odermatt et al. (2010) used the MERIS C2R processor for the retrieval of chl *a* in six perialpine lakes (including Lake Constance). It was shown that the C2R processer was applicable to oligotrophic and mesotrophic lakes, however, the RMSE of derived chl *a* in oligotrophic waters was similar in magnitude to the in situ chl *a* during oligotrophic periods. The authors concluded that the MERIS C2R chl *a* product did not possess the level of accuracy needed to replace traditional in situ monitoring, but rather was a compliment to it. Of particular note was that the authors found that remotely sensed estimates of chl *a* compared better to depth resolved in situ chl *a* (0-5 m) than to vertically integrated chl *a* (0-20 m) in Lake Constance, although visual comparison of Figures 6 and 10 in Odermatt et al. (2010) does not offer strong support for this statement.

While the MERIS C2R algorithms are applicable to chl *a* estimation in oligotrophic (with limitations discussed above) and mesotrophic lakes (Odermatt et al 2010), application to lakes with very high chl *a* concentrations associated with cyanobacteria blooms has been less successful (e.g., Matthews et al. 2010; Binding et al. 2011). For example, Matthews et al. (2010) found MERIS Eutrophic Lake and the standard Level 2 Case 2 coastal water quality retrieval algorithm estimations of chl *a* did not compare well with in situ chl *a* in a small hypertrophic lake . This failure was attributed to errors in atmospheric correction and the fact that the MERIS NN was not trained with comparable IOPs and concentration ranges to those of the lake in question. However, Matthews et al. (2010) showed strong empirical relationships between satellite data and in situ chl *a* and SS (particularly the 708/664 nm reflectance ratio), although these relationships had limited ability to separate reflectance contributions from co-varying constituents.

Odermatt et al. (2012b) evaluated MERIS C2R, Eutrophic Lakes, and the WeW (Schroeder et al. 2007) algorithms for the observation of phytoplankton blooms in a stratified eutrophic lake. Estimated chl *a* showed better comparison to in situ chl *a* than those in the study of Matthews et al. (2010), however, in situ chl *a* was much lower in their study. The authors suggested that with some regional calibration for the specific absorption coefficient of phytoplankton, the MERIS algorithms had good potential for monitoring chl *a* in eutrophic lakes. Using vertical measurements of chlorophyll fluorescence, however, Odermatt et al. (2012b) demonstrated that remote sensing estimates of chl *a* are constrained by inability to resolve vertical variations in chl *a*. For monitoring both vertical and horizontal distributions of phytoplankton, the authors recommended complementing remote sensing of chl *a* with vertical measurements of chl fluorescence.

For remote sensing of chl *a* in turbid eutrophic waters, red and NIR bands have proved to be effective. Gons et al. (2008) demonstrated that MERIS data combined with semi-analytical algorithm using red to NIR ratios and an apparent backscatter coefficient, worked well in the estimation of chl *a* in eutrophic Green Bay, Lake Michigan. Gitelson et al. (2008) developed a simple semi-analytical model for estimation of chl *a* in turbid waters, applicable to three bands of MERIS and two bands of MODIS sensors, using red and NIR bands. Their algorithm has application in waters with chl *a* ranging from 10-200 µg L^{-1}, however, in oligotrophic lakes the NIR reflectance peak required by the algorithm is not present (Giardino et al. 2007; Odermatt et al. 2008). More recently Gurlin et al. (2011) showed that simple two-band red-NIR models outperform more complex red-NIR algorithms for retrieving chl *a* using MERIS and MODIS applications to turbid productive waters. While these red-NIR based algorithms were applicable for estimation of chl *a* in turbid waters, they could not differentiate signals from covariant optically active constituents.

In order to obviate or minimise errors in optically active constituent retrieval which occur where multiple constituents contribute significantly to $r_{rs}(\lambda)$, there has been increased focus on analytical spectral inversion algorithms to estimate concentrations of chl *a*, CDOM and tripton/SS simultaneously (Matthews 2011, Odermatt et al. 2012a). For example, Campbell et al. (2011) applied a bio-optical model to retrieve chl *a*, CDOM and SS from a freshwater impoundment in Australia, using the MERIS satellite platform. They concluded that significant improvements in model accuracy could be achieved using differentially weighted and over-determined equation systems.

As demonstrated from the literature above, universally applicable algorithms for the remote sensing of optically active constituents have not yet been established, primarily due to spatio-temporal variation in OAC-specific IOPs. Algorithms that return IOPs (as opposed to retrieving OACs) in Case 2 waters have greater flexibility (e.g., Pinkerton et al. 2006; van der Woerd and Pasterkamp 2008), allowing for the total absorption and scattering to be decomposed into OACs in separate calculations. The current best-practice in models accounts for optically complex waters where temporal and spatial variation of OAC IOPs occurs (e.g., Doerffer and Schiller 2007, Brando et al. 2012). Of particular note, is the adaptive implementation of the linear matrix inversion method developed by Brando et al. (2012), which was demonstrated on a simulated MODIS data set for the retrieval of IOPs, OAC concentrations and CDOM absorption. The authors concluded that the adaptive implementation of linear matrix inversion resulted in greater accuracy of OAC and IOP retrievals, particularly for phytoplankton IOPs, and chl *a* concentrations.

Broadband applications of remote sensing for water quality retrieval

In a recent review of empirical algorithms (including some bio-optical algorithms) for the remote sensing of inland and coastal water quality (Matthews 2011), 27 studies were identified which used broadband Landsat ETM or TM satellite data to retrieve chl *a*, turbidity, SS, or Secchi depth. The review showed that these water quality parameters can in some instances be obtained with high coefficients of determination with satellite reflectance (e.g., $r^2 = 0.99$ for the retrieval of SS (Dekker et al. 2002), and $r^2 = 0.99$ for the retrieval of chl *a* (Giardino et al. 2001)). Despite the potential of the Landsat satellite to estimate water quality, there are only a small number of examples of remote sensing of inland water quality over landscape scales (e.g., Lillesand et al. 1983; Dekker et al. 2001; Koponen 2006), and even fewer applications over a time series of images (e.g., Dekker et al. 2001; Olmanson et al. 2008).

Of the Landsat studies cited above, only a few examine the underlying physical basis for the development of statistical algorithms (e.g., Dekker and Peters 1993; Gitelson et al. 1996; Brivio et al. 1997; Dekker et al. 2002). The study of Allan et al. (2011) is typical of many empirically based Landsat studies of remote sensing of water quality, and while useful for determining spatial distributions of chl *a* at landscape scape, any derived algorithms have limited applicability in time beyond the spatial domain used in calibration.

More complex empirical algorithms such as linear mixture modelling (LMM) (Tyler et al. 2006) attempt to differentiate OACs. Linear mixture modelling (Tyler et al 2006) and spectral decomposition algorithms (Oyama et al. 2007, 2009) applied to Landsat have shown considerable promise in differentiating SS or tripton, and chl *a*, and it surprising that there have been few other applications of this method, possibly due to difficulty in reproducing the methodology.

Broadband remote sensing instruments such as Landsat can simultaneously record average spectral slopes of both positive and negative radiance values, as opposed to hyperspectal data (Bukata et al. 1995), but there have also been successful applications of bio-optical models for single water quality parameter retrieval using broadband sensors where the optically active constituent of interest dominates reflectance. For example bio-optical models have been used to map horizontal distributions of SS concentrations in lakes using Landsat and Spot satellite data (Dekker et al. 2002). The advantage of bio-optical models is that in situ data are not needed at the time of image capture, allowing for multi-site, and multi-sensor comparisons over time. Dekker et al. (2002), for example, found that semi-analytical algorithms for SS were more reliable and temporally robust than empirical algorithms.

Hydrodynamic and ecological modelling and validation using remote sensing

Hydrodynamic and ecological models of lakes can help to understand the complex dynamics of abiotic and biotic interactions that affect water quality. Models can be used to forecast water quality at some future point in time and can provide a valuable tool for water quality managers to estimate the effect of future perturbation in environmental factors, including catchment land use and climate (Trolle et al. 2011). Only a small number of studies have attempted to synoptically quantify the validity of the modelled water quality or temperature in the horizontal direction using grab-samples (e.g., Huang et al. 2012; Leon et al. 2011), possibly owing to the difficulties and cost of acquisition of a large number of samples within a short time interval in aquatic systems of sufficient size to be suitable for remote sensing and examination of spatial variability. Remote sensing can provide synoptic data for this type of validation, although most studies have undertaken a qualitative (as opposed to quantitative) comparison between modelled and remotely sensed water quality or temperature (e.g., Spillman et al. (2007) for surface water temperature and chl *a* retrieval in the Northern Adriatic Sea, and Hedger et al. (2002) for chl *a* retrieval in Loch Leven).

Remote sensing derived water quality parameters can also be used to initialise 3-D models, and update simulated distributions. For example, Natvik & Evensen (2003) assimilated estimated chl *a* concentrations from SeaWiFS satellite imagery into a coupled 3-D hydrodynamic-ecological model, in order to improve the simulation of chl *a* spatial distributions. Similarly, Li (2007) assimilated reflectance derived from MODIS to provide a dynamic feedback mechanism to enable an improvement in the simulation of suspended sediment distributions in Lake Ontario. Landsat provides higher resolution data needed to validate fine scale features with lakes such as inflows. For example, Pahlevan et al. (2011) used thermal data derived from Landsat 7 to calibrate a 3-D hydrodynamic model of a river inflow plume in Lake Ontario. Multiple scenarios of environmental conditions (including varying inflow volumes) were run, and an optimization procedure was used in order to match model simulations of water surface temperature with satellite estimations, based on minimizing pixel-based root mean squared error (RMSE).

1.2 Major objectives

The overarching objective of this thesis was to develop methods for the remote sensing-based estimation of surface water temperature and optically active constituents (OACs) in lakes. Study sites of varying optical complexity and lake size have been selected to ensure that the methods developed within this thesis were applicable to a range of lake trophic states and sizes, and satellite spectral and spatial resolutions. The study investigates empirical, semi-analytical and analytical algorithms for OACs retrieval, for the purpose of providing flexibility to match specific algorithms to the optical complexity of the system and the OACs of interest.

Bio-optical theory has been used to identify possible sources of constituent estimation error and determine the potential transferability of derived algorithms. Additionally, image processing methodology was developed using discreet automated routines which can be executed individually or subsequently with a view to initiating a process of automation of image processing based on a repeatable method within a flexible code development environment.

A secondary overarching objective of this thesis was to combine remote sensing and 3-D hydrodynamic-ecological modelling of temperature and suspended sediment concentrations in a lake. This component was used to demonstrate application of state of the art spatial statistical methods to quantitatively validate 3-D numerical model simulations of surface water temperature and suspended minerals against those estimated from satellite imagery.

1.3 Thesis overview

This thesis consists of four self-contained research chapters (Chapters 2-5) which have been prepared for, or submitted to, scientific journals. In the final chapter (Chapter 6), the research of the thesis is summarised and conclusions are drawn based on the results from chapters 2-5.

In Chapter 2, empirical and semi-analytical algorithms were developed to estimate ch *a* in the Rotorua lakes, North Island, New Zealand. An automated image processing methodology was developed in order to process 106 atmospherically corrected Landsat satellite images. A bio-optical model was applied to examine the underlying physical mechanisms responsible for empirical relationships between Landsat subsurface irradiance reflectance and in situ chl *a*.

In Chapter 3, atmospheric correction of Landsat thermal imagery was evaluated for surface water temperature retrieval in the Rotorua lakes. The retrieved water temperatures from 14 images between 2007 and 2009 were validated using data from a high-frequency temperature sensor deployed at the water surface of a mid-lake monitoring buoy on one of the lakes, Rotorua. Within close proximity to Lake Rotorua, and within the same Landsat scene, is Lake Rotoehu for which a 3-D hydrodynamic model was run to assess spatial heterogeneity of surface water temperatures. Remotely sensed estimations of surface water temperature were then compared with simulated surface water temperature using statistics specific for spatially resolved data.

In Chapter 4, remote sensing of total suspended sediments (SS) and suspended minerals (SM) was evaluated using empirical and semi-analytical algorithms applied to MODIS B1 data. The study site was Lake Ellesmere (South Island, New Zealand), a large, highly turbid, shallow coastal lagoon which has undergone eutrophication. Remote sensing-derived estimations of SM concentrations were compared with simulations of SM derived from 1-D and 3-D hydrodynamic models, using multiple state of the art spatial statistic metrics.

In Chapter 5, a bio-optical model was used to derive chl *a* concentration, SS concentration and CDOM /detritus absorption at 443 nm in Lake Taupo, using MODIS imagery. The purpose of model development was to enable future near real time monitoring of water quality in a highly oligotrophic lake. The model was optimised using in situ IOPs from the literature and images were atmospherically corrected using a radiative transfer model. A seasonally varying specific phytoplankton absorption coefficient was applied, which resulted in a significant improvement in accuracy of chl *a* retrieval, as opposed to using a model with a fixed specific phytoplankton absorption coefficient. Use of empirical relationships between bio-optical-estimated SS and B1 subsurface remote sensing reflectance will allow increased temporal resolution of monitoring, and enable both basin-scale and fine-scale circulation features could be resolved.

1.4 References

Allan, M. G., D. P. Hamilton, B. J. Hicks, and L. Brabyn. 2011. Landsat remote sensing of chlorophyll *a* concentrations in central North Island lakes of New Zealand. International Journal of Remote Sensing **32**: 2037–2055.

Babin, M. 2003. Variations in the light absorption coefficients of phytoplankton, nonalgal particles, and dissolved organic matter in coastal waters around Europe. Journal of Geophysical Research **108**: 3211.

Babin, M., J.-C. Therriault, L. Legendre, and A. Condal. 1993. Variations in the specific absorption coefficient for natural phytoplankton assemblages: Impact on estimates of primary production. Limnology and Oceanography **38**: 154–177.

Bailey, S. W., B. A Franz, and P. J. Werdell. 2010. Estimation of near-infrared water-leaving reflectance for satellite ocean color data processing. Optics express **18**: 7521–7.

Binding, C. E., J. H. Jerome, R. P. Bukata, and W. G. Booty. 2007. Trends in water clarity of the lower Great Lakes from remotely sensed aquatic color. Journal of Great Lakes Research **33**: 828–841.

Binding, C. E., J. H. Jerome, R. P. Bukata, and W. G. Booty. 2010. Suspended particulate matter in Lake Erie derived from MODIS aquatic colour imagery. International Journal of Remote Sensing **31**: 5239–5255.

Binding, C. E., T. A. Greenberg, J. H. Jerome, R. P. Bukata, and G. Letourneau. 2011. An assessment of MERIS algal products during an intense bloom in Lake of the Woods. Journal of Plankton Research **33**: 793–806.

Blondeau-Patissier, D., V. E. Brando, K. Oubelkheir, A. G. Dekker, L. A. Clementson, and P. Daniel. 2009. Bio-optical variability of the absorption and scattering properties of the Queensland inshore and reef waters, Australia. Journal of Geophysical Research **114**: C05003.

Brando, V. E., A. G. Dekker, Y. J. Park, and T. Schroeder. 2012. Adaptive semianalytical inversion of ocean color radiometry in optically complex waters. Applied Optics **51**: 2808–2833.

Bricaud, A. 2004. Natural variability of phytoplanktonic absorption in oceanic waters: Influence of the size structure of algal populations. Journal of Geophysical Research **109**: C11010.

Bricaud, A., and A. Morel. 1981. Theoretical results concerning light absorption in a discrete medium, and application to specific absorption of phytoplankton. Deep Sea Research. Part A. Oceanographic Reseach Papapers **28**: 1375–1393.

Bricaud, A., A. Morel, and L. Prieur. 2009. Absorption by dissolved organic matter of the sea (yellow substance) in the UV and visible domains. Limnology **26**: 43–53.

Brivio, P. A., C. Giardino, and E. Zilioli. 1997. The satellite derived optical information for the comparative assessment of lacustrine water quality. Science of the Total Environment **196**: 229–245.

Budd, J. W., and D. S. Warrington. 2004. Satellite-based sediment and chlorophyll *a* estimates for Lake Superior. Journal of Great Lakes Research **30**: 459–466.

Bukata, R. P., J. E. Bruton, and J. H. Jerome. 1985. Application of direct measurements of optical parameters to the estimation of lake water quality indicators. Environment Canada Inland Waters Directorate Scientific Series, No 10, 35 pp.

Bukata, R. P., J. H. Jerome, K. Y. Kondratyev, and D. V Pozdnyakov. 1995. Optical Properties and Remote Sensing of Inland and Coastal Waters. CRC Press, Boca Raton, Florida, USA.

Bulgarelli, B., V. B. Kisselev, and L. Roberti. 1999. Radiative transfer in the atmosphere-ocean system: the finite-element method. Applied Optics **38**: 1530–1542.

Campbell, G., S. R. Phinn, A. G. Dekker, and V. E. Brando. 2011. Remote sensing of water quality in an Australian tropical freshwater impoundment using matrix inversion and MERIS images. Remote Sensing of Environment **115**: 2402–2414.

Carder, K. L., F. R. Chen, Z. P. Lee, S. K. Hawes, and D. Kamykowski. 1999. Semianalytic Moderate-Resolution Imaging Spectrometer algorithms for chlorophyll a and absorption with bio-optical domains based on nitrate-depletion temperatures. Journal of Geophysical Research **104**: 5403–5421.

Carder, K. L., R. G. Steward, G. R. Harvey, and P. B. Ortner. 1989. Marine humic and fulvic acids: Their effects on remote sensing of ocean chlorophyll. Limnology and Oceanography **34**: 68–81.

Chavez, P. S. 1996. Image-based atmospheric corrections-revisited and improved. Photogrammetric Engineering and Remote Sensing **62**: 1025–1036.

Davies-Colley, R. J., W. N. Vant, and D. G. Smith. 1993. Colour and Clarity of Natural Waters. Ellis Horwood, London.

Dekker, A. G., and S. W. M. Peters. 1993. The use of the Thematic Mapper for the analysis of eutrophic lakes: a case study in the Netherlands. International Journal of Remote Sensing **14**: 799–821.

Dekker, A. G., H. J. Hoogenboom, L. M. Goddijn, and T. J. M. Malthus. 1997. The relation between inherent optical properties and reflectance spectra in turbid inland waters. Remote Sensing Reviews **15**: 59–74.

Dekker, A. G., R. J. Vos, and S. W. M. Peters. 2001. Comparison of remote sensing data, model results and in situ data for total suspended matter (TSM) in the southern Frisian lakes. The Science of the Total Environment **268**: 197–214.

Dekker, A. G., R. J. Vos, and S. W. M. Peters. 2002. Analytical algorithms for lake water TSM estimation for retrospective analyses of TM and SPOT sensor data. International Journal of Remote Sensing **23**: 15–35.

Dekker, A. G., Ž. Zamurović-Nenad, H. J. Hoogenboom, and S. W. M. Peters. 1996. Remote sensing, ecological water quality modelling and in situ measurements: a case study in shallow lakes. Hydrological Sciences Journal **41**: 531–547.

Devred, E., S. Sathyendranath, V. Stuart, and T. Platt. 2011. A three component classification of phytoplankton absorption spectra: Application to ocean-color data. Remote Sensing of Environment **115**: 2255–2266.

Doerffer, R., and H. Schiller. 2007. The MERIS Case 2 water algorithm. International Journal of Remote Sensing **28**: 517–535.

Doerffer, R., and H. Schiller. 2008. Algorithm Theoretical Basis Document (ATBD) Lake Water Algorithm for BEAM. GKSS Forschungszentrum Geesthacht GmbH 21502 Geesthacht, pp. 15.

Dubelaar, G. B., J. W. Visser, and M. Donze. 1987. Anomalous behaviour of forward and perpendicular light scattering of a cyanobacterium owing to intracellular gas vacuoles. Cytometry **8**: 405–412.

Fell, F., and J. Fischer. 2001. Numerical simulation of the light field in the atmosphere-ocean system using the matrix-operator method. Journal of Quantitative Spectroscopy and Radiative Transfer **69**: 351–388.

Fischer, J., and H. Grassl. 1984. Radiative transfer in an atmosphere-ocean system: an azimuthally dependent matrix-operator approach. Applied Optics **23**: 1032.

Giardino, C., M. Pepe, P. Brivio, P. Ghezzi, and E. Zilioli. 2001. Detecting chlorophyll, Secchi disk depth and surface temperature in sub-alpine lake using Landsat Imagery. The Science of the Total Environment **268**: 19–29.

Giardino, C., V. E. Brando, A. G. Dekker, N. Strömbeck, and G. Candiani. 2007. Assessment of water quality in Lake Garda (Italy) using Hyperion. Remote Sensing of Environment **109**: 183–195.

Gitelson, A. A., Y. Z. Yacobi, A. Karnieli, and N. Kress. 1996. Reflectance spectra of polluted marinewaters in Haifa Bay, Southeastern Mediterranean: features and application for remote estimation of chlorophyll concentration. Israel Journal of Earth Sciences **45**: 127–136.

Gitelson, A., G. Dallolmo, W. Moses, D. Rundquist, T. Barrow, T. Fisher, D. Gurlin, and J. Holz. 2008. A simple semi-analytical model for remote estimation of chlorophyll-a in turbid waters: Validation. Remote Sensing of Environment **112**: 3582–3593.

Gons, H. J., M. T. Auer, and S. W. Effler. 2008. MERIS satellite chlorophyll mapping of oligotrophic and eutrophic waters in the Laurentian Great Lakes. Remote Sensing of Environment **112**: 4098–4106.

Gordon, H. R., and A. Morel. 1983. Remote Assessment of ocean color for interpretation of satellite visible imagery: A Review. T.R. Barber, C.N.K. Mooers, M.J. Bowman, and B. Zeitzsche [eds.]. Springer-Verlag, New York.

Gordon, H. R., and O. B. Brown. 1973. Irradiance reflectivity of a flat ocean as a function of its optical properties. Applied Optics **12**: 1549–1551.

Gordon, H. R., J. W. Brown, O. B. Brown, R. H. Evans, and R. C. Smith. 1988. A semianalytic radiance model of ocean color. Journal of Geophysical Research **93**: 10909–10924.

Goyens, C., C. Jamet, and T. Schroeder. 2013. Evaluation of four atmospheric correction algorithms for MODIS-Aqua images over contrasted coastal waters. Remote Sensing of Environment **131**: 63–75.

Guanter, L., A. Ruiz-Verdú, D. Odermatt, C. Giardino, S. Simis, V. Estellés, T. Heege, J. A. Domínguez-Gómez, and J. Moreno. 2010. Atmospheric correction of ENVISAT/MERIS data over inland waters: Validation for European lakes. Remote Sensing of Environment **114**: 467–480.

Gurlin, D., A. A. Gitelson, and W. J. Moses. 2011. Remote estimation of chl-a concentration in turbid productive waters — Return to a simple two-band NIR-red model? Remote Sensing of Environment **115:** 3479–3490

Hamill, K. 2006. Snapshot of Lake Water Quality in New Zealand. Ministry for the Environment, New Zealand, ISBN 0-478-30107-3, ME number: 776.

Han, L. H. 1997. Spectral reflectance with varying suspended sediment concentrations in clear and algae-laden waters. Photogrammetric Engineering and Remote Sensing **63**: 701–705.

Hedger, R. D., N. R. B. Olsen, T. J. Malthus, and P. M. Atkinson. 2002. Coupling remote sensing with computational fluid dynamics modelling to estimate lake chlorophyll-a concentration. Remote Sensing of Environment **79**: 116–122.

Heege, T., and J. Fischer. 2004. Mapping of water constituents in Lake Constance using multispectral airborne scanner data and a physically based processing scheme. Canadian Journal of Remote Sensing **30**: 77–86.

Heim, B. 2005. Qualitative and Quantitative Analyses of Lake Baikal’s Surface-Waters Using Ocean Colour Satellite Data (SeaWiFS). Ph.D. thesis. Mathematisch-Naturwissenschaftlichen Fakultät der Universität Potsdam, Germany.

Horion, S., N. Bergamino, S. Stenuite, J.-P. Descy, P.-D. Plisnier, S. A. Loiselle, and Y. Cornet. 2010. Optimized extraction of daily bio-optical time series derived from MODIS/Aqua imagery for Lake Tanganyika, Africa. Remote Sensing of Environment **114**: 781–791.

Huang, J., J. Gao, and G. Hörmann. 2012. Hydrodynamic-phytoplankton model for short-term forecasts of phytoplankton in Lake Taihu, China. Limnologica - Ecology and Management of Inland Waters **42**: 7–18.

Jorgensen, S. 2008. Overview of the model types available for development of ecological models. Ecological Modelling **215**: 3–9.

Kallio, K. 2012. Water quality estimation by optical remote sensing in boreal lakes. Ph.D. thesis. University of Helsinki, Finland.

Kirk, J. T. O. 1981. Monte Carlo procedure for simulating the penetration of light into natural waters. Australian Journal of Marine and Freshwater Research **36**: 1–16.

Kirk, J. T. O. 2010. Light and Photosynthesis in Aquatic Ecosystems, 3rd ed. Cambridge University Press, Cambridge, UK.

Kisselev, V. B., L. Roberti, and G. Perona. 1995. Finite-element algorithm for radiative transfer in vertically inhomogeneous media: numerical scheme and applications. Applied Optics **34**: 8460.

Kloiber, S. M., P. L. Brezonik, and M. E. Bauer. 2002. Application of Landsat imagery to regional-scale assessments of lake clarity. Water Research **36**: 4330–4340.

Koponen, S. 2006. Remote sensing of water quality for Finnish lakes and coastal areas. Ph.D. thesis. Helsinki University of Technology, Finland.

Kostadinov, T. S., D. A. Siegel, and S. Maritorena. 2010. Global variability of phytoplankton functional types from space: assessment via the particle size distribution. Biogeosciences **7**: 4295–4340.

Kotchenova, S. Y., E. F. Vermote, R. Levy, and A. Lyapustin. 2008. Radiative transfer codes for atmospheric correction and aerosol retrieval: intercomparison study. Applied Optics **47**: 2215–2226.

Lee, Z., K. L. Carder, and R. A. Arnone. 2002. Deriving inherent optical properties from water color: a multiband quasi-analytical algorithm for optically deep waters. Applied Optics **41**: 5755–5772.

Leon, L. F., R. E. H. Smith, M. R. Hipsey, S. A. Bocaniov, S. N. Higgins, R. E. Hecky, J. P. Antenucci, J. A. Imberger, and S. J. Guildford. 2011. Application of a 3D hydrodynamic–biological model for seasonal and spatial dynamics of water quality and phytoplankton in Lake Erie. Journal of Great Lakes Research **37**: 41–53.

Lesht, B. M., R. P. Barbiero, and G. J. Warren. 2011. Satellite ocean color algorithms: A review of applications to the Great Lakes. Journal of Great Lakes Research **38**: 49–60.

Li, H., J. W. Budd, and S. Green. 2004. Evaluation and regional optimization of bio-optical algorithms for central Lake Superior. Journal of Great Lakes Research **30**: 443–458.

Li, Y. 2007. An integrated water quality modeling system with dynamic remote sensing feedback. Ph.D. thesis. Rochester Institute of Technology, New York, USA.

Lillesand, T. M., W. L. Johnson, R. L. Deuell, O. M. Lindstrom, and D. E. Meisner. 1983. Use of Landsat data to predict the trophic state of Minnesota lakes. Photogrammetric Engineering and Remote Sensing **49**: 219–229.

Maritorena, S., D. A. Siegel, and A. R. Peterson. 2002. Optimization of a semianalytical ocean color model for global-scale applications. Applied optics **41**: 2705–14.

Matthews, M. 2011. A current review of empirical procedures of remote sensing in inland and near-coastal transitional waters. International Journal of Remote Sensing **32**: 6855–6899.

Matthews, M. W., S. Bernard, and K. Winter. 2010. Remote sensing of cyanobacteria-dominant algal blooms and water quality parameters in Zeekoevlei, a small hypertrophic lake, using MERIS. Remote Sensing of Environment **114**: 2070–2087.

Mobley, C. D. 1994. Light and Water, Radiative Transfer in Natural Waters. Academic Press, San Diego, USA.

Moisan, J. R., T. A. H. Moisan, and M. A. Linkswiler. 2011. An inverse modeling approach to estimating phytoplankton pigment concentrations from phytoplankton absorption spectra. Journal of Geophysical Research **116**: 1–16.

Morel, A., and L. Prieur. 1977. Analysis of variations in ocean color. Limonology and Oceanography **22**: 709–722.

Mouw, C. B., H. Chen, G. A. Mckinley, S. Effler, D. O. Donnell, M. G. Perkins, and C. Strait. 2013. Evaluation and optimization of bio-optical inversion algorithms for remote sensing of Lake Superior’s optical properties. Journal of Geophysical Research: Oceans **118**: 1–19.

Natvik, L., and G. Evensen. 2003. Assimilation of ocean colour data into a biochemical model of the North Atlantic Part 1. Data assimilation experiments. Journal of Marine Systems **40-41**: 127–153.

Odermatt, D., A. Gitelson, V. E. Brando, and M. Schaepman. 2012a. Review of constituent retrieval in optically deep and complex waters from satellite imagery. Remote Sensing of Environment **118**: 116–126.

Odermatt, D., C. Giardino, and T. Heege. 2010. Chlorophyll retrieval with MERIS Case-2-Regional in perialpine lakes. Remote Sensing of Environment **114**: 607–617.

Odermatt, D., F. Pomati, J. Pitarch, J. Carpenter, M. Kawka, M Schaepman, and A. Wüest. 2012b. MERIS observations of phytoplankton blooms in a stratified eutrophic lake. Remote Sensing of Environment **126**: 232–239.

Odermatt, D., T. Heege, J. Nieke, M. Kneubühler, and K. Itten. 2008. Water quality monitoring for Lake Constance with a physically based algorithm for MERIS data. Sensors **8**: 4582–4599.

Olmanson, L. G., M. E. Bauer, and P. L. Brezonik. 2008. A 20-year Landsat water clarity census of Minnesota’s 10,000 lakes. Remote Sensing of Environment **112**: 4086–4097.

Oyama, Y., B. Matsushita, T. Fukushima, K. Matsushige, and A. Imai. 2009. Application of spectral decomposition algorithm for mapping water quality in a turbid lake (Lake Kasumigaura, Japan) from Landsat TM data. ISPRS Journal of Photogrammetry and Remote Sensing **64**: 73–85.

Oyama, Y., B. Matsushita, T. Fukushima, T. Nagai, and A. Imai. 2007. A new algorithm for estimating chlorophyll-a concentration from multi-spectral satellite data in case II waters: a simulation based on a controlled laboratory experiment. International Journal of Remote Sensing **28**: 1437–1453.

Pahlevan, N., A. D. Gerace, and J. R. Schott. 2011. Using thermal remote sensing as a tool for calibrating a hydrodynamic model in inland waters. Proc. SPIE 8030, 803001, doi:10.1117/12.887212

Pinkerton, M., G. Moore, S. Lavender, M. Gall, K. Oubelkheir, K. Richardson, P. Boyd, and J. Aiken. 2006. A method for estimating inherent optical properties of New Zealand continental shelf waters from satellite ocean colour measurements. New Zealand Journal of Marine and Freshwater Research **40**: 227–247.

Preisendorfer, R. W. 1976. Hydrologic Optics. U.S. Dept. of Commerce, National Oceanic and Atmospheric Administration, Environmental Research Laboratories, Pacific Marine Environmental Laboratory, USA.

Ruddick, K. G., F. Ovidio, and M. Rijkeboer. 2000. Atmospheric correction of SeaWiFS imagery for turbid coastal and inland waters. Applied optics **39**: 897–912.

Rudorff, C. M., E. M. L. M. Novo, and L. S. Galvão. 2006. Spectral mixture analysis for water quality assessment over the Amazon floodplain using Hyperion / EO-1 images. Revista Ambiente and Água **1**: 65–79.

Santer, R., and C. Schmechtig. 2000. Adjacency effects on water surfaces: primary scattering approximation and sensitivity study. Applied optics **39**: 361–75.

Schroeder, T., I. Behnert, M. Schaale, J. Fischer, and R. Doerffer. 2007. Atmospheric correction algorithm for MERIS above case-2 waters. International Journal of Remote Sensing **28**: 1469–1486.

Shuchman, R., A. Korosov, C. Hatt, D. Pozdnyakov, J. Means, and G. Meadows. 2006. Verification and application of a bio-optical algorithm for Lake Michigan using SeaWiFS: a 7-year inter-annual analysis. Journal of Great Lakes Research **32**: 258–279.

Spillman, C. M., J. Imberger, D. P. Hamilton, M. R. Hipsey, and J. R. Romero. 2007. Modelling the effects of Po River discharge, internal nutrient cycling and hydrodynamics on biogeochemistry of the Northern Adriatic Sea. Journal of Marine Systems **68**: 167–200.

Stramski, D., E. Boss, D. Bogucki, and K. J. Voss. 2004. The role of seawater constituents in light backscattering in the ocean. Progress in Oceanography **61**: 27–56.

Trolle, D., D. P. Hamilton, C. A. Pilditch, I. C. Duggan, and E. Jeppesen. 2011. Predicting the effects of climate change on trophic status of three morphologically varying lakes: Implications for lake restoration and management. Environmental Modelling and Software **26**: 354–370.

Twardowski, M. S., E. Boss, J. B. Macdonald, W. S. Pegau, A. H. Barnard, and J. R. V. Zaneveld. 2001. A model for estimating bulk refractive index from the optical backscattering ratio and the implications for understanding particle composition in case I and case II waters. Journal of Geophysical Research **106**: 14129.

Tyler, A. N., E. Svab, T. Preston, M. Présing, and W. A. Kovács. 2006. Remote sensing of the water quality of shallow lakes: A mixture modelling approach to quantifying phytoplankton in water characterized by high-suspended sediment. International Journal of Remote Sensing **27**: 1521–1537.

Tzortziou, M., J. R. Herman, C. L. Gallegos, P. J. Neale, A. Subramaniam, L. W. Harding, and Z. Ahmad. 2006. Bio-optics of the Chesapeake Bay from measurements and radiative transfer closure. Estuarine, Coastal and Shelf Science **68**: 348–362.

Van der Woerd, H., and R. Pasterkamp. 2008. HYDROPT: A fast and flexible method to retrieve chlorophyll-a from multispectral satellite observations of optically complex coastal waters. Remote Sensing of Environment **112**: 1795–1807.

Verburg, P., K. Hamill, M. Unwin, and J. Abell. 2010. Lake water quality in New Zealand 2010: Status and trends. NIWA client report HAM2010-107, Hamilton, New Zealand.

Vidot, J., and R. Santer. 2005. Atmospheric correction for inland waters—application to SeaWiFS. International Journal of Remote Sensing **26**: 3663–3682.

Volten, H., J. De Haan, and J. Hovenier. 1998. Laboratory measurements of angular distributions of light scattered by phytoplankton and silt. Limnology and Oceanography **46**: 1180–1197.

Wang, M., S. Son, and W. Shi. 2009. Evaluation of MODIS SWIR and NIR-SWIR atmospheric correction algorithms using SeaBASS data. Remote Sensing of Environment **113**: 635–644.

Wetzel, R. G. 2001. Limnology: Lake and River Ecosystems, 3rd ed. Academic Press, San Diego, USA.

Williamson, C. E., W. Dodds, T. K. Kratz, and M. A. Palmer. 2008. Lakes and streams as sentinels of environmental change in terrestrial and atmospheric processes. Frontiers in Ecology and the Environment **6**: 247–254.

Witter, D. L., J. D. Ortiz, S. Palm, R. T. Heath, and J. W. Budd. 2009. Assessing the application of SeaWiFS ocean color algorithms to Lake Erie. Journal of Great Lakes Research **35**: 361–370.

Yacobi, Y. Z., A. Gitelson, and M. Mayo. 1995. Remote sensing of chlorophyll in Lake Kinneret using highspectral-resolution radiometer and Landsat TM: spectral features of reflectance and algorithm development. Journal of Plankton Research **17**: 2155–2173.

Yentsch, C. S., and C. M. Yentsch. 1979. Fluorescence spectral signatures: the characterization of phytoplankton populations by the use of excitation and emission spectra. Journal of Marine Research **37**: 471–483.

2 Remote sensing of chlorophyll *a* concentrations in Rotorua lakes of New Zealand

2.1 Introduction

Scientists and resource managers need to characterise lake water quality at increasingly fine temporal and spatial scales to provide information to lake users and to monitor water quality in relation to water quality targets. Historically, managers have relied on manual sampling which can be time consuming and costly, however, more recently satellite remote sensing has been adopted to provide cost effective high spatial resolution monitoring (e.g., Olmanson et al. 2008). The theoretical basis of remote sensing of water quality is that the inherent optical properties (IOPs) and concentrations of optically active constituents (OACs) found in water determine the reflected light emitted by water bodies. The main optically active constituents in lake water are phytoplankton, non-living suspended organic particles and minerals (collectively termed tripton), and coloured dissolved organic matter (CDOM) (Dekker et al. 2002a). Suspended sediment (SS) refers to the totality of suspended tripton and living seston.

While remote sensing can only contribute direct information on optically active water quality parameters, it has the advantage of greatly increasing spatial resolution of monitoring, compared with traditional in situ methods. In the past, Landsat has been the sensor of choice for monitoring inland water quality in small lakes, due to its high spatial resolution, and the freely available archive of data spanning more than 40 years. The Landsat 7 satellite has the Enhanced Thematic Mapper (ETM+) sensor with 30 m spatial resolution which compares favourably with ocean colour sensors (250 - 1000 m resolution), and provides sufficient resolution to monitor spatial variations in small lakes.

Whilst Landsat remote sensing provides high spatial resolution, spectral resolution is low, which can result in individual bands containing spectrally opposing absorption and scattering features of optically active constituents (Bukata et al. 1995). The low spectral resolution and low signal to noise ratio (SNR) limit the complexity of any derived algorithms and reduce the ability to discriminate between chl *a* and tripton (Dekker and Peters 1993; Matthews 2011).

Measurements of total radiance over water from satellite sensors may comprise up to 90% atmospheric path radiance, making it difficult to quantify radiance from optically active constituents of water (Vidot and Santer 2005). Atmospheric correction is therefore essential for the standardisation of a time series of images. Atmospheric path radiance originates from scattering of solar radiation by air molecules and aerosols, which can also attenuate radiation through absorption. The complexity of aerosol particulate distributions presents a major challenge for atmospheric correction (Bukata et al. 1995). Atmospheric correction through accurate numerical radiative transfer modelling of the atmosphere requires data on atmospheric conditions at the time of image capture (e.g., water vapour, aerosol optical depth (AOD), and ozone) and has become increasingly commonplace with the operation of satellites such as MODIS Terra and Aqua which can be used to derive atmospheric conditions on a daily basis.

In a recent review of algorithms for the remote sensing of OACs (Matthews, 2011), 27 studies were identified which used Landsat ETM+ or Thematic Mapper (TM) satellite data to retrieve chl *a*, turbidity, SS, or Secchi depth spatial distributions. The review showed that in some instances some of these constituents had high coefficients of determination with satellite reflectance (e.g., $r^2 = 0.99$ for the retrieval of both SS (Dekker et al. 2002), and chl *a* (Giardino et al. 2001)). Only a small number of examples exist, however, of remote sensing of inland water quality at landscape scales (e.g., Lillesand et al. 1983; Dekker et al. 2001; Kloiber et al. 2002; Koponen 2006), and even fewer applications have considered time series of images to attempt to determine temporal changes in water quality (e.g., Dekker et al. 2001; Olmanson et al. 2008). A major barrier to time series analysis of Landsat imagery is the time required to process large numbers of images. Automation of image processing could result in higher productivity, minimize user error, and potentially enable near real-time image processing.

Of the Landsat studies cited above, only a few examine the underlying physical basis for the development of statistical algorithms (e.g., Dekker and Peters 1993; Gitelson et al. 1996; Brivio et al. 1997; Dekker et al. 2002). The study of Allan et al. (2011) is typical of many empirically-based Landsat studies of remote sensing of water quality, and while useful for determining spatial distributions of chl *a*, any derived algorithms have limited applicability beyond the spatial and temporal domain that was used in calibration within in situ samples, especially in more optically complex environments.

Bio-optical modelling algorithms have potential to more clearly differentiate OACs. Bio-optical models have generally been applied to high spectral resolution satellite imagery, such as that from MODIS, and to hyperspectral data, both of which allow precise measurement of spectral slopes. However, successful applications of simplified bio-optical models for single water quality parameter retrieval exist using broadband sensors where the optically active constituent dominates the absorption and scattering budget. For example semi-analytical models have been used to map SS concentrations using Landsat and Spot satellite data (Dekker et al. 2002). The advantage of bio-optical models is that in situ data are not needed at the time of image capture, allowing for multi-site and multi-sensor comparisons through time. Dekker et al. (2002) found that bio-optical algorithms for SS were more reliable and temporally robust than empirical algorithms. Their study also found that random point samples within the synoptic estimations for SS were on average within a mean value of ±20-30% of in situ grab-samples, however, in the worst case scenario values they deviated by as much as 4000%.

The Rotorua lakes (North Island, New Zealand) include a number of lakes within a relatively small geographical area, which are subject to a regular programme of water quality monitoring (Burns et al. 2005). They provide an ideal location to investigate remote sensing of water quality within and between lakes. In order to construct robust algorithms for chl *a* estimation, algorithms must be validated both temporally and spatially over a time series of images. For algorithms to be robust, some knowledge of the physical mechanisms underpinning algorithms function is needed, especially in terms of identifying potential sources of error. The objectives of this study were to (1) determine the underlying physical mechanisms by which Landsat may be used to distinguish changes in chl *a* using a bio-optical model, (2) determine the accuracy of different remote sensing models in estimating chl *a* over a wide range of concentrations within and between lakes, and (3) develop an automated image processing methodology to enable the processing of large numbers of images. A radiative transfer-based atmospheric correction was used with empirical and semi-analytical modelling for chl *a* retrieval. The results from this study allowed a synoptic representation of chl *a* in the Rotorua lakes, both spatially and temporally.

2.2 Methods

Study site

The Rotorua lakes (Figure 2.1(a)) have a wide range of trophic states and mixing regimes (Burns et al. 2009). These include eutrophic and monomictic (Okaro), mesotrophic and monomictic (Okareka, Tikitapu, Rotoiti, Rotokakahi and Okataina), oligotrophic and monomictic (Tarawera, Rotoma, and Rotomahana) and meso to eutrophic and polymictic (Rotorua, Rotoehu, and Rerewhakaaitu) (Hamilton 2003) (Table 2.1). Many of the lakes have nutrient-enriched geothermal inputs (Hoellein et al. 2012), including Rotorua, Rotoiti, Rotoehu, Rotomahana and Tarawera. A geothermal stream enters Lake Rotoehu in the south-west corner of the lake (Figure 2.1).

In August 2008, a diversion wall was constructed in Lake Rotoiti (Figure 2.1(b)). Its purpose was to divert nutrient rich water from Lake Rotorua, which enters Lake Rotoiti via the Ohau Channel inflow, away from the main body of Lake Rotoiti, and towards the main Katituna River outflow in the north-west region of the lake. This study included images and in situ data captured before and after the construction of the diversion wall.

Methods overview

Cloud-free Landsat ETM+ images were processed using automated procedures, which included conversion from radiance to atmospherically corrected subsurface irradiance reflectance (*R*(0-)). Forward bio-optical models were applied to investigate the effect of increasing concentrations of chl *a* on Landsat *R*(0-), creating an semi-analytical algorithm to estimate chl *a*. Empirical relationships between Landsat *R*(0-) and in situ chl *a* were also investigated using statistical methods, with results used to inform empirical algorithm development for chl *a* estimation. Symbolic regression (Koza 1992) was also applied to create algorithms to estimate chl *a*.

Satellite imagery and software

A total of 106 Landsat 7 satellite images were captured from 1999 to 2011 from path 72, rows 84 and 85. All image processing routines were automated using scripts written in Interactive Data Language (IDL), linked to ENVI routines when necessary. All images were downloaded from the GloVis website created by USGS (http://glovis.usgs.gov/).

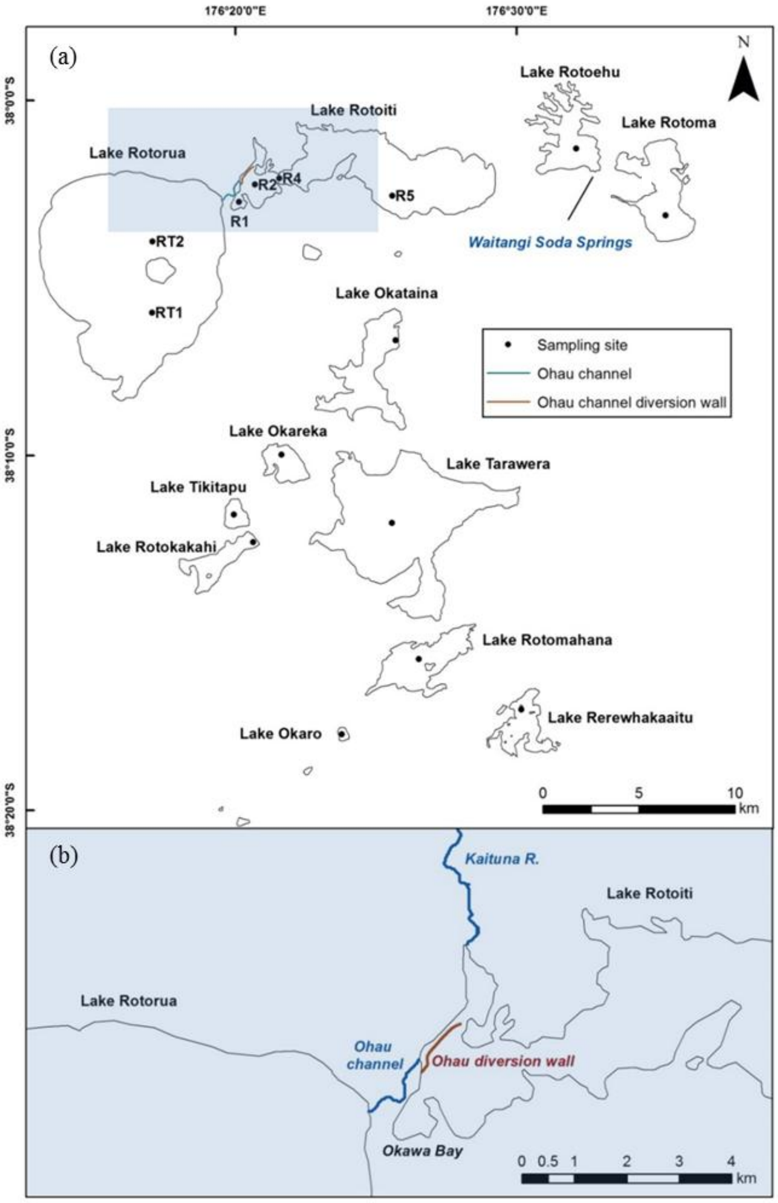

Figure 2.1. (a) The Rotorua lakes' study site showing in situ sampling locations and (b) the extent of expanded area represented with shading from (a), showing the location of the Ohau diversion wall, Lake Rotoiti. Each in situ sampling location corresponds to a 5 x 5 matrix (30-m pixels) average from Landsat ETM+ satellite images.

Table 2.1. Lake and catchment characteristics of the Rotorua lakes Source: (Scholes and Bloxham 2008; Scholes 2011).

Lake name	Lake area	Maximum lake depth	Mean lake depth	Annual mean chl *a*	Trophic state	Catchment pasture	Catchment indigenous forest/scrub	Catchment exotic forest
	km²	m	m	µg L^{-1}		%	%	%
Okareka	3.4	33.5	20.0	3.9	Mesotrophic	37.8	51.6	7.6
Okaro	0.3	18.0	12.1	33.5	Supertrophic	90.6	2.1	6.3
Okataina	10.8	78.5	39.4	2.1	Oligotrophic	10.7	84.1	7.8
Rerewhakaaitu	5.3	15.8	7.0	2.9	Mesotrophic	75.3	7.2	15.2
Rotoehu	8.0	13.5	8.2	10.6	Eutrophic	34.2	33.4	32.0
Rotoiti	34.0	125.0	60.0	9.6	Mesotrophic	15.9	36.4	46.2
Rotokakahi	4.4	32.0	17.5		Eutrophic	26.3	16.6	57.1
Rotoma	11.1	83.0	36.9	1.3	Oligotrophic	23.4	46.0	26.7
Rotomahana	9.0	125.0	60.0	4.2	Mesotrophic	43.2	39.7	16.3
Rotorua	80.6	44.8	11.0	22.8	Eutrophic	51.8	25.1	14.3
Tarawera	41.3	87.5	50.0	1.5	Oligotrophic	19.7	62.4	16.0
Tikitapu	1.5	6.2	18.0	1.8	Oligotrophic	7.0	74.3	17.9

In situ data

Monthly in situ samples of chl *a* for the Rotorua lakes were obtained from Bay of Plenty Regional Council (Scholes 2011). Surface samples are depth integrated (0 to 4-9 m depth in eutrophic lakes and 0 to 10-17 m in meso-oligotrophic lakes, Table 2.1). Of all the satellite image capture dates, there were 27 in situ samples that were taken on the same date. In addition, all in situ samples corresponding to images from 24 January 2002 (UTC) and 23 October 2002 (n=29) were included, for which samples were collected within three days of image capture, except for Lake Rerewhakaaitu (10 January 2002), Site R3 (18 January 2002), and Site R1/R3 (30 October 2002).

All Lake Rotoma samples (n=35) captured within one month of satellite overpass were included in the algorithm development in order to ensure any derived models were suitable for estimation of chl *a* in oligotrophic lakes. The average in situ chl *a* in Lake Rotoma over the study period was 1.4 µg L^{-1}, with maximum concentration usually in winter or spring. There has been low variation in chl *a* concentrations in this lake (Paul et al. 2012), and therefore we assumed that data from satellite overpass dates could be matched to the corresponding monthly in situ samples.

Lake Rotorua is the most optically complex lake of the 12 Rotorua lakes and sediment resuspension has previously been observed in the past during high winds (Stephens et al. 2004. Suspended sediment was not routinely measured during the study period in Lake Rotorua, however a previous study (Vant and Davies-Colley 1986) using monthly samples from July 1983 - October 1984 yielded mean concentration of 6.7 mg L^{-1}, with range 2.4-15.9 mg L^{-1}). Lake Rotoma is the most optically simple (the highest water clarity), and Lake Rotoehu exhibits the greatest spatial variability of chl *a* concentrations. These three lakes were chosen to assess the feasibility of developing time series analysis of chl *a* from remote sensing based on ground truthing with in situ data.

Image processing

Landsat images were first clipped to the Rotorua lakes area of interest (Appendix 2: batch_subset_via_roi_landsat_rot.pro) and an image of B4 (Appendix 2: landsat_tiff.pro) was created to enable visual inspection for cloud cover. Conversion from Landsat scaled radiance to spectral radiance at the sensor aperture (L_λ; W m^{-2} sr^{-1} μm^{-1}) used an IDL procedure (Appendix 2: landsat_rad_sixsin_gen.pro) which read the Landsat metadata file in order to apply gains and offsets in the radiance conversion calculation. In order to generate inputs to each band for 6sv (Second Simulation of a Satellite Signal in the Solar Spectrum) atmospheric correction (Kotchenova et al. 2008), this procedure also read the acquisition date and solar elevation angle from the Landsat metadata (to calculate solar zenith angle).

In New Zealand, AOD is only measured at Lauder (860 km south-west of Lake Taupo, New Zealand). AOD records from this station are among the lowest recorded globally, ranging from about 0.01 to 0.08 (Liley and Forgan 2009). To account for variations in AOD between Lauder and Lake Rotorua, Giovanni Data and Information Services Center (NASA) was used to create time series outputs of AOD, water vapour (derived from MODIS Terra MOD08) and total column ozone (derived from MODIS Atmospheric Infrared Sounder AIRS), for input to the radiative transfer atmospheric correction model 6sv. The global validation of MODIS AOD estimation error over land, ε, is given as:

$$\varepsilon = \pm 0.03 + 0.05\ \mathrm{AOD} \qquad \text{(Remer et al. 2005)} \qquad (2.1)$$

For instances when the MODIS Terra-retrieved AOD was negative, values were set to 0.05. Monthly mean values measured at Lauder range between 0.02 and 0.05 (Liley and Forgan 2009). It was assumed AOD over the Rotorua lakes would likely be higher than at Lauder, therefore the value of 0.05 was chosen.

Once the atmospheric correction parameters were derived, another IDL procedure was used to write input files for 6sv for each band of Landsat (Appendix 2: landsat_rad_sixsin_gen.pro). The 6sv input file also contained the lake elevation (300 m), sensor elevation (705 km), chosen spectral band, and chosen aerosol model (continental). The bidirectional reflectance distribution function was chosen along with a non-homogenous target. The radiative transfer model (6sv) was then run using the generated input files using a shell script loop function. The output files were then read (Appendix 2: sixsauto.pro) in order to convert radiance to water surface irradiance reflectance (R(0+)).

Finally, a water-only image of R(0+) was created using a mask that intersected lake polygons and a classification of Landsat B5 (landsat_mask.pro), in which water was differentiated from land, based on absorption of electromagnetic radiation in B5. R (0+) was converted to subsurface irradiance reflectance (R(0-)) using an air-water interface parameter of 0.544 (Mobley 1994).

In order to fill missing data in Landsat images caused by the failure of the Scan Line Corrector (SLC), the ENVI routine DEM_BAD_DATA_DOIT was used in an IDL procedure (Appendix 2: repalcebaddata.pro). Delany triangulation was used to fill reflectance values less than -0.000001.

Forward and inverse bio-optical modelling

Forward bio-optical modelling was used to quantify the physical processes responsible for relationships between Landsat measured reflectance and chl *a* concentration. These relationships were used to estimate chl *a* using a semi-analytical model of Landsat reflectance.

Dekker et al. (1997) found the following bio-optical model to be suitable to estimate R(0-) from absorption and scattering for turbid waters:

$$R(0-) = r_1 \left[\frac{b_b}{b_b + a} \right] \tag{2.2}$$

where r_1 depends on the anisotropy of the downwelling light field and scattering processes within the water, b_b (m^{-1}) is the total backscattering and a (m^{-1}) is total absorption. A value of r_1 of 0.31 was used in this study (cf. Gordon et al. 1988).

The absorption and backscattering coefficients are made up of the sum of individual optically active components:

$$b_b(\lambda) = b_{bw}(\lambda) + B_{bTR}\, b^*_{TR}(\lambda)\, C_{TR} + B_{b\phi}\, b^*_{\phi}(\lambda)\, C_{\phi} \tag{2.3}$$

$$a(\lambda) = a_w(\lambda) + \mathrm{C}_{\phi}\, a^*_{\phi}(\lambda) + C_{TR}\, a^*_{TR} + a_{CDOM}(\lambda) \tag{2.4}$$

$$a_{CDOM}(\lambda) = a_{CDOM(440)}\, a^*_{CDOM}(\lambda) \tag{2.5}$$

where:
(λ) = wavelength
$b_{bw}(\lambda)$ = backscattering coefficient of water
$B_{bTR}(\lambda)$ = backscattering ratio of tripton
$b^*_{TR}(\lambda)$ = specific scattering coefficient of tripton
C_{TR} = concentration of tripton
$B_{b\phi}(\lambda)$ = backscattering ratio of phytoplankton

$b^*_\phi(\lambda)$ = specific scattering coefficient of phytoplankton
$a_w(\lambda)$ = absorption coefficient of pure water
C_ϕ= concentration of chl *a*
$a^*_\phi(\lambda)$ = specific absorption coefficient of phytoplankton
$a^*_{TR}(\lambda)$ = specific absorption coefficient of tripton
$a_{CDOM(440)}$ = coloured dissolved organic matter (CDOM) absorption at 440 nm
$a^*_{CDOM}(\lambda)$ = specific absorption of CDOM

Values of $a_w(\lambda)$ and $b_{bw}(\lambda)$ were assigned to literature values (Morel 1974; Pope and Fry 1997). The bio-optical model was implemented in BIOPTI (bio-optical model for inland waters (version 1.0)) (Dekker et al. 2001a) using IOPs of Dutch inland waters (Dekker et al. 1997). The bio-optical simulations were run by varying chl *a* concentration using 30 intervals: 0.5 µg L^{-1} - 9.5 µg L^{-1} using 1 µg L^{-1} intervals, 10 - 30 µg L^{-1} using 2 µg L^{-1} intervals and 30 - 300 µg L^{-1} using 30 µg L^{-1} intervals. Over these simulations $a_{CDOM\,(440)}$ was fixed at 0.16 m^{-1} and tripton concentration was fixed at 0.5 mg L^{-1} (SS/tripton and CDOM were not measured over the study period). In Lake Rotorua $a_{CDOM\,(440)}$ has been measured previously (mean for consecutive months of 0.23 m^{-1}, n=23) as well as for Lake Rotokakahi (mean over 11 months between October 1983 and September 1984 of 0.09 m^{-1}, n=29) and the average value for these two lakes (0.16 m^{-1}) was assigned to the model (Davies-Colley and Vant 1987).

Statistical analysis

For all the tested algorithms, root mean square error (RMSE) and coefficient of determination (r^2) were calculated between in situ-observed and model-estimated chl *a*. The RMSE combines residuals from differences of estimated and observed values into a single measure of predictive power. It is defined as:

$$RMSE = \sqrt{\frac{\sum_{i=1}^{n}(y_i - x_i)^2}{n}} \tag{2.6}$$

where y_i is the observed value and x_i is the modelled value corresponding to a given time and location *i*.

Symbolic regression

Eureka Formulize is a scientific data mining software tool that detects mathematical patterns in experimental data. This software uses symbolic regression (Koza 1992) to search for equations that describe the mechanisms that produce the data. Symbolic regression uses evolutionary computation algorithms to search a space of mathematical expressions while minimising selected error metrics. Traditional linear and non-linear regressions fit parameters to a standard equation, whereas symbolic regression searches both the parameter space and the form of the equation simultaneously (Schmidt and Lipson 2009).

Symbolic regression was used in this study in order to include all the visible bands of Landsat in algorithm development. We selected the following mathematical operators for use in a symbolic regression equation: constant, integer constant, addition, subtraction, multiplication, division, exponential, natural log, and power. The absolute error was used as the error metric to determine the suitability of derived models. The data were randomly shuffled, and split into training and validation data sets.

2.3 Results

Bio-optical modelling simulations of the influence of phytoplankton on R(0-)

Subsurface irradiance reflectance (*R*(*0*-)) was modelled theoretically from the forward bio-optical model (Figure 2.2), varying chl *a* concentrations from 0 to 450 µg L^{-1} in 10 equal steps (with fixed values of CDOM absorption of 0.16 m^{-1} and tripton concentrations of 0.5 mg L^{-1}). Relative Landsat 7 spectral response functions ranging from 0 to 1 are shown for the B1, B2 and B3 bands. A water column with no chl *a* yields high *R*(0-) at blue wavelengths and minimal *R*(0-) at red wavelengths.

For Landsat B1, the bio-optical model estimates a reduction in *R*(0-) with increasing chl *a* concentration, due to phytoplankton pigment absorption. For B2 there is a peak in reflectance at 580 nm coinciding with an increasing influence of phytoplankton backscattering and decreasing phytoplankton absorption. Band 2 also includes a spectral pivot point at 530 nm, where subsurface irradiance reflectance is independent of chl concentration. Band 3 includes a local reflectance peak at 645 nm (due to locally decreased phytoplankton absorption) and a reflectance trough at 680 nm caused by phytoplankton absorption. Above 680 nm the base of the reflectance peak at 706 nm is captured, which results from very low phytoplankton absorption and a local increase in phytoplankton backscattering.

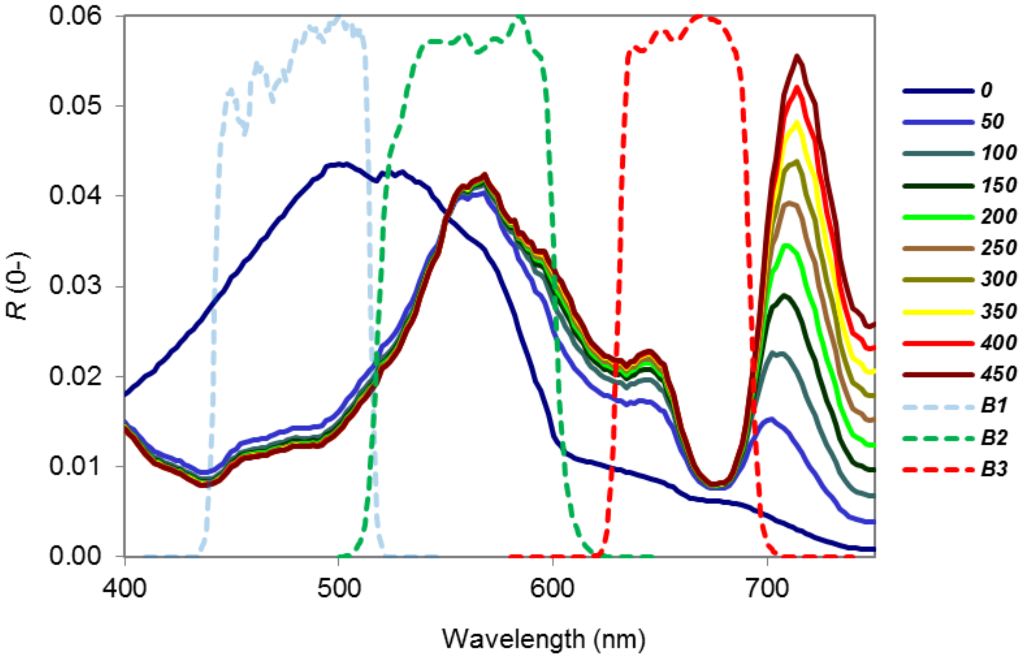

.

Figure 2.2. Modelled subsurface reflectance (*R*(0-)) for varying chlorophyll *a* concentrations ranging from 0 to 450 µg L^{-1} with fixed CDOM absorption of 0.16 m^{-1} and tripton concentration of 0.5 mg L^{-1}. The relative spectral response of Landsat bands B1, B2 and B3 is overlaid.

The modelled *R*(0-) from the bio-optical model was averaged over Landsat bandwidths B2 and B3, allowing analytical determination of an relationship between chl *a* and *R*(0-) (Figure 2.3). An exponential relationship was then used to approximate the analytical relationship (r^2 = 0.97 for B2 and 0.95 for B3).

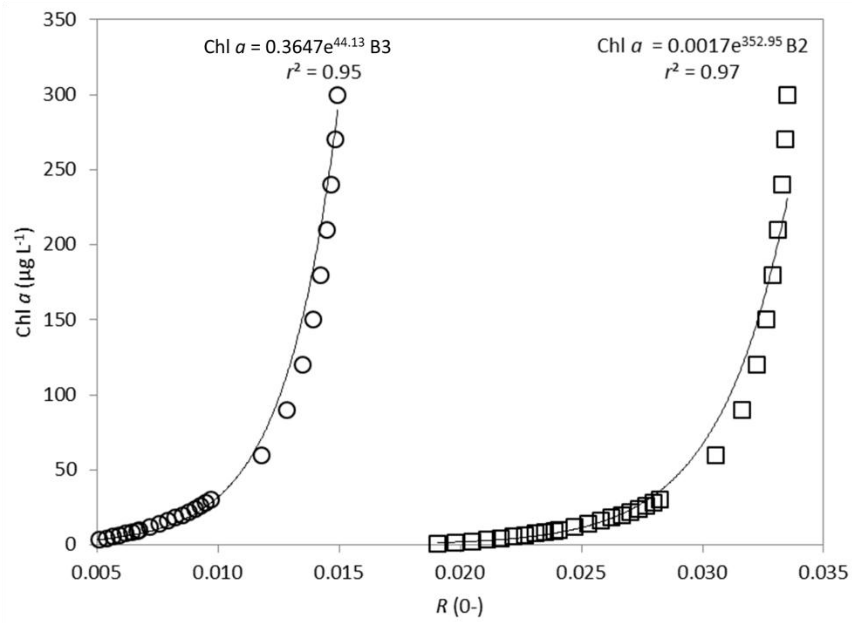

Figure 2.3. The semi-analytical relationship between chlorophyll (chl) *a* concentrations and Landsat band-averaged subsurface irradiance reflectance *R*(0-) in B3 (open circles) and B2 (open squares) based on individual analytical solutions. An exponential relationship (black line) is used to fit the analytical relationship with closeness of fit given by r^2. This function was used to estimate chlorophyll *a* from *R*(0-).

Statistical analysis and regression models

In order to determine which Landsat parameters have potential use in modelling chl *a*, values of r^2 were examined for relationships of in situ chl *a* to Landsat bands or band ratios (Table 2.2). Amongst the relationships of in situ chl *a* (and ln(chl *a*)) to Landsat bands *R*(0-) and *R*(0-) B1/B3, the highest r^2 value was for ln(chl) vs. ln(B1/B3) (r^2=0.55) followed by ln(chl) vs. B1/B3 (r^2=0.48). The ln(B1/B3) ratio was subsequently used in the empirical model to estimate chl *a*.

Table 2.2. Coefficient of determination (r^2) for regression relationships between in situ chlorophyll *a* and Landsat. * represents $p>0.05$ (n=87).

	ln(Chl *a*)	Chl *a*
Parameter	r^2	r^2
B1	0.014*	0.002*
B2	0.242	0.317
B3	0.347	0.314
B4	0.010	0.069
B5	0.024*	0.003*
B7	0.001	0.007
B1/B3	0.483	0.198
Ln(B1/B3)	0.553	0.277
ln(B2)	0.240	0.202
ln(B3)	0.352	0.211
ln(B4)	0.189	0.138

The symbolic regression algorithm was derived using the entire dataset of satellite *R*(0-) and corresponding in situ data as detailed above:

$$\text{Chl } a = (4618\ \text{B2} - 20)/((\text{B1}/\text{B3})^2) \qquad (2.7)$$

with r^2=0.68, RMSE=10.32 µg L^{-1}, $p<0.05$, n=87

Of the regression analysis results of in situ chl *a* and estimated chl *a* from the four models, the symbolic regression model showed the highest r^2 (0.68), lowest RMSE (10.3 µg L^{-1}), a slope of 0.88 and a constant of 1.52 µg L^{-1} (Figure 2.4). Based on these results, this model was selected to estimate chl *a* henceforth.

The semi-analytical model was also applied to estimate chl *a* from B2 and B3, using the two fitted equations shown in Figure 2.3. These two models were deemed unsuitable for the estimation of chl *a*, due to either having a high constant (6.5 µg chl *a* L^{-1} for the B2 semi-analytical model) or low slope (0.65 µg chl *a* L^{-1} for the B3 semi-analytical model).

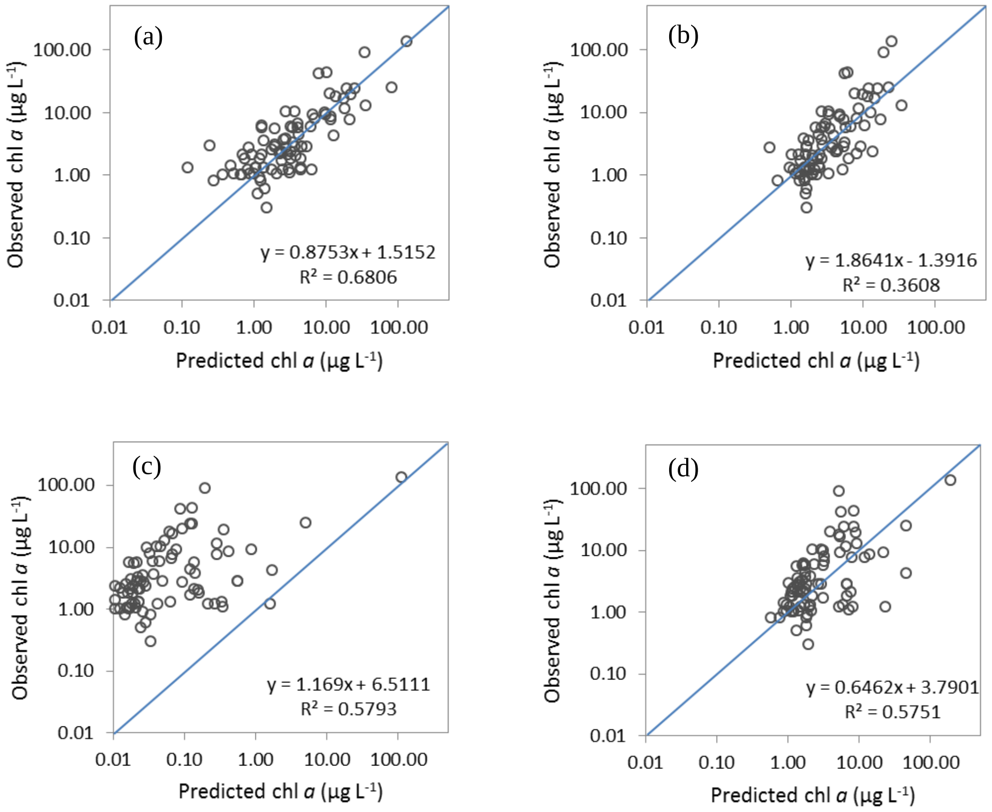

Figure 2.4. Observed chlorophyll *a* (µg L^{-1}) (y) versus estimated chlorophyll *a* (x) from the four different algorithms, plotted on a log-log scale. A 1:1 line (blue line), and r^2 value are shown on each plot (n=87). (a) Symbolic regression algorithm equation: Chl *a* = (4618 B2 - 20)/((B1/B3)^2) with r^2=0.68 and RMSE=10.5 µg L^{-1}. (b) Empirical algorithm equation: Chl *a* = exp(-2.12*(ln(B1/B3)) + 3.17) with r^2=0.36 and RMSE=15.7 µg L^{-1}. (c) Semi-analytical model B2: Chl *a* = 0.0017e$^{352.95\ B2}$ with r^2=0.58 and RMSE=13.8 µg L^{-1}. (d) Semi-analytical model B3: Chl *a* = 0.36e$^{447.13\ B3}$ with r^2=0.58 and RMSE=14.1 µg L^{-1}.

Influence of CDOM and tripton on R(0-)

Running the bio-optical model with a fixed absorption of CDOM absorbtion (0.16 m^{-1}) and concentration of chl *a* (20 µg L^{-1}), and with tripton concentrations ranging from 0 to 9 mg L^{-1}, revealed that increases in tripton concentration increase *R*(0-) over all visible wavelengths (Figure 2.5).

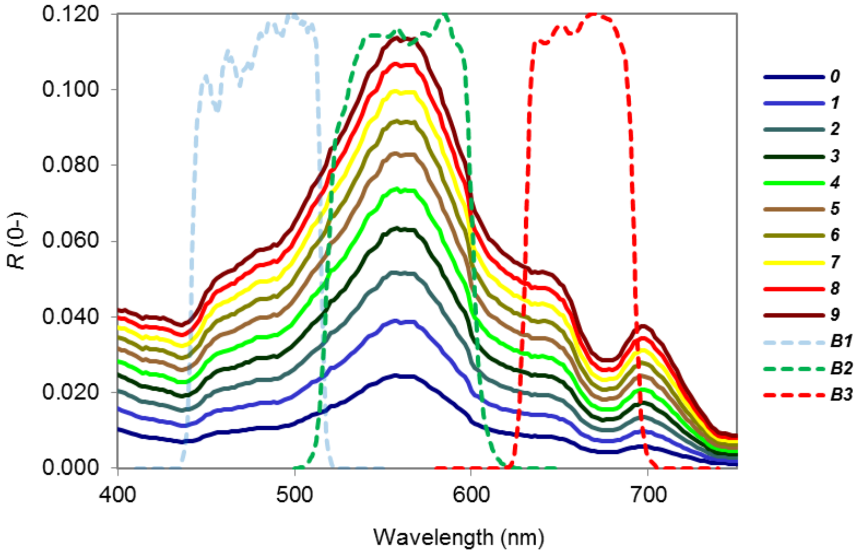

Figure 2.5. Modelled subsurface reflectance (*R*(0-)) for varying tripton concentrations ranging from 0 to 9 mg L^{-1}, with fixed CDOM absorption of 0.16 m^{-1} and chl *a* concentration of 20 µg L^{-1}. The relative spectral response of Landsat bands B1, B2 and B3 is overlaid.

Running the bio-optical model with fixed concentration of chl *a* (20 µg L^{-1}) and tripton (0.5 mg L^{-1}), and varying CDOM absorption from 0 to 1.8 m^{-1}, revealed that increases in CDOM absorption decrease *R*(0-) below 680 nm (Figure 2.6).

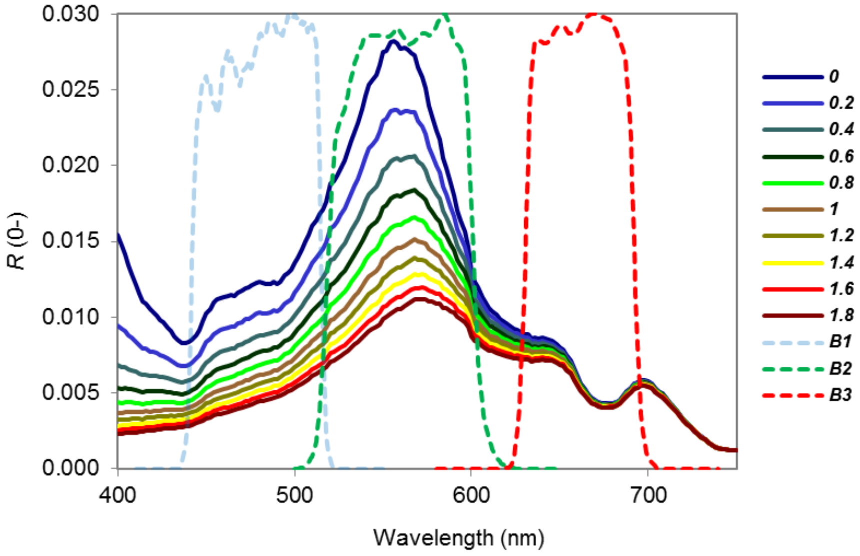

Figure 2.6. Modelled subsurface reflectance (*R*(0-)) for varying CDOM absorption ranging from 0 to 1.8 m^{-1}, with fixed tripton concentrations of 0.5 mg L^{-1} and chl *a* of 20 µg L^{-1}. The relative spectral response of Landsat bands B1, B2 and B3 is overlaid.

Time series satellite estimation of chl a concentration

In lakes Rotorua, Rotoehu and Rotoiti, monthly in situ chl *a* concentrations were compared to chl *a* derived from the symbolic regression algorithm. Although a direct comparison is not possible due to the time difference between in situ sample and satellite overpass, some general features can be identified. In Lake Rotoma satellite estimations were usually of a similar magnitude to observed values for each date of comparison, although it is likely that that the symbolic regression produced an underestimate for some periods. For example, on 15 August 2000 estimated chl *a* was only 0.12 µg L^{-1} (Figure 2.7 (a)) whereas the in situ measured chl *a* closest to the overpass was 2.2 µg L^{-1} (on 23 August 2000). The lowest in situ value over the study period was 0.3 µg L^{-1} in Lake Rotoma. From 2004 through 2010 there were eight instances when satellite-estimated chl *a* was greater than 3.0 µg L^{-1}, however, over that period in situ chl *a* was greater than 3.0 µg L^{-1} only twice. Notably, towards the end of the study period, estimated chl *a* was consistently higher than in situ chl *a*.

In Lake Rotoehu, chl *a* derived from the symbolic regression model on 5 February 2000 (222 µg L^{-1}), 6 January 2001 (169 µg L^{-1}), and 25 February 2002 (81 µg L^{-1}) was not only high in magnitude but also much higher than the corresponding in situ data (2.7 (b)). In this lake surface distributions of chl *a* derived from symbolic regression are highly heterogeneous (Figure 2.8) and appear to be influenced by wind speed and direction as high concentrations were estimated in the downwind direction in several cases (e.g., Figure 2.8 (d), (e) and (f)). Lake wide statistics (excluding a 100-m buffer zone from the shoreline) showed that the maximum-estimated chl *a* of 838 µg L^{-1} occurred on 5 February 2000 (Figure 2.8 (a)), located in the southeast of the lake c. 500 m from the shoreline. This date also had the highest range of chl *a* values at 823 µg L^{-1}. The highest chl *a* concentrations were observed when wind speed was less than 4 m s^{-1} (e.g., Figures 2.8 (a)-(f)).

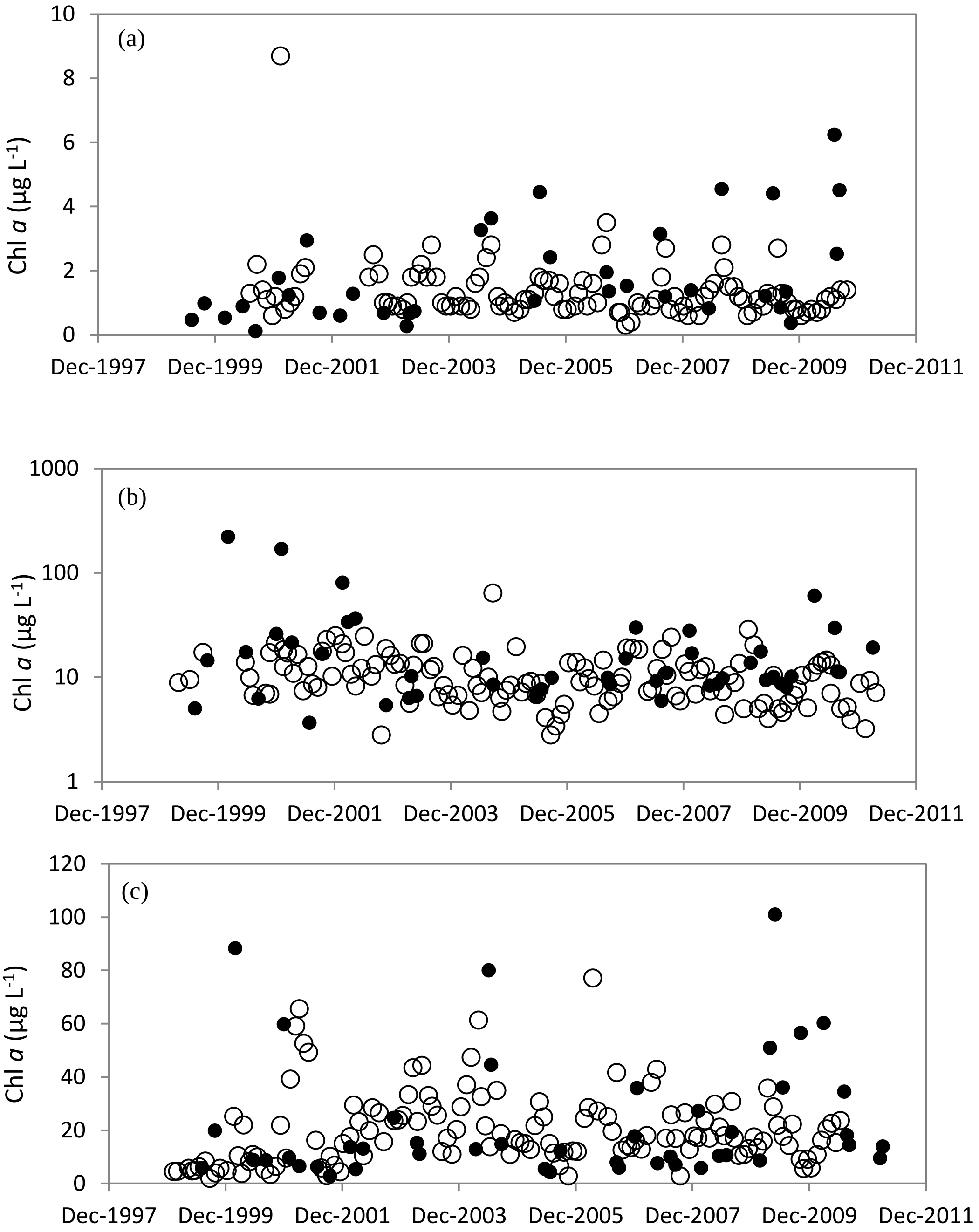

Figure 2.7. Time series plots of estimated chlorophyll *a* (µg L^{-1}) from the symbolic regression (closed circles) and from all in situ data (open circles) for Lake Rotoma (a), Lake Rotoehu (b), and Lake Rotorua (c). Note that in most cases dates of in situ and satellite sampling dates are not identical.

In Lake Rotorua, the estimated chl *a* derived from symbolic regression may have been erroneously affected by the presence of tripton (Figure 2.7 (c)). Lake Rotorua is a large shallow, wind-exposed lake which has potential for sediment resuspension. Figure 2.5 demonstrates that additions of tripton increase $R(0\text{-})$ at all visible wavelengths, which introduces the potential for error when using empirical algorithms.

Spatial variation of estimated chl a concentration

For chl *a* derived from the symbolic regression algorithm, there was large spatial variation both within and between lakes on 24 January 2002. Within-lake spatial variation was high in Rotoiti (3.2-136 μg L^{-1}), Rotoehu (22.1-203 μg L^{-1}), and Rotomahana (0.9-168 μg L^{-1}) (Figure 2.9). In Lake Rotorua estimated chl *a* was elevated near the lake edge (affecting up to 10 pixels from the lake edge), possibly as a result of additions from bottom reflection or from elevated levels of suspended minerals in shallow areas. In other lakes, elevated chl *a* also often occurred near the lake edge in some locations, however, this generally only affected one or two pixels. Surface chl *a* derived from symbolic regression was highest within lakes for Rotorua, Rotoiti, and Rotoehu. In contrast, nearby lakes Rotoma and Okataina had relatively low chl *a* concentrations on all dates. Figure 2.10 shows chl *a* derived using the symbolic regression model on selected dates when there was high spatial variation of chl *a*. On 5 February 2000 (Figure 2.10 (a)) estimated chl *a* concentrations were > 200 μg L^{-1} in lakes Rotorua and Rotoehu, while concentrations in Lake Rotoiti including Okawa Bay were < 40 μg L^{-1}. On 6 January 2001 (Figure 2.12 (b)), chl *a* concentrations were > 200 μg L^{-1} at Site R1 (Okawa Bay) in Lake Rotoiti and in Lake Rotoehu, while in the main body of Lake Rotorua concentrations were < 40 μg L^{-1}. On 19 March 2004 (Figure 2.10 (c)) there was high spatial variation of chl *a* in Lake Rotorua, particularly on the western shore. On 19 February 2011 (Figure 2.10 (d)), relatively high concentrations of chl *a* were observed at Rotoiti Site R1 compared with the main basin of Lake Rotoiti.

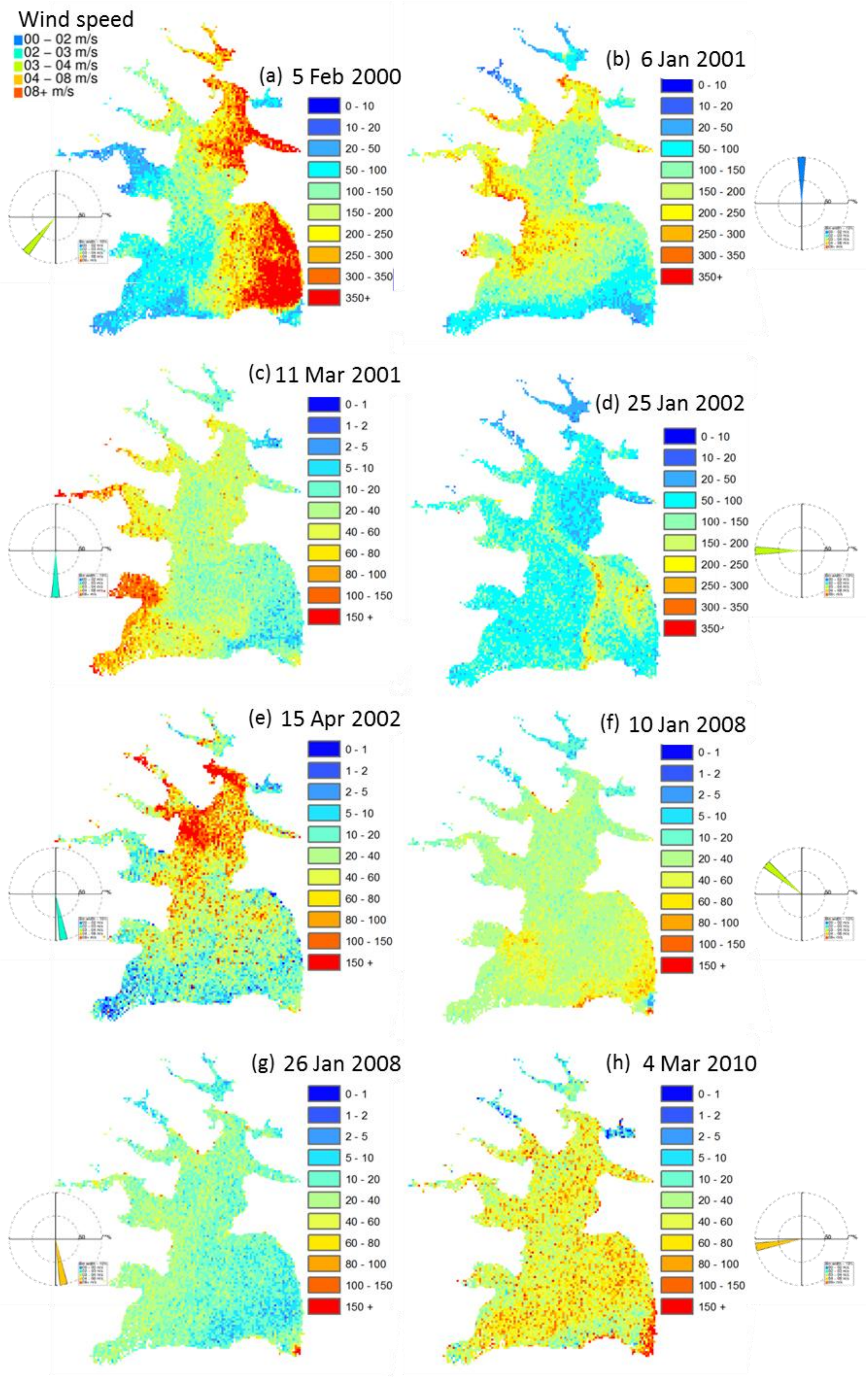

Figure 2.8. Chlorophyll *a* concentration (μg L^{-1}) in Lake Rotoehu derived from the symbolic regression model.

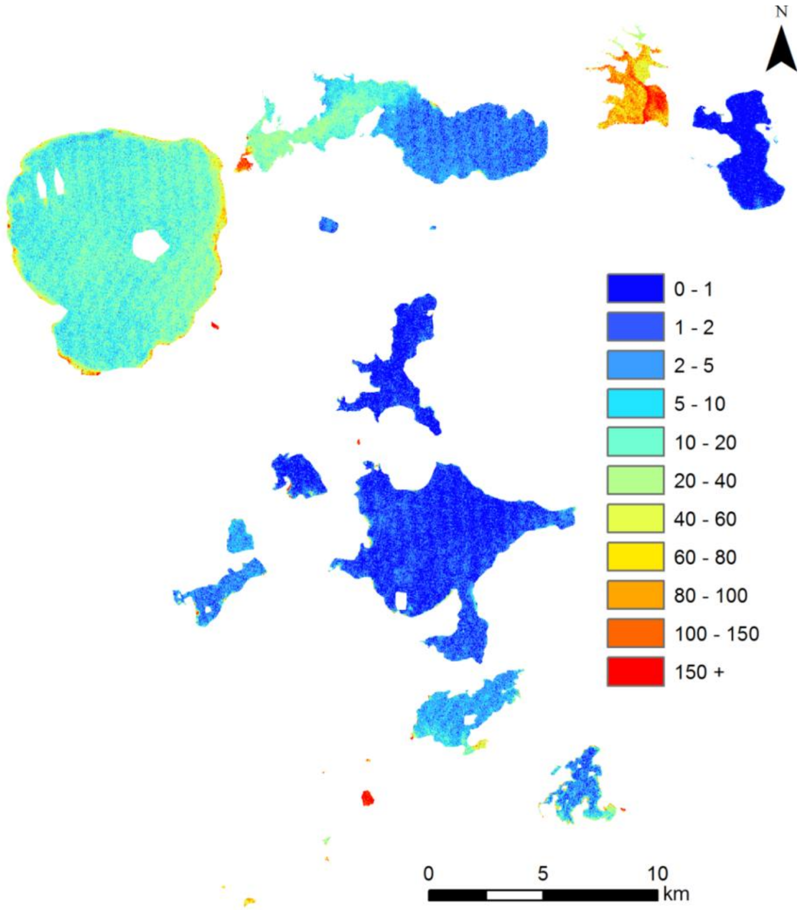

Figure 2.9. Chlorophyll *a* (µg L^{-1}) derived from the symbolic regression model on 24 January 2002. White areas within lakes represent masked areas of cloud.

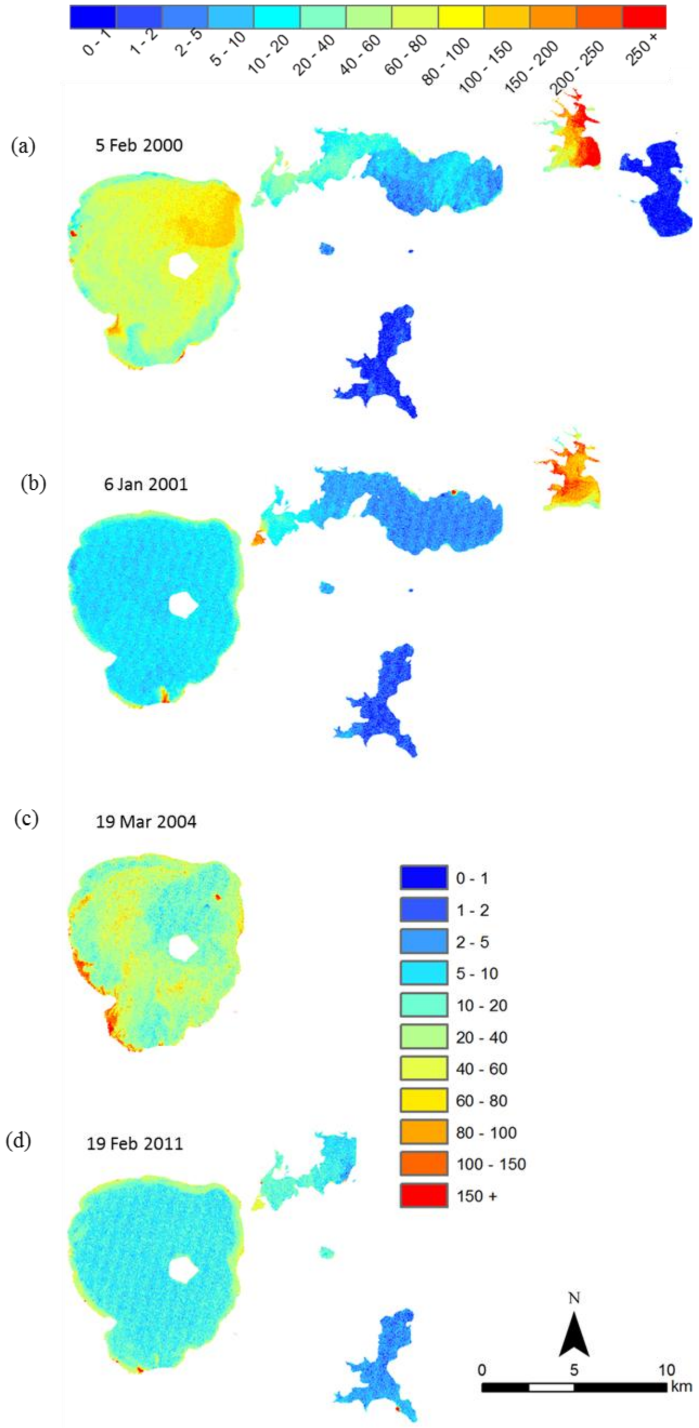

Figure 2.10. Chlorophyll *a* (μg L^{-1}) derived from the symbolic regression model in north-western Rotorua lakes on selected dates with high spatial variation. Note: some lakes were removed due to cloud cover.

2.4 Discussion

In this study a symbolic regression algorithm was used to estimate chl *a* from Landsat ETM+ subsurface irradiance reflectance. Hindcast estimations of chl *a* concentration displayed large inter- and intra-lake variations that tended to be greater than those documented by water quality monitoring programs on the Rotorua lakes (Burns, 2009). My study demonstrated the ability of the derived symbolic regression model to estimate chl *a* over landscape scales and long time periods, potentially capturing greater variability, which opens up new possibilities for applying remote sensing to lakes with sparse or no monitoring history.

The ability of symbolic regression to discover both model form (e.g., mathematical operators and constants) and parameters resulted in a novel algorithm. The use of combinations of spectral bands, while increasing correlation coefficient values for relationships with chl *a*, can produce results that are difficult to interpret based on bio-optical theory (Dekker et al. 1993). However, in the present chapter, the symbolic regression model used the commonly applied ratio of B1/B3. The underlying physical basis for the relationship of the ratio of B1 (450-515 nm)/B3(630-690 nm) to chl *a* is well understood (Matthews 2011). Increasing concentrations of chl *a* are associated with a decrease in reflectance at blue wavelengths (B1) corresponding to a local chl *a* absorption maximum (Gitelson et al. 1993, 1996; Han and Jordan 2005). The Landsat B3 wavelength range includes a local reflectance peak near 650 nm which is caused by a combination of decreasing chl *b* and phycocyanin absorption and relatively low chl *a* absorption (in comparison to chl *a* absorption maxima at 662 nm), and low absorption relative to scattering at these wavelengths (Dekker et al. 2002a). In addition, B3 captures the initial part of the reflectance peak centred at 690-720 nm (due to increased algal scattering). Chlorophyll fluorescence is often erroneously attributed to contributing to the 690-720 nm peak in eutrophic waters, however, it was not simulated in the bio-optical model in this study, and it has previously been deemed insignificant compared with contribution from elastic scattering (Dekker et al. 2002a; Gilerson et al. 2007). The Landsat B3 wavelength range includes part of the reflectance trough centred at 624 nm (caused by chl *a* and phycocyanin absorption) and the entire trough centred at

676 nm which is attributed to chl *a* absorption (Dekker et al. 2002a). Increasing chl *a* concentrations, however, still lead to increased reflectance at these troughs, although at 676 nm the sensitivity is minimal (Gitelson et al. 2000). The net result of these spectrally counteracting forces is that increasing concentrations of chl *a* are associated with increased subsurface irradiance reflectance in Landsat B3.

The symbolic regression algorithm also includes Landsat B2 (520-600 nm). Bio-optical modelling in the present study indicates that B2 is positively correlated with chl *a* concentrations. Band 2 contains a local reflectance peak at 570-600 nm corresponding to a chlorophyll *a* and *b* absorption minimum. The bio-optical model also simulated the existence of a spectral pivot point at 530 nm, where subsurface irradiance reflectance is independent of chl *a* concentration. This wavelength is somewhat higher than the value of 497 nm used by Bukata et al. (1995) for a three-component bio-optical model with no CDOM or tripton present, but is closer to the spectral pivot point of 510 nm measured in situ by Schalles et al. (1997) during a tank enrichment/dilution experiment. Regardless of the pivot point, there is a positive correlation between reflectance and chl *a* concentration in Landsat B2.

When applying the symbolic regression algorithm (and other empirical algorithms), there is potential for error in estimated chl *a* induced from independently varying concentrations of CDOM or tripton. From the limited data available on CDOM concentrations in Rotorua lakes, concentrations are relatively low in Lake Rotorua and Rotoiti (0.16 – 0.23 m^{-1}). However, CDOM concentrations may be higher in Rotorua lakes with forest dominated catchments such as Lake Tikitapu. The symbolic regression blue-red band ratio could be perturbed in waters with high CDOM (Reinart and Kutser 2006). Further investigation is needed regarding the spectral slope and concentraion of CDOM found in the Rotorua lakes. Lakes with high CDOM would likely require the use of bands in the red and near infrared wavelengths, to avoid high CDOM absorption wavelengths (Gitelson et al. 2008). The presence of independently varying concentrations of tripton poses a greater potential for error in hindcasting chl *a* estimates. The bio-optical model shows that the addition of small amounts of tripton (e.g., c. 1 mg L^{-1}) increases subsurface irradiance reflectance in Landsat B1-B3, which leads to potential for errors in chl *a* hindcasts.

A potential solution to the chl *a* hindcast errors induced from independently varying concentrations of optically active components is the use of bio-optical algorithms that allow simultaneous estimation of CDOM absorption and SS, and chl *a* concentrations. However, the Landsat series of satellite sensors possess spectrally broad bands which do not allow for a stable inversion with a bio-optical model. Further research will be critical to address shortcomings in broadband-based algorithms, however, inherent limitations of the Landsat sensor will ultimately limit the ability of component discrimination (Mathews 2011). A recent review of the literature (Matthews 2011) revealed that there is currently no operational algorithm for remote sensing of chl *a* in inland waters using Landsat. This shortcoming has also been attributed to sensor-specific limitations including a low signal to noise ratio (SNR) (Matthews 2011). The application of three-dimensional hydrodynamic-ecological models to estimate CDOM and tripton concentrations may be able to identify locations and time periods when chl *a* estimation error is likely to occur using symbolic regression, while providing increased temporal and vertical resolution of analysis.

While bio-optical modelling is not applicable to simultaneous determination of independently varying optically active constituent concentrations when applied to Landsat, it is useful in the simulation of the physical processes that results in varying subsurface irradiance reflectance with increasing chl *a* concentration. In particular, bio-optical modelling could be further developed to quantify potential sources of error when using empirical algorithms. In the Rotorua lakes, it is likely that there is both inter-lake and seasonal variability of phytoplankton specific absorption and scattering, based on the diverse assemblage of phytoplankton present (Paul et al. 2012). Phytoplankton-specific absorption, $a^*_\phi(\lambda)$, not only depends on cell size, but pigment composition and the packaging effect (Babin et al. 1993; Babin 2003; Bricaud 2004; Blondeau-Patissier et al. 2009).

Variations in the specific scattering coefficient of phytoplankton are known to produce up to two-fold differences in chl *a* concentrations retrieved from bio-optical models (Dierssen 2010). The backscattering ratio and the specific scattering coefficient of phytoplankton are determined by the size, physical structure, and the outer coating of cells (Stramski et al. 2004). With increasing phytoplankton biomass there is greater cell wall surface area, resulting in increased scattering (Yacobi et al. 1995). In addition, gas vacuoles in some cyanobacteria have been found to be efficient at backscattering light (Dubelaar et al. 1987; Volten et al. 1998). Backscattering is inherently difficult to measure and there is considerable uncertainty in measured backscattering of phytoplankton (Stramski et al. 2004). Aquatic reflectance is determined by the ratio of backscattering to absorption (Gordon and Brown 1973), therefore variation in the backscattering ratio and the specific scattering coefficient of phytoplankton that is not accounted for in bio-optical and empirical algorithms, has the potential to introduce error in estimates for chl *a* .

While remote sensing can provide information on temporal and spatial variations in chl *a* in surface waters, it does not capture variations deeper in the water column. It has been shown that in a homogenous water body, 90% of reflectance emanating from beneath the water surface originates from water depths extending from immediately below the surface to the penetration depth where downwelling radiance decreases to 36.8% of its surface value (Gordon and McCluney 1975). This depth depends on the inherent optical properties of the optically active constituents and their concentrations, as well as the apparent optical properties of the ambient light field, and the layer from which the reflectance emanates can vary from as shallow as a few centimetres (Kutser 2004) to as deep as 60 m (Stramska and Stramski 2005). Similar to what has been shown with oceanic distributions of chl (e.g., Hill and Zimmerman 2010), lakes Rotoma, Rotoiti and Tarawera have a deep chlorophyll maximum (DCM) which occurs when the lakes are stratified, and is closely associated with the thermocline depth, but is even more closely associated with the depth where light is 1% of the surface value (i.e., the euphotic depth) (Hamilton et al. 2010). In Lake Rotoma, approximations of penetration depth of c. 5.5 m (PAR) from in situ measured light attenuation (Hamilton et al. 2010) have been recorded within the present study period, whereas chl *a* sampling is a depth-integrated value from the surface to 17 m. Therefore, where chl *a* distributions are not homogenous over 0- 17 m, remote sensing will not be representative of the in situ sample and estimates of chl *a* will not capture the DCM which has been recorded at c. 35 m in Lake Rotoma. For lakes with DCMs, the increasing development and deployment of real time autonomous monitoring buoys with vertical chlorophyll fluorescence profiling capabilities is needed for effective monitoring of vertical chlorophyll distributions.

The use of a single station to monitor in situ chl *a* has been found to both over- and underestimate concentrations compared with remotely-sensed chl *a* averaged over the lake area (Kallio et al. 2003; Kutser 2004). In Lake Rotorua, for example, complex spatial and temporal variations occur where the interaction of high cyanobacterial biomass can combine with diurnal stratification of the surface mixed layer so that positively buoyant cyanobacterial cells tend to aggregate at the water surface during calm conditions (Oliver et al. 2012). This is often disrupted on a daily basis, e.g. by afternoon wind (Hamilton 2004), which can cause highly temporally heterogeneous chl *a* distributions both vertically and horizontally. The representativeness of grab samples from lakes can therefore be compromised by these strong gradients of chl *a* (Kutser 2008). Remote sensing provides an opportunity to understand some of these horizontal complexities and, when combined with other tools such as three-dimensional hydrodynamic-ecological models (Chen et al. 2004; Chapter 4) and real time remote monitoring of chl *a* fluorescence or phytoplankton-related IOPs (Babin et al. 2005), provides vital information for a deeper understanding of variations in phytoplankton biomass in all spatial and temporal domains.

Variations in nutrients may be an important driver of intra-lake spatial variation of chl *a* in the Rotorua lakes, in addition to phytoplankton cell buoyancy, stratification and wind. For example, the high concentrations of chl *a* on the eastern shore of Lake Rotorua indicated in the image on 19 March 2004 may be associated with increased phytoplankton biomass associated with elevated nutrient concentrations in geothermal inflows (Hoellein et al. 2012). While a dilution zone effect corresponding to relatively low chl *a* concentrations near stream inflows has been observed in Lake Rotorua (Abell 2013) and elsewhere (Mackey et al. 2011), localised “hot spots” of increased fluorescence have been observed in stream inflow transition zones in Lake Rotorua (Abell 2013). Any localised increases in chl *a* concentration will depend on the relative time scales of phytoplankton growth compared to phytoplankton mixing and transport processes (Hillmer and Imberger 2007).

Variations in inflow volume and lake morphometry, in conjunction with variations in nutrient concentrations, also contribute to intra-lake variability (Håkanson 2005). For example higher chl *a* concentrations observed in the western basin relative to the eastern basin of Lake Rotoiti (before the creation of the diversion wall) were found to be driven by the gradient in nutrients generated by inflowing water from the Ohau channel (from eutrophic Lake Rotorua), which was high in nutrients (Vincent et al. 1991; Westernhagen et al. 2010). The higher chl *a* concentrations observed in Okawa Bay (Lake Rotoiti) on 24 January 202 may be at least partly attributed to the shallow depth and associated high sediment surface:water column ratio and enhanced nutrient supply from sediment-water column exchange processes (Westernhagen et al. 2010).

Lake Rotoehu has high intra-lake variability of chl *a* based on the analysis of remotely sensed images. This lake has complex dendritic morphology, and, combined with frequent algal blooms, gives rise to the most heterogeneous spatial variation in of all the Rotorua lakes (maximum satellite estimated intra-lake range of 838 µg L^{-1}). Cyanobacteria blooms are commonly observed in summer (Burns et al. 2009), and satellite-estimated concentrations of chl *a* were often higher in downwind locations, as noted in other studies (e.g., Hutchinson and Webster 1994; Oliver and Ganf 2000; Oliver et al. 2012). The highest chl *a* concentrations were estimated during time periods where wind speeds were less than 4 m s^{-1}. Wind speeds above 2–3 m s^{-1} have been identified as critical to inducing entrainment of floating phytoplankton colonies into a turbulent surface layer (Webster and Hutchinson 1994), preventing the concentration of colonies on leeward shores. Remote sensing is the only tool able to synoptically quantify temporal and spatial dynamics of algal blooms that occur in Lake Rotoehu.

The automated operational procedure developed in this study for remote sensing of chl *a* in the Rotorua is applicable to other lakes, however, the symbolic regression model is likely to be specific to the Rotorua lakes. The automation of procedures for retrieving chlorophyll allowed for processing large amounts of data and encompassed many operations which enabled a novel comparison of empirical and semi-analytical algorithms over a time series of images. However, as discussed above, the potential for error must be carefully considered in any quantitative estimates of chl *a* concentration.

2.5 References

Abell, J. M. 2013. Variability in nutrient loading to lake ecosystems and associated impacts on water quality. Ph.D. thesis, University of Waikato, New Zealand.

Allan, M. G., D. P. Hamilton, B. J. Hicks, and L. Brabyn. 2011. Landsat remote sensing of chlorophyll a concentrations in central North Island lakes of New Zealand. International Journal of Remote Sensing **32**: 2037–2055.

Babin, M. 2003. Variations in the light absorption coefficients of phytoplankton, nonalgal particles, and dissolved organic matter in coastal waters around Europe. Journal of Geophysical Research **108**: 3211.

Babin, M., J. Cullen, and C. Roesler. 2005. New approaches and technologies for observing harmful algal blooms. Oceanography **18**: 210–227.

Babin, M., J.-C. Therriault, L. Legendre, and A. Condal. 1993. Variations in the specific absorption coefficient for natural phytoplankton assemblages: Impact on estimates of primary production. Limnology and Oceanography **38**: 154–177.

Blondeau-Patissier, D., V. E. Brando, K. Oubelkheir, A. G. Dekker, L. A. Clementson, and P. Daniel. 2009. Bio-optical variability of the absorption and scattering properties of the Queensland inshore and reef waters, Australia. Journal of Geophysical Research **114**: C05003.

Bricaud, A. 2004. Natural variability of phytoplanktonic absorption in oceanic waters: Influence of the size structure of algal populations. Journal of Geophysical Research **109**: C11010.

Brivio, P. A., C. Giardino, and E. Zilioli. 1997. The satellite derived optical information for the comparative assessment of lacustrine water quality. Science of the Total Environment **196**: 229–245.

Bukata, R. P., J. H. Jerome, K. Y. Kondratyev, and D. V Pozdnyakov. 1995. Optical Properties and Remote Sensing of Inland and Coastal Waters. CRC Press, Boca Raton, Florida, USA.

Burns, N., J. McIntosh, and P. Scholes. 2005. Strategies for managing the lakes of the Rotorua District, New Zealand. Lake and Reservoir Management **21**: 61–72.

Burns, N., J. McIntosh, and P. Scholes. 2009. Managing the lakes of the Rotorua District, New Zealand. Lake and Reservoir Management **25**: 284–296.

Campbell, G., S. R. Phinn, A. G. Dekker, and V. E. Brando. 2011. Remote sensing of water quality in an Australian tropical freshwater impoundment using matrix inversion and MERIS images. Remote Sensing of Environment **115**: 2402–2414.

Chen, C., L. Wang, R. Ji, J. W. Budd, D. J. Schwab, D. Beletsky, G. L. Fahnenstiel, H. Vanderploeg, B. Eadie, and J. Cotner. 2004. Impacts of suspended sediment on the ecosystem in Lake Michigan: A comparison between the 1998 and 1999 plume events. Journal of Geophysical Research **109**: 1–18.

Chu, D. A., Y. J. Kaufman, C. Ichoku, L. A. Remer, D. Tanre, and B. N. Holben. 2002. Validation of MODIS aerosol optical depth retrieval over land. Geophysical Research Letters **29**: 8007.

Davies-Colley, R. J., and W. N. Vant. 1987. Absorption of light by yellow substance in freshwater lakes. Limnology and Oceanography **32**: 416–425.

Dekker, A. G., V. E. Brando, J. M. Anstee, N. Pinnel, T. Kutser, H. J. Hoogenboom, R. Pasterkamp, S. W. M. Peters, R. J. Vos, C. Olbert, and T. J. Malthus. 2002a. Imaging spectrometry of water, p. 307–359. *In* F. van der Meer and S. M. de Jong [eds.], Imaging Spectrometry: Basic Principles and Prospective Applications. Kluwer, Dordrecht, Netherlands.

Dekker, A. G., H. J. Hoogenboom, L. M. Goddijn, and T. J. M. Malthus. 1997. Relation between inherent optical properties and reflectance spectra in turbid inland waters. Remote Sensing Reviews **15**: 59–74.

Dekker, A. G., and S. W. M. Peters. 1993. The use of the Thematic Mapper for the analysis of eutrophic lakes: a case study in the Netherlands. International Journal of Remote Sensing **14**: 799–821.

Dekker, A. G., S. W. M. Peters, R. Vos, and M. Rijkeboer. 2001a. Remote sensing for inland water quality detection and monitoring, *In* A. Van Dijk and M.G. Bos [eds.], GIS and remote Sensing Techniques in Land- and Water management. Kluwer Academic Publishers, Netherlands.

Dekker, A. G., R. J. Vos, and S. W. M. Peters. 2001b. Comparison of remote sensing data, model results and in situ data for total suspended matter (TSM) in the southern Frisian lakes. The Science of the Total Environment **268**: 197–214.

Dekker, A. G., R. J. Voss, and S. W. M. Peters. 2002b. Analytical algorithms for lake water TSM estimation for retrospective analysis of TM and SPOT sensor data. International Journal of Remote Sensing **23**: 15–35.

Dierssen, H. M. 2010. Perspectives on empirical approaches for ocean color remote sensing of chlorophyll in a changing climate. Proceedings of the National Academy of Sciences of the United States of America **107**: 17073–8.

Dubelaar, G. B., J. W. Visser, and M. Donze. 1987. Anomalous behaviour of forward and perpendicular light scattering of a cyanobacterium owing to intracellular gas vacuoles. Cytometry **8**: 405–12.

Giardino, C., M. Pepe, P. Brivio, P. Ghezzi, and E. Zilioli. 2001. Detecting chlorophyll, Secchi disk depth and surface temperature in sub-alpine lake using Landsat Imagery. The Science of the Total Environment **268**: 19–29.

Gilerson, A., J. Zhou, S. Hlaing, I. Ioannou, J. Schalles, B. Gross, F. Moshary, and S. Ahmed. 2007. Fluorescence component in the reflectance spectra from coastal waters. Dependence on water composition. Optics Express: 15: 15702-15721.

Gitelson, A, G. Dallolmo, W. Moses, D. Rundquist, T. Barrow, T. Fisher, D. Gurlin, and J. Holz. 2008. A simple semi-analytical model for remote estimation of chlorophyll-a in turbid waters: Validation. Remote Sensing of Environment **112**: 3582–3593.

Gitelson, A. A., Y. Z. Yacobi, A. Karnieli, and N. Kress. 1996. Reflectance spectra of polluted marinewaters in Haifa Bay, Southeastern Mediterranean: features and application for remote estimation of chlorophyll concentration. Israel Journal of Earth Sciences **45**: 127–136.

Gitelson, A., G. Garbuzov, F. Szilagyi, K. Mittenzwey, A. Karnieli, and A. Kaiser. 1993. Quantitative remote sensing methods for real-time monitoring of inland waters quality. International Journal of Remote Sensing **14**: 1269–1295.

Gordon, H. R., and O. B. Brown. 1973. Irradiance reflectivity of a flat ocean as a function of its optical properties. Applied Optics **12**: 1549–1551.

Gordon, H. R., J. W. Brown, O. B. Brown, R. H. Evans, and R. C. Smith. 1988. A semianalytic radiance model of ocean color. Journal of Geophysical Research **93**: 10909–10924.

Gordon, H. R., and W. R. McCluney. 1975. Estimation of the depth of sunlight penetration in the sea for remote sensing. Applied Optics **14**: 413–6.

Håkanson, L. 2005. The importance of lake morphometry for the structure and function of lakes. International Review of Hydrobiology **90**: 433–461.

Hamilton, D. P. 2003. An historical and contemporary review of water quality in the Rotorua lakes. *In* Rotorua Lakes 2003, Practical Management for Acheiving Better Water Quality Conference, Proceedings of the Lakes Water Quality Society, 9-10 October 2003, Rotorua, NZ.

Hamilton, D. P. 2004. Deciphering causal mechanisms of variability in phytoplankton biomass and succession in the Rotorua lakes. *In* Rotorua Lakes 2004, Restoring Lake Health - Nutrient Targets and Cyanobacteria Conference, 16-17 September 2004, Rotorua, NZ. p. 151–161.

Hamilton, D. P., K. R. O'Brien, M. A. Burford, J. D. Brookes, and C. G. McBride. 2010. Vertical distributions of chlorophyll in deep, warm monomictic lakes. Aquatic Sciences **72**: 295–307.

Han, L., and K. J. Jordan. 2005. Estimating and mapping chlorophyll-a concentration in Pensacola Bay, Florida using Landsat ETM+ data. International Journal of Remote Sensing **26**: 5245–5254.

Hill, V. J., and R. C. Zimmerman. 2010. Estimates of primary production by remote sensing in the Arctic Ocean: Assessment of accuracy with passive and active sensors. Deep Sea Research Part I: Oceanographic Research Papers **57**: 1243–1254.

Hillmer, I., and J. Imberger. 2007. Estimating in situ phytoplankton growth rates with a Lagrangian sampling strategy. Limnology and Oceanography: Methods **5**: 495–509.

Hoellein, T. J., D. A. Bruesewitz, and D. P. Hamilton. 2012. Are geothermal streams important sites of nutrient uptake in an agricultural and urbanising landscape (Rotorua, New Zealand)? Freshwater Biology **57**: 116–128.

Kallio, K., S. Koponen, and J. Pulliainen. 2003. Feasibility of airborne imaging spectrometry for lake monitoring-a case study of spatial chlorophyll a distribution in two meso-eutrophic lakes. International Journal of Remote Sensing **24**: 3771–3790.

Kloiber, S. M., P. L. Brezonik, and M. E. Bauer. 2002. Application of Landsat imagery to regional-scale assessments of lake clarity. Water Research **36**: 4330–4340.

Koponen, S. 2006. Remote sensing of water quality for Finnish lakes and coastal areas. Ph.D. thesis, Helsinki University of Technology, Finland.

Kotchenova, S. Y., E. F. Vermote, R. Levy, and A. Lyapustin. 2008. Radiative transfer codes for atmospheric correction and aerosol retrieval: intercomparison study. Applied Optics **47**: 2215–2226.

Koza, J. R. 1992. Genetic Programming: On the Programming of Computers by Means of Natural Selection, The MIT Press, Cambridge, Massachusetts, USA.

Kutser, T. 2004. Quantitative detection of chlorophyll in cyanobacterial blooms by satellite remote sensing. **49**: 2179–2189.

Kutser, T., L. Metsamaa, and A. G. Dekker. 2008. Influence of the vertical distribution of cyanobacteria in the water column on the remote sensing signal. Estuarine, Coastal and Shelf Science **78**: 649–654.

Liley, J. B., and B. W. Forgan. 2009. Aerosol optical depth over Lauder, New Zealand. Geophysical Research Letters **36**: L07811.

Lillesand, T. M., W. L. Johnson, R. L. Deuell, O. M. Lindstrom, and D. E. Meisner. 1983. Use of Landsat data to predict the trophic state of Minnesota lakes. Photogrammetric Engineering and Remote Sensing **49**: 219–229.

Mackay, E. B., I. D. Jones, A. M. Folkard, and S. J. Thackeray. 2011. Transition zones in small lakes: the importance of dilution and biological uptake on lake-wide heterogeneity. Hydrobiologia **678**: 85–97.

Matthews, M. 2011. A current review of empirical procedures of remote sensing in inland and near-coastal transitional waters. International Journal of Remote Sensing **32**: 6855–6899.

Mobley, C. D. 1994. Light and Water: Radiative Transfer in Natural Waters. Academic Press, San Diego, CA, USA.

Morel, A. 1974. Optical properties of pure water and pure seawater, p. 1–24. *In* N.G. Jerlov and E. Steemann Nielsen [eds.], Optical Aspects of Oceanography. Academic Press, London.

Oliver, R., and G. Ganf. 2000. Freshwater blooms, p. 149–194. *In* M.P. B. Whitton [ed.], The Ecology of Cyanobacteria: Their Diversity in Time and Space. Kluwer Academic Publishers, Netherlands.

Oliver, R., D. Hamilton, J. Brookes, and G. Ganf. 2012. Physiology, blooms and prediction of planktonic Cyanobacteria, p. 155–194. *In* B.A. Whitton [ed.], Ecology of Cyanobacteria II. Springer, Netherlands.

Olmanson, L. G., M. E. Bauer, and P. L. Brezonik. 2008. A 20-year Landsat water clarity census of Minnesota’s 10,000 lakes. Remote Sensing of Environment **112**: 4086–4097.

Paul, W. J., D. P. Hamilton, I. Ostrovsky, S. D. Miller, A. Zhang, and K. Muraoka. 2012. Catchment land use and trophic state impacts on phytoplankton composition: a case study from the Rotorua lakes’ district, New Zealand. Hydrobiologia **698**: 133–146.

Pope, R. M., and E. S. Fry. 1997. Absorption spectrum (380-700 nm) of pure water. II. Integrating cavity measurements. Applied Optics **36**: 8710–8723.

Reinart, A., and T. Kutser. 2006. Comparison of different satellite sensors in detecting cyanobacterial bloom events in the Baltic Sea. Remote Sensing of Environment **102**: 74–85.

Remer, L. A., Y. J. Kaufman, D. Tanré, S. Mattoo, D. A. Chu, J. V. Martins, R.-R. Li, C. Ichoku, R. C. Levy, R. G. Kleidman, T. F. Eck, E. Vermote, and B. N. Holben. 2005. The MODIS Aerosol Algorithm, Products, and Validation. Journal of the Atmospheric Sciences **62**: 947–973.

Schmidt, M., and H. Lipson. 2009. Distilling free-form natural laws from experimental data. Science **324**: 81–85.

Scholes, P. 2011. 2010 / 2011 Rotorua Lakes Trophic Level Index Update. Environmental Publication 2011/17. Bay of Plenty Regional Council, Whakatane, New Zealand.

Scholes, P., and M. Bloxham. 2008. Rotorua Lakes Water Quality 2007 Report. Environmental Publication 2008/04. Bay of Plenty Regional Council, Whakatane, New Zealand.

Søndergaard, M., J. Windolf, and E. Jeppesen. 1996. Phosphorus fractions and profiles in the sediment of shallow Danish lakes as related to phosphorus load, sediment composition and lake chemistry. Water Research **30**: 992–1002.

Stephens, S., M. Gibbs, I. Hawes, E. Bowman, and J. Oldman. 2004. Ohau Channel Groynes. NIWA client report HAM2004-047, Hamilton, New Zealand.

Stramska, M., and D. Stramski. 2005. Effects of a nonuniform vertical profile of chlorophyll concentration on remote-sensing reflectance of the ocean. Applied Optics **44**: 1735–1747.

Stramski, D., E. Boss, D. Bogucki, and K. J. Voss. 2004. The role of seawater constituents in light backscattering in the ocean. Progress in Oceanography **61**: 27–56.

Vant, W. N., and R. J. Davies-Colley. 1986. Relative importance of clarity determinants in lakes Okaro and Rotorua. New Zealand Journal of Marine and Freshwater Research **20**: 355–363.

Vidot, J., and R. Santer. 2005. Atmospheric correction for inland waters—application to SeaWiFS. International Journal of Remote Sensing **26**: 3663–3682.

Vincent, W., M. Gibbs, and R. Spigel. 1991. Eutrophication processes regulated by a plunging river inflow. Hydrobiologia **226**: 51–63.

Volten, H., J. De Haan, and J. Hovenier. 1998. Laboratory measurements of angular distributions of light scattered by phytoplankton and silt. Limnology and Oceanography **46**: 1180–1197.

Webster, I. T., and P. A. Hutchinson. 1994. Effect of wind on the distribution of phytoplankton cells in lakes revisited. Limnology and Oceanography **39**: 365–373.

Westernhagen, N., D. P. Hamilton, and C. A. Pilditch. 2010. Temporal and spatial variations in phytoplankton productivity in surface waters of a warm-temperate, monomictic lake in New Zealand. Hydrobiologia **652**: 57–70.

Yacobi, Y. Z., A. Gitelson, and M. Mayo. 1995. Remote sensing of chlorophyll in Lake Kinneret using highspectral-resolution radiometer and Landsat TM:

spectral features of reflectance and algorithm development. Journal of Plankton Research **17**: 2155–2173.

3 Atmospheric correction of Landsat thermal imagery for surface water temperature retrieval and three-dimensional hydrodynamic model validation of spatial heterogeneity in geothermally-influenced lakes

3.1 Introduction

Knowledge of water temperature is crucial to understanding of lake ecosystem functioning (Hutchinson 1957). Furthermore, there is increasing recognition of the potential for lakes to act as sentinels of climate change, as physical, chemical and biological indicators in standing waters reflect atmospheric forcing and may reflect a changing climate within lake catchments (Williamson et al. 2008; Adrian et al. 2009).

High-frequency (e.g., 15 min interval) in situ temperature measurements are commonly used to monitor the vertical structure of temperature in lakes (Yeates et al. 2008), however, such techniques are not cost effective for characterising horizontal temperature variation in large lakes. The use of measurements obtained from satellites potentially provides a solution to this problem (Hook et al. 2003). Of particular note is the large increase in the use of Landsat visible, infra-red and thermal-infrared imagery for water monitoring, prompted by the release of the entire data archive for free public use. Satellite thermal imagery has been used for a wide variety of lake applications including: temperature monitoring of volcanic lakes (Oppenheimer 1993); characterising upwelling and circulation (Steissberg et al. 2005a); observing surface current speed/direction (Steissberg et al. 2005b) and near-shore thermal bars (Schott et al. 2001); identification of groundwater discharge areas (Tcherepanov et al. 2005); and estimating the influence of lake morphology and clarity on water surface temperature (Becker and Daw 2005).

Remote sensing radiometers measure the lake water ‘skin’ temperature (upper 100 µm) rather than the bulk surface temperature usually measured with in situ sensors. The skin temperature differs from bulk temperature due to heat transfer at the air-water interface from sensible and latent heat fluxes and longwave radiation. The skin temperature is usually lower than the bulk temperature due to net heat loss, however, very shallow diurnal thermoclines (< 100 mm) can sometimes cause skin temperature to be warmer than bulk temperature. Bulk and skin temperature differences have been found to be at a minimum (average daily temperature difference of -0.1 °C) from 0900 to 1100 h, which corresponds to the theoretical time of Landsat overpass (Schneider and Mauser 1996). Hook et al. (2003) found consistent differences between near-real-time measurements of lake skin temperature from radiometers and bulk surface water temperature measurements in Lake Tahoe (California, USA) over a diurnal cycle, with daytime and night time skin temperatures cooler by an average of 0.11°C and 0.46°C, respectively.

Atmospheric correction (AC) is a crucial step in determining water quality from satellite data, as differences between bulk water temperature and uncorrected satellite-derived water skin temperature can be as large as 4.55 °C (Fisher et al. 2004). Limited availability of meteorological data and difficulty of radiative transfer-based AC have previously limited temperature retrieval algorithms to empirically based methods (e.g., Lathrop and Lillesand 1987; Baban 1993). However, theoretically-based AC of Landsat data has been achieved with the Low Resolution Transmission model (LOWTRAN) for retrieval of Lake Ontario water surface temperature (Schott and Volchok 1985). The LOWTRAN 7 model (spectral resolution measured by spectroscopic wavenumber at 20 cm^{-1}) has now been superseded by Moderate Resolution Transmission (MODTRAN) which uses spectral resolutions ranging from 2 cm^{-1} (MODTRAN 3.7-4.0) to 0.2 cm^{-1} (MODTRAN 5.0). There is little information about the accuracy of atmospheric profiles of temperature, pressure and relative humidity (RH) used in radiative transfer modelling for thermal atmospheric correction, particularly in relation to Landsat water temperature retrieval.

Process-based modelling of lake water temperature offers opportunities to interpolate temporal data gaps derived from satellite and traditional periodical monitoring data whilst also extrapolating surface water temperatures to an entire waterbody. However, many of these models either do not apply, or, are not well validated in the horizontal dimension. Validation of three-dimensional (3-D) models is difficult using traditional point-based monitoring, but the synthesis of satellite thermal imagery with high-frequency temperature measurements from thermistor chains presents an opportunity to spatially evaluate temperature outputs from 3-D hydrodynamic models. In addition, determination of initial conditions over a whole 3-D model simulation domain can be especially challenging, but may be usefully resolved with satellite imagery (e.g., Alvarez et al. 2007). However, a high level of accuracy and confidence is required in satellite data for it to be useful in validation of 3-D models.

The Rotorua lakes, North Island, New Zealand, provide a unique opportunity to assess remote sensing of surface water temperature, due to the significant geothermal activity giving rise to large temperature variations in some lakes. Thermal imaging from helicopter has previously shown the relative distribution of geothermal inflows to Lake Rotorua (Mongillo and Bromley 1992), and thermal springs in lakes Tarawera, Rotomahana and Frying Pan amongst lakes of the Rotorua region (Mongillo 1994). Airborne thermal imaging has been used previously on Lake Rotorua to determine spatial variations in water temperature and geothermal inflows (Timmins and Belliss 1983) but the transport and mixing of geothermal plumes have rarely been observed in detail. Due to the large variation in temperature created by geothermal plumes and the availability of thermal remote sensing data, a unique opportunity exists in this region to study the transport path of geothermal inflows. Positively buoyant warm inflows create plumes or jets, which have been shown to support unique biogeochemical processes (Amon and Benner 1998).

The major objective of this work was to compare AC of Landsat thermal imagery using MODTRAN with four sources of atmospheric profile data, thereby informing global users of Landsat data about the most appropriate AC methods. A further objective was to use remotely sensed temperature data to validate output from a 3-D hydrodynamic model of a polymictic lake that has high horizontal variability in water temperature due to the influence of a warm geothermal inflow.

3.2 Methods

Study site

The Rotorua lakes (Figure 3.1(a)) are of recent volcanic origin (<140 000 yr. BP.) and were formed by explosion craters and subsidence associated with volcanic activity (Lowe and Green 1987). The mean depth of these lakes ranges from 6.9 m in Lake Rotoehu (Figure 3.2) to 60 m in Lake Tarawera. Lake Taupo (Figure 3.1(b)) (area = 616 km^2, mean depth 97 m) is located in a caldera created by a super-volcanic eruption which occurred 26,500 yr BP. Many of the lakes have geothermal inputs including Rotorua, Rotoiti, Rotoehu, Rotomahana and Tarawera. In Lake Rotorua (area = 80 km^2, mean depth = 10 m) this influence is clearly visible due to high reflectance caused by scattering of sulphur particles in a thermal plume in the south of the lake. Lake Rotoehu is a eutrophic lake with a surface area of 7.95 km^2, mean depth of 6.9 m and maximum depth of 13.5 m (Trolle et al. 2011; Figure 3.2). A geothermal stream enters the lake in the south-west corner of the lake.

Methods overview

Atmospheric correction of Landsat 7 thermal data was carried out for the purpose of retrieval of lake water surface temperature in Rotorua lakes, and Lake Taupo. The effect of the atmosphere on the images was modelled using four sources of atmospheric profile data as input to MODTRAN. The retrieved water temperatures

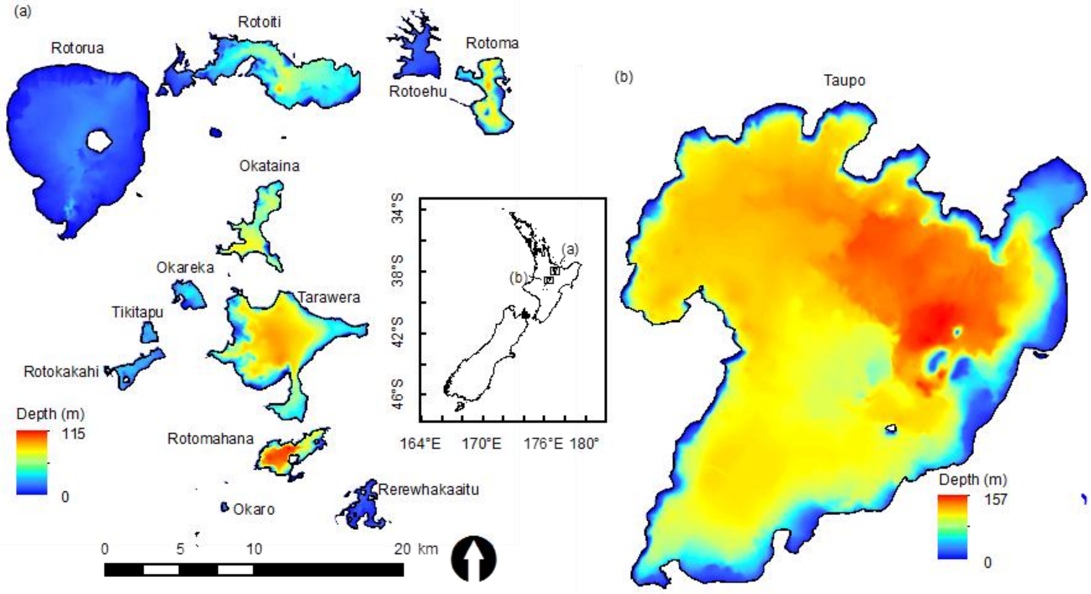

Figure 3.1. Study site map including depth for (a) Rotorua lakes and (b) Lake Taupo.

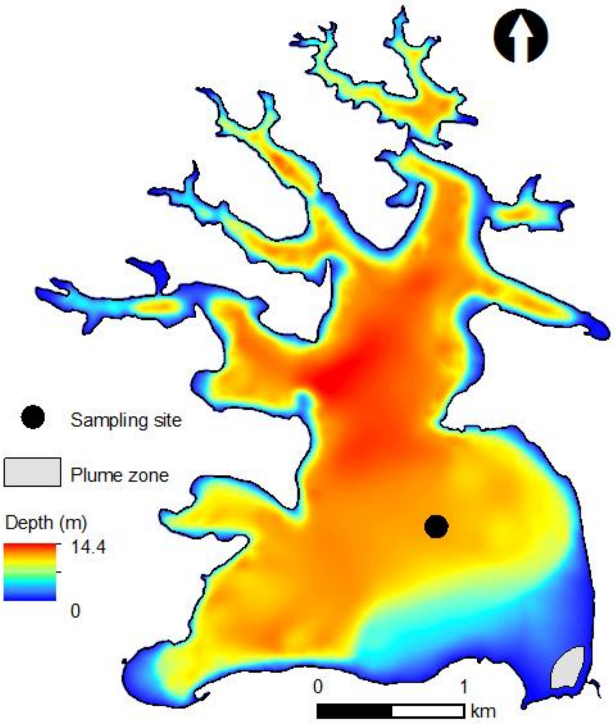

Figure 3.2. Lake Rotoehu study site, showing the location of the water quality monitoring station, and the Waitangi Soda Springs inflow plume zone for comparison of ELCOM and Landsat temperature data.

from 14 images between 2007 and 2009 were validated using a high-frequency temperature sensor deployed from a mid-lake monitoring buoy at the water surface of Lake Rotorua. Retrieved surface water temperature was used for assessing spatial heterogeneity of surface water temperature simulated with a 3-D hydrodynamic model of Lake Rotoehu (using eight Landsat images captured during the simulation period). The transport and mixing of a geothermal inflow and basin-scale circulation patterns was inferred from thermal distributions from satellite estimated and model simulations of surface water temperature and a spatially resolved statistical evaluation was used to validate simulations.

Image analysis

Landsat satellite images captured from 1 September 2006 until 10 November 2009 were ordered and downloaded from USGS Global Visualisation Viewer (GloVis). Images were captured at approximately 1000 h NZST. Band 6 high-gain (60-m resolution) was used for temperature derivation. Conversion from Landsat-scaled radiance (DN) to 32-bit spectral radiance at the sensor aperture ($L(\lambda)$; W m^{-2} sr^{-1} μm^{-1}) was performed according to Landsat (2008):

$$L(\lambda) = G_r \cdot Q_c + B_r \tag{3.1}$$

where G_r= rescaled gain (W m^{-2} sr^{-1} μm^{-1}/DN), B_r= rescaled bias (W m^{-2} sr^{-1} μm^{-1}) and Q_c= quantized calibrated pixel value in DN.

Atmospherically corrected water-leaving radiance L_w was calculated according to Coll et al. (2010), with wavelength dependence for all parameters:

$$L_w = \frac{L_t - L_a}{\varepsilon\tau} - \left(\frac{1-\varepsilon}{\varepsilon}\right) L_{sky} \tag{3.2}$$

where:
L_t= at-sensor radiance (W m^{-2} sr^{-1} μm^{-1})
L_a= atmospheric or upwelling radiance emitted by the atmosphere (W m^{-2} sr^{-1} μm^{-1})
ε= emissivity of the water surface

τ= atmospheric transmission
L_{sky}=downwelling or sky radiance reflected from the water surface (W m^{-2} sr^{-1} μm^{-1})

Since the emissivity of water is very high, the reflected downwelling sky radiance is negligible in the region of the Landsat thermal infrared bands. MODTRAN 3.7 was used to calculate L_a and τ using four sources of atmospheric data detailed below, with L_a weighted with the Landsat 7 relative spectral response function. For upper atmosphere heights not included in the four sources of atmospheric profile data, mid-latitude summer or winter (USA) standard atmospheres were used, corresponding to the season closest to the date of image capture. In all cases the atmospheric boundary layer was defined using meteorological data from Rotorua Airport weather station.

NASA Atmospheric Parameter Calculator

An Atmospheric Parameter Calculator (using MODTRAN 4.0; NASA) was used to determine L_a and τ using National Centres for Environmental Prediction (NCEP) atmospheric profile data including pressure, temperature and RH. This tool allows estimation of surface temperature to c. ±2 ºC globally if emissivity is known and the atmosphere is reasonably clear (Barsi et al. 2005). There is limited validation of this method for ground-based targets, especially in the Southern Hemisphere where there is greater uncertainty in NCEP data. In all cases the atmospheric boundary layer was defined using meteorological data from Rotorua Airport weather station.

Radiosonde atmospheric profile data

Radiosonde data were taken at Whenuapai weather station at 1200 h NZST (NZ Metservice). This location (latitude 36.793ºS, longitude 174.624ºE) is 200 km north-west of the Rotorua lakes. Pressure, temperature (T), and calculated RH were used for the lower 30 km of the atmosphere. Dew point temperature (T_d) and T were used to calculate vapour pressure (e), saturation vapour pressure (e_s) and then RH:

$$\mathrm{RH} = [e(T)/e_s(T)] \times 100\% \qquad (3.3)$$

where e and e_s are calculated from the Clausius-Clapeyron equation:

$$\mathrm{Ln}(e_s/6.11) = (L/R_v)(1/273.15 - 1/T) \qquad (3.4)$$

where;
L = latent heat of vaporization = 2.453 × 10^6 J kg^{-1}, R_v = gas constant for moist air = 461.5 J kg^{-1}, and T = temperature (ºK).

Atmospheric Infrared Sounder (AIRS) atmospheric profile data

The Atmospheric Infrared Sounder (AIRS) is an instrument on-board the MODIS Aqua satellite launched in 2002. AIRS is a hyperspectral infrared sounder with 2,378 spectral channels and is currently the most advanced atmospheric sounding system in orbit. AIRS is used to measure temperature and water vapour as a function of height for the lower 18.5 km of the atmosphere. The uncertainty is within 15% for 2 km layer thickness water vapour, and 1 ºC for 1 km layer thickness temperature profiles. However, Tobin et al. (2006) found higher errors for mid-latitude sites, with RMSE of 1 to 2 ºC for temperature and 25-35% for water vapour. Over the Rotorua lakes the AIRS overpass time (0225 h UTC) is approximately 4 h and 25 min after the Landsat overpass time (2150 h UTC). For this study, AIRS level 3 data were used (AL3).

MODIS Terra atmospheric profile data

MODIS Terra atmospheric profile data were used from the MOD07 product which includes atmospheric profiles of T and T_d at 20 pressure levels. These data were used to calculate RH as above. Due to the lower spectral resolution of this instrument the accuracy of derived atmospheric data is lower. The RMSE for temperature retrieval has been found to be consistently 1 ºC higher than that derived from AIRS, although for the mixing ratio the RMSE is similar to AIRS above 900 hPa (Seemann et al. 2006). For the Rotorua lakes 19 pressure levels were used corresponding to altitudes of approximately 300 to 35 000 m. The Terra satellite has an identical orbit to Landsat 7 and c. 15 min between overpass times.

Remotely sensed temperature validation

Water surface temperature estimated by Landsat averaged within a 180 m x 180 m area of interest was compared to that for the identical location corresponding to a BOPRC monthly monitoring site on Lake Rotoehu (Figure 3.2) and the Rotorua buoy location (Figure 3.1). For a comparison of temperature in the Waitangi soda springs geothermal plume in Lake Rotoehu (Figure 3.1), a polygon was used which encompassed the location of the plume whilst maintaining a 60 m buffer from the shoreline, equal to the resolution of a Landsat ETM+ B6 pixel.

Hydrodynamic model description and setup

The Estuary and Lake Computer Model (ELCOM) is a 3-D numerical model developed at Centre for Water Research at the University of Western Australia (Hodges et al. 2000; Hodges and Dallimore 2001). ELCOM uses hydrodynamic and thermodynamic models in order to simulate velocity, salinity and temperature in waterbodies. The hydrodynamic model solves the unsteady, viscous Navier-Stokes equations for incompressible flow using the hydrostatic assumption for pressure. A Euler-Lagrange method is used for advection of momentum with a conjugate-gradient solution for the free-surface height (Casulli and Cheng 1992). Passive and active scalars are advected using a conservative ultimate quickest discretization (Leonard 1991).

For application of the model to Lake Rotoehu a numerical grid of 30-m x 30-m horizontal cells was used, with varying vertical resolution ranging from 0.2-m to 1.6-m over a depth of 12-m. Model forcing data included hourly meteorological data from the Rotorua Airport station (19 km from Lake Rotoehu). The data included wind speed, wind direction, air temperature, RH, air pressure and solar radiation. Daily cloud cover was used as input to the model to calculate longwave radiation. Stream inflow volumes and temperatures were measured monthly (BOPRC database) and linear interpolation was used to produce daily flow input to the model. Residual inflow or outflow were derived from a water balance of the lake at daily time scales, and also included input data of lake inflows, outflows, rainfall calculated evaporation, and changes in lake height adjusted to volume based on a hypsographic curve.

Differences were found between air temperature measured at the Lake Rotorua monitoring buoy and at Rotorua Airport, which were attributed to air mass modification by thermal inertia effects of the lake. In our study ELCOM was run using air temperature data from both the Rotorua Airport (T_a) and a modified air temperature (T_r) based on air temperature measured at the lake monitoring buoy, T_b, based on comparison of data from the two sites (r^2=0.97, p<0.01):

$$T_r = 0.0121\ T_a^2 + 0.5797\ T_a + 3.95 \qquad (3.5)$$

where $T_r = T_a$ for $T_a \geq 15$ ºC.

Plume flow process classification and comparison of ELCOM and Landsat surface water temperature

A comprehensive classification framework proposed by Jones et al. (2007) was applied in order to describe the geothermal inflow symbolically. Buoyant surface jet dynamics are determined largely by near-field jet processes, which are characterised by discharge fluxes for volume, momentum and buoyancy. Length scales are defined from these dynamic quantities and the ambient lake velocity, including the discharge length scale, jet-to-plume length scale, jet-to-crossflow length scale, and plume-to-crossflow length scale. Using a comparison of length scales and applicable geometric parameters, four flow categories can be identified; free jets, shoreline-attached jets, wall jets, and upstream intruding plumes. These categories have been subdivided into ten flow classes based mostly on the degree of bottom interaction. Stepwise classification methodology of the inflow is used based on a set of criteria allowing a tree-like decision framework. This classification was applied to all observed discharge volumes/buoyancy fluxes, and model simulated lake ambient velocities near the major geothermal inflow to Lake Rotoehu (Waitangi Soda Springs).

The first criterion in the four inflow classifications determines whether the flow is jet-like or plume-like. It is equivalent to an inverse Froude number which also includes the influence of the aspect ratio (effectively a depth-based Froude number), therefore indicating the distance for the flow to become affected by buoyancy relative to the source depth. For plumes there is one more criterion which distinguishes between strong plumes with significant upstream intrusion and weak plumes which are affected more by ambient currents and remain close to the shoreline.

3.3 Results

Accuracy of Landsat temperature estimation

The highest accuracy of Landsat ETM+ temperature estimation in Lake Rotorua was achieved with radisonde data as an input into MODTRAN, with a RMSE of 0.37 ºC (Table 3.1). The RMSE values of MODIS Level 2, AIRS Level 3, and NASA data were 0.55 ºC, 0.75 ºC, and 1.05 ºC, respectively. Errors for non-radiosonde data were generally higher in summer. The average calibrated temperature (no AC) was 2.50 °C lower than atmospherically corrected temperatures (using radiosonde atmospheric profiles), with a range of -1.04 to -4.78 °C.

Table 3.1. Root-mean-square-error (RMSE) and mean difference between in situ measured water temperature (Lake Rotorua buoy) and Landsat-derived temperature using different sources of atmospheric data over 14 separate dates (RASO - radiosonde, ML2 - MODIS Level 2, AL3 - Airs Level 3).

Method	RMSE (°C)	Mean buoy-Landsat (°C)
RASO	0.37	-0.04
ML2	0.55	0.27
AL3	0.75	-0.17
NASA	1.05	-0.59

Figure 3.3 shows four sources of atmospheric profile data for RH at different pressure levels on two separate dates: (a) 27 January 2009 and (b) 8 September 2009. Water surface temperature retrieval errors were higher on 27 January 2009 (-2.62°C)

using NASA data (Table 3.2) and RH measured at Rotorua meteorological station was low (39%). On this date, large differences occurred between the vertical profiles of RH at both high and low altitudes. By contrast, on 8 September 2009 water surface temperature retrieval errors were low (-0.02°C), and again, significant differences between atmospheric profiles were observed at high altitude, whilst at low altitude atmospheric profiles were similar. On this date, RH measured at Rotorua meteorological station was high (91%).

Table 3.2. Error in temperature estimation in Lake Rotorua (estimated – measured, ºC) for different AC methods (RASO - radiosonde, ML2 - MODIS Level 2, AL3 - Airs Level 3) and relative humidity (RH) measured at the Rotorua meteorological station.

Date (UTM)	RASO	ML2	AL3	NASA	RH (%)
17/07/2007	0.05	1.18	-0.07	-0.13	94
18/08/2007	-0.22	0.25	0.27	-0.09	70
9/01/2008	0.37	-0.50	1.65	-0.98	76
25/01/2008	0.17	0.78	-0.57	-1.67	49
3/07/2008	0.34	0.14	-0.16	-0.37	80
4/08/2008	0.22	0.17	0.16	0.49	84
10/12/2008	-0.03	-0.21	-0.92	-1.40	68
11/01/2009	0.22	1.26	-1.00	-1.19	60
27/01/2009	-0.95	0.00	-1.13	-2.62	39
1/04/2009	-0.61	0.35	-1.00	-0.79	64
3/05/2009	-0.31	0.06	-0.08	0.35	65
20/06/2009	0.25	0.29	0.68	0.34	61
8/09/2009	-0.03	-0.17	-0.48	-0.02	91
10/10/2009	-0.17	0.14	-0.04	-0.18	64

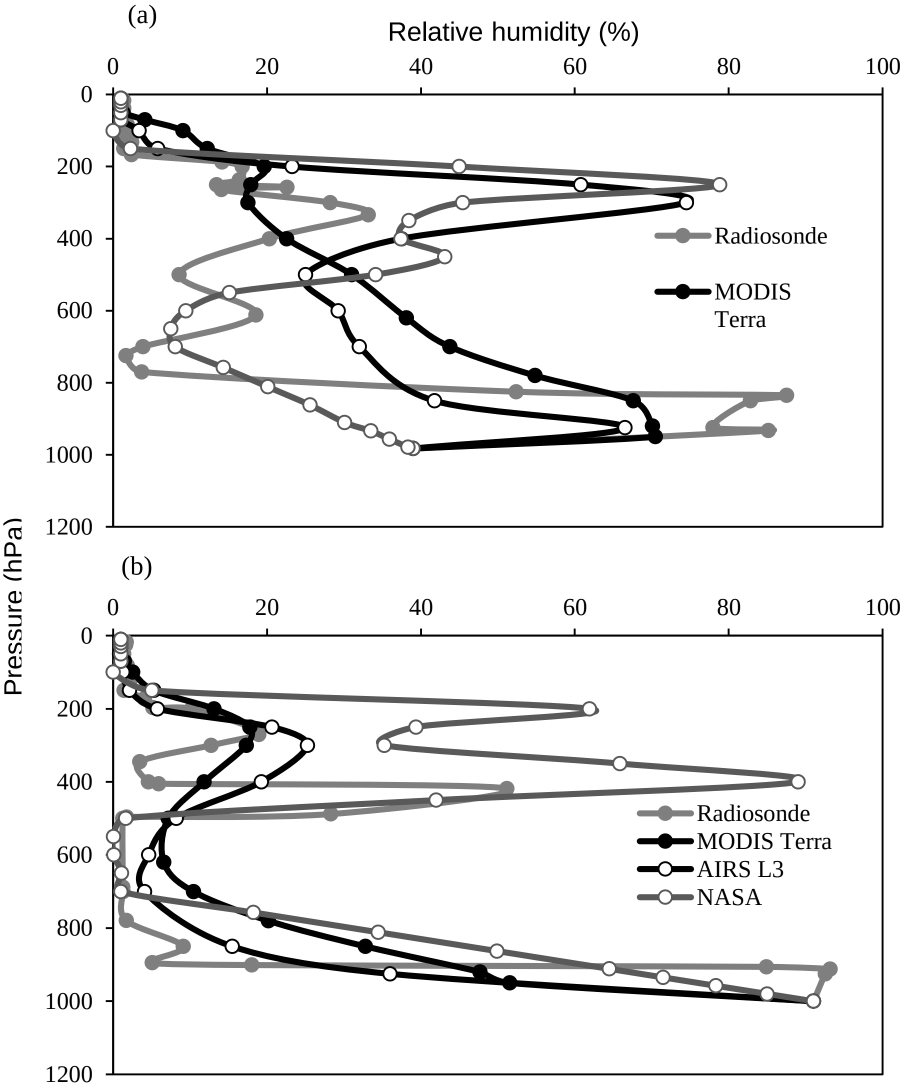

Figure 3.3. Comparison of relative humidity versus pressure profiles from four sources of atmospheric data used in MODTRAN on two different dates: (a) 27 January 2009 and (b) 8 September 2009.

Derived water temperature maps

Landsat-estimated surface water temperatures (radiosonde) are shown in Figure 3.4 for large lakes in the Rotorua region on 20 July 2009. Large spatial variations occurred both within and between lakes, with a major geothermal inflow apparent as higher temperature on the south shore of Lake Rotorua. The Waitangi Soda Springs geothermal inflow to Lake Rotoehu is identifiable from elevated water temperature in the south east of the lake. In this image (Figure 3.4) temperature ranged from 4.5 °C in the shallow south-east bay of Lake Rerewhakaaitu (satellite-estimated

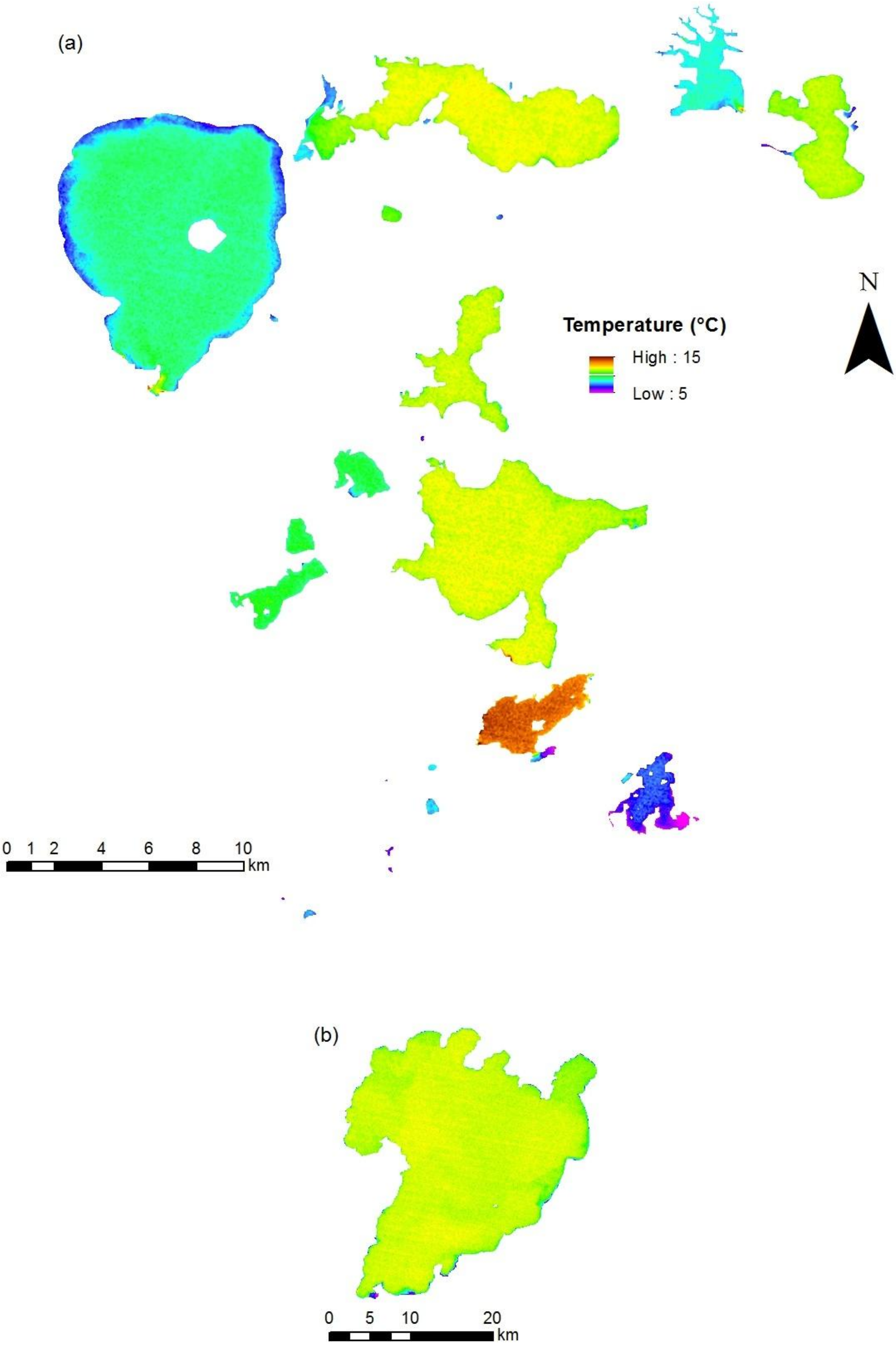

Figure 3.4. Landsat-estimated temperature (ºC) on 20 June 2009 using radiosonde atmospheric data in (a) Rotorua lakes, and (b) Lake Taupo. The stripes of missing data caused by the failure of the scan line corrector have been filled using linear interpolation.

temperature at Rerewhakaaitu BOPRC monitoring site near the centre of the lake was 7.2 °C) to 36.8 °C in Frying Pan Lake. The largest temperature range was in Lake Rotomahana (9.8 °C) which also had the highest temperature of 14.6 °C (apart from Frying Pan Lake), which was near geothermal springs on the western shore of this lake. Within-lake variations in temperature showed a general correspondence with water depth, especially in lakes with shallow margins such as Rotorua, and in lakes with sheltered bays such as Rotoiti, and Rotomahana (Figure 3.4). For example, shallow margins of Lake Rotorua were significantly cooler than open water surface temperature by c. 3 °C on 21 June 2009. Surface water temperature derived from Landsat data on 25 January 2008 shows cooler water on the northern shore of Lake Rotorua, and in some areas around the western shore (Figure 3.5). Shallow lakes such as Rotorua and Rotoehu display larger seasonal variations in temperature amongst seasons than deeper lakes such as Tarawera (Figure 3.4).

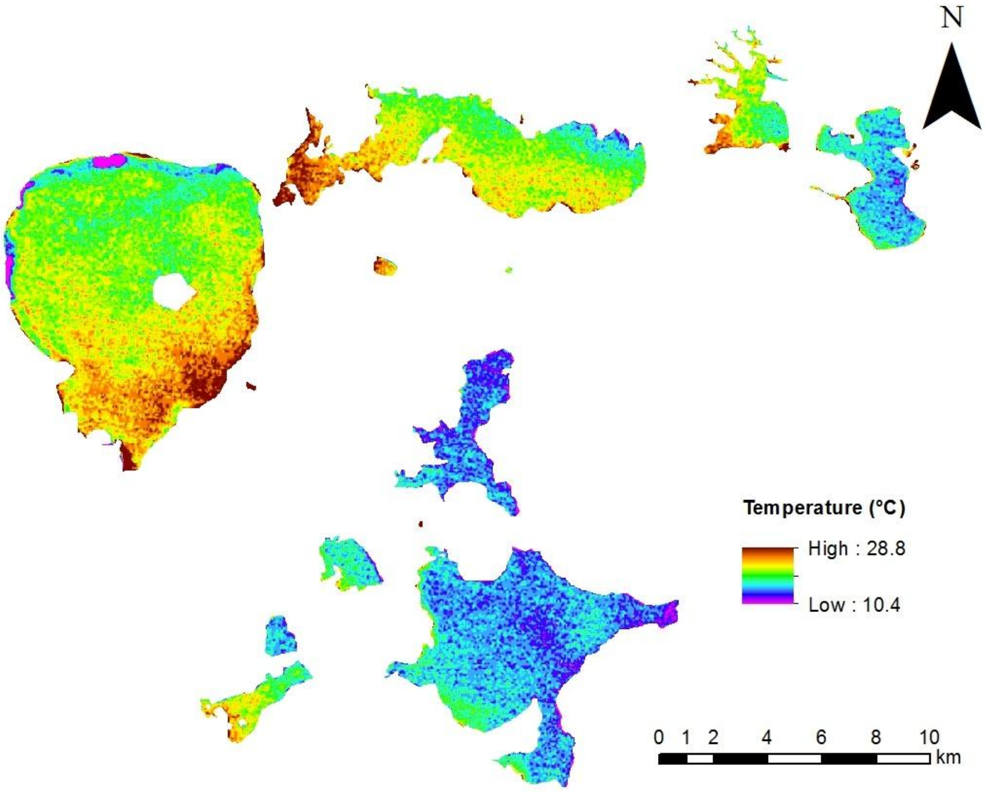

Figure 3.5. Landsat-estimated temperature (ºC) on 25 January 2008 using radiosonde atmospheric data with a standard deviation stretch. The stripes of missing data caused by the failure of the scan line corrector have been filled using linear interpolation.

ELCOM application to Lake Rotoehu

ELCOM simulations of water temperature were undertaken for Lake Rotoehu from 20 July 2005 to 30 December 2007. The RMSE between measured and modelled lake water temperature at the BOPRC site using Rotorua Airport air temperature data was 1.02 °C (Table 3.1). Use of the modified air temperature (Eq.3. 5) reduced the RMSE to 0.61 °C. A comparison was made of in situ Lake Rotoehu surface water temperature with Landsat- estimated (radiosonde) data, and ELCOM-simulated surface temperature, including the simulations with modified air temperature from the lake buoy. Errors between observed and modelled water temperature data are highest at the end of austral winter (Figure 3.6). A more detailed spatial comparison is given in Figure 3.7, which shows Landsat- estimated and ELCOM-simulated surface water temperature in the region of the plume created by the Waitangi Soda Springs geothermal inflow to Lake Rotoehu. It shows that ELCOM-simulations and Landsat observations are in general agreement but the methodology to invoke direct comparisons may have been affected by different resolutions of Landsat (60-m pixels) and ELCOM (30-m grid) data, together with possible georeferencing errors involved in the georectification of simulated data. Furthermore, whilst geothermal inflow volume and composition are generally stable, measurements are conducted only bimonthly, with linear interpolation used between measurements to provide daily input data to ELCOM.

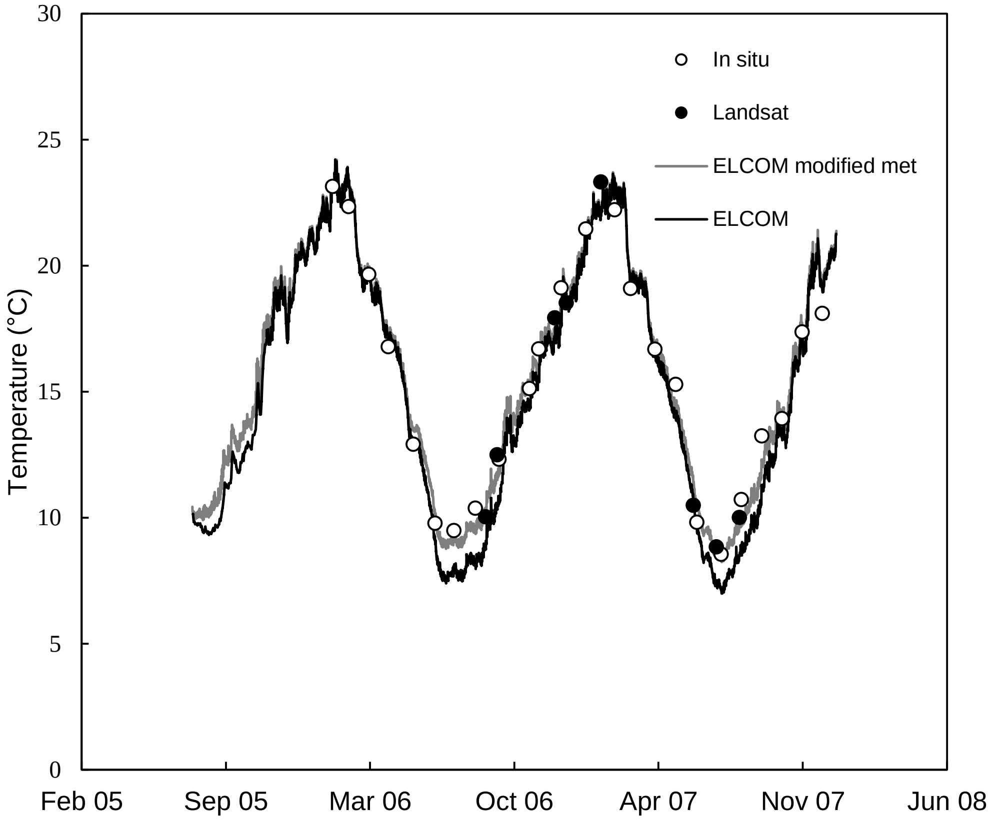

Figure 3.6. Surface water temperature simulations at the BOPRC monitoring site using Rotorua Airport meteorological temperature data (ELCOM), modified temperature data (using equation 3.5) (ELCOM modified met), in situ temperature and Landsat-derived temperature data (radiosonde).

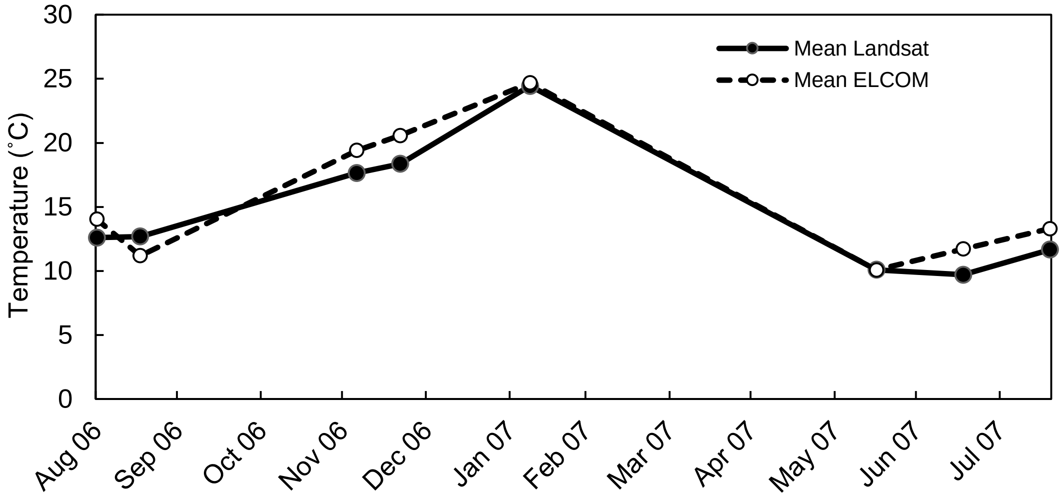

Figure 3.7. Mean water surface temperature in the Waitangi Soda Springs geothermal plume zone of Lake Rotoehu estimated by Landsat (black line) compared that simulated (dashed line).

A spatially resolved comparison of surface water temperature observed in Lake Rotoehu using Landsat data and ELCOM-simulated temperature and currents is shown in Figure 3.8. The simulated geothermal inflow path, based on temperature gradients, generally follows what may be construed from Landsat temperature gradients. The 60-m pixel resolution of Landsat data may mean that temperature in the narrow north arms of Lake Rotoehu (Figure 3.2) is influenced by adjacent land pixels, despite use of a 60 m buffer. The dispersion of the modelled geothermal inflow appears to be heavily influenced by lake surface ambient current direction and velocity (Figure 3.8 (b)), although all cases the geothermal plume does not separate from the shoreline.

ELCOM simulated basin scale surface temperature variation reasonably well on some dates (Figure 3.8). For example, on 1 September 2006 Landsat data showed cooler surface temperature in the southern and western part of the lake which agreed with the spatial variability simulated by ELCOM. On this date, wind speed was moderately strong (4.1 m s^{-1}), and radial spreading of the plume front was discernible as well as some deflection of the plume in an anticlockwise direction as it became entrained into more coherent lake circulation currents (Figure 3.8 (a), 3.9 (a) and 3.9 (c)).

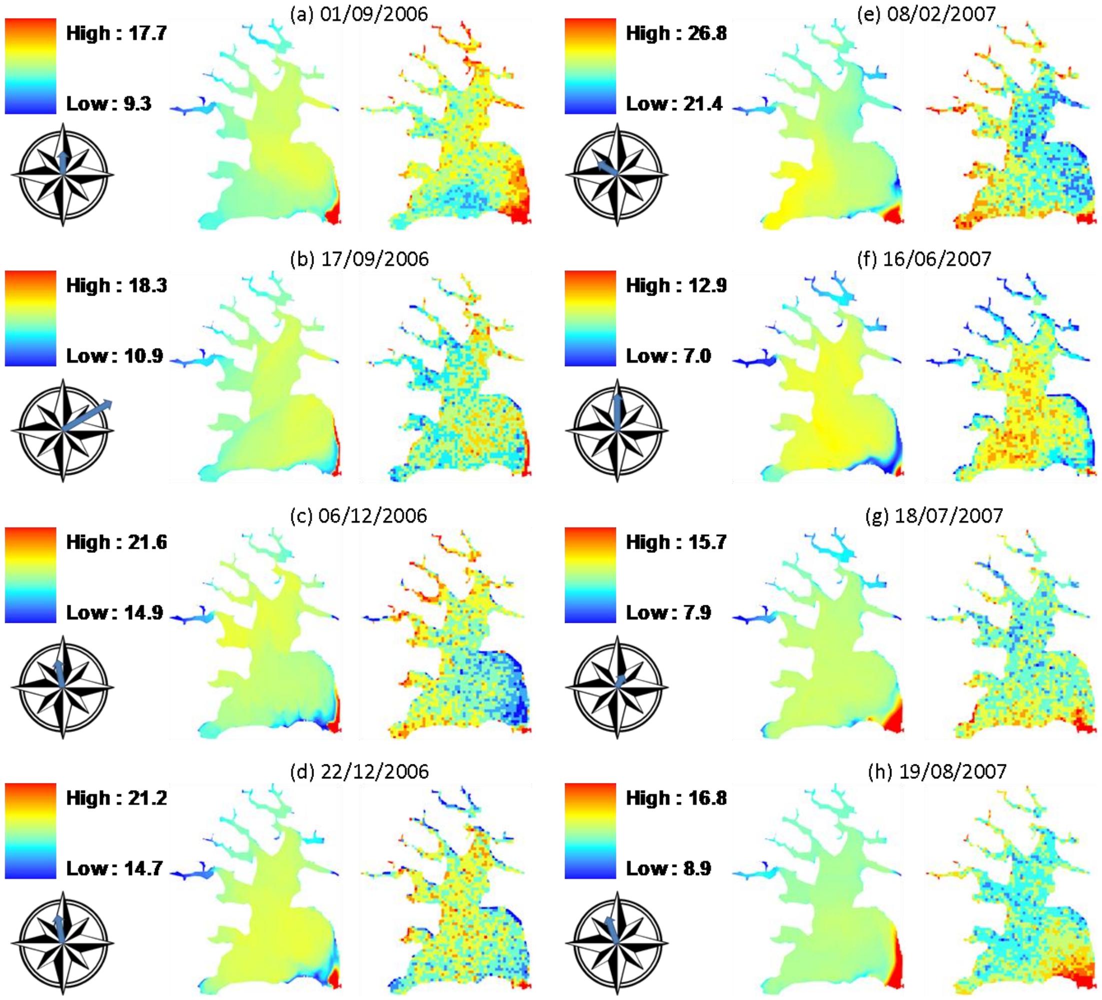

Figure 3.8. ELCOM surface water temperature simulation (column 1 and 3), Landsat-derived water surface temperature (columns 2 and 4) with standard deviation stretched colour ramp (ºC). Wind speed and direction are represented on the compass plot with compass radius representing a wind speed of 10 m s^{-1}, compass north direction is zero degrees.

On 17 September 2006 (Figure 3.8 (b)) high wind speed (10.3 m s^{-1}) resulted in correspondingly high-velocity lake currents which deflected the geothermal inflow strongly to the eastern direction, creating a narrow plume along the shoreline, which was simulated with ELCOM. A visualisation of the geothermal inflow was created using a conservative tracer input in this inflow. From Figure 3.9 the path of the inflow can be seen as it intrudes into the lake initially as a buoyant surface overflow

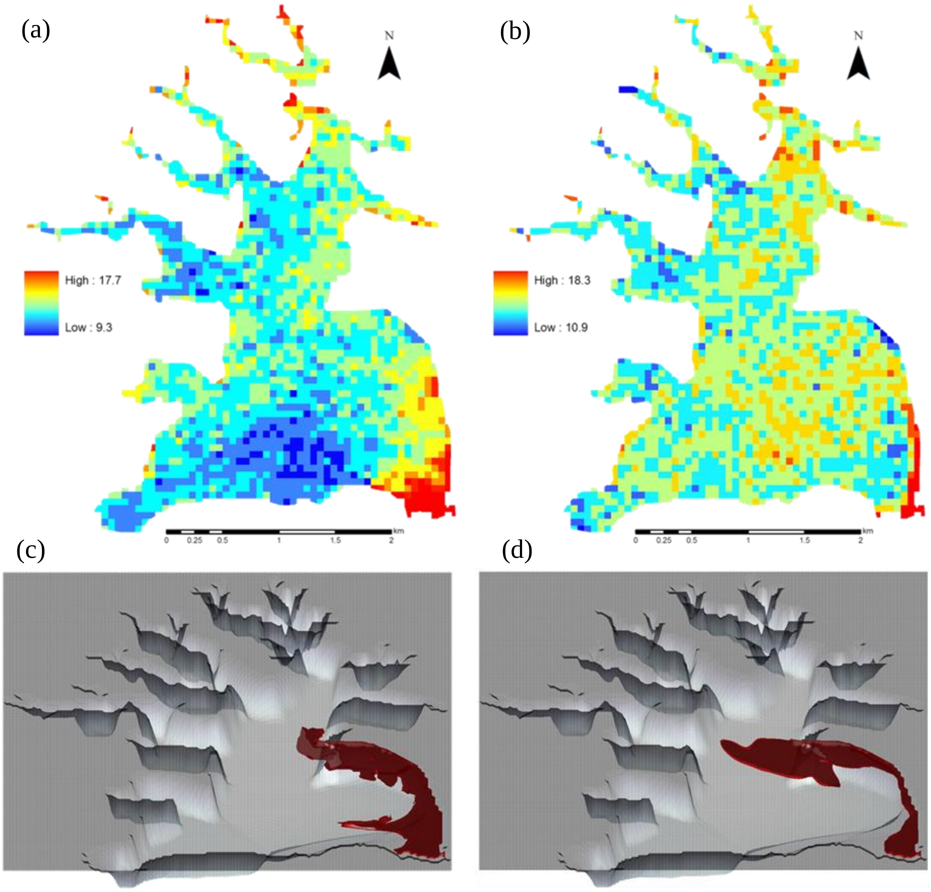

Figure 3.9. Landsat-estimated surface water temperature of Lake Rotoehu on (a) 1 September 2006 and (b) 17 September 2006 and visualization of ELCOM-simulated tracer on the corresponding dates of (c) 1 September 2006 with 25% and (d) 17 September 2006 (25%). The percent tracer concentration is relative to 100% tracer concentration in the inflow.

and then as it becomes entrained into ambient lake water. There were also instances when water surface temperature distributions were not well represented with ELCOM within the vicinity of the geothermal inflow. For example, on 22 December 2006 (Figure 3.8 (f)), there was a limited spread of the Landsat-observed geothermal plume relative to that simulated with ELCOM. On 19 August 2007 the ELCOM-simulated plume was deflected north of the outlet, however Landsat data showed that the plume was dispersed more radially, with some deflection to the south.

Flow classification

The flow classification indicates that the Waitangi Soda Springs geothermal inflow is an upstream-intruding plume which is shore-hugging over all of the measured flow regimes and lake current velocities given by ELCOM simulations. The receiving depth of this inflow is shallow (0.2 m), therefore the inflow occupies the full depth of the receiving water, which blocks off the ambient current. This creates a zone of recirculating discharge along the shoreline, with limited mixing occurring until the inflow temperature at cools to that of the ambient lake temperature (Jones et al. 2007).

3.4 Discussion

Positively buoyant gravity flows have been well studied for industrial discharges into lakes and oceans (e.g., Gibbins et al. 1989; Davies and Mofor 1993; Davies et al. 1997), compared with the limited number of studies of natural geothermal inflows into lakes. This chapter has validated ELCOM-simulated temperature at high resolution, on eight separate dates, using Landsat-estimated surface water temperature. It highlights the ability of a 3-D hydrodynamic model to accurately simulate physical properties of lakes such as temperature and circulation, while demonstrating the applicability of using satellite imagery for 3-D model validations. The Waitangi soda springs geothermal plume in Lake Rotoehu was usually well represented by ELCOM, and the distribution of this plume was primarily affected by lake ambient water current velocity and direction. Remote sensing is an ideal candidate for studying the dispersion of buoyant plumes and jets, due to its synoptic capabilities. The relationships between the Landsat- estimated surface geothermal inflow path and the ELCOM-simulated geothermal inflow path indicates that algorithms for buoyant inflow intrusions and their in-lake dispersion perform adequately in ELCOM. Large spatial gradients in temperature exist in Lake Rotoehu which allows inflow water masses to be tracked as well as basin scale water spatial variation. The upstream-intruding geothermal plume in Lake Rotoehu occurs due to the strongly buoyant discharge entering the relatively slow-moving ambient lake current. This case is characterised by a front in which the buoyant upstream intrusion is balanced by a drag force at the head of the plume. For this strongly buoyant discharge, buoyancy-induced lateral spreading becomes the dominant spreading mechanism within a very short distance from the mouth of the discharge (Jones et al.

2007). However, as the plume becomes progressively entrained through depth, and more widely distributed within the lake, it is not possible to validate its path using satellite imagery, due to temperature becoming largely homogenous. The 3-D modelling and visualisation of the plume allows the simulation of the wider distribution within the lake.

The spatial variation in temperature observed in the Rotorua lakes is caused by a number of factors. In individual lakes morphology plays a key role in inducing gradients between deep and shallow areas such as in Lake Rotorua which has extensive shallow margins, or between sheltered bays and arms and a main basin such as in lakes Rotoehu, Rotoiti, Rerewhakaaitu and Rotomahana. The regularity of these geomorphological variations suggests that they are the norm rather than infrequent, and that single-station sampling may grossly under-represent the range of surface temperature responses to climatic forcing, particularly where there is substantial differential heating and cooling (Imberger et al. 1989) which creates horizontal and vertical instabilities leading to convectively induced motions (e.g., Sturman et al. 1999). Differential heating or cooling and associated mixing processes can also be caused by differences in wind speed between sheltered and open-water areas, as latent and sensible heat vary with wind speed (Fischer 1979). These temperature and density gradients can induce density-driven flows which can transport nutrients and biota between littoral and pelagic areas (MacIntyre and Melack 1995). This process has been termed the "thermal siphon", and has been shown to increase horizontal exchange between side-arms and the main basin of lakes (Monismith et al. 1990), and drive large-scale convective circulations (Verburg et al. 2011). The results of this chapter demonstrate that in Lake Rotoehu there is evidence of differential cooling and heating between the main lake body and side-arms, which is evident in simulation and satellite estimated water surface temperatures.

The accuracy of hydrodynamic models to simulate lake water temperature relies on the quality of forcing data (Imberger 1985). The use of adjusted air temperature data based on the relationship between Lake Rotorua buoy measurements and land-based data improved the ELCOM temperature simulation accuracy. We attribute the improvements with use of lake buoy data to the effect of thermal inertia of the water body on the above-water air temperature. This thermal inertia modifies the atmospheric boundary layer, which in turn affects atmospheric stability and heat fluxes (Long et al. 2007). Thus air temperature inputs to lake models should, whenever possible, be on-lake to avoid direct errors from conductive exchanges and indirect errors for other heat flux components (e.g., sensible and longwave radiation transfers).

Monitoring the spatial variability of lake surface water temperature using satellite imagery provides truly synoptic horizontal quantification, resolving fine and large-scale temperature variation, but requires accurate AC. This work has shown that radiosonde data taken two hours after image capture and 200 km from the study site provided atmospheric profiles that produced accurate water surface temperature estimations. Schneider and Mauser (1996) similarly found that radiosonde data for AC taken 120 km from the study site gave atmospheric profiles applicable for radiative transfer based atmospheric correction. The RMSE of bulk water surface temperature estimations using the radiosonde-based AC method was 0.37 °C, which is comparable to the combined Landsat noise-equivalent change in temperature (NEΔT) of 0.22 °C and buoy error of ±0.1 °C (as specified by the temperature string manufacturer). Radiosonde data are captured regularly at only two sites in New Zealand, thus areas further away than 200 km may need alternate sources of atmospheric data.

Of the globally available atmospheric profile data for atmospheric correction, MOD07 provided the most accurate water temperature retrieval, with an error comparable to that obtained from radiosonde data. The MODIS Terra satellite has a near-synchronous orbit to Landsat and has the highest spatial resolution (5 km), however, data are only available post 1 March 2000, whereas thermal imaging was available in Landsat 4, 5 and 7 post-1982. Atmospheric corrections applied to the global archive of Landsat thermal data could apply MODIS atmospheric profile data, whilst NASA atmospheric correction methods are applicable for preceding periods. MODIS TERRA is better suited to Landsat atmospheric correction applications as the time difference between the overpass of MODIS AQUA (AIRS sensor) and

Landsat (approximately 4 h) is likely to produce larger errors in temperature retrieval than using MODIS and radiosonde data. The accuracy of the NASA method relies on the accuracy of NCEP data, which may be better for areas where the model has been extensively validated such as North America. However, this correction tool (Barsi et al. 2005) allowed water temperature in Lake Rotorua to be estimated with a RMSE of 1.05 °C, while being the least time-consuming to apply amongst four different AC methods, as the web-based input requires few parameters. Notably, the largest errors in surface water temperature retrieval occurred during summer, when RH measured at the Rotorua meteorological station was low, indicating that NCEP atmospheric profile data near the boundary layer may overestimate RH at these times.

Inflows to lakes influence lake circulation, thermal structure, residence time, and sediment transport and ultimately biogeochemical responses (Pickrill and Irwin 1982; Spigel et al. 2005, Chung et al. 2009). In this chapter remote sensing was demonstrated to be an effective means if identifying the location, path and dispersion of geothermal inflows. Geothermal inflows in the Rotorua lakes have been shown to have high nutrient concentrations, particularly NH_4^+ (Hoellein et al. 2012), thus creating concentration gradients of nutrients which have the potential for influencing fine and basin scale variation of phytoplankton concentration. The present also study demonstrated the usefulness of remote sensing for identification of large cold water inflows, and could further be used to estimate their plunge point.

The present chapter has demonstrated that remote sensing of water surface temperature is accurate; however, sources of atmospheric profile data used in atmospheric correction need to be carefully considered for the effect on the accuracy of temperature retrieval. The use of high-frequency autonomous buoy measurements of temperature allowed for concurrent validation of satellite retrieved surface temperature, and the combination of the two data sources with 3-D hydrodynamic modelling allows high spatial and temporal resolution water temperature analysis.

3.5 References

Adrian, R., C. M. O'Reilly, H. Zagarese, S. B. Baines, D. O. Hessen, W. Keller, D. M. Livingstone, R. Sommaruga, D. Straile, E. Van Donk, G. A. Weyhenmeyer, and M. Winder. 2009. Lakes as sentinels of climate change. Limnology and Oceanography **54**: 2283–2297.

Alvarez, G. A., R. A. Salinas, and T. J. Malthus. 2007. Integrating CFD modelling, neural networks and remote sensing: controlled prediction of chlorophyll-a concentration in the Mejillones of South Bay. Computer Vision **1**: 55–65.

Amon, R. M. W., and R. Benner. 1998. Seasonal patterns of bacterial abundance and production in the Mississippi River plume and their importance for the fate of enhanced primary production. Microbial Ecology **35**: 289–300.

Baban, S. M. J. 1993. Detecting and evaluating the influence of water depth, volume and altitude on the variations in the surface temperature of lakes using Landsat imagery. International Journal of Remote Sensing **14**: 2747–2758.

Barsi, J. A., J. R. Schott, F. D. Palluconi, and S. J. Hook. 2005. Validation of a web-based atmospheric correction tool for single thermal band instruments. Proceedings of SPIE 5882, 58820E.

Becker, M. W., and A. Daw. 2005. Influence of lake morphology and clarity on water surface temperature as measured by EOS ASTER. Remote Sensing of Environment **99**: 288–294.

Casulli, V., and R. T. Cheng. 1992. Semi-implicit finite difference methods for three dimensional shallow water flow. International Journal for Numerical Methods in Fluids **15**: 629–648.

Chung, S. W., M. R. Hipsey, and J. Imberger. 2009. Modelling the propagation of turbid density inflows into a stratified lake: Daecheong Reservoir, Korea. Environmental Modelling & Software 24: 1467–1482.

Coll, C., J. M. Galve, J. M. Sanchez, and V. Caselles. 2010. Validation of Landsat-7/ETM+ thermal-band calibration and atmospheric correction with ground-based measurements. IEEE Transactions on Geoscience and Remote Sensing **48**: 547–555.

Davies, P. A., L. A. Mofor, and M. J. V. Neves. 1997. Comparisons of remotely sensed observations with modelling predictions for the behaviour of wastewater plumes from coastal discharges. International Journal of Remote Sensing **18**: 1987–2019.

Davies, P. A., and L. A. Mofor. 1993. Remote sensing observations and analyses of cooling water discharges from a coastal power station. International Journal of Remote Sensing **14**: 253–273.

Fischer, H. B., E. J. List, R. C. Y. Koh, J. Imberger, and N. H. Brooks. 1979. Mixing in Inland and Coastal Waters. Academic Press, San Diego, USA.

Gibbons, D. E., G. E. Wukelic, J. P. Leighton, and M. J. Doyle. 1989. Application of Landsat Thematic Mapper data for coastal thermal plume analysis at Diablo Canyon. Photogrammetric Engineering and Remote Sensing **55**: 903–909.

Hodges, B. R., J. Imberger, A. Saggio, and K. B. Winters. 2000. Modelling basin scale waves in a stratified lake. Limnology and Oceanography **45**: 1603–1620.

Hodges, B., and C. Dallimore. 2001. Estuary and Lake Computer Model: ELCOM Science Manual Code Version 2.0.0. Centre for Water Research, University of Western Australia, Perth, Australia.

Hoellein, T. J., D. A. Bruesewitz, and D. P. Hamilton. 2012. Are geothermal streams important sites of nutrient uptake in an agricultural and urbanising landscape (Rotorua, New Zealand)? Freshwater Biology **57**: 116–128.

Hook, S. J., F. E. Prata, R. E. Alley, A. Abtahi, R. C. Richards, S. G. Schladow, and S. Ó. Pálmarsson. 2003. Retrieval of lake bulk and skin temperatures using Along-Track Scanning Radiometer (ATSR-2) data: a case study using Lake Tahoe, California. Journal of Atmospheric and Oceanic Technology **20**: 534–548.

Hutchinson, G. E. 1957. A Treatise on Limnology. Wiley and Sons, New York, USA.

Imberger, J. 1985. Thermal characteristics of standing waters: an illustration of dynamic processes. Hydrobiologia **125**: 7–29.

Jones, G. R., J. D. Nash, R. L. Doneker, and G. H. Jirka. 2007. Buoyant surface discharges into water bodies. I: Flow classification and prediction methodology. Journal of Hydraulic Engineering **133**: 1010–1020.

Lathrop Jr, R. G., and T. M. Lillesand. 1987. Calibration of thematic mapper thermal data for water surface temperature mapping: Case study on the Great Lakes. Remote Sensing of Environment **22**: 297–307.

Leonard, B. P. 1991. The ULTIMATE conservative difference scheme applied to unsteady one-dimensional advection. Computer Methods in Applied Mechanics and Engineering **88**: 17–74.

Long, Z., W. Perrie, J. Gyakum, D. Caya, and R. Laprise. 2007. Northern lake impacts on local seasonal climate. Journal of Hydrometeorology **8**: 881–896.

Lowe, D.J. and Green, J.D. 1987. Origins and development of lakes, p. 1–64. *In* A.B. Viner [ed.], Inland Waters of New Zealand. Science Information Publishing Centre, Department of Scientific and Industrial Research, Wellington, New Zealand.

MacIntyre, S., and J. M. Melack. 1995. Vertical and horizontal transport in lakes: linking littoral, benthic, and pelagic habitats. Journal of the North American Benthological Society **14**: 599–615.

Mongillo, M. A. 1994. Aerial thermal infrared mapping of the Waimangu-Waiotapu geothermal region, New Zealand. Geothermics **23**: 511–526.

Mongillo, M. A., and C. J. Bromley. 1992. A helicopter-borne video thermal infrared survey of the Rotorua geothermal field. Geothermics **21**: 197–214.

Monismith, S. G., J. Imberger, and M. L. Morison. 1990. Convective motions in the sidearm of a small reservoir. Limnology and Oceanography **35**: 1676–1702.

Oppenheimer, C. 1993. Infrared surveillance of crater lakes using satellite data. Journal of Volcanology and Geothermal Research **55**: 117–128.

Pickrill, R. A., and J. Irwin. 1982. Predominant headwater inflow and its control of lake-river interactions in Lake Wakatipu. New Zealand Journal of Marine and Freshwater Research **16**: 201–213.

Schneider, K., and W. Mauser. 1996. Processing and accuracy of Landsat Thematic Mapper data for lake surface temperature measurement. International Journal of Remote Sensing **17**: 2027–2041.

Schott, J. R., J. A. Barsi, B. L. Nordgren, N. G. Raqueño, and D. de Alwis. 2001. Calibration of Landsat thermal data and application to water resource studies. Remote Sensing of Environment **78**: 108–117.

Schott, J. R., and W. J. Volchok. 1985. Thematic Mapper thermal infrared calibration. Photogrammetric Engineering and Remote Sensing **51**: 1351–1357.

Seemann, S. W., E. V. A. E. Borbas, J. Li, W. P. Menzel, and L. E. Gumley. 2006. MODIS atmospheric profile retrieval - algorithm theoretical basis document version 6, October 25. Cooperative Institute for Meteorological Satellite Studies University of Wisconsin-Madison, USA.

Steissberg, T. E., S. J. Hook, and S. G. Schladow. 2005. Characterizing partial upwellings and surface circulation at Lake Tahoe, California-Nevada, USA with thermal infrared images. Remote Sensing of Environment **99**: 2–15.

Steissberg, T. E., S. J. Hook, and S. G. Schladow. 2005. Measuring surface currents in lakes with high spatial resolution thermal infrared imagery. Geophysical Research Letters **32**: L11402.

Sturman, J. J., C. E. Oldham, and G. N. Ivey. 1999. Steady convective exchange flows down slopes. Aquatic Sciences **61**: 260–278.

Tcherepanov, E. N., V. A. Zlotnik, and G. M. Henebry. 2005. Using Landsat thermal imagery and GIS for identification of groundwater discharge into shallow groundwater-dominated lakes. International Journal of Remote Sensing **26**: 3649–3661.

Timmins, S. M., and S. E. Belliss. 1983. Lake Rotorua aircraft scanner mosaic. New Zealand Journal of Science **26**: 473–480.

Tobin, D. C., H. E. Revercomb, R. O. Knuteson, B. M. Lesht, L. L. Strow, S. E. Hannon, W. F. Feltz, L. A. Moy, E. J. Fetzer, and T. S. Cress. 2006. Atmospheric Radiation Measurement site atmospheric state best estimates for Atmospheric Infrared Sounder temperature and water vapor retrieval validation. Journal of Geophysical Research **111**: D09S14.

Trolle, D., D. P. Hamilton, C. A. Pilditch, I. C. Duggan, and E. Jeppesen. 2011. Predicting the effects of climate change on trophic status of three morphologically varying lakes: Implications for lake restoration and management. Environmental Modelling and Software **26**: 354–370.

Verburg, P., J. P. Antenucci, and R. E. Hecky. 2011. Differential cooling drives large-scale convective circulation in Lake Tanganyika. Limnology and Oceanography **56**: 910–926.

Williamson, C. E., W. Dodds, T. K. Kratz, and M. A. Palmer. 2008. Lakes and streams as sentinels of environmental change in terrestrial and atmospheric processes. Frontiers in Ecology and the Environment **6**: 247–254.

Yeates, P. S., J. Imberger, and C. Dallimore. 2008. Thermistor chain data assimilation to improve hydrodynamic modelling skill in stratified lakes and reservoirs. Journal of Hydraulic Engineering **134**: 1123–1135.

4 MODIS-based estimates of suspended minerals to evaluate performance of a three-dimensional hydrodynamic-ecological model application to a large, shallow coastal lagoon

4.1 Introduction

Shallow coastal lakes are characterised by highly heterogeneous concentrations of suspended sediments (SS) (both mineral and organic) which have significant implications for nutrient concentrations, phytoplankton production (Hamilton and Mitchell 1997), zooplankton (Kirk and Gilbert 1990) and benthic algae (Horppila and Nurminen 2003). Wind-induced waves are the dominant force involved in resuspension of sediments in shallow lakes (Cole and Miles 1983; Luettich et al. 1990; Lick et al. 1994; Bloesch 1995). Resuspended sediments act as a transport mechanism for phosphorus which can be adsorbed onto the sediments, and this phosphorus has the potential to be desorbed in the water column (Søndergaard et al. 1992). Suspended sediments attenuate light through scattering and absorption, and thereby play a critical role in determining the depth of the photic zone (Scheffer 1998) and production of phytoplankton and macrophytes. Considering the critical role of SS in regulating physical and biological properties of aquatic environments, it is essential to effectively monitor concentrations, however, monitoring spatial heterogeneity using traditional grab-samples can be inaccurate (Dekker et al. 2002) and costly.

The development of an operational algorithm to monitor SS using Moderate Resolution Imaging Spectroradiometer (MODIS) Terra and Aqua satellite imagery would complement conventional monitoring regimes by extending the spatial and temporal resolution of data capture. In this study I investigate the potential of MODIS band 1 (B1) imagery for remote sensing of tripton (suspended non-living component of SS) and suspended minerals (SM). I also calibrate a three-dimensional hydrodynamic model for simulation of SM, and use surface distributions of SM estimated from MODIS B1 to validate model-simulated surface SM distributions, using visual comparisons and statistical metrics.

Remote sensing of SS was originally developed for Case 1 ocean waters where suspended sediments are comprised mostly of algal and detrital particles (Morel 1980; Sturm 1981). The algorithms were applied in a similar way to early empirically-based band ratio algorithms for chlorophyll *a* (chl *a*). For low to moderate concentrations of SS subsurface remote sensing reflectance ($r_{rs}(\lambda)$) is nearly linearly related to the concentration of SS at visible and near infrared wavelengths. For high SS, the relationship becomes non-linear, characterised by an asymptote where increases in SS concentration cannot be detected by increased $r_{rs}(\lambda)$ (Bowers et al. 1998; Doxaran et al. 2002). With increasing wavelength, saturation occurs at higher SS concentrations, meaning that for turbid waters the retrieval of suspended sediment can be more accurate at wavelengths corresponding to the red and near infrared (NIR) region (Ruddick et al. 2006). At NIR wavelengths the absorption by phytoplankton and coloured dissolved organic matter (CDOM) is minimal, and water dominates absorption relative to other optically active constituents. Therefore at NIR wavelengths the variation in $r_{rs}(\lambda)$ is primarily determined by changes in the scattering due to SS (Ruddick et al. 2006).

Many empirical relationships for estimations of SS have been developed from single-band wavelengths, especially in the red wavelengths (e.g., Hu et al. 2004; Miller and McKee 2004; Kutser et al. 2007; Nechad et al. 2010). For high concentrations of SS (>2000 mg L^{-1}), reflectance ratios in red and NIR bands have been used to estimate SS (Doxaran et al. 2009). A major limitation of empirically based models, however, is that satellite imagery needs to be calibrated concurrently with in situ data. Additionally, inaccuracies in estimated SS may occur when concentrations are outside of those used in the model calibration (Dekker et al. 2002).

In order to overcome limitations of empirical models, analytical models have been developed which are based on physical relationships between absorption and scattering properties of optically active constituents in the water column. Since the optical model of Gordon et al. (1988) was applied to eutrophic inland waters (Dekker et al 1997), semi-analytical models have been used widely to estimate suspended sediment concentrations in Case 2 waters (e.g. Dekker et al. 2002; Eleveld et al. 2008; Binding et al. 2010). Recently, there has been increased focus on analytical spectral inversion algorithms to estimate concentrations of chl *a*, CDOM and SS simultaneously (Matthews 2011), using bio-optical models that are parameterised with inherent optical properties (IOPs) of the water body of interest (Brando and Dekker 2003; Santini et al. 2010; Campbell et al. 2011). Furthermore, bio-optical modelling approaches have now been developed account for optically complex waters where temporal and spatial variation of IOPs occurs (Doerffer and Schiller 2007; Schroeder et al. 2007; Brando et al. 2012).

Remote sensing algorithms to estimate SS are based on relationships between particle backscattering and suspended sediment. Light scattering is quantified by a volume scattering function ($\beta(\theta)$), where θ is the forward scattering angle (Mobley 1994). The integral of $\beta(\theta)$ for angles from 0 to π angles yields the scattering coefficient (b):

$$b = 2\pi \int_{0}^{\pi} \beta(\theta) \sin(\theta) d\theta$$

The backscattering coefficient is a subset of the angle used to define b:

$$b_b = 2\pi \int_{\pi/2}^{\pi} \beta(\theta) \sin(\theta) d\theta$$

The backscattering ratio (*Bb*) is defined as b_b / b.

Variations in the specific backscattering per unit concentration of SS affect accuracy of remote sensing of SS (Bowers and Binding 2006). The relationship between particle backscattering and suspended sediment concentration varies in time and space, mostly due to variations in particle size distribution and the bulk refractive index of the particles (Tzortziou et al. 2006). The refractive index of minerals is generally higher than that of organic particles (including phytoplankton), mostly due to the high water content of organic material (Twardowski et al. 2001). The slope of the backscattering coefficient is related to the particle size distribution and, in combination with angular scattering, can be used to estimate the refractive index of particles (Twardowski et al. 2001).

The top of the atmosphere radiance of oceans and lakes measured by Earth observation satellite sensors can be comprised of 90% atmospheric path radiance (Vidot and Santer 2005), making atmospheric correction essential. Methods developed for Case 1 ocean waters rely on the high absorption of water in the NIR, and an assumption of negligible scattering from optically active constituents. Therefore any radiance measured at these wavelengths is used to estimate path radiance (Gordon and Wang 1994). This assumption does not apply to Case 2 waters which have elevated levels of SS that scatter NIR radiation (Vidot and Santer 2005). Other factors that complicate atmospheric correction for inland waters include variations in elevation, heterogeneous concentrations of aerosols, and adjacency effects caused by land contamination of water reflectance. The application of radiative transfer models to correct for variations in atmospheric attenuation provides an ability to address the complexities of atmospheric correction over inland waters (e.g., Campbell et al. 2011b).

Three-dimensional (3-D) modelling of SS concentrations in shallow lakes can complement remote sensing by providing insights into the complex physical dynamics leading to satellite-estimated SS distributions. Deterministic water quality models offer the opportunity to more fully understand complex physical and biogeochemical processes and their interactions at high spatial and temporal resolution. Previous studies comparing randomly located grab-samples with synoptic remote sensing estimates of SS have been shown to be within ±20 to 30%, however, they could deviate by as much as 4000% (Dekker et al. 2002). Effective validation of deterministic 3-D models in turbid waters using in situ monitoring and grab-sample collection is therefore not practical. Use of remote sensing to provide synoptic measurements of water quality provides an opportunity for comparisons against surface layer outputs of these variables from 3-D models. Of the limited number of 3-D modelling studies which have compared water quality parameters or temperature with estimates derived from remote sensing data, most have used qualitative comparison (primarily visual) to assess the quality of the comparison, without quantifying the comparison spatially (Hedger et al. 2002; Spillman et al. 2007).

Visual comparison of two raster images provides a fast and efficient way of comparing spatial and numerical differences and similarities. Visual comparison has generally outperformed automated procedures as human perception will naturally identify multiple spatial and numerical quantities, including global and local similarities, logical coherence and pattern recognition (Hagen 2003; Kuhnert et al. 2005). The problem with visual comparison is that it is subjective and produces no quantitative output. In addition, visual comparison is not practical over large numbers of images (Kuhnert et al. 2005), and quantitative algorithms become essential for this purpose.

The application of traditional statistical algorithms may not be applicable to qualitative comparison of variables derived from remote sensing and from modelling simulations due to spatial autocorrelation, and scale and edge effects (O'Sullivan and Unwin 2002). Geographical patterns tend to be spatially variable in nature, which can lead to a phenomenon referred to as spatial nonstationarity, where a "global" model cannot explain the relationship between some sets of variables (Fotheringham et al. 1996). For example, shallow areas within lakes could constitute regions of nonstationarity, and lead to spatial autocorrelation. While state of the art spatial statistical methods have been developed to overcome the limitations of traditional statistical methods (Kuhnert et al. 2005), the inherent complication of spatially explicit comparisons has in the past limited their application. However, spatial statistics have been developed within Geographic Information System (GIS) software such as ArcGIS, and the publically available Map Comparison Kit (MCK) (Visser and De Nijs 2006).

The high temporal resolution of MODIS Terra and Aqua data provides a unique opportunity to develop remote sensing algorithms capable of twice-daily estimation of SS. The high temporal resolution and synoptic capabilities of satellite estimations in turn present a cost-effective method to validate 3-D simulations. However, non-subjective comparison of satellite estimation and 3-D simulations is required. Therefore, the objectives of this study were three-fold: 1) to compare empirical and semi-analytical relationships between the MODIS B1 subsurface remote sensing reflectance (r_{rs}(B1)) and tripton concentrations in a large shallow lake, 2) to calibrate a 3-D hydrodynamic-ecological model for the simulation of SM in the lake, and 3) to carry out a spatially resolved quantitative comparison of simulated SM from a 3-D coupled hydrodynamic-ecological model of the lake against synoptic remote sensing estimates of tripton distributions (adjusted to concentrations of SM) for comparative purposes.

4.2 Study site

Lake Ellesmere (also known as Te Waihora) is the fifth-largest lake in New Zealand by area (199 km^2; Figure 4.1). It is a coastal lake in the South Island of New Zealand with a maximum depth of 2.43 m (mean depth of 1.33 m) and is highly turbid, wind-exposed and hypertrophic (Gerbeaux and Ward 1991; Hamilton and Mitchell 1997).

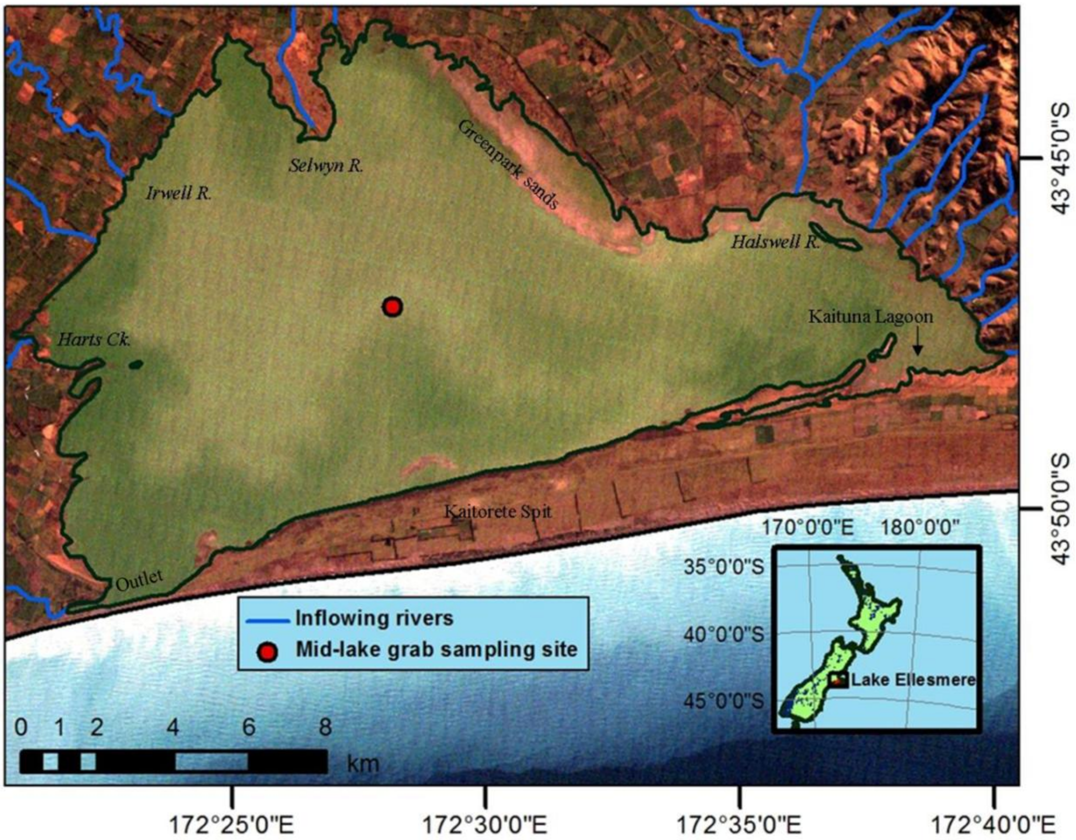

Figure 4.1. Study site Lake Ellesmere (overlaid on a Landsat 5 background captured 2 July 2005) showing inflows, outlet, mid-lake grab-sampling site, Kaituna Lagoon and Kaitorete Spit.

Lake Ellesmere is a RAMSAR wetland of international significance for the large number of birds (166 species recorded) occupying its periodically inundated margins and wadeable areas. The lake has no natural outlet but is artificially opened (average of 3.3 times per year) to prevent inundation of surrounding farmland, which was originally wetland that has since been drained. The water level fluctuations change the total lake area from 160 km^2 at 0.3 m above mean sea level (AMSL) to 242 km^2 at 1.5 m AMSL (Hemmingsen 1997), which has a significant effect on bird habitat area and emergent macrophyte distributions. Prior to 1968

Lake Ellesmere had up to 80 000 black swans (*Cygnus atratus*), abundant submerged macrophytes and relatively high water clarity (Hughes et al. 1974). In 1968 a severe storm (which also sank the "Wahine") destroyed the submerged macrophyte beds and transformed the lake to an alternate state dominated by high concentrations of suspended sediment and phytoplankton (Gerbeaux 1993; Hamilton and Mitchell 1997). Submerged macrophyte populations have not recovered since the storm and remain negligible (Schallenberg et al. 2010).

4.3 Methods

Overview of methods

MODIS Aqua and Terra B1 radiance were atmospherically corrected using a radiative transfer model, and then converted to subsurface remote sensing reflectance (r_{rs}(B1)). Empirical algorithms were created between r_{rs}(B1) and in situ grab-sample tripton concentrations measured within 40 min of satellite overpass. A semi-analytical model to estimate tripton was calibrated and validated with this situ data. A 3-D coupled hydrodynamic-ecological model was calibrated for the estimation of SM concentrations. Satellite-estimated tripton concentrations were converted to SM concentrations to enable visual comparisons and analysis of spatial statistics against simulated SM from the numerical model.

Field data used for calibration of MODIS

Canterbury Regional Council (CRC) has monitored water quality in Lake Ellesmere and its tributaries at monthly frequency since 1992. Sampling has included three within-lake sites, of which a mid-lake site (Figure 4.1) was used in my study to examine SS. Volatile suspended sediment (VSS) are measured infrequently. Samples were usually taken c. 1000 h. These data were compared with r_{rs}(B1) from the MODIS Terra satellite over an average area of interest of 1 km x 1 km centred on the sampling point (averaging the 250-m resolution pixels of MODIS B1), at the overpass time of approximately 1000 h New Zealand Standard Time (NZST).

Tripton concentration was calculated from in situ SS concentration (Gons et al. 1992) as:

$$C_{TR} = SS - (0.07 * C_{\phi}) \tag{4.1}$$

where C_{ϕ} is the in situ concentration of chl *a*.

ELCOM-CAEDYM simulates SM and therefore C_{TR} was used to estimate the concentration of SM from the relationship between in situ C_{TR} and non-algal volatile suspended sediment (NAVSS). Non-algal volatile suspended sediment was estimated from volatile suspended sediment (VSS) as:

$$NAVSS = VSS - (0.07 * C_{\phi}) \tag{4.2}$$

Satellite imagery

MODIS is a remote sensing instrument on-board both the Terra and Aqua satellites. In this study, data from MOD02QKM and MYD02QKM B1 (620 - 670 nm) was used, which has a 250 m resolution and captures images twice daily, at approximately 1000 and 1400 h for MODIS Terra and Aqua, respectively. For the creation of an empirical relationship between MODIS r_{rs}(B1) and in situ tripton, 12 MODIS Terra images were used from 25 July 2001 until 11 April 2007. These images were selected when the satellite overpass was within 1.5 h of an in situ grab-sample. For validation of the 3-D hydrodynamic model used in this study, 24 MODIS Aqua and Terra cloud-free images were used from 18 December 2006 until 1 March 2007.

MODIS MOD02QKM data were atmospherically corrected with the 6sv (Second Simulation of a Satellite Signal in the Solar Spectrum) radiative transfer model, to account for atmospheric scattering and absorption effects of gases, and aerosols. The radiative transfer model was parameterised with atmospheric conditions and angular geometry extracted from MODIS data. The solar zenith, solar azimuth, sensor zenith and sensor azimuth angles were used from the MOD03 data, MOD04 for Aerosol Optical Depth (AOD), and MOD07 for total ozone and water vapour. For instances of negative AOD, values were set to 0.025.

Bio-optical model for inland waters

Forward bio-optical modelling was used to develop an analytical relationship between MODIS r_{rs}(B1) and tripton concentration. This semi-analytical relationship was then used to estimate tripton from MODIS r_{rs}(B1). Water surface remote sensing reflectance is given as:

$$R_{rs}(\lambda) \equiv \frac{L_w(\theta,\varphi,\lambda)}{E_d} \qquad [\mathrm{sr}^{-1}] \qquad (4.3)$$

where L_w is radiance leaving the water,, E_d is downwelling irradiance immediately above the water surface, θ is the zenith angle, φ is the azimuth angle and the symbol λ represents wavelength. Subsurface remote sensing reflectance $r_{rs}(\lambda)$ was estimated from $R_{rs}(\lambda)$ by correcting for air-sea interface effects, assuming a nadir viewing sensor and optically deep waters (Lee et al. 2002):

$$r_{rs}(\lambda) \approx \frac{R_{rs}(\lambda)}{0.52 + 1.7R_{rs}(\lambda)} \qquad (4.4)$$

The relationship between $r_{rs}(\lambda)$ and the total backscattering coefficient (b_b) (m^{-1}) and total absorption a (m^{-1}) is (Gordon et al. 1988):

$$r_{rs}(\lambda) = g_0 u(\lambda) + g_1[u(\lambda)]^2 \qquad (4.5)$$

where u is defined as (Dekker et al. 1997):

$$u(\lambda) = \frac{b_b(\lambda)}{a(\lambda) + b_b(\lambda)} \qquad (4.6)$$

and g_o and g_1 are empirical constants that depend on the anisotropy of the downwelling light field and scattering processes within the water. The constant g_o is equivalent to f/Q (where f represents geometrical light factors and Q represents the light distribution factor, which is defined as upwelling subsurface irradiance/upwelling subsurface radiance) (Maritorena et al. 2002). For open ocean waters and nadir-viewed $r_{rs}(\lambda)$, values of g_o and g_1 of 0.049 and 0.0794 have been derived using Monte Carlo simulations (Gordon et al. 1988). For coastal waters values of g_o and g_1 of 0.084 and 0.17 have been derived from Hydrolight simulations (Lee et al. 1998). In turbid waters, variation of g_o and g_1 is more complex, and can depend on bio-optical states, solar and viewing geometry, and wind speed (Gould et al. 2001; Morel et al. 2002; Aurin and Dierssen 2012; Li et al. 2013), and can vary between water bodies (Aurin and Dierssen 2012). It has been suggested that g_o and g_1 should be considered as variables in optically complex inland waters (Aurin and Dierssen 2012; Li et al. 2013). Therefore for the present study, in addition to using values from the literature, an iterative solution of equation 4.5 was used to derive values of g_o and g_1 using Microsoft Excel Solver. In this process bio-optically modelled r_{rs}(B1)were adjusted iteratively for each date to match r_{rs}(B1) from MODIS (with modelled and in situ tripton concurrent with the MODIS image being equal), and an average g_o and g_1 was calculated over all dates.

The absorption and backscattering coefficients are comprised of individual optically active constituents:

$$b_b(\lambda) = b_{bw}(\lambda) + B_{bTR}\, b^*_{TR}(\lambda)\, C_{TR} + B_{b\phi}\, b^*_{\phi}(\lambda)\, C_{\phi} \tag{4.7}$$

$$a(\lambda) = a_w(\lambda) + C_{\phi}\, a^*_{\phi}(\lambda) + a_{CDOMD}(\lambda) \tag{4.8}$$

$$a_{CDOMD}(\lambda) = a_{CDOMD}(\lambda_{440}) \exp[-S\,(\lambda - \lambda_{440})] \tag{4.9}$$

where:

$b_{bw}(\lambda)$ = backscattering coefficient of water
B_{pTR} = backscattering ratio from tripton
$b^*_{TR}(\lambda)$ = specific scattering coefficient of tripton
C_{TR} = concentration of tripton
$B_{p\phi}$ = backscattering ratio from phytoplankton
$b^*_{\phi}(\lambda)$ = specific scattering coefficient of phytoplankton
$a_w(\lambda)$ = absorption coefficient of pure water
C_{ϕ} = concentration of chl *a*
$a^*_{\phi}(\lambda)$ = specific absorption coefficient of phytoplankton

$a_{CDOMD}(\lambda)$ = combined absorption coefficient for coloured dissolved organic matter (CDOM) and detritus
S = spectral slope coefficient

Literature values of $a_w(\lambda)$ and $b_{bw}(\lambda)$ were prescribed (Morel 1974; Pope and Fry 1997). The backscattering ratio of tripton, B_{pTR} , was set to 0.016, equating to measured values for suspended marine particles in turbid coastal waters (Lubac and Loisel 2007), and not dissimilar to the commonly used value of 0.019 arising from Petzold (1972). The specific scattering coefficient of tripton at the MODIS B1 wavelength was estimated using a power function (Morel and Prieur 1977):

$$b^*_{TR}(\lambda) = b^*_{TR}(555)\left(\frac{555}{\lambda}\right)^n \tag{4.10}$$

where the value $b^*_{TR}(555)$ was set to 0.51 m^2 g^{-1}, typical of backscattering values for particles in coastal waters (Babin et al. 2003). The hyperbolic exponent n was set to 0.63, equating to a value measured in Lake Taupo, New Zealand (Belzile et al. 2004). The specific absorption coefficient of phytoplankton $a^*_{\phi}(645)$ was taken to be equal to the average value measured in eight Dutch lakes (0.0077 m^2 mg^{-1}) (Dekker 1993). The bio-optical simulations were run by varying tripton concentration from 0 to 380 mg L^{-1} in increments of 10 mg L^{-1} while $a_{CDOMD(440)}$ was fixed at 0.68 m^{-1}, which is an average value of seven in situ samples of $a_{CDOM(440)}$ in Lake Ellesmere (Gerbeaux and Ward 1991), and chl a was fixed at 90.5 µg L^{-1} which is the average in situ chl a measured at the mid-lake station in Lake Ellesmere in 2007 (n=12).

1-D and 3-D coupled hydrodynamic-ecological model description and setup

DYRESM-CAEDYM (DYCD) is a one-dimensional (1-D) water quality model developed at the Centre for Water Research, University of Western Australia (Gal et al. 2009). DYRESM simulates vertical distribution of temperature, salinity and density based using a horizontal Lagrangian layer approach. The layers are free to move vertically and can contract and expand based on changes in inflows and outflows and surface mass fluxes, as well as to achieve appropriate resolution to represent vertical density gradients. DYRESM is based on an assumption of one dimensionality where variations in the vertical dimension are assumed to be greater than variations in the horizontal dimension (Imerito 2007). The coupled model of DYRESM and CAEDYM (Computational Aquatic Ecosystem Dynamics Model) was used to simulate several biological and chemical variables broadly constituting 'water quality'. CAEDYM is a general biogeochemical model that can simulate specific ecological interactions between species or groups. A detailed description of the model can be found in Hamilton and Schladow (1997) and Hipsey and Hamilton (2008).

ELCOM (Estuary, Lake, Coastal Ocean Model) is a three-dimensional (3-D) numerical model (Hodges and Dallimore 2007) that uses hydrodynamic and thermodynamic models in order to estimate velocity, salinity and temperature in waterbodies. The hydrodynamic model solves the unsteady, viscous Navier-Stokes equations for incompressible flow using the hydrostatic assumption for pressure. A Euler-Lagrange method is used for advection of momentum with a conjugate-gradient solution for the free-surface height (Casulli and Cheng 1992). Passive and active scalars are advected using a conservative Ultimate Quickest discretisation (Leonard 1991). ELCOM was also coupled to CAEDYM for the purpose of resolving horizontal distributions of biological and chemical variables for MODIS comparisons. A horizontal cell size of 200 x 200 m was used in the coupled model simulations, with a vertical resolution of 15 cells, each 0.2 m in the vertical, which allowed the model to run with a real-time to run-time ratio of approximately 180:1.

Meteorological forcing variables for each of these models included hourly air temperature (ºC), shortwave radiation (W m^{-2}), cloud cover (fraction of whole sky), vapour pressure (hPa), wind speed (m s^{-1}) and rainfall (m), which were acquired from the National Institute of Water and Atmosphere (NIWA) weather station at Lincoln (Broadfield), Christchurch (latitude 43.626^{o}S, longitude 172.470^{o}E). For the period of ELCOM-CAEDYM simulation runs, hourly average wind speed values were taken from Birdlings flat (University of Canterbury Physics Department Weather Station (latitude 43.825^{o}S, longitude 172.707 ^{o}E) located 4.3 km east of Lake Ellesmere. Wind speed and direction instrument failure periods at Birdlings flat were filled with data from the Broadfield weather station. A linear regression of average hourly wind speed at Birdlings flat (BF_w) on that at Broadfield (B_w) yielded:

$$BF_w = 1.3704\, B_w + 4.1938 \qquad (r^2 = 0.59,\ n=368) \qquad (4.11)$$

and was used to synthesise wind speeds at Birdlings flat. There was no clear relationship of wind directions between the two stations, so the wind direction of Broadfield was not modified.

Daily inflow and outflow data were derived by using linear interpolation between monthly samples for flow, and concentrations of nutrients and SM. A daily water balance was determined for the lake, which included inflows, estimates of groundwater inflow and seawater overtopping (Horrell 1992), rainfall and calculated evaporation from estimates of the evaporative heat flux (Fischer 1979) and the saturation vapour pressure (Wunderlich 1972), together with water-level induced changes in lake volume. A residual term in the water balance was used to derive a daily outflow. Nutrient concentrations in ungauged inflows were estimated based on volume-weighted averages of observed inflow concentrations. A full description of the Lake Ellesmere model set-up and calibration can be found in Trolle (2009) and Trolle et al. (2011). The present study uses the same input data, apart from wind speed and direction, but adjustment was made for the calibration of SM.

Within the ecological model CAEDYM, SM is simulated from settling and resuspension, with advection and mixing simulated using the hydrodynamic model. The equation for simulating SM is:

$$\frac{\partial SM_s}{\partial t} = \frac{\upsilon_s}{\Delta z} SM_s + \alpha s_s + \frac{\tau - \tau_{cs}}{\tau_{ref}} \; \frac{SM_{s-sed}}{K_{SM\,s} + SM_{s-sed}} \; \frac{1}{\Delta z bot} \tag{4.12}$$

where SM_s is the concentration of SM (g m^{-3}) for each size class *s*, υ_s is the settling velocity (m s^{-1}), Δz is layer thickness (m), *bot* is bottom, αs_s is the resuspension rate (g m^{-2} s^{-1}), τ is shear stress (N m^{-2}) , τ_{cs} is the critical shear stress (N m^{-2}), τ_{ref} is a reference shear stress (set to 1 N m^{-2}), and K_{TP_s} limits resuspension as the sediment supply in the bottom, $SM_{s\text{-}sed}$ (*g*), is exhausted. Further details of the application of the algorithm can be found in Hipsey and Hamilton (2008).

Validation of 3-D model simulation of SM using satellite imagery

The spatial statistics methods for comparison of raster images from 3-D model simulations of SM, and raster images of SM estimated from satellite imagery, are introduced briefly below. Potentially land-contaminated pixels were removed from the analysis. A channel to the north-east of the lake was not included, as it was too narrow (approximately 250 m wide) to be free of land contamination.

Geographically Weighted Regression (GWR) (Brunsdon et al. 1996) was applied using ArcGIS. The GWR regression equation is defined as:

$$y_i = \alpha_i + \beta_i x + \varepsilon_i \tag{4.13}$$

where ε_i represents an error term and the point *i* is generalizable and can simply refer to points at which data are collected. GWR then uses a weighted approach depending on the location of *i*. A fixed Gaussian kernel was used to solve each local regression, using a bandwidth of 4000 m. This was selected by first running GWR using the Akaike Information Criterion (Akaike 1969) to determine the optimal bandwidth, which was close to 4000 m for the concurrent model and satellite image on 18 December 2006.

The remaining spatial statistic methods were implemented using in MCK software (Visser and De Nijs 2006). The first of these is the Fuzzy Numerical Statistic (FNS), which is based on the rationale of Fuzzy Kappa as introduced in Hagen (2003). For raster map comparison, fuzziness was considered in terms of location and accuracy, and as a means of accounting for the fact that maps always contain a level of uncertainty. The fuzzy numerical statistic was determined by the degree of similarity of the raster value at a specific location between two raster maps. The outcome of the comparison depends on the distance weight function, which introduces subjectivity into the statistic (Hagen-Zanker 2006). The default settings were used for the calculation of FNS within MCK, which used a radius neighbourhood of four cells and an exponential decay halving distance of two.

The wavelet verification algorithm (WVA) (Briggs and Levine 1997) uses discrete wavelet transformations to forecast verification problems. The technique was designed to reduce noise while developing measures of performance assessment for weather forecasting. The discrete wavelet transformation transforms input maps to a variety of different scales. These maps are then compared against each other in terms of root squared error (RSE) and correlation. The default MCK settings were used for the calculation.

The image warping algorithm (Reilly et al. 2004) distinguishes pixel to pixel differences and location differences within two rasters. Location differences are quantified by warping the estimated raster (as opposed to the validation raster) until an optimal fit is found to the validation raster. The degree of warping (stretching and contracting) is given as the Warping Defamation Penalty Statistic (WDPS) (Reilly et al. 2004). The default Map Comparison Kit warping setting was used in the calculation of WDPS.

Model parameters

Table 4.1 shows the CAEDYM sediment resuspension parameters used in the 3-D model. Parameters used in the 1-D model were identical to the 3-D model except for the resuspension rate, which was set to 0.1 g m^{-2} d^{-1}, as opposed to 0.4 g m^{-2} d^{-1} used in the 3-D model. Resuspension rate in the two models was different to account for spatial effects on parameters (Romero et al. 2004). Three different SM particle sizes were used, with particle size 1 (3.75 µm) and 2 (2.16 µm) being chosen to represent two different size fractions of clay, and particle size 3 (0.83 µm) chosen in order to represent colloidal particles. These three size classes were assigned a fractional composition of total SM. Particle size 3 effectively remained in suspension continuously, with the fraction of total SM set to 0.001, therefore limiting the available supply of this sediment size class for resuspension. Critical shear stress was increased with particle size, from 0.10 N m^{-2} for particle size group one to 0.05 N m^{-2} for particle size group three (Table 4.1).

Table 4.1. ELCOM-CAEDYM parameters related to suspended mineral (SM) resuspension and sedimentation.

Parameter	Particle size 1	Particle size 2	Particle size 3
SM particle density (kg m^{-3})	2650	2650	2650
Diameter (μm)	3.75	2.16	0.83
Critical shear stress (N m^{-2})	0.10	0.07	0.05
Fraction of total SM	0.25	0.25	0.001
Sediment organic fraction	0.05	0.05	0.05
Sediment porosity	0.54	0.54	0.54
Resuspension rate (g m^{-2} d^{-1})	0.40	0.40	0.40

The values of critical shear stress used in this study, which ranged from 0.05 - 0.10 N m^{-2} across the three assigned size classes, are somewhat lower than the value of 0.49 N m^{-2} used by Hamilton and Mitchell (1996) for a zero-dimensional model application to Lake Ellesmere, but are comparable to values for other shallow lakes (e.g., 0.05 N m^{-2} used by Sheng and Lick (1979) for an application to Lake Erie, USA).

4.4 Results

Estimates of suspended mineral concentration from tripton

The relationship between in situ C_{TR} and NAVSS is shown in Figure 4.2. This equation is then used to estimate C_{SM} as:

$$C_{SM} = C_{TR} - (0.199 * C_{TR} - 7.65) \qquad (\text{RMSE}=2.7 \text{ mg L}^{-1}) \qquad (4.14)$$

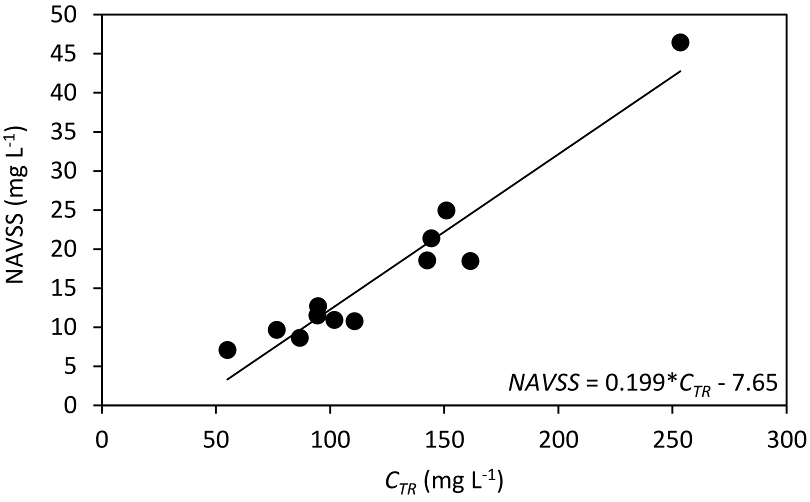

Figure 4.2. Relationship between non-algal volatile suspended sediment (NAVSS) and tripton concentration (*C_{TR}*) in Lake Ellesmere (*r^2*=0.92, n=12) from 9 July 2008 to 1 September 2008.

Empirical remote sensing of suspended minerals

The empirical equation used to estimate tripton concentration from r_{rs}(B1) was:

C_{TR}= exp(2.51 ln(r_{rs}(B1)) + 12.26) (4.15)

with r^2=0.61, p<0.0001, RMSE=58.9, and n=12 (Figure 4.3).

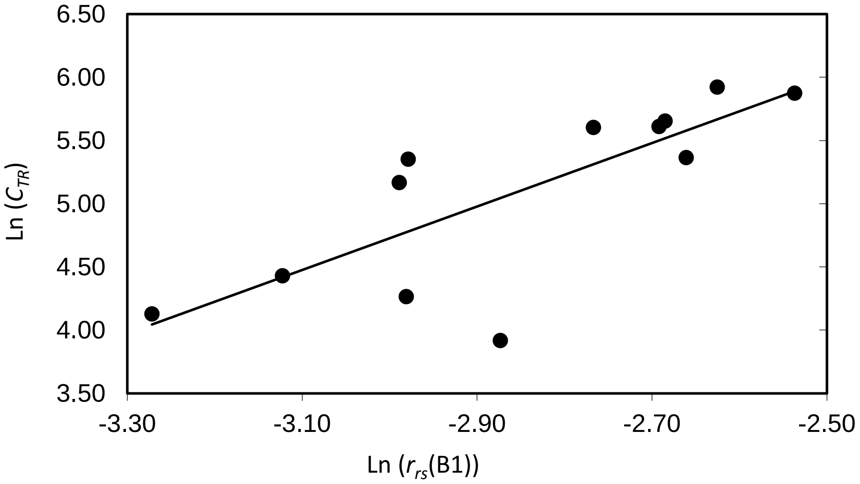

Figure 4.3. Relationship between MODIS reflectance and tripton concentration (*C_{TR}*) (mg L^{-1}). The line shows the linear regression with *r^2*=0.61 and p<0.0001.

Although the relationship potentially contained outliers, there was not sufficient statistical evidence to remove these.

Bio-optical modelling

The analytical relationship between tripton concentration and MODIS r_{rs}(B1) was approximated using an exponential equation which was then used to estimate tripton concentration from MODIS r_{rs}(B1) (Figure 4.4(a)). The RMSE in tripton concentration retrieval using literature values of g_o and g_1 has been found to be 111.8 mg L^{-1} for open ocean waters (Gordon et al. 1988), 156.2 mg L^{-1} for coastal waters (Lee et al. 1998) and 58.4 mg L^{-1} using fitted values of 0.103 and 0.009 (using the fitting routine described in the methods). The retrieval error using fitted values is comparable to the RMSE of the empirical model of 58.9 mg L^{-1}. The linear regression between tripton derived in situ and from semi-analytical methods using MODIS r_{rs}(B1) produced a slope of 1.02 and a constant of 11.2 mg L^{-1} (r^2=0.72). The linear regression between in situ and empirically estimated tripton produced a slope of 1.04 and a constant of -6.2 mg L^{-1} (r^2=0.73) (Figure 4.5). While there are differences in the error metrics of the two models, plots of observed and estimated tripton reveal that the two models produce very similar results.

The saturation reflectance of MODIS r_{rs}(B1) with increasing tripton concentrations was investigated by running the bio-optical model over a larger range of tripton concentrations (Figure 4.4(b)). An asymptote can be observed near r_{rs}(B1) of 0.1, indicating a theoretical saturation value of r_{rs}(B1) (i.e. at tripton concentrations c. 1000 mg L^{-1}).

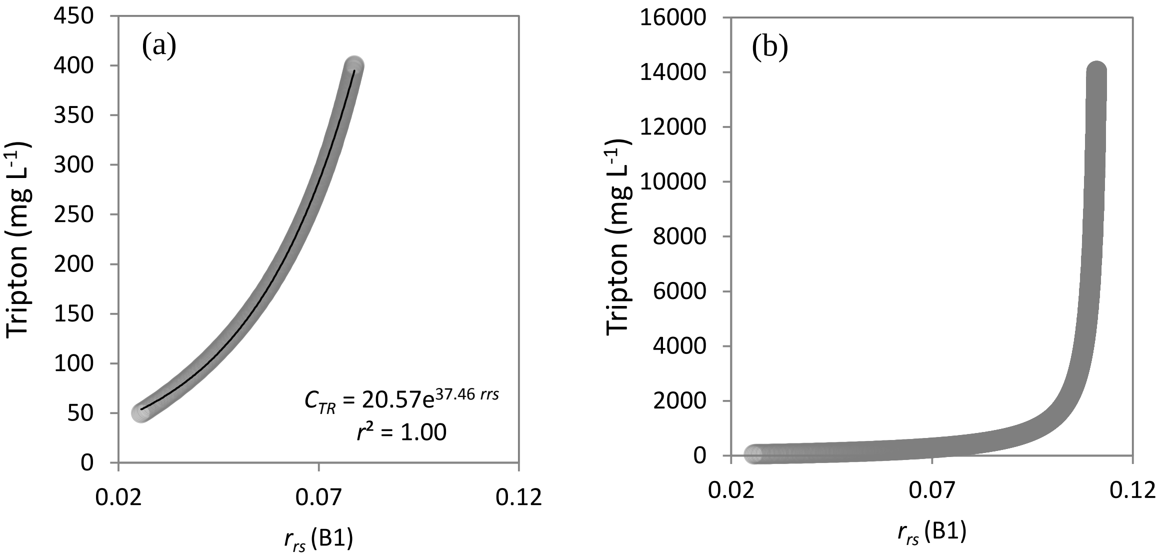

Figure 4.4. (a) The analytical relationship between tripton concentrations as a function of MODIS subsurface remote sensing reflectance (r_{rs}(B1)) represented by open grey circles. An exponential relationship is used to approximate the analytical relationship (black line). This function was used to estimate tripton concentration from MODIS r_{rs}(B1). (b) Graph of the same relationship as (a) but extended over a larger range of tripton concentrations.

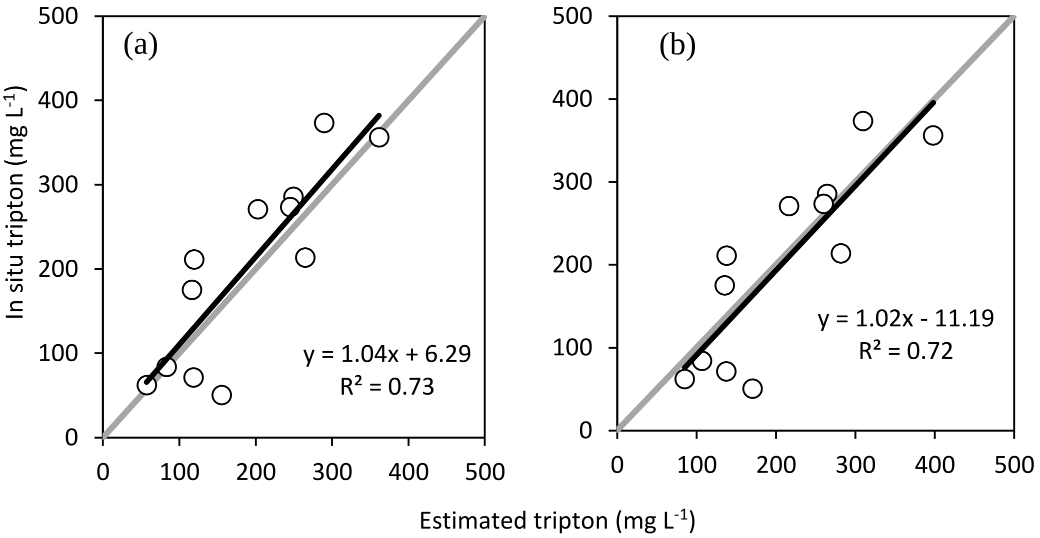

Figure 4.5. In situ concentration of tripton and estimates using (a) the semi-analytical model (RMSE=58.4 mg L^{-1}) and (b) empirical model (RMSE=58.9 mg L^{-1}). A 1:1 line (grey) and the observed vs. estimated regression equation and line (black) and associated r^2 are shown on each plot (n=9).

One-dimensional model results

Over the simulation period from 1 March 2006 to 31 August 2007 the RMSE between SM from mid-lake grab-samples and from the 1-D simulations was 126 mg L^{-1}. Suspended mineral concentrations in the model ranged from 34 to 481 mg L^{-1}, with an average of 212 mg L^{-1} and 82 mg L^{-1} (Figure 4.6). The minimum and maximum simulated change in SM concentration over a single day (24 h) was 0.001 and 207 mg L^{-1}, respectively

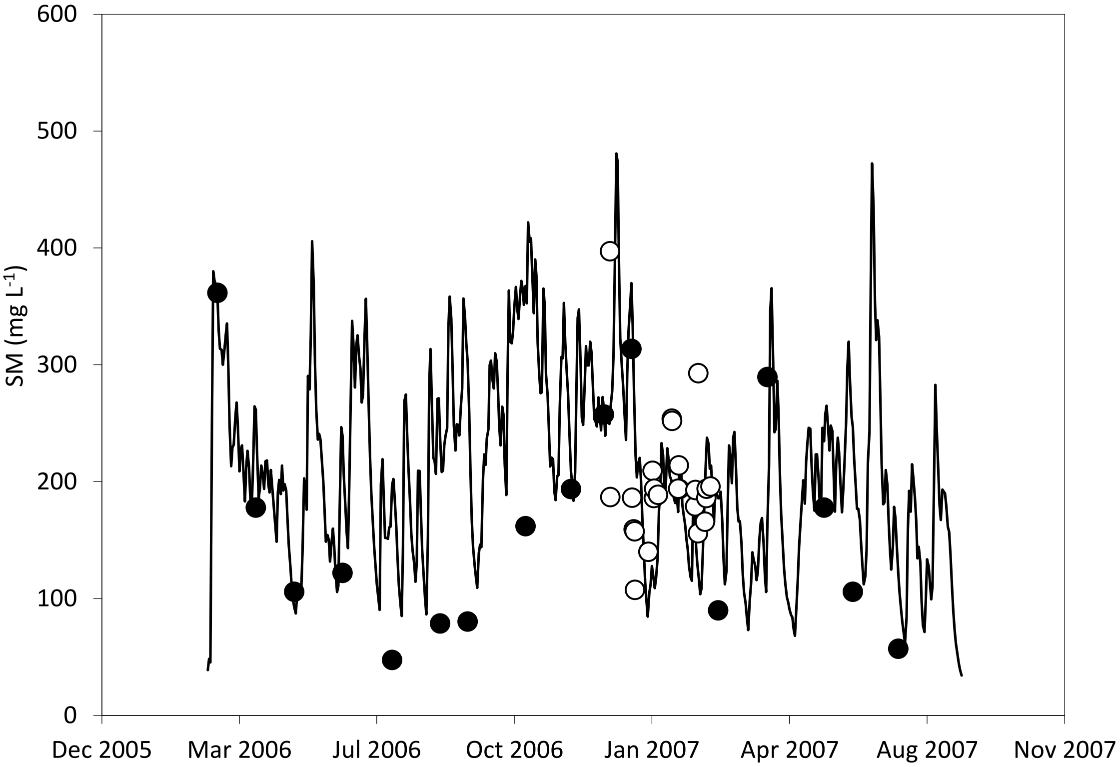

Figure 4.6. Suspended mineral (SM) concentrations (mg L^{-1}) simulated using the 1-D model (line), measured with situ grab-samples (closed circles) and estimated from remote sensing (open circles) for the period 1 March 2006 to 31 August 2007.

SM from 3-D modelling and satellite image retrieval

The 3-D model simulation period was from 1 December 2006 to 11 March 2007. Figure 4.8 shows simulated SM from the 3-D model (at the mid-lake site) and from the 1-D model, compared to in situ and satellite-estimated SM measurements at the same location. On 19 December 2006 a large storm occurred, with maximum wind speeds of 28 m s^{-1}

(100.8 km hr^{-1}) (refer to Figure 4.7). The resulting resuspension event was reflected in strongly elevated SM in both the 1-D and 3-D models. Over the period of the 3-D model simulation SM concentrations at the mid-lake station averaged 217 mg L^{-1} and ranged from 123 to 600 mg L^{-1}, with the maximum SM concentration observed during the storm event at 1600 h on 23 December. The minimum and maximum change in SM concentration over any one-day (24 h) was 0.002 and 184 mg L^{-1}, respectively.

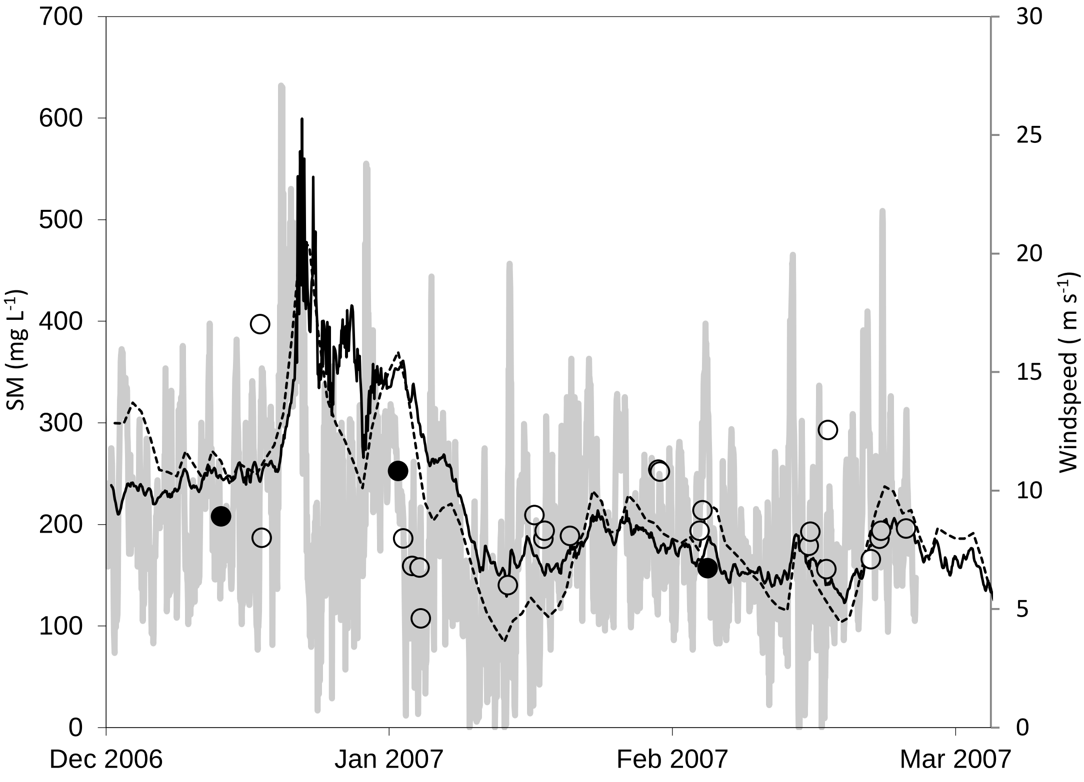

Figure 4.7. Simulated concentrations of suspended minerals (SM) (mg L^{-1}) using the 3-D model (black line) and 1-D model (dashed line), in situ concentrations (closed circles for the period 1 December 2006 to 11 March 2007), and satellite-estimated concentrations (open circles). Average hourly wind speed (m s^{-1}) is represented by the grey line.

The simulated SM from the 1-D and 3-D models followed the same general pattern of fluctuation as the in situ data and the values estimated by the semi-analytical model using MODIS B1 data. However, after the storm event, there was a deviation of the simulated SM from the MODIS estimates and the measurements. Concentrations of SM in the simulation decreased slower than those indicated by satellite imagery and in situ data. At the end of the storm event at 1400 h on 5 January 2007, SM simulated with the 3-D model was 288 mg L^{-1}

compared with estimated SM of 107 mg L^{-1}. After 18 January 2007 and until the end of the study period on 11 March 2007, SM simulated with the model was much closer to the in situ and estimated values, with exceptions on 1 and 20 February 2007. After the storm (excluding exceptions mentioned above) the difference in SM between satellite calculations and 3-D simulations ranged from 1 to 46 mg L^{-1}.

Visual analysis of SM from 3-D simulations and satellite estimation

There was considerable spatial heterogeneity of SM concentration across the lake on most days based on the MODIS semi-analytical estimation. Large gradients were observed on some dates (Figure 4.8a-d). For example, at 10:00 h on 18 December 2006 (Figure 4.8a (i)) MODIS-estimated SM ranged from 134 to 502 mg L^{-1}. Areas of higher SM were usually associated with littoral areas (e.g. Figure 4.8b (ii)). The highest SM concentrations tended to occur in littoral areas on the northern shore (Figure 4.8b (ii)) corresponding to Greenpark Sands (see Figure 4.1), and in areas near the southern shore (Kaitorete Spit; Figure 4.1), though the highest SM was recorded on the eastern shore (Figure 4.8a (vi)) near Kaituna Lagoon (Figure 4.1). Occasionally there were areas of elevated SM concentration within the main body of the lake (e.g., 4.8d (i)).

Suspended mineral concentrations derived from model simulations were highly heterogeneous with elevated concentrations in littoral areas. Basin-scale variations in SM were sometimes captured based on visual comparison with SM derived from MODIS data (Figure 4.8b (ii), 4.8b (iv), 4.8c (ii)). On some other dates SM distribution patterns estimated from satellite data were quite different from model simulation cases (e.g. Figure 4.8a (i), 4.8a (vi), 4.8c(vi), 4.8d (i), 4.8d (iv)). Generally, simulations over-estimated SM concentrations in shallow lake margins (e.g. Figure 4.8d (ii)), however, there were also instances when MODIS-estimated SM concentrations were elevated in association with shorelines; these were not simulated well by the 3-D model (e.g., Figure 4.8a (i) and (ii)). The elevated shoreline SM estimated from MODIS cannot be attributed to land contamination, as the surrounding land has a lower reflectance than that of nearby lake water. Similarly, high SM concentrations near river entrances in simulations with the 3-D model were not observed in MODIS output (Figure 4.8d (i) and 4.8d (iv)) corresponding to the Selwyn and Halswell rivers (Figure 4.1), respectively.

Statistical comparisons of SM from MODIS data and 3-D model simulations compared to visual comparison

The Geographically Weighted Regression between concurrent MODIS image and simulation estimated water surface SM concentration produced r^2 values that ranged from 0.13 (Figure 4.8d (iii)) to 0.62 (Figure 4.8d (i)), with a mean of 0.41. Visual comparison of SM spatial distributions in Figure 4.8d (iii) reveals some basin scale similarities in patterns of horizontal variation, which does not conform with having the lowest r^2. The visual comparison of 4.8d (i) shows very different basin scale patterns, and again does not conform to a case with the highest r^2. In Figure 1.9b (v) patterns of spatial distribution of SM match reasonably well on a basin scale, however, the GWR r^2 is only 0.19, the second lowest of all dates.

Linear regression r^2 values conform better than GWR r^2 values when compared to visual comparisons of similarities in spatial patterns. The largest r^2 was 0.11 ($p > 0.05$; Figure 1.9c (ii)), when visual patterns of spatial distribution have basin scale similarities. The lowest r^2 (with $p > 0.05$) was for SM on 3 January 2007 (Figure 4.8a (iii)) when patterns of spatial distribution did not match well.

While there is a clear difference in performance between GWR and traditional regression as statistical measures of spatial similarities and differences between model simulations and MODIS estimations of SM, the same cannot be said for the differences between the three MCT-derived statistics. There was general agreement amongst the three MCT statistics as far as ranking comparison performance. All three statistics compared well with the visual spatial pattern ranking, and dates with visual similarities corresponded to high Fuzzy Numerical Statistic (FNS), high Wavelet Verification Algorithm (VWA) r values, and low Warping Defamation Penalty Statistic (WDPS). The WVA r values were highest for Figure 4.8b (vi) and 4.8c (ii) and lowest for Figure 4.8a (vi) and 4.8c (i). The FNS was highest for 4.8a (iv) and 4.8b (iii) and lowest for 4.8b (v) and 4.8a (i). WDPS identified Figure 4.8b (ii) and 4.8d (iii) as the closest matching rasters and Figure 4.8c (vi) and 4.8d (i) as the most different.

There was no clear relationship between the 3-D model forcing variables of wind speed and wind direction, and comparisons of similarities between spatial distributions from model and MODIS based estimations of SM concentration on a basin scale. Stronger winds, however, were associated with high simulated SM concentrations in littoral areas (e.g., Figure 4.8c (ii), 4.8d (ii), 4.8d (ii), 4.8d (iii)), which were not present in MODIS-estimated SM concentrations.

Table 4.2. Statistical comparison of SM concentrations estimated from the semi-analytical algorithm and simulated from the 3-D model (n = 2414 for each instance). Statistical fit is represented using r^2 values based on linear regression, Geographically Weighted Regression (GWR r^2), Fuzzy Numerical Statistic (FNS), Wavelet Verification Algorithm (WVA *r* and WVA RSE), and Warping Defamation Penalty Statistic (WDPS). Relationships that were not significant (p > 0.05) were represented by *.

Date	Time (h)	Linear r^2	p	Slope	RMSE	GWR r^2	FNS	WVA *r*	WVA RSE	WDPS	Figure
18/12/2006	10:00	0.022	0.000	-0.29	120.4	0.57	0.47	0.9950	976.6	0.00354	4.8a (i)
18/12/2006	14:00	0.007	0.000	-0.04	97.4	0.54	0.78	0.9970	35.4	0.00177	4.8a (ii)
03/01/2007	14:00	0.000*	0.718	-0.01	182.3	0.41	0.73	0.9980	71.1	0.00141	4.8a (iii)
05/01/2007	10:00	0.000*	0.610	0.01	125.6	0.51	0.90	0.9970	7.4	0.00147	4.8a (iv)
05/01/2007	14:00	0.001*	0.067	-0.02	126.8	0.43	0.79	0.9820	57.7	0.00154	4.8a (v)
15/01/2007	10:00	0.015	0.000	-0.46	45.0	0.31	0.63	0.8530	235.1	0.00105	4.8a (vi)
18/01/2007	10:00	0.019	0.000	0.08	54.9	0.43	0.74	0.9960	70.8	0.00090	4.8b (i)
19/01/2007	10:00	0.013	0.000	0.17	59.6	0.24	0.83	0.9790	11.2	0.00057	4.8b (ii)
19/01/2007	14:00	0.009	0.000	-0.07	37.3	0.58	0.90	0.9930	6.7	0.00227	4.8b (iii)
22/01/2007	10:00	0.009	0.000	-0.09	41.6	0.52	0.85	0.9890	8.1	0.00128	4.8b (iv)
01/02/2007	10:00	0.058	0.000	0.3	38.2	0.19	0.45	0.9980	1195.2	0.00482	4.8b (v)
01/02/2007	14:00	0.020	0.000	-0.24	61.4	0.48	0.84	0.9990	49.1	0.00176	4.8b (vi)
06/02/2007	10:00	0.078	0.000	0.37	59.1	0.45	0.83	0.9780	69.3	0.00093	4.8c (i)
06/02/2007	14:00	0.112	0.000	0.21	28.2	0.27	0.76	0.9990	60.1	0.00161	4.8c (ii)
18/02/2007	10:00	0.043	0.000	-0.27	43.6	0.36	0.83	0.9880	10.3	0.00118	4.8c (iii)
18/02/2007	14:00	0.033	0.000	-0.19	29.1	0.43	0.84	0.9890	8.2	0.00151	4.8c (iv)
20/02/2007	10:00	0.009	0.000	0.19	69.5	0.45	0.72	0.9850	47.1	0.00231	4.8c (v)
20/02/2007	14:00	0.001*	0.093	-0.05	39.9	0.23	0.66	0.9980	230.4	0.02046	4.8c (vi)
25/02/2007	10:00	0.044	0.000	-0.22	92.5	0.62	0.70	0.9820	169.5	0.00494	4.8d (i)
26/02/2007	10:00	0.000*	0.221	0.03	57.1	0.36	0.78	0.9870	71.1	0.00381	4.8d (ii)
26/02/2007	14:00	0.001*	0.087	-0.04	44.7	0.13	0.68	0.9860	201.2	0.00064	4.8d (iii)
01/03/2007	10:00	0.060	0.000	-0.18	44.4	0.47	0.85	0.9870	13.8	0.00163	4.8d (iv)
01/03/2007	14:00	0.008	0.000	0.07	43.7	0.35	0.86	0.9980	21.4	0.00240	4.8d (v)

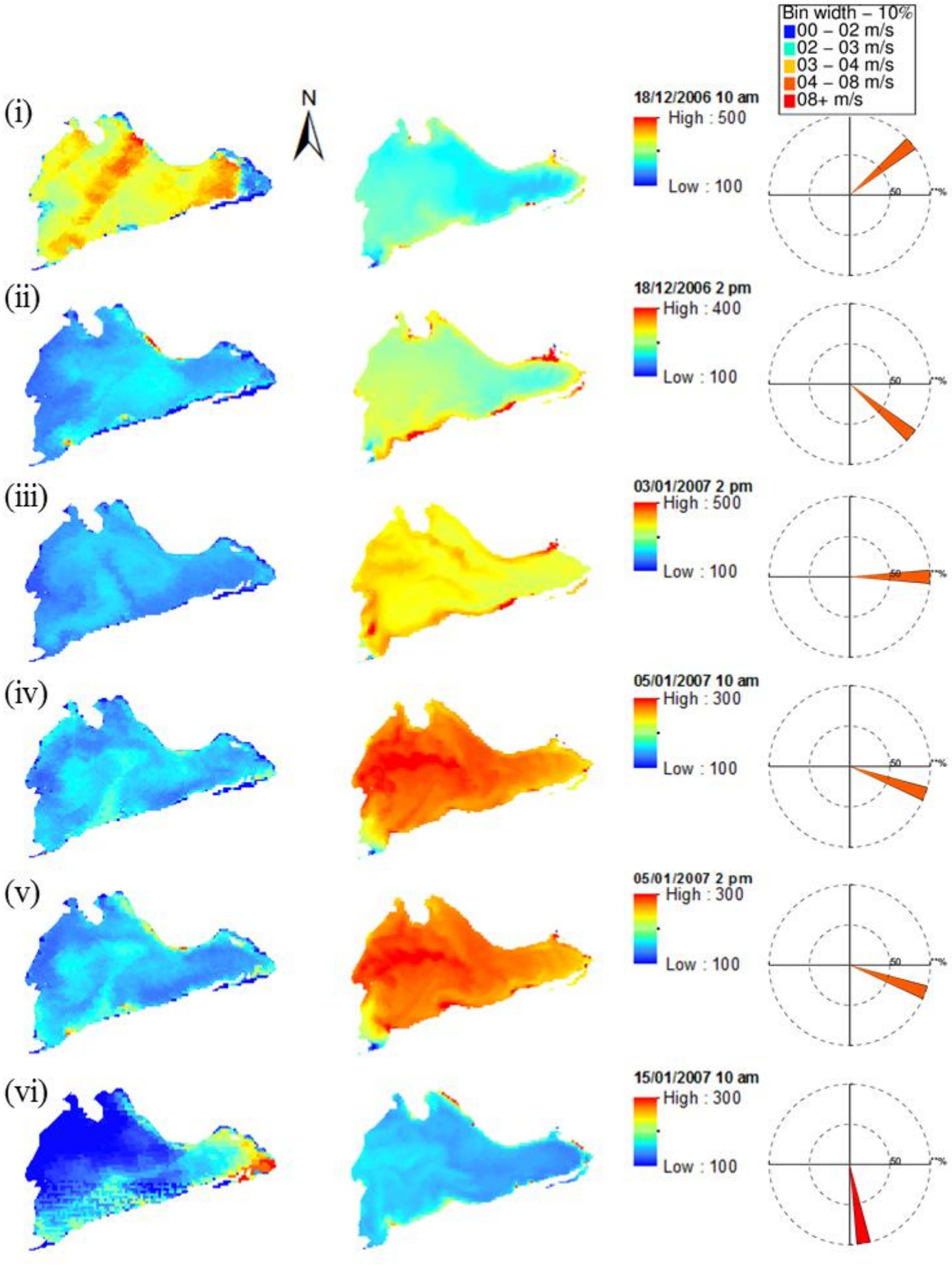

Figure 4.8a. Suspended mineral concentration (mg L^{-1}) estimated from MODIS data (left) and from 3-D model simulations (right). Note colour scale differences in some instances. Hourly average wind speed and direction are plotted on the wind rose, with changes in colour representing wind speed.

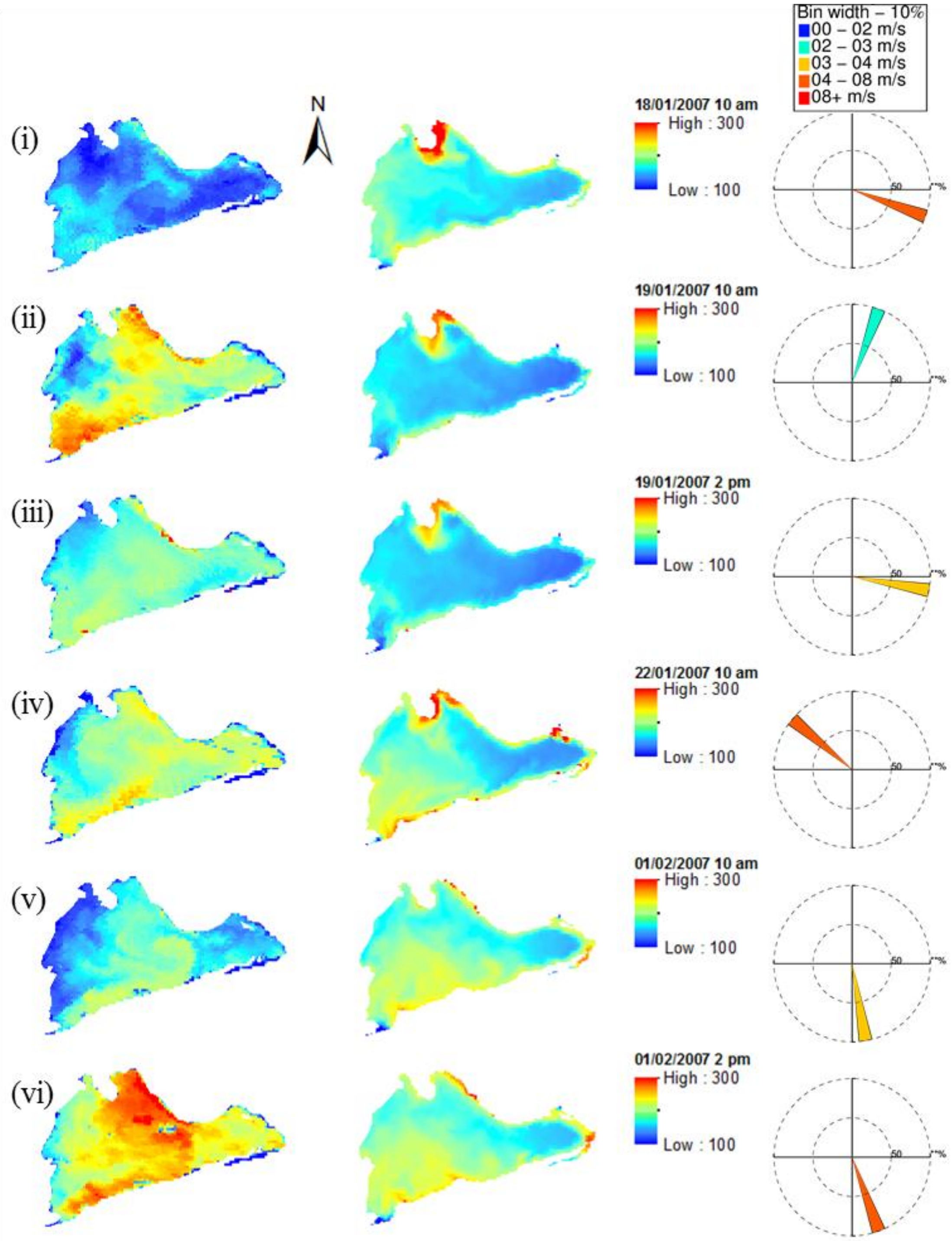

Figure 4.8b. Suspended mineral concentration (mg L^{-1}) estimated by MODIS (left) compared to simulations from the 3-D model (right). Hourly average wind speed and direction are plotted on the wind rose, with changes in colour representing wind speed.

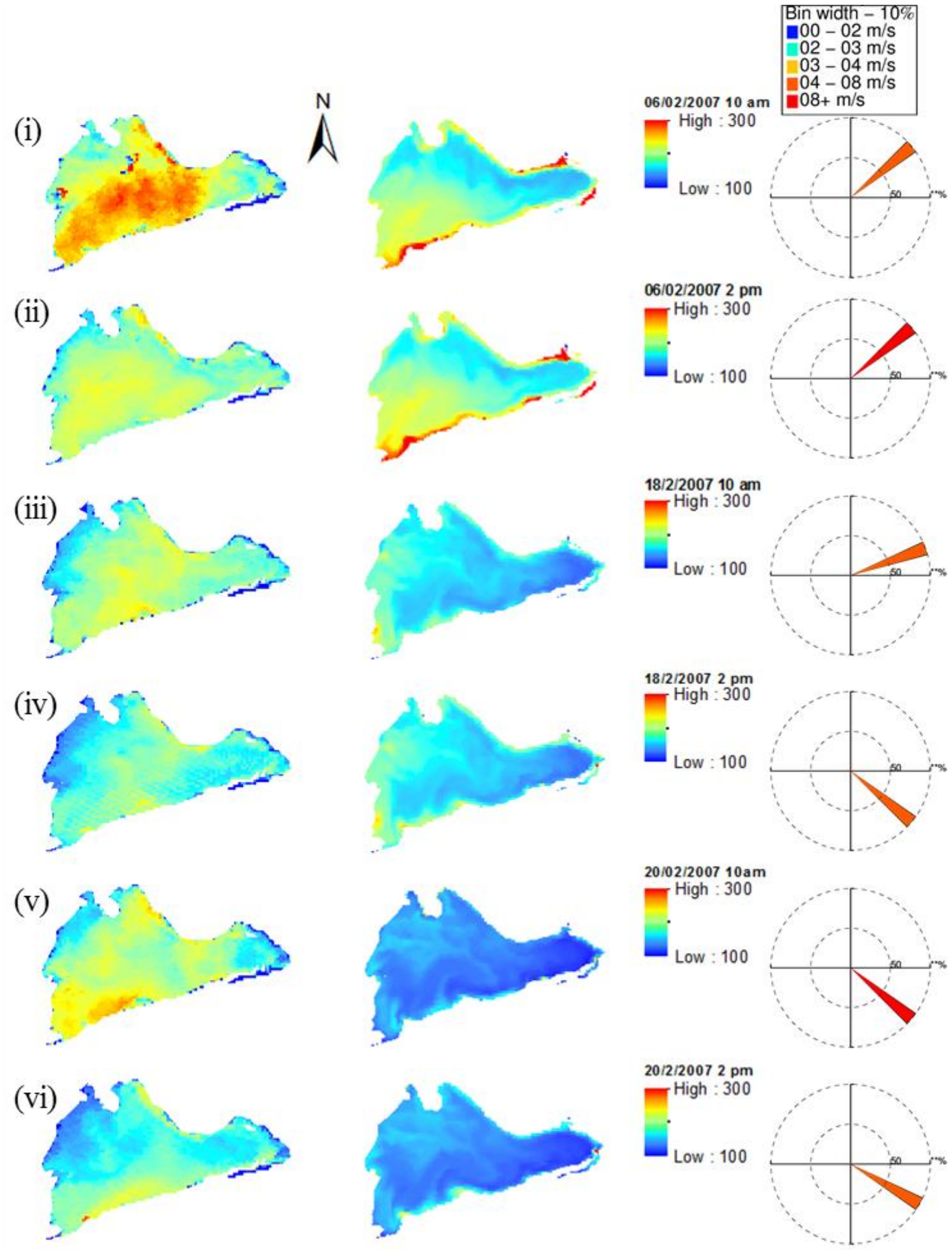

Figure 4.8c. Suspended mineral concentration (mg L^{-1}) estimated by MODIS (left) compared to simulations from the 3-D model (right). Hourly average wind speed and direction is plotted on the wind rose, with changes in colour representing wind speed.

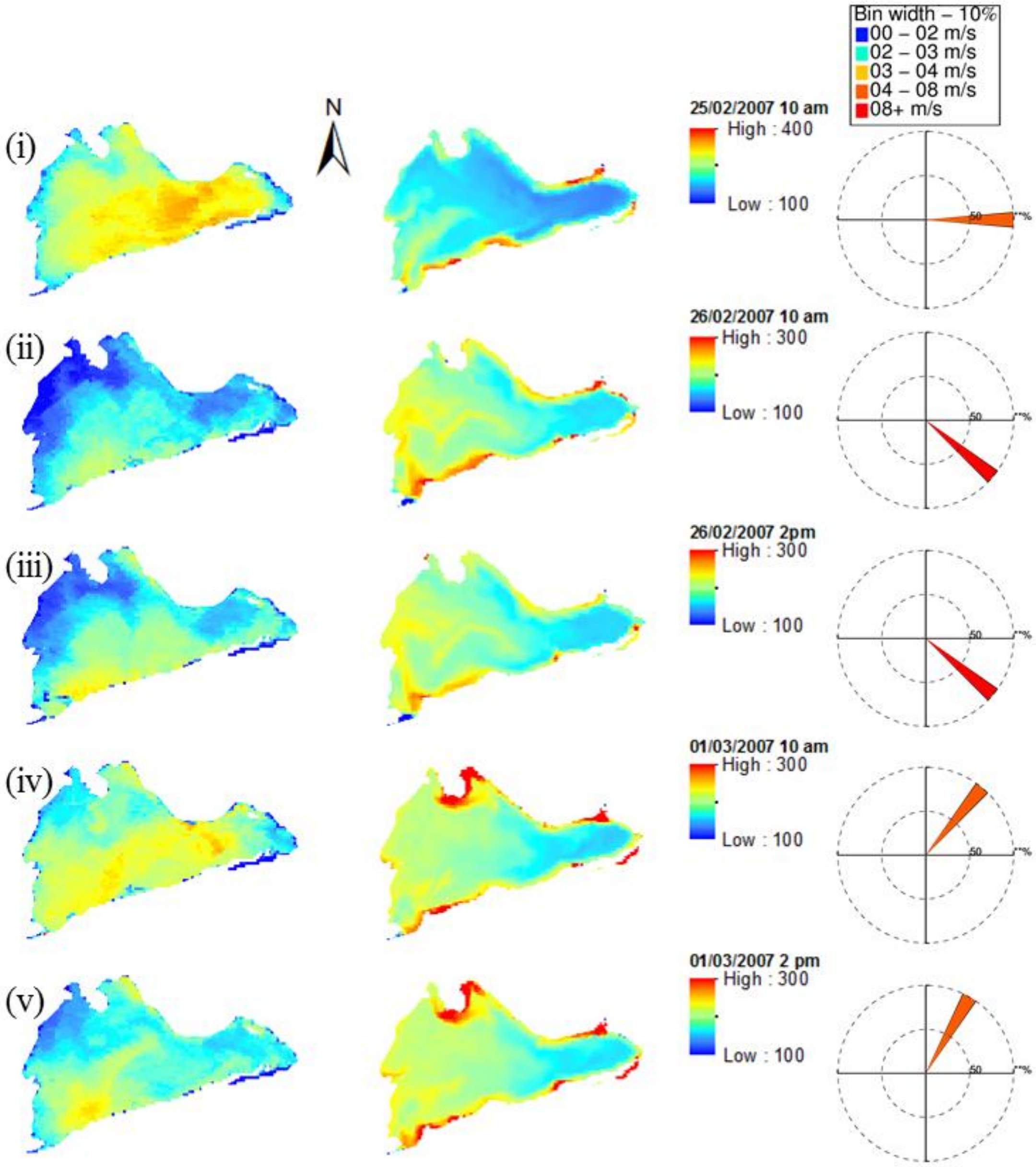

Figure 4.8d. Suspended mineral concentration (mg L^{-1}) estimated by MODIS (left) compared to simulations from the 3-D model (right). Note colour scale differences in some instances. Hourly average wind speed and direction is plotted on the wind rose, with changes in colour representing wind speed.

4.5 Discussion

The synoptic estimations of SM from MODIS have provided a tool to directly compare with simulated SM from 1-D and 3-D models on a twice-daily basis, i.e., at substantially higher frequency than is used in most routine lake sampling programmes involving grab-sample collection. In addition, the development of a semi-analytical model to estimate tripton concentration from MODIS Aqua and Terra subsurface remote sensing reflectance will greatly extend the current spatial and temporal coverage of monitoring. State of the art spatial statistical methods were applied for comparison of the horizontal distributions from 3-D model simulations with those estimated from the MODIS-based semi-analytical model, using the Map Comparison Kit (MCK) (Visser and De Nijs 2006), which allowed for a quantitative validation.

There have been few comparisons of semi-analytical and empirical methods for remote sensing of tripton or suspended sediment concentrations. Empirical methods may be advantageous because they can be calibrated specifically for the images and in situ data in question, and provide robust estimates within the calibrated concentration range (Matthews 2011). The present study has demonstrated, however, that semi-analytical methods are capable of a similar level accuracy over the same series of images. Moreover, semi-analytical methods are applicable to a wider range of tripton concentrations as the algorithm accounts for non-linearity of the relationship between tripton and r_{rs}(B1). Furthermore, semi-analytical algorithms can be developed independently from in situ data and the methodology is transferable to other sensors such as Landsat (e.g., Dekker et al. 2002).

Remote sensing and modelling revealed that tripton concentrations are highly dynamic temporally and spatially in Lake Ellesmere, which can lead to potential for large differences between the spatial representation of in situ data and MODIS AOI. Obtaining representative in situ samples of SS corresponding to a MODIS AOI presents some challenges. The MODIS AOI represents average r_{rs}(B1) over 0.56 km^2, as opposed to a point in situ sample. An ideal situation for the calibration and validation of SS algorithms would involve multiple samples over the AOI, synchronous with the satellite overpass.

The values of the parameters g_0 and g_1 used in semi-analytical models have a significant effect on the accuracy of inversion of ocean colour (Brando et al. 2012). For eutrophic inland waters, variations in g_0 and g_1 are larger than for coastal waters and oceans (Dekker et al. 1997). In the present study it was found that the application of commonly applied values g_0 and g_1 from the open ocean (Gordon et al. 1988), and coastal zones (Lee et al. 1998), were not applicable for the simplified semi-analytical model applied to Lake Ellesmere. The use of fitted g_0 and g_1 was required in order to obtain a semi-analytical model with comparable accuracy to the empirical model. The value of g_0 derived by this study (0.103 sr^{-1}) is within the reported range of 0.08 to 0.15 sr^{-1} (Morel et al. 2002) and is approximately equal to the optimized value at 650 nm for highly turbid waters derived by Aurin and Dierssen (2012) of 0.10305 sr^{-1}. These authors concluded that waters with extremely high SS concentrations displayed more spectral variability of g_0. The value of g_1 derived by this study of 0.009 sr^{-1} is significantly lower than the value of Gordon et al. (1988) and Lee et al. (1998) however Aurin and Dierssen (2012) reported instances where g_1 was not significantly different from zero where waters were highly turbid.

For the remote sensing of suspended sediment in aquatic systems using MODIS B1, an above-surface saturation irradiance reflectance of 0.16 has been suggessted (Sipelgas et al. 2009), not dissimilar to that estimated by the semi-analytical model used in this study (r_{rs}(B1)=0.10 or B1 above surface irradiance reflectance =0.17 sr^{-1}). The accuracy of semi-analytical and empirical algorithms for estimating tripton or suspended sediment may be constrained by saturation of $r_{rs}(\lambda)$, whereby at high suspended sediment concentrations there is limited sensitivity of $r_{rs}(\lambda)$ to any changes in concentration (Bowers et al. 1998; Doxaran et al. 2002). The present study demonstrated the applicability of a MODIS B1-based semi-analytical model to estimate suspended sediments over a concentration range from 62 to 356 mg L^{-1}. While these concentrations are relatively high compared to those found in most lakes, simplified semi-analytical models using MODIS B1 have also been successfully applied to estimate suspended sediment concentrations from c. 0 to 29 mg L^{-1} (Binding et al. 2010).

Several spatial statistics were used to make quantitative comparisons between SM estimated from remote sensing and from a 3-D model simulation. Kuhnert et al. (2005) found that the literature is lacking in methods to quantify the numerical and spatial differences between two raster maps. Since these methods are lacking, visual analysis has been used to compare the relative performance of spatial statistics (e.g., Kuhnert et al. 2005). In the present study, the three MCT statistics tested were more closely linked to visual comparison than the Geographically Weighted Regression, however, the relative difference between the three MCT methods was not clearly identified. The MCK approach avoids violating statistical assumptions made by traditional regression methods that require independence of adjacent cells (O’Sullivan and Unwin 2002). Quantitative statistics are essential for comparison of multiple rasters, however, it is important that they retain features of visual comparison as human perception is able to quickly determine the appropriate scale for comparison (Kuhnert et al. 2005). Quantitative synoptic validation is a clear improvement on qualitative validation techniques for 3-D modelling, as it provides the ability to establish a quantitative ranking (Kuhnert et al. 2005). This quantitative ranking is essential for the evaluation of model performance over large numbers of images.

The 1-D and 3-D models have niches suited to different time and space scales of interest. High real-time to run-time ratios of 1-D models make them readily applicable for long term simulations over periods of years to decades (e.g., Trolle et al. 2008; Trolle et al., 2011). By contrast, 3-D models, even those with a non-hydrostatic computational scheme, tend to have low real-time to run-time ratios and are best applied to addressing spatial variations on time scales of a few days to a few seasons (e.g., Leon et al. 2011; Huang et al. 2012). Application of 1-D models potentially allows a more robust calibration process through repeated calibration runs in which it is possible to ‘tune’ parameters to observations over time scales that capture seasonal and inter-annual variations. The parameters from the 1-D model can then potentially be used directly in 3-D model simulations with little or no recalibration. Romero et al. (2004) have demonstrated that ecological parameter configurations derived from calibration of a 1-D model (DYRESM-CAEDYM) could be applied with reasonable accuracy in a 3-D (ELCOM-CAEDYM) hydrodynamic-ecological model to simulate seasonal spatial dynamics of nitrogen and phosphorus in a meso-oligotrophic reservoir, but algal growth and particle resuspension/settling were re-calibrated specifically for the 3-D model application.

The 3-D model reproduced some of the basin-scale and fine-scale features of SM that were observed with MODIS imagery, but differences between the simulation and satellite estimation may have arisen from factors such as the accuracy of input data to the hydrodynamic model (e.g., Imberger et al. 1989). For example, basin-scale, wind-induced circulation currents depend on interactions of spatially and temporally varying wind-fields (Laval et al. 2003). In the case of the model application to Lake Ellesmere, the Birdlings flat weather station is located at the southern end of Banks Peninsula where the wind field may potentially be highly variable due to mesoscale topographic effects. In order to more accurately model surface circulation, wind data at several different locations on the lake would ideally be required. Here again, remote sensing may provide a cost-effective solution to investigate wind fields for large shallow lakes such as Ellesmere, as algorithms are emerging to derive high resolution wind vectors from Synthetic Aperture Radar (Vachon et al. 2000; Koch and Feser 2006).

The over-estimation by ELCOM-CAEDYM of SM concentrations in littoral areas may be a result of coarser sediments in these areas than those parameterised in the model application. In the application of the 3-D model used in this study, particle size distribution was assumed to be homogeneous across the lake and the model set-up does not allow for considerations of spatial variations in sediment properties. Sediment sorting and redistribution based on erosional, transportational and depositional environments across a lake bottom have been well documented for both in shallow and deep lakes (Hakanson 1982). In Lake Ellesmere, the littoral areas, and river-mouths in particular, represent relatively high-energy environments where sediment grain sizes are likely to be correspondingly coarse, particularly considering that there may be interacting effects of wave shear and river currents. Additionally, the composition of the sediments is not fixed and depends on the recent resuspension/deposition history resulting from temporal variations in wind speed and wind direction, which in turn affect sediment compaction (Einstein and Krone 1962; Lick et al. 1995).

Differences in the spatial distribution between simulated and satellite-estimated SM concentrations may be partly attributable to simplifications in the representation of waves in the simulation model. In shallow lakes the dominant resuspension mechanism is due to waves that create oscillatory motions and shear stress (Luettich et al. 1990; Scheffer 1998; Jin and Sun 2007). Horizontal currents may also be involved in the resuspension of sediments, however, the bottom shear stresses associated with these currents are usually too small in shallow lakes to affect suspended sediment concentrations substantially (Luettich et al. 1990; Bailey and Hamilton 1997). The estimation of waves in the 3-D model used in this study does not account for refraction, diffraction, shoaling, breaking, and wave-current interactions (Hamilton and Schladow 1997). The process of wave refraction tends to focus wave energy on headlands or protrusions, and disperses it in embayments (Komar 1998). This phenomenon could be responsible for the over-estimation of simulated SM concentrations in embayments in Lake Ellesmere. However, at the headland near the Selwyn River entrance, SM was over-estimated, which could be due to the high-energy environment in this region leading to coarser sediments that are more difficult to entrain into the water column. There exists the possibility to couple the 3-D hydrodynamic model ELCOM with a numerical wave model such as SWAN (Simulating Waves Nearshore) (Yajima, Tottori University, Japan, pers. comm). SWAN is a third generation spectral model developed at the Delft University of Technology, the Netherlands (http://www.swan.tudelft.nl), and is capable of simulating wave generation, dissipation and non-linear wave interactions including shoaling and refraction (Moeini 2009). The coupled 3-D model should in theory provide more accurate simulation of suspended mineral resuspension in shallow areas, especially in bays where wave refraction is occurring.

As in previous studies of sediment resuspension in Lake Ellesmere (Gerbeaux and Ward 1991; Hamilton and Mitchell 1996), the present study used a background concentration of sediment to represent fine material with very low settling velocities (which effectively remains in suspension continuously). Sediment cores taken in the main basin of Lake Ellesmere show that sediment in the upper 10 cm is comprised mostly of fine silt, with small fractions of clay and sand (Kitto 2010). Sediment cohesiveness and flocculation may therefore influence the critical shear stress for resuspension as well as the settling process. In contrast to modelling of resuspension of non-cohesive sediments, modelling of resuspension of cohesive sediments is far less advanced due to the difficulties of quantifying the complex interactions between hydrodynamics, inter-particle electrochemical attraction, and biological stabilisation or destabilisation. Bio-stabilisation induced from extracellular polymeric substances (EPS) produced by phytoplankton, in particular benthic diatoms and bacteria, has been shown to increase the critical shear stress of sediment (MacIntyre et al. 1990; Black et al. 2002; De Backer et al. 2010). At present no general analytical theory exists to account for sediment cohesiveness (Black et al. 2002), although significant progress has been made with empirical models (Lick and Lick 1988; Lick et al. 1994). The model used in this study does not account for sediment cohesiveness and flocculation, which may partly account for the post-storm deviation of SM measured in situ and that estimated by MODIS. Luettich et al. (1990) found the largest deviation between modelled and in situ suspended sediment concentrations occurred after resuspension events, when sediment settled faster in simulations than was observed. In this study, the opposite effect was observed in which in situ suspended minerals settled faster than what was simulated by the 1-D and 3-D models.

The sediment-water exchange of phosphorus is highly important in influencing the trophic state of shallow lakes (Scheffer 1998; de Vicente et al. 2006). Sediment resuspension exacerbates phosphorus internal loading and eutrophication. Internal loading can delay long-term recovery of trophic state in lakes following reductions in external loads (Søndergaard et al. 2007), especially in shallow eutrophic lakes such as Ellesmere. Lake level manipulation is possible in Lake Ellesmere and could be used as a means to reduce trophic status through reduction of sediment resuspension. Restoring a natural opening regime would result in less frequent but longer duration openings due to larger barrier breaches (Schallenberg et al. 2010) and higher water levels in Lake Ellesmere, which would reduce turbulent shear stress and sediment resuspension in the main body of water (Hamilton and Mitchell 1997). It has been suggested, however, that reduced suspended sediment concentrations would increase light availability to phytoplankton, resulting in increased phytoplankton biomass (Schallenberg et al. 2010). Maintaining the current lake level management regime limits the potential for macrophyte re-establishment due to high turbidity and shear stress (Gerbeaux 1993), however, locations estimated via remote sensing with consistently lower SM, could be used to identify focal areas for recovery of macrophytes either through re-planting or using barriers to reduce effects of wave action (Cook 2005). In the long term, however, reductions in external nutrient inputs are required to bring about a sustained improvement in water quality (Webster and Graham 2004). Processed-based lake models could be used to elucidate complex biological and physical interactions resulting from various lake opening regimes, the interactions of internal and external loads, and climate change, particularly in relation to alternate stable states (e.g., Webster and Graham 2004).

The bio-optical modelling approach used in this study was demonstrated to be applicable for the estimation of suspended sediment and minerals in Lake Ellesmere. It was demonstrated that the combination of remote sensing and modelling can greatly increase the spatial and temporal resolution of analysis and improve understanding of the causal factors leading to observed spatial distributions. The patterns of spatial variation of water quality divulged by 3-D models and remote sensing can aid in understanding ecosystem function and have applications in lake environmental management (Jorgensen 2008). However, the quantitative methods of 3-D comparison presented in this study highlighted clearly that improvement is needed in the both the 3-D simulation forcing data and the processes represented. Future improvements in model application can be evaluated quantitatively using the spatial statistics investigated in the present study.

4.6 References

Aurin, D. A., and H. M. Dierssen. 2012. Advantages and limitations of ocean color remote sensing in CDOM-dominated, mineral-rich coastal and estuarine waters. Remote Sensing of Environment **125**: 181–197.

Babin, M., A. Morel, V. Fournier-Sicre, F. Fell, and D. Stramski. 2003. Light scattering properties of marine particles in coastal and open ocean waters as related to the particle mass concentration. Limnology and Oceanography **48**: 843–859.

Bailey, M., and D. P. Hamilton. 1997. Wind induced sediment resuspension: a lake-wide model. Ecological Modelling **99**: 217–228.

Belzile, C., W. F. Vincent, C. Howard-Williams, I. Hawes, M. R. James, M. Kumagai, and C. S. Roesler. 2004. Relationships between spectral optical properties and optically active substances in a clear oligotrophic lake. Water Resources Research **40**: W12512.

Binding, C. E., J. H. Jerome, R. P. Bukata, and W. G. Booty. 2010. Suspended particulate matter in Lake Erie derived from MODIS aquatic colour imagery. International Journal of Remote Sensing **31**: 5239–5255.

Black, K. S., T. J. Tolhurst, D. M. Paterson, and S. E. Hagerthey. 2002. Working with natural cohesive sediments. Journal of Hydraulic Engineering **128**: 2–8.

Bloesch, J. 1995. Mechanisms, measurement and importance of sediment resuspension in lakes. Marine and Freshwater Research **46**: 295–304.

Bowers, D. G., and C. E. Binding. 2006. The optical properties of mineral suspended particles: A review and synthesis. Estuarine, Coastal and Shelf Science **67**: 219–230.

Bowers, D. G., S. Boudjelas, and G. E. L. Harker. 1998. The distribution of fine suspended sediments in the surface waters of the Irish Sea and its relation to tidal stirring. International Journal of Remote Sensing **19**: 2789–2805.

Brando, V. E., A. G. Dekker, Y. J. Park, and T. Schroeder. 2012. Adaptive semianalytical inversion of ocean color radiometry in optically complex waters. Applied Optics **51**: 2808–33.

Brando, V. E., and A. G. Dekker. 2003. Satellite hyperspectral remote sensing for estimating estuarine and coastal water quality. IEEE Transactions on Geoscience and Remote Sensing **41**: 1378–1387.

Briggs, W., and R. Levine. 1997. Wavelets and field forecast verification. Monthly Weather Review **125**: 1329–1341.

Brunsdon, C., A. S. Fotheringham, and M. E. Charlton. 1996. Geographically weighted regression: a method for exploring spatial nonstationarity. Geographical Analysis **28**: 281–298.

Campbell, G., S. R. Phinn, A. G. Dekker, and V. E. Brando. 2011. Remote sensing of water quality in an Australian tropical freshwater impoundment using matrix inversion and MERIS images. Remote Sensing of Environment **115**: 2402–2414.

Campbell, G., S. Phinn, and P. Daniel. 2011b. The specific inherent optical properties of three sub-tropical and tropical water reservoirs in Queensland, Australia. Hydrobiologia **658**: 233–252.

Casulli, V., and R. T. Cheng. 1992. Semi-implicit finite difference methods for three-dimensional shallow water flow. International Journal for Numerical Methods in Fluids **15**: 629–648.

Cole, P., and G. V. Miles. 1983. Two dimensional model of mud transport. Journal of Hydraulic Engineering **109**: 1–12.

Cooke, G. D., Welch, E. B., Peterson, S. A., and S.A. Nichols. 2005. Restoration and Management of Lakes and Reservoirs. Third edition. Taylor and Francis, Boca Raton, USA.

De Backer, A., C. Van Colen, M. Vincx, and S. Degraer. 2010. The role of biophysical interactions within the ijzermonding tidal flat sediment dynamics. Continental Shelf Research **30**: 1166–1179.

de Vicente, I., V. Amores, and L. Cruz-Pizarro. 2006. Instability of shallow lakes: A matter of the complexity of factors involved in sediment and water interaction? Limnetica **25**: 253–270.

Dekker, A. G. 1993. Detection of optical water quality parameters for eutrophic waters by high resolution remote sensing. Ph.D. thesis. Free University of Amsterdam, The Netherlands.

Dekker, A. G., H. J. Hoogenboom, L. M. Goddijn, and T. J. M. Malthus. 1997. The relation between inherent optical properties and reflectance spectra in turbid inland waters. Remote Sensing Reviews **15**: 59–74.

Dekker, A. G., R. J. Vos, and S. W. M. Peters. 2002. Analytical algorithms for lake water TSM estimation for retrospective analyses of TM and SPOT sensor data. International Journal of Remote Sensing **23**: 15–35.

Doerffer, R., and H. Schiller. 2007. The MERIS Case 2 water algorithm. International Journal of Remote Sensing **28**: 517–535.

Doxaran, D., J. Froidefond, S. Lavender, and P. Castaing. 2002. Spectral signature of highly turbid waters Application with SPOT data to quantify suspended particulate matter concentrations. Remote Sensing of Environment **81**: 149–161.

Doxaran, D., J. M. Froidefond, P. Castaing, and S. M. J. Babin. 2009. Dynamics of the turbidity maximum zone in a macrotidal estuary (the Gironde, France): Observations from field and MODIS satellite data. Estuarine Coastal and Shelf Science **81**: 321–332.

Einstein, H. A., and R. B. Krone. 1962. Experiments to determine modes of cohesive sediment transport in salt water. Journal of Geophysical Research **67**: 1451–1461.

Eleveld, M. A., R. Pasterkamp, H. J. van der Woerd, and J. D. Pietrzak. 2008. Remotely sensed seasonality in the spatial distribution of sea-surface suspended particulate matter in the southern North Sea. Estuarine, Coastal and Shelf Science **80**: 103–113.

Fischer, J. 1979. Modelling of water quality processes in lakes and reservoirs. Hydrological Sciences **24**: 157–160.

Fotheringham, A. S., M. Charlton, and C. Brunsdon. 1996. The geography of parameter space: an investigation of spatial non-stationarity. International Journal of Geographical Information Science **10**: 605-627.Gal, G., M. R. Hipsey, A. Parparov, U. Wagner, V. Makler, and T. Zohary. 2009. Implementation of ecological modeling as an effective management and investigation tool: Lake Kinneret as a case study. Ecological Modelling **220**: 1697–1718.

Gerbeaux, P. 1993. Potential for re-establishment of aquatic plants in Lake Ellesmere. Journal of Aquatic Plant Management **31**: 122–128.

Gerbeaux, P., and J. C. Ward. 1991. Factors affecting water clarity in Lake Ellesmere, New Zealand. New Zealand Journal of Marine and Freshwater Research **25**: 289–296.

Gons, H., T. Burger-Wiersma, J. Otten, and M. Rijkeboer. 1992. Coupling of phytoplankton and detritus in a shallow, eutrophic lake (Lake Loosdrecht, The Netherlands). Hydrobiologia **233**: 51–59.

Gordon, H. R., and M. Wang. 1994. Retrieval of water-leaving radiance and aerosol optical thickness over the oceans with SeaWiFS: a preliminary algorithm. Applied Optics **33**: 443–452.

Gordon, H. R., J. W. Brown, O. B. Brown, R. H. Evans, and R. C. Smith. 1988. A semianalytic radiance model of ocean color. Journal of Geophysical Research **93**: 10909–10924.

Gould, R. W., R. A. Arnone, and M. Sydort. 2001. Absorption , Scattering , and Remote-Sensing Reflectance Relationships in Coastal Waters : Testing a New Inversion Algorithm. Journal of Coastal Research **17**: 328–341.

Hagen, A. 2003. Fuzzy set approach to assessing similarity of categorical maps. International Journal of Geographical Information Science **17**: 235–249.

Hagen-Zanker, A. 2006. Map Comparison Kit: Beta extension for continuous valued data. Research Institute for Knowledge Systems (RIKS), Maastricht, Netherlands.

Hakanson, L. 1982. Bottom dynamics in lakes. Hydrobiologia **91**: 9–22.

Hamilton, D. P., and S. F. Mitchell. 1996. An empirical model for sediment resuspension in shallow lakes. Hydrobiologia **317**: 209–220.

Hamilton, D. P., and S. Mitchell. 1997. Wave-induced shear stresses, plant nutrients and chlorophyll in seven shallow lakes. Freshwater Biology **38**: 159–168.

Hamilton, D. P., and S. G. Schladow. 1997. Prediction of water quality in lakes and reservoirs. Part I - Model description. Ecological Modelling **96**: 91–110.

Hedger, R. D., N. R. B. Olsen, T. J. Malthus, and P. M. Atkinson. 2002. Coupling remote sensing with computational fluid dynamics modelling to estimate lake chlorophyll-a concentration. Remote Sensing of Environment **79**: 116–122.

Hemmingsen, M. A. 1997. The coastal geomorphology of Te Waihora (Lake Ellesmere). Ph.D. thesis. University of Canterbury, New Zealand.

Hipsey, M. R., and D. P. Hamilton. 2008. Computational Aquatic Ecosystem Dynamics Model: CAEDYM v3.3 Science Manual. Centre for Water Research, University of Western Australia, Perth, Australia.

Hodges, B., and C. Dallimore. 2007. Estuary, Lake and Coastal Ocean Model: ELCOM, v2.2 User Manual. Centre for Water Research, University of Western Australia, Perth, Australia.

Horppila, J., and L. Nurminen. 2003. Effects of submerged macrophytes on sediment resuspension and internal phosphorus loading in Lake Hiidenvesi (southern Finland). Water Research **37**: 4468-4474.

Horrell, G. A. 1992. Lake Ellesmere water balance model: variable analysis and evaluation. M.Sc. thesis. University of New South Wales, Australia.

Hu, C., Z. Chen, T. D. Clayton, P. Swarzenski, J. C. Brock, and F. E. Muller-Karger. 2004. Assessment of estuarine water-quality indicators using MODIS medium-resolution bands: Initial results from Tampa Bay, FL. Remote Sensing of Environment **93**: 423–441.

Huang, J., J. Gao, and G. Hörmann. 2012. Hydrodynamic-phytoplankton model for short-term forecasts of phytoplankton in Lake Taihu, China. Limnologica **42**: 7–18.

Hughes, H. R., R. H. S. McColl, and D. J. Rawlence. 1974. Lake Ellesmere, Canterbury, New Zealand. A review of the lake and its catchment. DSIR Information Series No. 99, Wellington, New Zealand.

Imberger, J., J. C. Patterson, and W. H. and T. Y. W. John. 1989. Physical limnology. Advances in Applied Mechanics **27**: 303–475

Imerito, A. 2007. Dynamic Reservoir Simulation Model DYRESM v4.0 Science Manual. Centre for Water Research, University of Western Australia, Perth, Australia.

Jin, K-R., and D. Sun. 2007. Sediment resuspension and hydrodynamics in Lake Okeechobee during the late summer. Journal of Engineering Mechanics **133**: 899–910.

Jorgensen, S. 2008. Overview of the model types available for development of ecological models. Ecological Modelling **215**: 3–9.

Kirk, K. L., and J. J. Gilbert. 1990. Suspended clay and the population dynamics of planktonic rotifers and cladocerans. Ecology **71**: 1741–1755.

Kitto, S. G. 2010. The Environmental History of Te Waihora – Lake Ellesmere. Ph.D. thesis. University of Canterbury, Christchurch, New Zealand.

Koch, W., and F. Feser. 2006. Relationship between SAR-derived wind vectors and wind at 10-m height represented by a mesoscale model. Monthly Weather Review **134**: 1505–1517.

Komar, P. D. 1998. Beach Processes and Sedimentation, 2nd ed. Prentice-Hall, Englewood Cliffs, New Jersey, USA.

Kuhnert, M., A. Voinov, and R. Seppelt. 2005. Comparing raster map comparison algorithms for spatial modeling and analysis. Photogrammetric Engineering and Remote Sensing **71**: 975–984.

Kutser, T., and L. Metsamaa. 2007. Operative monitoring of the extent of dredging plumes in coastal ecosystems using MODIS satellite imagery. Journal of Coastal Research **50**: 180–184.

Laval, B., J. Imberger, and B. Hodges. 2003. Modeling circulation in lakes: Spatial and temporal variations. Limnology and Oceanography **48**: 983–994.

Lee, Z., K. L. Carder, and R. A. Arnone. 2002. Deriving inherent optical properties from water color: a multiband quasi-analytical algorithm for optically deep waters. Applied Optics **41**: 5755–5772.

Lee, Z., K. L. Carder, C. D. Mobley, R. G. Steward, and J. S. Patch. 1998. Hyperspectral remote sensing for shallow waters. I. A semianalytical model. Applied Optics **37**: 6329–6338.

Leon, L. F., R. E. H. Smith, M. R. Hipsey, S. A. Bocaniov, S. N. Higgins, R. E. Hecky, J. P. Antenucci, J. A. Imberger, and S. J. Guildford. 2011. Application of a 3-D hydrodynamic–biological model for seasonal and spatial dynamics of water quality and phytoplankton in Lake Erie. Journal of Great Lakes Research **37**: 41–53.

Leonard, B. P. 1991. The ULTIMATE conservative difference scheme applied to unsteady one-dimensional advection. Computer Methods in Applied Mechanics and Engineering **88**: 17–74.

Li, L., L. Li, K. Song, Y. Li, L. P. Tedesco, K. Shi, and Z. Li. 2013. An inversion model for deriving inherent optical properties of inland waters: Establishment, validation and application. Remote Sensing of Environment **135**: 150–166.

Lick, W., and J. Lick. 1988. Aggregation and disaggregation of fine-grained lake sediments. Journal of Great Lakes Research **14**: 514–523.

Lick, W., J. Lick, and C. Kirk Ziegler. 1994. The resuspension and transport of fine-grained sediments in Lake Erie. Journal of Great Lakes Research **20**: 599–612.

Lick, W., Y.-J. Xu, and J. McNeil. 1995. Resuspension properties of sediments from the Fox, Saginaw, and Buffalo Rivers. Journal of Great Lakes Research **21**: 257–274.

Lubac, B., and H. Loisel. 2007. Variability and classification of remote sensing reflectance spectra in the eastern English Channel and southern North Sea. Remote Sensing of Environment **110**: 45–58.

Luettich, R. A., D. R. F. Harleman, and L. Somlyody. 1990. Dynamic behaviour of suspended sediment concentrations in a shallow lake perturbed by episodic wind events. Limnology and Oceanography **35**: 1050–1067.

MacIntyre, S., W. Lick, and C. H. T. Han Tsai. 1990. Variability of entrainment of cohesive sediments in freshwater. Biogeochemistry **9**: 187–209.

Maritorena, S., D. A Siegel, and A. R. Peterson. 2002. Optimization of a semianalytical ocean color model for global-scale applications. Applied optics **41**: 2705–14.

Matthews, M. 2011. A current review of empirical procedures of remote sensing in inland and near-coastal transitional waters. International Journal of Remote Sensing **32**: 6855–6899.

Miller, R. L., and B. A. McKee. 2004. Using MODIS Terra 250 m imagery to map concentrations of total suspended matter in coastal waters. Remote Sensing of Environment **93**: 259–266.

Mobley, C. D. 1994. Light and Water, Radiative Transfer in Natural Waters. Academic Press, San Diego, USA.

Moeini, M. H. 2009. Wave parameter hindcasting in a lake using the SWAN model. Iranica Scientia **16**: 156–164.

Morel, A. 1974. Optical properties of pure water and pure seawater, p. 1–24. In N.G. Jerlov and E. Steemann Nielsen [eds.], Optical Aspects of Oceanography. Academic Press, London, England.

Morel, A. 1980. In-water and remote measurements of ocean color. Boundary-Layer Meteorology **18**: 177–201.

Morel, A., and L. Prieur. 1977. Analysis of variations in ocean color. Limnology and Oceanography **22**: 709–722.

Morel, A., D. Antoine, and B. Gentili. 2002. Bidirectional reflectance of oceanic waters: accounting for Raman emission and varying particle scattering phase function. Applied Optics **41**: 6289–6306.

Nechad, B., K. G. Ruddick, and Y. Park. 2010. Calibration and validation of a generic multisensor algorithm for mapping of total suspended matter in turbid waters. Remote Sensing of Environment **114**: 854–866.

O’Sullivan, D., and D. Unwin. 2002. Geographic Information Analysis. Wiley, Hoboken, N.J., USA.

Petzold, T.J. 1972. Volume scattering functions for selected ocean waters, p. 150–174. *In* , J.E. Tyler [ed.], Light in the Sea. University of Hawaii Press, Honolulu, Hawaii.

Pope, R. M., and E. S. Fry. 1997. Absorption spectrum (380-700 nm) of pure water. II. Integrating cavity measurements. Applied Optics **36**: 8710–8723.

Reilly, C., P. Price, A. Gelman, and S. A Sandgathe. 2004. Using image and curve registration for measuring the goodness of fit of spatial and temporal predictions. Biometrics **60**: 954–64.

Romero, J. R., J. P. Antenucci, and J. Imberger. 2004. One- and three-dimensional biogeochemical simulations of two differing reservoirs. Ecological Modelling **174**: 143–160.

Ruddick, K. G., V. De Cauwer, Y.-J. Park, and G. Moore. 2006. Seaborne measurements of near infrared water-leaving reflectance: The similarity spectrum for turbid waters. Limnology and Oceanography **51**: 1167–1179.

Santini, F., L. Alberotanza, R. M. Cavalli, and S. Pignatti. 2010. A two-step optimization procedure for assessing water constituent concentrations by hyperspectral remote sensing techniques: An application to the highly turbid Venice lagoon waters. Remote Sensing of Environment **114**: 887–898.

Schallenberg, M., S. T. Larned, S. Hayward, and C. Arbuckle. 2010. Contrasting effects of managed opening regimes on water quality in two intermittently closed and open coastal lakes. Estuarine, Coastal and Shelf Science **86**: 587–597.

Scheffer, M. 1998. Ecology of Shallow Lakes. Chapman and Hall, London, UK.

Schroeder, T., M. Schaale, and J. Fischer. 2007. Retrieval of atmospheric and oceanic properties from MERIS measurements: A new Case-2 water processor for BEAM. International Journal of Remote Sensing **28**: 5627–5632.

Sheng, Y. P., and W. Lick. 1979. The transport and resuspension of sediments in a shallow lake. Journal Geophysical Research **84**: 1809–1826.

Sipelgas, L., V. Ossipova, U. Raudsepp, and Antti Lindfors. 2009. A bio-optical model for the calculation of suspended matter concentration from MODIS data in the Pakri Bay, the Gulf of Finland. Boreal Environment Research **14**: 415–426.

Søndergaard, M., E. Jeppesen, T. L. Lauridsen, C. Skov, E. H. van Nes, R. Roijackers, E. Lammens, and R. Portielje. 2007. Lake restoration: successes, failures and long-term effects. Journal of Applied Ecology **44**: 1095–1105.

Søndergaard, M., P. Kristensen, and E. Jeppesen. 1992. Phosphorus release from resuspended sediment in the shallow and wind-exposed Lake Arresø, Denmark. Hydrobiologia **228**: 91–99.

Spillman, C. M., J. Imberger, D. P. Hamilton, M. R. Hipsey, and J. R. Romero. 2007. Modelling the effects of Po River discharge, internal nutrient cycling and hydrodynamics on biogeochemistry of the Northern Adriatic Sea. Journal of Marine Systems **68**: 167–200.

Sturm, B. 1981. The atmospheric correction of remotely sensed data and the quantitative determination of suspended matter in marine water surface layers. *In* A.P. Cracknell [ed.] Remote Sensing in Meteorology Oceanography and Hydrology. Ellis Horwood, Chichester, London.

Trolle, D., D. P. Hamilton, C. A. Pilditch, I. C. Duggan, and E. Jeppesen. 2011. Predicting the effects of climate change on trophic status of three morphologically varying lakes: Implications for lake restoration and management. Environmental Modelling and Software **26**: 354–370.

Trolle, D., T. Jorgensen, and E. Jeppesen. 2008. Predicting the effects of reduced external nitrogen loading on the nitrogen dynamics and ecological state of deep

Lake Ravn, Denmark, using the DYRESM–CAEDYM model. Limnologica **38**: 220–232.

Twardowski, M. S., E. Boss, J. B. Macdonald, W. S. Pegau, A. H. Barnard, and J. R. V. Zaneveld. 2001. A model for estimating bulk refractive index from the optical backscattering ratio and the implications for understanding particle composition in case I and case II waters. Journal of Geophysical Research **106**: 14129.

Tzortziou, M., J. R. Herman, C. L. Gallegos, P. J. Neale, A. Subramaniam, L. W. Harding, and Z. Ahmad. 2006. Bio-optics of the Chesapeake Bay from measurements and radiative transfer closure. Estuarine, Coastal and Shelf Science **68**: 348–362.

Vachon, P. W., P. Adlakha, H. Edel, M. Henschel, B. Ramsay, D. Flett, M. Rey, G. Staples, and S. Thomas. 2000. Canadian progress toward marine and coastal applications of synthetic aperture radar. Johns Hopkins APL Technical Digest **21**: 33–40.

Vermote, E. F., N. El Saleous, C. O. Justice, Y. J. Kaufman, J. L. Privette, L. Remer, J. C. Roger, and D. Tanr. 1997. Atmospheric correction of visible to middle-infrared EOS-MODIS data over land surfaces: Background , operational algorithm and validation. Journal of Geophysical Research **102**: 17131–17141.

Vidot, J., and R. Santer. 2005. Atmospheric correction for inland waters—application to SeaWiFS. International Journal of Remote Sensing **26**: 3663–3682.

Visser, H., and T. de Nijs. 2006. The Map Comparison Kit. Environmental Modelling & Software 21: 346–358.

Webster, I. T., and P. H. Graham. 2004. Anthropogenic impacts on the ecosystems of coastal lagoons: modelling fundamental biogeochemical processes and management implications. Marine and Freshwater Research **55**: 67–78.

Wunderlich, W. O. 1972. Heat and Mass Transfer between a Water Surface and the Atmosphere. Water resources research laboratory report no. 14, Tennessee Valley Authority, Division of Water Control Planning, USA.

5 Optimization of a semi-analytical model for remote sensing of chlorophyll *a* and suspended sediments in a large, oligotrophic lake

5.1 Introduction

High spectral resolution sensors used for remote sensing of reflectance from waterbodies, such as the Moderate Resolution Imaging Spectroradiometer (MODIS), may be used to infer surface values for optically active water quality variables (Becker et al. 2009; Binding et al. 2010; Horion et al. 2010). The high satellite revisit capability (twice daily), moderate spatial resolution (1 km and 250 m) and appropriate spectral resolution have input data for the bio-optical modelling of inland waters (Xiaoyu et al. 2005). Therefore in Case 2 waters bio-optical algorithms can then be used to allow estimation of the optically active water quality variables.

Inversion of bio-optical models requires a measure of irradiance reflectance or remote sensing reflectance above or just below the water surface, which requires some form of atmospheric correction. Atmospheric path radiance measured by Earth observation satellites can comprise 90% contribution of total radiance over water, which originates from scattering of solar radiation by air molecules and aerosols (suspended liquid and particles such as salt, dust, ash, pollen and sulphuric acid) (Vidot and Santer 2005). The application of radiative transfer models used to correct for variations in atmospheric attenuation offers the flexibility to address the complexities of atmospheric correction over inland waters (e.g., Campbell et al. 2011). Such complexities include variations in elevation, which affects molecular calculations due to changes in air pressure, adjacency effects, and heterogeneous concentrations of aerosols and aerosol content at coastal and inland locations. However, it is often assumed that aerosol optical depth (AOD) is homogenous at spatial scales of 50 to 100 km (Vidot and Santer 2005), which is a spatial scale comparable to the maximum size of most lakes.

The colour and clarity of water depend on its optical character, and relate to the bulk optical processes of absorption and scattering. Absorption refers to the transfer of light into another form of energy (e.g., heat) and is quantified by the absorption coefficient, $a(\lambda)$, which is the fraction of incident light absorbed divided by the thickness of the layer. Scattering is defined as the change in deflection of photons from their original path (Davies-Colley et al. 1993), and is quantified by the scattering coefficient, $b(\lambda)$, which is the fraction of the incident light scattered divided by the thickness of the layer (Kirk 2010). These two variables are referred to as inherent optical properties (IOPs) as they are dependent on the concentration and specific IOPs of optically active substances comprising the aquatic medium (which are independent of the ambient light field). In contrast apparent optical properties (AOPs) depend on the geometric structure of the light field (Kirk 2010), which are partly determined by the solar zenith angle and local atmospheric conditions (Bukata et al. 1995).

Light absorption by pure water increases exponentially towards longer wavelengths of the electromagnetic spectrum, whilst scattering increases at shorter wavelengths of the visible near-infrared range (Rudorff et al. 2006). Clear lake water possesses a spectral reflectance that is similar to pure water. Algae-laden water exhibits a reflectance peak in the green region, which represents an aggregate absorption minimum, and another reflectance peak at 700 nm. Absorption troughs occur in the blue and red/infrared wavelengths (Han 1997), with the exact location and width of these troughs dependent on phytoplankton species' assemblages and their physiological state (Kirk 2010). Suspended minerals (SM) include sand, silt, clay and other inorganic material such as atmospheric dust (Koponen 2006) and their optical absorption and scattering properties are affected by the shape and size distribution of particles (Bukata et al. 1995). In clear water, increasing concentrations of SM result in a near-linear increase in reflectance in the infra-red region. In this area of the electromagnetic spectrum the effect of chl *a* on reflectance is negligible (Han 1997). In algae-laden water, however, SM adds to reflectance at all wavelengths (Bukata et al. 1995). Coloured dissolved organic matter (CDOM) shows exponentially increasing absorption at shorter wavelengths (< c. 500 nm) and little absorption above 700 nm (Bricaud et al. 2009). The effect of CDOM on light scattering can largely be ignored (Koponen 2006).

Analytical bio-optical models relate water subsurface reflectance to the concentration and IOPs of optically active constituents (OACs) and the IOPs of water itself. Different techniques have been used for solving these analytical models including Monte Carlo methods (Gordon and Brown 1973; Morel and Prieur 1977; Kirk 1981), the invariant embedding technique (Preisendorfer 1976; Mobley 1994), the matrix operator method (Fischer and Grassl 1984; Fell and Fischer 2001), and the finite-element method (Kisselev et al. 1995; Bulgarelli et al. 1999). More recently, ocean colour algorithms have been implemented, focusing on optically-complex Case 2 waters (Lee and Carder 2004). Many of these models are based on the assumption that pigment-specific particulate absorption is invariant. However, IOPs vary temporally and spatially (Kostadinov et al. 2010; Devred et al. 2011; Moisan et al. 2011). Variance in the specific chlorophyll absorption coefficient ($a^*_{\phi}(\lambda)$), for example, is based on many factors including phytoplankton pigment composition, cell size, the packaging effect, light accumulation and nutrient limitation (Sathyendranath et al. 1987; Bricaud et al. 1995).

The MODIS satellite has two bands at 250 m resolution in the red and near infra-red wavelengths. Whilst having broader bandwidths and lower spectral sensitivity than MODIS 1 km resolution bands, data at 250 m resolution has proven useful in monitoring total suspended sediment (SS) concentration (Doxoran et al. 2009), and has potential to monitor chl *a* concentrations during algal blooms (Reinart et al. 2006). Kopenen et al. (2004) found MODIS B1 was applicable to estimate general measures of water quality such as trophic state, rather than for monitoring CDOM and chl *a* (Koponen et al. 2006). High spectral resolution MODIS bands are more suitable for remote sensing of chl *a* than MODIS B1 and B2. For example, Gitelson et al. (2008) developed a simple semi-analytical model for estimation of chl *a* in turbid waters, based on three bands of MEdium Resolution Imaging Spectrometer (MERIS) or two bands of MODIS Aqua/Terra. Their algorithm has proved applicable for waters with chl *a* ranging from 10-200 µg L^{-1}, however, in oligotrophic lakes the near-infrared (NIR) reflectance peak critical to algorithm function is not present (Giardino et al. 2007; Odermatt et al. 2008). For the estimation of low chl *a* concentrations in inland waters, more complex, physically-based inversion models are needed (Odermatt et al. 2008).

The specific IOPs Lake Taupo are now known (Belzile et al. 2004), which presents an opportunity to investigate bio-optical modelling to enable future remote sensing based near-real time monitoring of OACs. The objective of this study was to develop algorithms to determine chl *a*, CDOM absorption, and SS using subsurface remote sensing reflectance derived from MODIS Aqua. A further objective was to parameterise the bio-optical model across seasons based on the different absorption properties of the seasonally-varying dominant phytoplankton groups, in order to refine estimations of chl *a* as a proxy for total phytoplankton biomass. Finally, this study will investigate the relationship between bio-optical estimated SS (1 km resolution) and MODIS Terra/Aqua B1 remote sensing reflectance (250 m resolution). If relationships can be developed which enable estimation of SS at 250 m, the enhanced resolution of monitoring may enable the future study of lake inflow effects on circulation and mixing.

5.2 Methods

Study site

Lake Taupo (Figure 5.1(a)) (area = 616 km^2, mean depth 97 m) is located in a caldera created by a super-volcanic eruption which occurred 26 500 yr BP. The present lake was formed after the last massive eruption in 186 AD. Its major inflows are from the Tongariro River and Tokaano Tailrace (a hydropower diversion of the Tongariro River) at the south end of the lake (Figure 5.1(b)). Annual average flow rate in the Tongariro River is 29.2 m^3 s^{-1} and 49.7 m^3 s^{-1} in the Tokaano Tailrace. The latter flow is highly variable depending on power generation by the Tokaano hydropower plant. The outflow is to the Waikato River in the northeast.

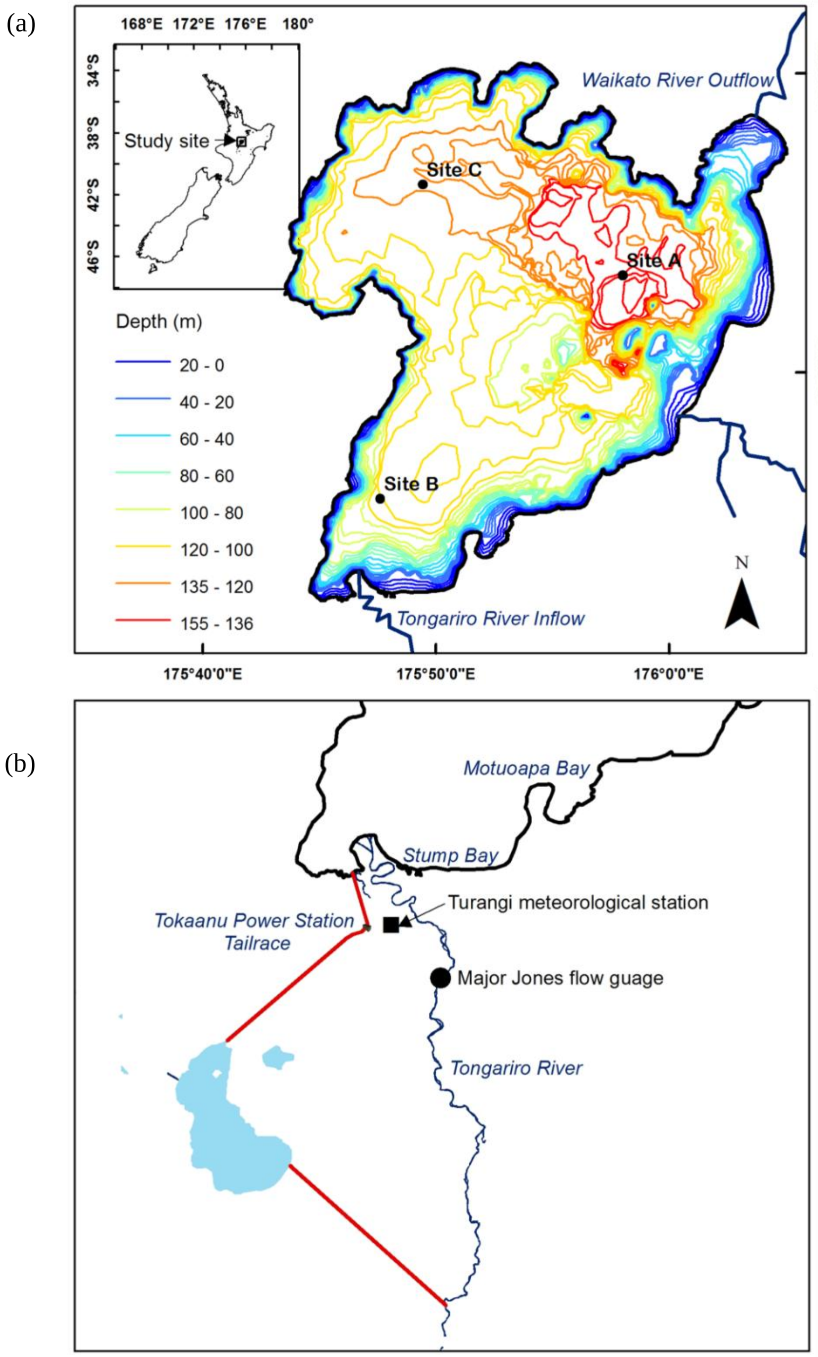

Figure 5.1. Lake Taupo study site. (a) Sites A , B and C represent water quality monitoring stations used in this study and bathymetry contours (m) are shown as a colour gradient from blue (shallow) to red (deep). (b) Tongariro/Tokaanu inflows and locations of Turangi meteorological station and Tongariro flow gauge at Major Jones.

Lake Taupo is in a mid-temperate zone (38°50’0”S latitude) but seasonal variations in phytoplankton biomass and productivity are considered to be similar to those of sub-tropical lakes, with maxima occurring during winter isothermy (Vincent 1983).

The winter production maxima is thought to be stimulated by increased availability of nutrients, particularly nitrate and ammonium, as nitrogen tends to most strongly limit phytoplankton productivity in the lake (White et al. 1980). Decreased grazing pressure in winter, when the lake is mixed, may also contribute to this phenomenon (Vincent 1983). Chlorophyll *a* is increasing at a rate of 0.021 ± 0.015 (95% confidence limit) µg L^{-1} y^{-1} in the upper 10 m of the water column (Gibbs 2011).

Methods overview

This study used 23 MODIS Aqua images captured from 13 Aug 2003 to 8 Jul 2008. Atmospheric correction was achieved using a radiative transfer model. The Garver-Seigel-Maritorena 2001 (GSM01) bio-optical model (Maritorena et al. 2002) was optimised using in situ IOPs specific for Lake Taupo (Belzile et al. 2004) and then inverted to determine chl *a*, CDOM absorption, and SS, using MODIS Aqua bands 8-12. The bio-optical algorithm used two specific phytoplankton absorption curves, for each seasonally dominant phytoplankton phyla observed in Lake Taupo (Gibbs 2011), with concurrent field chl *a* concentrations used for algorithm validation. Further investigation into flood event commencing on the 28th of February 2004 was carried out, using empirical relationships developed between MODIS subsurface remote sensing reflectance (250 m resolution) and SS estimated from the bio-optical model (1 km resolution) to estimate SS at 250 m resolution on the 4th and 5th of March 2004. Also in relation to the flood event, Secchi depth measurements were available from Site A and B from November 2003 to June 2004 (Gibbs 2011). Coinciding with the flood event, wind speed from a nearby weather station and thermistor chain data (Site B, Figure 5.1(a)) from 13 January 2004 to 8 March 2004 were available, as were flows from the Tongariro River (refer to Figure 5.1(b)) for the period 27 February to 6 March 2004.

Field data

Phytoplankton biomass, water clarity and nutrient concentrations have been monitored Site A (Figure 5.1(a)) monthly since 1994 (Taupo Long Term Monitoring Programme, TLTMP). This study made use of monthly 0-10 m integrated chl *a* concentrations, usually taken from Site A (Figure 5.1(a)) corresponding satellite overpass date of MODIS Aqua (August 2003 to July 2008). Algal species composition and abundance were available (Gibbs 2011), determined using the sedimentation procedure (Utermöhl 1931) with up to 100-ml samples and enumeration using an inverted microscope. Biovolume was estimated from cell dimensions of each species and dominance was estimated from relative biovolumes (Gibbs 2011). Additional sites (B and C; Figure 5.1(a)) were monitored between January 2002 and December 2004. Secchi depth measurements were available from Site A and B from November 2003 to June 2004 (Gibbs 2011).

Over the study period (13 Aug 2003 to 8 Jul 2008), the phytoplankton assemblage at Site A included Cyanophytes, Bacillariophytes, Chlorophytes, Chrysophytes, and Dinophytes. Often all of these taxa coexisted, however, dominance or co-dominance usually varied with season. In summer the dominant species were Chlorophytes and Chrysophytes, in particular *Botryococcus braunii* and *Dinobryon* sp. Cyanophytes were usually present at low levels, however, they dominated in late summer and early autumn 2006 (mostly *Aphanizomenon gracile* and *Anabaena sp*.). Bacillariophytes were also present at low levels throughout summer. In autumn the assemblage was dominated by Chlorophytes (*Botryococcus braunii)* and Chrysophytes (*Dinobryon* sp.). Of note was that the Cyanophyte *Anabaena flos-aquae* was a major component of the assemblage between April and June 2005 and became dominant in May. In winter Bacillariophytes dominated, mainly *Asterionella formosa* (dominant in 2003 and 2006), *Aulacoseira granulata* (dominant in 2005), and *Fragilaria crotonensis.* In spring there was a return of Chlorophytes and Chrysophytes in moderate densities, and to a lesser extent Cyanophytes, however, Bacillariophytes were often still dominant, especially *Asterionella formosa* and *Aulacoseira granulata* (Gibbs 2004, 2005, 2007, 2008, 2009).

Wind speed data from 13 January 2004 to 8 March 2004 were taken from National Institute of Water and Atmosphere (NIWA) weather station at Turangi (Figure 5.1(b), (-38.9753°S, 175.7908° E); 2.6 km south of Lake Taupo. Flows from the Tongariro River (refer to Figure 5.1(b)) were measured by Genesis Energy at

Turangi (Major Jones Pool shown in Figure 5.1(b)) for the period 27 February to 6 March 2004.

Satellite imagery

Twenty-three MODIS Aqua (1 km resolution) images were obtained during a period from 13 August 2003 to 8 July 2008. For validation of satellite estimated chl *a*, eight in situ samples were taken on the day of image capture, three samples were within one day of image capture and nine within five days of image capture. The remaining three images had in situ samples that were taken 7, 8 and 19 days apart from the day of image capture. For images captured > 3 d from the date of the in situ sample, images were selected during time periods in between monthly sampling dates when chl *a* concentrations varied by ≤ 0.03 µg L^{-1}, with the assumption of low variation between these dates. MODIS Aqua and Terra imagery at 250 m resolution was obtained on 4 and 5 March 2004 (four images), and B1 was used to develop an algorithm to estimate SS concentrations.

Atmospheric correction

All images were converted from radiance to subsurface remote sensing reflectance, using the radiative transfer atmospheric correction model *Second Simulation* of a *Satellite* Signal in the *Solar Spectrum* (6sv) (Kotchenova et al. 2008) and parameterised with concurrent MODIS atmosphere data including water vapour and ozone concentration. Estimation of aerosol optical depth (AOD) is the most challenging of the parameters required to assist with atmospheric correction. For New Zealand conditions AOD measured at Lauder (860 km south-west of Lake Taupo, South Island, NZ) is among the lowest recorded globally, ranging from about 0.01 to 0.08 (Liley and Forgan 2009). However, AOD over Lake Taupo may deviate significantly from this. The error in AOD retrieval by MODIS is comparable to the actual levels of AOD commonly recorded at Lauder, New Zealand. The global validation of MODIS AOD error over land, ε, is given as:

$$\varepsilon = \pm 0.03 + 0.05\ \mathrm{AOD} \qquad \text{(Remer et al. 2005)} \qquad (2.1)$$

AOD is likely to be higher in Taupo, but would likely still be low relative to global measurements. Considering the uncertainty in AOD retrieval over Lake Taupo, AOD was fixed at 0.05 for this study (the upper limit of the manly average measured at Lauder). A horizontally homogeneous atmosphere was assumed across Lake Taupo for each image used in this study.

Bio-optical model

A semi-analytical bio-optical inversion model (Gordon et al. 1988) was optimised with locally derived absorption and scattering coefficients from Lake Taupo (Belzile et al. 2004), and additional values from the literature discussed below:

$$r_{rs}(\lambda) = \sum_{i=1}^{2} li \left[\frac{b_b(\lambda)}{b_b(\lambda) + a(\lambda)} \right]^i \tag{5.2}$$

where $r_{rs}(\lambda)$ = subsurface remote sensing reflectance, $b_b(\lambda)$ is the total backscattering, $a(\lambda)$ is total absorption, λ is the wavelength, with $l_1 = 0.0949\ sr^{-1}$ and $l_2 = 0.0794\ sr^{-1}$ taken from Gordon et al. (1988) (applicable to waters with $b_b(\lambda)/\ b_b(\lambda)+a(\lambda) > 0.3$).

This equation was applied in the form of the GSM01 model as detailed below. GSM01 inverts observations of $r_{rs}(\lambda)$ into chl *a* concentration, CDOM and detrital absorption coefficient at 443 nm, as well as the particle backscatter coefficient at 443 nm. This model was modified to estimate SS.

The absorption and backscattering coefficients in Eq. 5.2 are made up of the sum of individual optically active components;

$$b_b(\lambda) = b_{bw}(\lambda) + b_{bss}(\lambda) \tag{5.3}$$

$$a(\lambda) = a_w(\lambda) + a_\phi(\lambda) + a_{CDOMD}(\lambda) \tag{5.4}$$

where $a_w(\lambda)$ and $b_{bw}(\lambda)$ are the respective absorption and scattering values due to water, $a_\phi(\lambda)$ is phytoplankton absorption, $b_{bSS}(\lambda)$ is SS backscatter, and $a_{CDOMD}(\lambda)$ is the combined absorption due to CDOM and detrital materials. Values of $a_w(\lambda)$ and $b_{bw}(\lambda)$ were taken from the literature, and are the values specified in GSM01 for the wavelength of each MODIS band (Morel 1974; Pope and Fry 1997). In Eq. 5.4 CDOM and detritus absorption are described by a single exponential shape over the spectral range, due to their similar spectral signatures (termed CDOMD).

The values for non-water IOP spectra are assumed to have a known shape but with an unknown magnitude;

$$a_\phi(\lambda) = C_\phi\, a^*_\phi(\lambda) \tag{5.5a}$$

$$a_{CDOMD}(\lambda) = a_{CDOMD}(\lambda_0)\, \exp[-S(\lambda - \lambda_0)] \tag{5.5b}$$

$$b_{bss}(\lambda) = b_{bss}(\lambda_0)\, (\lambda/\lambda_0)^{-n} \tag{5.5c}$$

$$b_{bss}(\lambda) = Bb_{ss}\, b^*_{ss}(\lambda)\, C_{ss} \tag{5.5d}$$

where $a^*_\phi(\lambda)$ is the specific chlorophyll absorption coefficient, C_ϕ is chlorophyll concentration, S is the spectral slope coefficient for a_{CDOMD}, λ_0 is a reference wavelength (443 nm), n is the power law exponent for the SS backscattering coefficient, Bb_{ss} is the backscattering ratio of SS, and $b^*_{ss}(\lambda)$ is specific scattering of SS. A functional form of the GSM01 model is expressed as:

$$r_{rs}(\lambda) = \sum_{i=1}^{2} li \left[\frac{b_b(\lambda)}{b_b(\lambda) + a_w(\lambda) + C_\phi a^*_\phi + a_{CDOMD}(\lambda_0)\exp(-S(\lambda - \lambda_0))} \right]^i \tag{5.6}$$

Values of $a^*_\phi(\lambda)$, S, and n were taken from the literature, leaving three unknowns; C_ϕ, $a_{CDOMD}(\lambda_0)$ and $b_{bSS}(\lambda_0)$, which can be retrieved from $r_{rs}(\lambda)$ values measured at five different wavelengths (412, 443, 488, 531 and 551 nm) with MODIS Aqua. Equation 5.6 is solved using the Levenberg–Marquardt algorithm for least-squares estimation of nonlinear parameters (Levenberg 1944).

Between 5 and 10 May 2002, Belzile et al. (2004) completed a detailed study on light absorption and scattering coefficients in the euphotic zone of Lake Taupo. Optical properties were consistent with Case 2 marine waters. Belzile et al. (2004) enumerated most of the IOPs necessary for the optimization of the above bio-optical model. The dominant genera observed during their study were *Asterionella, Ceratium*, *Anabaena, Dinobyron*, and *Botryococcus.* A high chl-specific absorption coefficient was observed (mean = 0.027 m^{-1} (µg $L^{-1})^{-1}$ at 674 nm), which the authors suggested was indicative of minimal package effect consistent with small cells, high light accumulation and/or nutrient limitation (cf. Bricaud et al. 1995; Stramski et al. 2001). For the present study, the lowest phytoplankton absorption was taken from the 19 stations of Belzile et al. (2004), and was converted to $a^*_\phi(\lambda)$ by dividing by the lowest observed chl *a* concentration measured in their study (0.86 µg L^{-1}). This $a^*_\phi(\lambda)$ (at MODIS Aqua wavelengths) was used to represent the period from October to May for all years (Figure 5.2). From June to September, $a^*_\phi(\lambda)$ for the $a^*_\phi(\lambda)$ for the Bacillariophyte *Chaetoceros protuberans* was used (Sathyendranath et al. 1987) (Figure 5.2). The $a^*_\phi(\lambda)$ absorption spectrums were chosen based on similar morphology to species found in Lake Taupo (the literature did not contain $a^*_\phi(\lambda)$ for any common species found in Lake Taupo).

In the Lake Taupo optical study of Belzile et al. (2004) from 5 and 10 May 2002, CDOM absorption at 443 nm ranged from 0.03 to 0.09 m^{-1}, with the highest values found near inflows in the south of the lake. *S* varied from 0.013-0.024 m^{-1} with a mean of 0.017 m^{-1}, and this was the value of *S* adopted in the model. No significant correlation was found by Belzile et al. (2004) between CDOM and $a_\phi(\lambda)$. The model also adopted SS bio-optical parameters from their study; mean B_{bss} 0.011, $b^*_{SS}(555)$ = 0.54 m^2 g^{-1} at the Tokaanau tail race and n = 0.63. The value of $b^*_{SS}(443)$ was calculated from $b^*_{SS}(555)$ using a power function (Belzile et al. 2004):

$$b^*_{SS}(443) = b^*_{SS}(555)\left(\frac{555}{443}\right)^n \qquad (5.7)$$

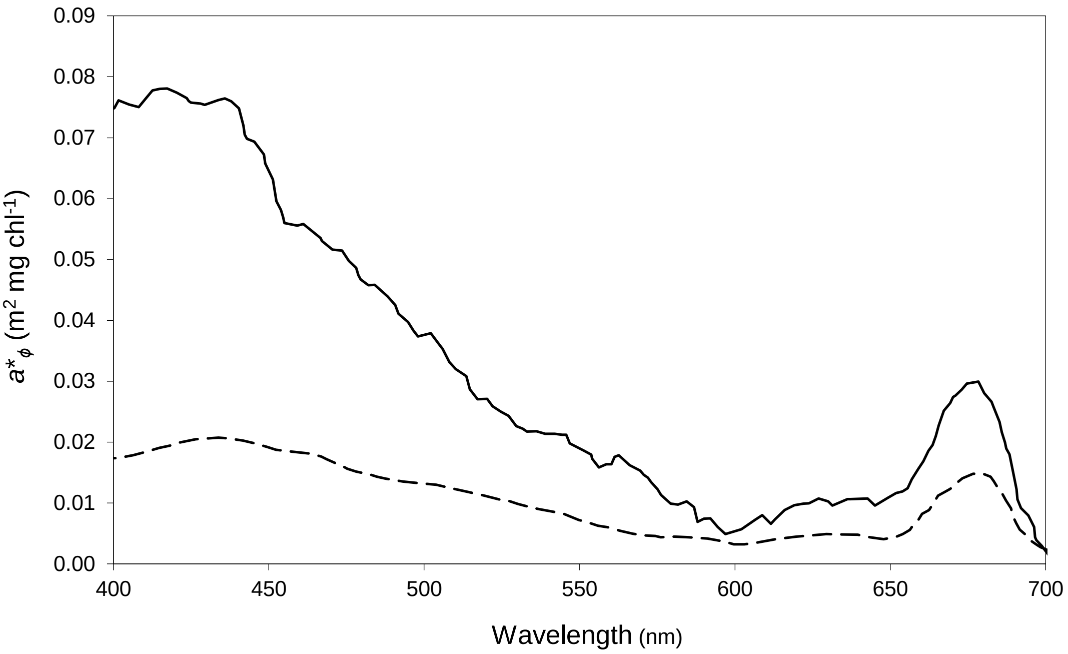

Figure 5.2. Chlorophyll absorption cross section with wavelength. Black line is the lowest absorption measured by Belzile (2004), and the dashed line is from the Bacillariophyte *Chaetoceros protuberans* (Sathyendranath et al. 1987).

MODIS Aqua and Terra band 1 correlation to bio-optical modelled SS

On 4 and 5 March 2004, SS was also estimated from MODIS Aqua B1 using linear regression relationships between SS estimated from the MODIS Aqua bio-optical model (1000 m resolution) and atmospherically corrected subsurface remote sensing reflectance from MODIS Aqua band 1 (250 m resolution) on corresponding dates. For estimation of SS from MODIS Terra, B1 on 4 (1100 h) and 5 (1000 h) March 2004, no Terra bio-optical estimated SS was available for the regression, so SS was estimated from the regression relationship on 5 March 2004 (1415 h) created for MODIS Aqua. For regression relationships, a 1500 m buffer zone from the land-water boundary into the lake was used to mask the influence of bottom reflectance and land contamination (e.g., stay light from land pixels), and any areas of cloud were also masked. For the estimation of SS from these regression relationships, all water areas were included by using an unsupervised classification of MODIS B2 to differentiate water and land. Adjacency effects (land contamination) and bottom reflection affect estimations of SS (Guanter et al. 2009), however, for the present study all areas of the lake were included, including the near shore, as there was a need to distinguish certain nearshore features associated with inflows.

5.3 Results

Field data

Field meteorological and water temperature data from 1 February to 14 March 2004 are shown in Figure 5.3. This time period is of particular significance to the study, due to a one in one-hundred year high-discharge event in the Tongariro River. Figure 5.3(a) shows rainfall for this time period and flow data from the Tongariro River from 27 February 2004 to 6 March 2004. A number of major rainfall events occurred of which the largest occurred on 20 February 2004 (max. 19 mm in one hour). On 29 February 2004 Tongariro River flow peaked at 1325 $m^3 s^{-1}$(mean base flow is c. 30 $m^3 s^{-1}$). The average flow on 4 and 5 March 2004 (corresponding to the two dates for which MODIS imagery was captured) was 89 $m^3 s^{-1}$.

On 15 February average wind speed from hourly values between from 0400 and 2100 h was > 4.7 $m s^{-1}$ (SSE direction), with a maximum of 7.6 $m s^{-1}$ at 1000 h (Figure 5.3(b)). The effect of the sustained high wind speed on lake thermal stratification can be seen on this day in Figure 5.3(c) as a seiche setup event. The seiching resulted in the largest displacement of the thermocline between 1 and 16 February (Figure 5.3(c)), with an internal wave displacement of up to 95 m based on displacement of temperature isotherms in the metalimnion region. Figure 5.4 shows Secchi depth (m) at Site A (unshaded Secchi disk) and Site B (shaded Secchi disk). On 8 March 2004 Secchi depth at Site B was 5 m, the lowest ever recorded in Lake Taupo (Gibbs, unpubl. data). Nutrient concentrations and chl *a* did not show large fluctuations after the storm inflow event, except for particulate phosphorus at Site B, which increased from 1.8 $\mu g L^{-1}$ on 26 February 2004 to 3.1 $\mu g L^{-1}$ on 8 March 2004. This is consistent with phosphorus associated with particulate material originating from the Tongariro River (Viner 1988).

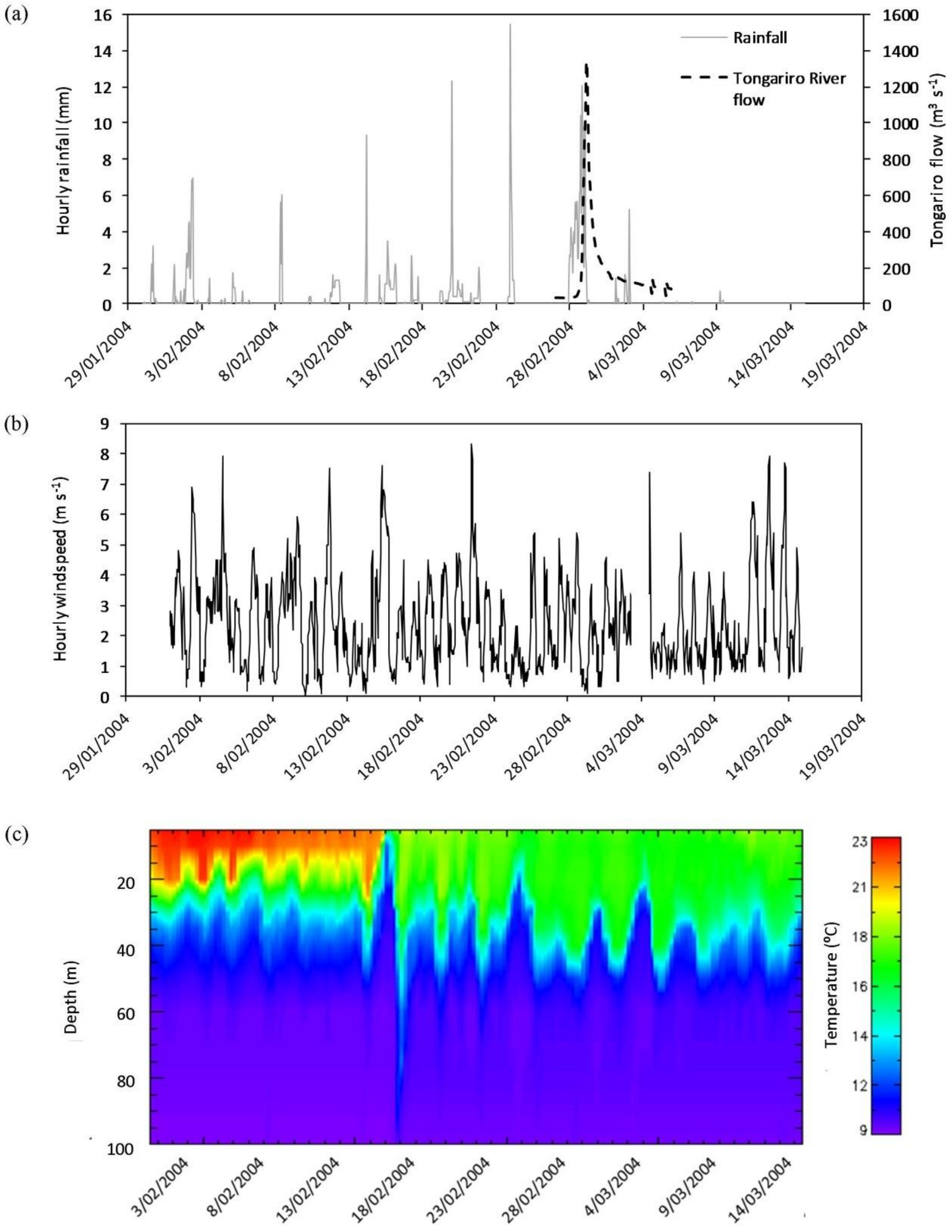

Figure 5.3. Plots of field data used in this study from 1 February to 14 March 2004. (a) Hourly rainfall (mm) and Tongariro River flow from 27 February to 6 March 2004 ($m^3 s^{-1}$) measured at Turangi. (b) Hourly wind speed ($m s^{-1}$) measured at Turangi. (c) Interpolated thermistor chain data (ºC) from Site B in Lake Taupo.

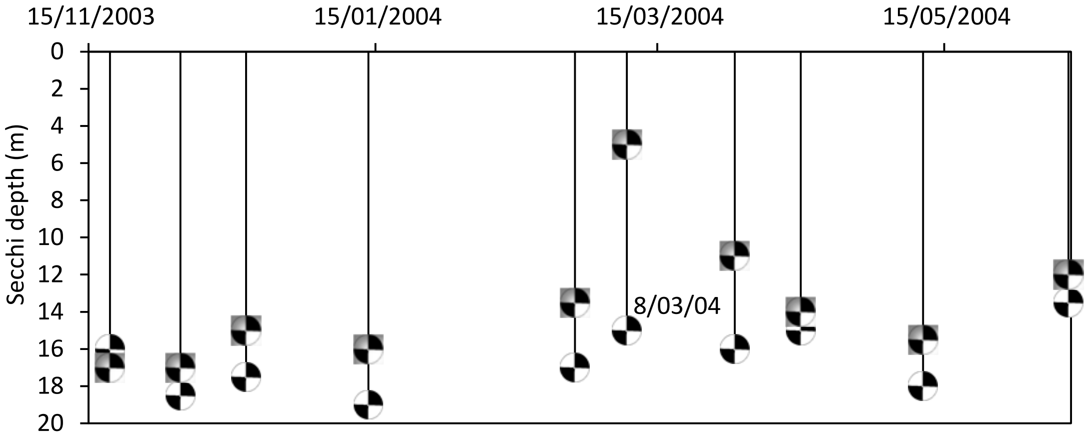

Figure 5.4. Secchi depth (m) from 19 November 2003 to 10 June 2004 from Site A (unshaded disk symbol) and Site B (shaded disk symbol).

During the study period, in Site A in situ chl *a* close to the time of MODIS overpasses ranged from 0.3 µg L^{-1} (17 January 2008) to 2.9 µg L^{-1} (13 and 14 August 2003). Succession of phytoplankton species followed a regular pattern in Lake Taupo (Gibbs 2011).

Bio-optical modelling results

Linear regression between observed and in situ values of chl *a* was not significant ($p>0.05$) when only one $a^*_\phi(\lambda)$ value, corresponding to that for the Chlorophyte *Dunaliella sp.*, was used. With a seasonally varying value of $a^*_\phi(\lambda)$ (refer to Figure 5.2), linear regressions were highly significant (see Figure 5.5; $r^2 = 0.71$, $p<0.01$, root mean squared error (RMSE) = 0.522 µg L^{-1} and normalised RMSE = 16%). Using a seasonally varying value of $a^*_\phi(\lambda)$, the highest magnitude (1.51 µg L^{-1}) of residual values from the linear regression of estimated and in situ chl *a* occurred in August. Clouds were present in most images in this study, but for the images with the four largest chl *a* estimation residuals (three in August and one in December), clouds were present near the lake edge and may have affected chl *a* retrievals. Additionally, low solar elevation meant the signal to noise ratio would be higher in August.

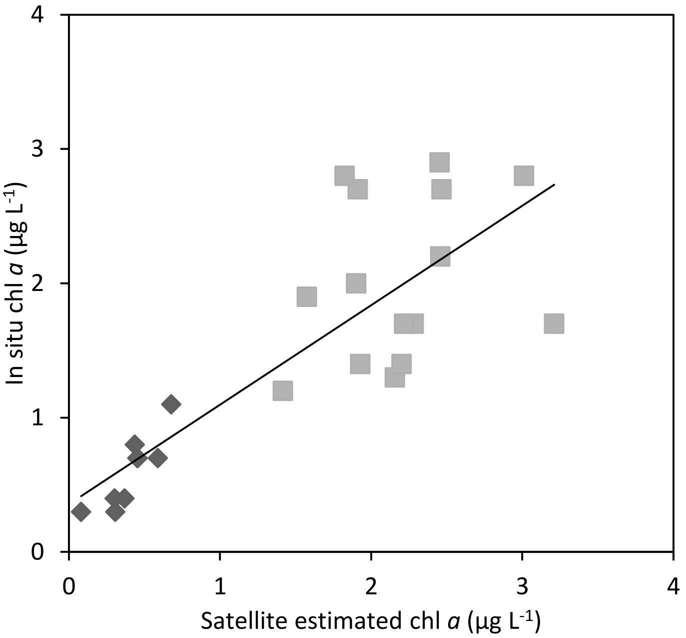

Figure 5.5. In situ versus MODIS-estimated chlorophyll *a*. The line denotes the regression relationship (satellite-estimated chl *a* = 0.741 (In situ chl *a*) + 0.356) using a seasonally adjusted chlorophyll specific absorption coefficient (n = 23, $r^2 = 0.71$, $p<0.01$, root mean squared error (RMSE) = 0.522 µg L^{-1}). The estimations using the $a^*_\phi(\lambda)$ from Belzile (2004) are shown with a diamond, and using $a^*_\phi(\lambda)$ from the Bacillariophyte *Chaetoceros protuberans* (Sathyendranath et al. 1987) shown with a square.

Figure 5.6 shows MODIS-estimated chl *a* (µg L^{-1}), CDOMD absorption at 443 nm (m^{-1}), and SS (mg L^{-1}) on 3 August 2004. A 1500 m buffer from the lake edge is shown as grey, in order to mask possible influences of bottom reflection and/or land contamination. In most cases the MODIS-estimated chl *a* showed little spatial variation, however, on this day relatively high chl *a* (max 2.65 µg L^{-1}) and SS (max 0.98 mg L^{-1}) was observed in the south and east of Lake Taupo, and higher CDOMD absorption was evident in the south and west (max. absorption = 0.026 m^{-1} at 443 nm).

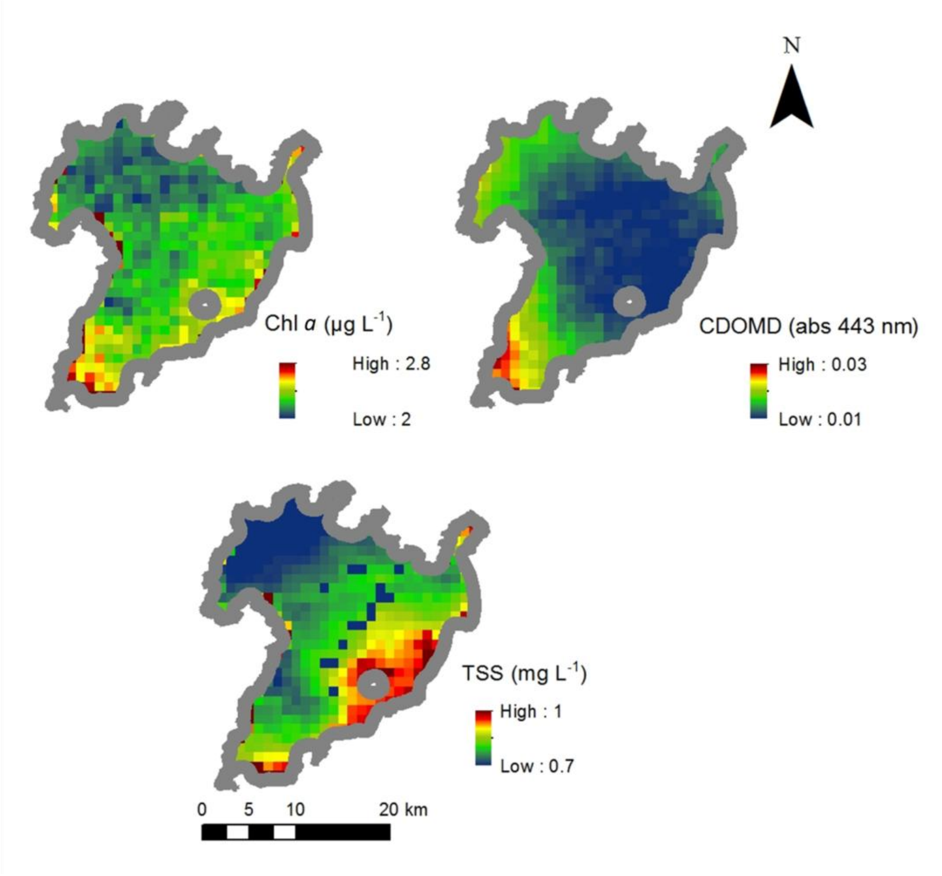

Figure 5.6. MODIS-derived chl *a* (µg L^{-1}), CDOMD absorption (abs) (m^{-1}) at 443 nm and SS (mg L^{-1}) on 3 August 2004. A grey-coloured buffer is used from the lake edge to 1500 m into the lake, to avoid possible areas of bottom reflectance and stray light from regions close to the shoreline.

Figures 5.7 and 5.8 show MODIS-estimated chl *a*, CDOMD absorption at 443 nm, and SS on 4 and 5 March 2004, respectively. The white oval shape is used to mask a small area of cloud on 4 March 2004. In both images, there is higher chl *a*, SS and CDOMD absorption in the south basin, in close proximity to, and at a time of, high discharge from the Tongariro River (inflow location shown in Figure 5.1). On 4 March 2004, a distinct broad plume is visible (Figure 5.7). Within the plume, maximum values were 2.3 µg chl *a* L^{-1}, 0.038 m^{-1} CDOMD absorption, and 14.2 mg SS L^{-1}. The bio-optical algorithm produced negative CDOMD absorption in northern areas of Lake Taupo at the opposite end to the plume. The plume front was associated with unusually high or low values of chl *a*, high CDOMD absorption, and low SS. On 5 March 2004 the plume was narrower, with lower concentrations of chl *a* (max 1.61 µg L^{-1}) and SS (max 7.08 mg L^{-1}), however, CDOMD absorption was higher (0.060 m^{-1}) at this time.

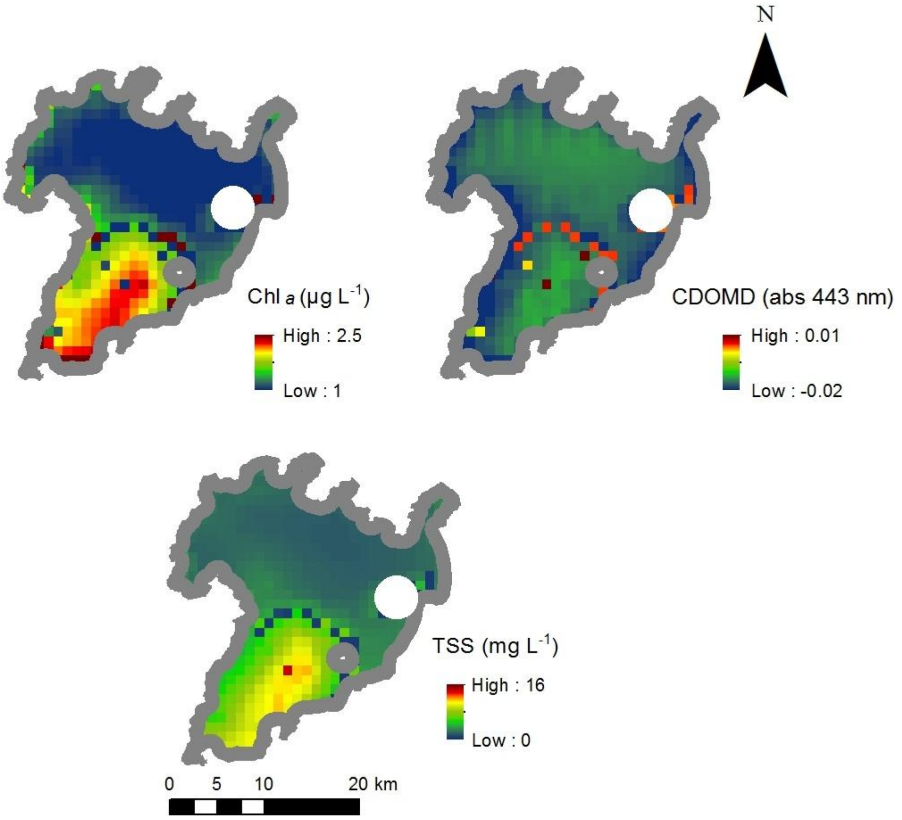

Figure 5.7. MODIS-derived chl *a* (µg L^{-1}), CDOMD absorption (abs) (m^{-1}) at 443 nm and SS (mg L^{-1}) on 4 March 2004. The white oval shape is used to mask a small area of cloud, and a grey-coloured buffer is used from the lake edge to 1500 m into the lake, to avoid possible areas of bottom reflectance and stray light from regions close to the shoreline.

MODIS Aqua and Terra band 1 estimations of SS

The relationship from linear regression between SS calculated from MODIS Aqua using bio-optical modelling and MODIS Aqua r_{rs}(B1) on 4 March 2004 was:

$$SS = 1022\, r_{rs}(B1) - 3.35 \qquad (r^2 = 0.89, p<0.01, n = 3785) \qquad (5.8)$$

This relationship was used to estimate the lake-wide distributions of SS in Figure 5.9(b). At 1330 h on 5 March 2004 the relationship between MODIS Aqua SS derived from bio-optical modelling and MODIS Aqua r_{rs}(B1), was:

$$SS = 1159.6\, r_{rs}(B1) - 0.48 \qquad (r^2 = 0.77,\ p<0.01,\ n = 3785) \qquad (5.9)$$

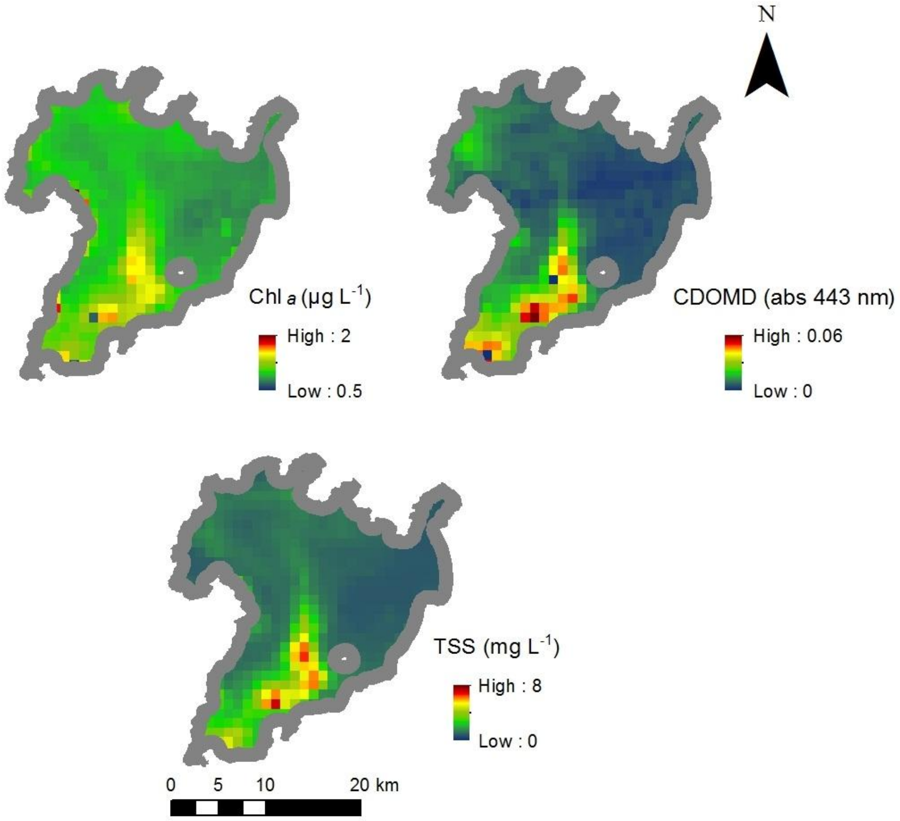

Figure 5.8. MODIS-derived chl *a* (µg L^{-1}), CDOMD absorption (abs) (m^{-1}) at 443 nm and SS (mg L^{-1}) on 5 March 2004. A grey-coloured buffer is used from the lake edge to 1500 m into the lake, to avoid possible areas of bottom reflectance and stray light from regions close to the shoreline.

Equation 5.9 was used to estimate lake-wide distributions of SS in Figure 5.9(a), (b), (c) and (d). Even though r^2 was higher in Eq. 5.8, it produced negative SS values in estimations based on MODIS Terra r_{rs}(B1). The high resolution of MODIS B1 enabled quantification of plume features on a much finer scale than MODIS 1 km resolution bio-optical estimations. In Figure 5.9 the Tongariro River mouth is clearly identified as the source of the plume, and the high SS emanating into the lake and continuing in an easterly direction suggests that it was deflected along the shoreline before moving towards the central part of the lake. On 4 March a region of water with high SS near Motuoapa Bay (Figure 5.9 (a) and (b)) suggests that the plume detaches from the shoreline near this bay, while on 5 March the plume travels a shorter distance before detaching from the shoreline near Stump Bay (bay locations shown in Figure 5.1(b)). On 5 March the plume is much narrower and appears to be deflected first right and then left, encountering what appears to be two separate gyres. On 5 March SS concentrations were high near the Tongariro inflow, with an abrupt decrease as the plume entered the main body of the lake. There was high variability of SS concentrations at this transition point, possibly associated with differential advection into the gyre.

Figure 5.10 shows a photograph coincidentally taken from an aircraft early on the morning on 5 March. This photograph was captured from above the north-eastern shore of Lake Taupo looking south-west. The plume appears to take a similar path to that shown in Figure 5.9 (c) and 5.9 (d), and the photo shows evidence of a large clockwise gyre in the area where the plume enters the main basin of Lake Taupo from the southern basin.

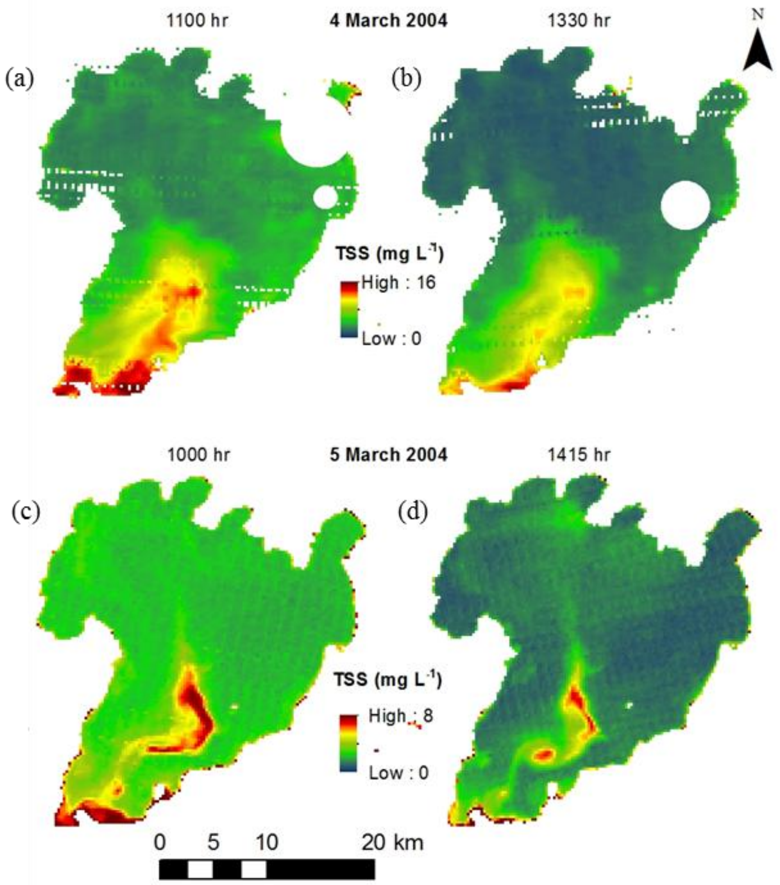

Figure 5.9. MODIS band 1 SS calculated from eq. 5.8 and 5.9, on 4 and 5 March 2004. The white oval shape shows areas where cloud has been masked.

Figure 5.10. Photograph of Lake Taupo taken from c. 3000 m above Taupo Airport on the north eastern shore looking towards the south-west shore (Photo by Jonathan King, 5 March 2004).

5.4 Discussion

Increased focus has been placed on the contribution of inherent optical property constituents on the accuracy of any derived products from remote sensing (Sathyendranath et al. 2001; Stramski et al. 2001). Our study confirms previous oceanographic optical studies that show that inclusion of varying phytoplankton IOPs can increase the accuracy of derived water quality parameters such as chl *a* (Carder et al. 1999). While choice of $a^*_\phi(\lambda)$ values was made based on time of year and historical patterns of species succession, an ideal algorithm would derive a suitable $a^*_\phi(\lambda)$ value from reflectance. In oligotrophic lakes deriving a suitable $a^*_\phi(\lambda)$ becomes difficult, however, as the low concentration of chl *a* results in low total absorption and similar spectral signatures throughout the year. In winter in particular, there is low solar elevation, lower signal to noise ratio and greater cloud cover, which collectively hinder remote sensing accuracy, suggesting that more testing of the algorithm is needed. Gons et al. (2008), for example identified chl *a* concentrations of 2 to 5 µg L^{-1} as being the most problematic for remote sensing retrieval in the Laurentian Great Lakes, a problem which the author termed the 'mesotrophic blind'.

The two different $a^*_\phi(\lambda)$ values used in this study are analogous to those used by Carder (1999); (1) high photoprotective pigment to chlorophyll ratio and low self-shading unpackaged chloroplasts (using Belzile $a^*_\phi(\lambda)$, representing small celled chloropytes and cyanobacteria), (2) low photoprotective pigment to chlorophyll ratio and high self-shading (Bacillariophyte $a^*_\phi(\lambda)$), however this study did not include a transitional phase. The value of Belzile $a^*_\phi(\lambda)$ is within literature ranges for other lakes (Campbell et al. 2011b), estuaries (Mercado et al. 2006), and coastal waters (Blondeau-Patissier et al. 2009), and it of similar magnitude to $a^*_\phi(\lambda)$ measured in coastal oligotrophic waters of the North Atlantic (Babin et al. 2003). Although there has been increased interest in the development of bio-optical algorithms to account for varying inherent optical properties associated with different phytoplankton groups, sizes and physiological status (e.g., based on nutrient and irradiance exposure levels), there has been limited application of such algorithms for ocean colour satellite imagery. Our study could benefit from further investigation into a^*_ϕ (λ) values in Lake Taupo during winter, when chl *a* concentrations attain their annual maximum (e.g., Vincent 1983), and residuals from the model are highest.

The previously observed phytoplankton succession in Lake Taupo can be related to specific physiological and morphological adaptations of the species represented but perhaps at a more general level, for the purposes of remote sensing, the succession could be denoted by transitions in phytoplankton functional groups denoted by letters of the alphabet (Reynolds et al. 2002). In the stratified months *Botryococcus braunii* dominated (Group F: adapted to clear epilimnia and low-nutrient tolerance), and *Dinobyron* sp. sometimes dominated (Group E, adapted to low nutrients, high light, and can resort to mixotrophy). The cyanophyte *Anabaena flos-aquae* appeared in autumn (group HI: adapted to low nitrogen/nitrogen-fixing, low phosphorus, low light). The dominance of Bacillariophytes (Group C and P) in winter reflects their tolerance to disturbance (particularly mixing), however, group C and P are specified as representative of eutrophic lakes in the classification. Winter may represent a time when nutrients are largely replete (as in eutrophic lakes) due to a fully mixed water column, offsetting low light availability and low temperature (Vincent 1983). Additionally greater turbulence and mixing in winter would allow negatively buoyant siliceous diatoms to remain in suspension.

Neither in situ measurements of CDOM absorption or SS concentration were available to fully validate the model results of my study. The retrieval of negative CDOMD absorption values for some images may indicate problems with either the model parameterisation or atmospheric correction. Since measured IOPs were used to parameterise the bio-optical model, it is more likely that they are a result of inaccuracies in atmospheric correction. The assumption of an AOD value of 0.5 used in atmospheric correction may have led to unrealistically high reflectance at lower wavelengths, and since CDOMD absorbs most strongly in this region of the spectrum, high reflectance would be treated by the model as low CDOMD absorption. In future studies a more accurate source of AOD data may be needed for CDOMD quantification. Remote sensing of North Island lakes would benefit from measurements of AOD at a North Island site in addition to the South Island Lauder site. Retrieved SS values were realistic for non-flood conditions, and were comparable to those previously measured (Belzile et al. 2004), however, flood conditions were unprecedented in the measurement history and no in situ data exist for comparison of SS in the flood inflow plume.

Horizontal variability of water quality parameters in Lake Taupo is considered to be minimal and mid-lake Site A is currently used in the TLTMP to represent long-term changes in lake water quality. My study found little spatial variability in most images, however, the two exceptions discussed show that this was not always the case. The accuracy of monitoring in Lake Taupo would benefit from at least one additional monitoring site in the southern basin, the present study shows that conditions in this part of the lake are more variable. This variability appears to be contributed in large part from the influence of the major inflow, the Tongariro River. The presence of gyres that appear to be more specific to, and mostly contained in, the southern end of the lake may limit exchange between the southern and northern lake basins. Monitoring of CDOM and SS in Lake Taupo would also aid in further algorithm development for applications of remote sensing to enhance the spatial and temporal coverage which is currently limited with in situ sampling to just one station (A) in the central basin of the lake.

Turbid inflows often propagate as relatively discrete density currents into stratified waters (Imberger et al. 1989). The large flood-derived turbid inflow from the Tongariro River provided insights into Lake Taupo hydrodynamics and circulation. The presence of gyres and internal waves indicates complex physical mixing and transport phenomena. Of particular interest is the elevated SS present in gyre locations. Gyres can cause upwelling (MacIntyre and Melack 1995), and this may be responsible for locally elevated SS concentrations in upwelling areas. It is possible that there was floating debris such as low-density pumice (floating volcanic-origin rock) and organic matter at the head of the plume, which may have caused the highly variable SS and chl *a* estimation at the plume front. In Lake Taupo floating pumice plumes in the lake are often associated with storm flow discharges (M. Gibbs, NIWA, personal communication).

No water temperature data were available for the Tongariro inflow, so it was only possible to speculate on its fate, but Spigel et al. (2005) has previously shown that water temperature is the dominant driver of inflow insertion depth into the water column of Lake Taupo. The Tongariro inflow enters the lake as numerous turbulent jets in close proximity, and subsequently merging. At 25 m from the entrance the plume extended as a turbulent jet moving (via deflection) in a northeast direction over the entire 10 m of the water column (Spigel et al. 2005). The authors postulated that this deflection to the northeast was likely due to ambient lake currents rather than Coriolis forces which would act in the northwest direction. The inflow then plunged down a very steep lake bed slope but eventually lifted to form an interflow at a depth of c. 45 m. In contrast, in the present study, the satellite-observed inflow was deflected strongly to the northwest, remaining attached to the shoreline for some distance, indicating ambient lake currents and possibly Coriolis effects played a greater role at this time.

Phytoplankton did not show any concentration fluctuation in response to increased particulate phosphorus associated with the flood flow event in March 2004. Post-flood winter levels of chl *a* in 2004 were little different to previous years, and it is likely that the high SS in the inflow plume was primarily composed of allochthonous particulate matter which was predominantly inorganic (Bloesch 1995). This inorganic matter likely contains phosphorus adsorbed onto Fe and Mn oxy-hydroxides (Viner 1978), and would eventually settle to the lake bed. This absorbed phosphorous in the sediment can be released to the water column by active redox processes that reduce the metal oxides (Wilson et al. 2010), however, oxic surface sediments in Lake Taupo may prevent the reduction of these metals and therefore the release of phosphorus.

Using an optimised semi-analytical bio-optical model the present study found that MODIS estimates of chl a concentration can be accurately related to in situ data. The bio-optical model used in this study is applicable to other high spectral resolution satellites such as the Envisat MERIS, which has a resolution of 260 m x 300 m, presenting to opportunities to increase the spatial resolution of remote sensing for water quality retrieval, depending on weather conditions. This study has highlighted the importance of accurate input data for atmospheric correction including an alternative source of AOD data to ensure accuracy, especially in blue wavelengths. Remote sensing can complement the current Taupo long term monitoring programme through increased spatial and temporal resolution of monitoring. Use of empirical relationships between bio-optical-estimated SS and band 1 subsurface remote sensing reflectance would allow increased temporal and spatial resolution of monitoring, allowing for resolution to study fine-scale features.

5.5 References

Babin, M. 2003. Variations in the light absorption coefficients of phytoplankton, nonalgal particles, and dissolved organic matter in coastal waters around Europe. Journal of Geophysical Research **108**: 3211.

Becker, R. H., M. I. Sultan, G. L. Boyer, M. R. Twiss, and E. Konopko. 2009. Mapping cyanobacterial blooms in the Great Lakes using MODIS. Journal of Great Lakes Research **35**: 447–453.

Belzile, C., W. F. Vincent, C. Howard-Williams, I. Hawes, M. R. James, M. Kumagai, and C. S. Roesler. 2004. Relationships between spectral optical properties and optically active substances in a clear oligotrophic lake. Water Resources Research **40**: W12512.

Binding, C. E., J. H. Jerome, R. P. Bukata, and W. G. Booty. 2010. Suspended particulate matter in Lake Erie derived from MODIS aquatic colour imagery. International Journal of Remote Sensing **31**: 5239–5255.

Bloesch, J. 1995. Mechanisms, measurement and importance of sediment resuspension in lakes. Marine and Freshwater Research **46**: 295–304.

Blondeau-Patissier, D., V. E. Brando, K. Oubelkheir, A. G. Dekker, L. A. Clementson, and P. Daniel. 2009. Bio-optical variability of the absorption and scattering properties of the Queensland inshore and reef waters, Australia. Journal of Geophysical Research **114**: C05003.

Bricaud, A., S. M. J. Babin, and A. Morel. 1995. Variability in the chlorophyll-specific absorption coefficients of natural phytoplankton: analysis and parameterization. Journal of Geophysical Research **100**: 13321–13332.

Bricaud, A., A. Morel, and L. Prieur. 2009. Domains Absorption by dissolved organic matter of the sea (yellow substance) in the UV and visible domains. Limnology and Oceanography **26**: 43–53.

Bukata, R. P., J. H. Jerome, K. Y. Kondratyev, and D. V. Pozdnyakov. 1995. Optical Properties and Remote Sensing of Inland and Coastal Waters. CRC Press, Boca Raton, Florida, USA.

Bulgarelli, B., V. B. Kisselev, and L. Roberti. 1999. Radiative transfer in the atmosphere-ocean system: the finite-element method. Applied Optics **38**: 1530–1542.

Campbell, G., S. R. Phinn, A. G. Dekker, and V. E. Brando. 2011. Remote sensing of water quality in an Australian tropical freshwater impoundment using matrix inversion and MERIS images. Remote Sensing of Environment **115**: 2402–2414.

Campbell, G., S. Phinn, and P. Daniel. 2011b. The specific inherent optical properties of three sub-tropical and tropical water reservoirs in Queensland, Australia. Hydrobiologia **658**: 233–252.

Carder, K. L., F. R. Chen, Z. P. Lee, S. K. Hawes, and D. Kamykowski. 1999. Semianalytic Moderate-Resolution Imaging Spectrometer algorithms for chlorophyll-a and absorption with bio-optical domains based on nitrate-depletion temperatures. Journal of Geophysical Research **104**: 5403–5421.

Chu, D. A., Y. J. Kaufman, C. Ichoku, L. A. Remer, D. Tanre, and B. N. Holben. 2002. Validation of MODIS aerosol optical depth retrieval over land. Geophysical Research Letters **29**: 8007.

Davies-Colley, R. J., W. N. Vant, and D. G. Smith. 1993. Colour and Clarity of Natural Waters. Ellis Horwood, New York, USA.

Devred, E., S. Sathyendranath, V. Stuart, and T. Platt. 2011. A three component classification of phytoplankton absorption spectra: Application to ocean-color data. Remote Sensing of Environment **115**: 2255–2266.

Doxaran, D., J.-M. Froidefond, P. Castaing, and M. Babin. 2009. Dynamics of the turbidity maximum zone in a macrotidal estuary (the Gironde, France): Observations from field and MODIS satellite data. Estuarine, Coastal and Shelf Science **81**: 321–332.

Fell, F., and J. Fischer. 2001. Numerical simulation of the light field in the atmosphere-ocean system using the matrix-operator method. Journal of Quantitative Spectroscopy and Radiative Transfer **69**: 351–388.

Fischer, J., and H. Grassl. 1984. Radiative transfer in an atmosphere-ocean system: an azimuthally dependent matrix-operator approach. Applied Optics **23**: 1032–1039.

Giardino, C., V. E. Brando, A. G. Dekker, N. Strömbeck, and G. Candiani. 2007. Assessment of water quality in Lake Garda (Italy) using Hyperion. Remote Sensing of Environment **109**: 183–195.

Gibbs, M. 2004. Lake Taupo Long-Term Monitoring Programme 2002-2003: Including Two Additional Sites. Waikato Regional Council Technical Report 2004/05, Hamilton, New Zealand.

Gibbs, M. 2005. Lake Taupo long-term monitoring programme 2003-2004: Including Two Additional Sites. Waikato Regional Council Technical Report 2005/18, Hamilton, New Zealand.

Gibbs, M. 2007. Lake Taupo Long-Term Monitoring Programme 2005-2006. Waikato Regional Council Technical Report 2007/21, Hamilton, New Zealand.

Gibbs, M. 2008. Lake Taupo long-term monitoring programme 2006-2007. Waikato Regional Council Technical Report 2008/25, Hamilton, New Zealand.

Gibbs, M. 2009. Lake Taupo long-term monitoring programme 2007-2008. Waikato Regional Council Technical Report 2009/09, Hamilton, New Zealand.

Gibbs, M. 2011. Lake Taupo Long-Term Monitoring Programme 2009–2010. Waikato Regional Council Technical Report 2011/12, Hamilton, New Zealand.

Gitelson, A, G. Dallolmo, W. Moses, D. Rundquist, T. Barrow, T. Fisher, D. Gurlin, and J. Holz. 2008. A simple semi-analytical model for remote estimation of chlorophyll-a in turbid waters: Validation. Remote Sensing of Environment **112**: 3582–3593.

Gons, H., M. Auer, and S. Effler. 2008. MERIS satellite chlorophyll mapping of oligotrophic and eutrophic waters in the Laurentian Great Lakes. Remote Sensing of Environment **112**: 4098–4106.

Gordon, H. R., J. W. Brown, O. B. Brown, R. H. Evans, and R. C. Smith. 1988. A semianalytic radiance model of ocean color. Journal of Geophysical Research **93**: 10909–10924.

Gordon, H. R., and O. B. Brown. 1973. Irradiance reflectivity of a flat ocean as a function of its optical properties. Applied Optics **12**: 1549–1551.

Guanter, L., A. Ruiz-Verdú, D. Odermatt, C. Giardino, S. Simis, V. Estellés, T. Heege, J. A. Domínguez-Gómez, and J. Moreno. 2010. Atmospheric correction of ENVISAT/MERIS data over inland waters: Validation for European lakes. Remote Sensing of Environment **114**: 467–480.

Han, L. H. 1997. Spectral reflectance with varying suspended sediment concentrations in clear and algae-laden waters. Photogrammetric Engineering and Remote Sensing **63**: 701–705.

Horion, S., N. Bergamino, S. Stenuite, J.-P. Descy, P.-D. Plisnier, S. A. Loiselle, and Y. Cornet. 2010. Optimized extraction of daily bio-optical time series derived from MODIS/Aqua imagery for Lake Tanganyika, Africa. Remote Sensing of Environment **114**: 781–791.

Imberger, J., J. C. Patterson, and W. H. and T. Y. W. John. 1989. Physical limnology, p. 303-475. *In* Advances in Applied Mechanics. Academic Press, Boston, USA.

Kirk, J. T. O. 1981. A Monte Carlo study of the nature of the light field in, and the relationship between optical properties of, turbid yellow waters. Australian Journal of Marine and Freshwater Research **36**: 1–16.

Kirk, J. T. O. 2010. Light and Photosynthesis in Aquatic Ecosystems, 3rd ed. Cambridge University Press, Cambridge and New York.

Kisselev, V. B., L. Roberti, and G. Perona. 1995. Finite-element algorithm for radiative transfer in vertically inhomogeneous media: numerical scheme and applications. Applied Optics **34**: 8460–8471.

Koponen, S., K. Kallio, J. Pulliainen, J. Vepsalainen, T. Pyhalahti, and M. Hallikainen. 2004. Water Quality Classification of Lakes Using 250-m MODIS Data. IEEE Geoscience and Remote Sensing Letters **1**: 287–291.

Koponen, S. 2006. Remote sensing of water quality for Finnish lakes and coastal areas. Ph.D. thesis. Helsinki University of Technology, Finland.

Kostadinov, T. S., D. A. Siegel, and S. Maritorena. 2010. Global variability of phytoplankton functional types from space: assessment via the particle size distribution. Biogeosciences **7**: 4295-4340.

Kotchenova, S. Y., E. F. Vermote, R. Levy, and A. Lyapustin. 2008. Radiative transfer codes for atmospheric correction and aerosol retrieval: intercomparison study. Applied Optics **47**: 2215–2226.

Lee, Z., and K. L. Carder. 2004. Absorption spectrum of phytoplankton pigments derived from hyperspectral remote-sensing reflectance. Remote Sensing of Environment **89**: 361–368.

Levenberg, K. 1944. A method for the solution of certain non-linear problems in least squares. The Quarterly of Applied Mathematics **2**: 164–168.

Liley, J. B., and B. W. Forgan. 2009. Aerosol optical depth over Lauder, New Zealand. Geophysical Research Letters **36**: L07811.

MacIntyre, S., and J. M. Melack. 1995. Vertical and Horizontal Transport in Lakes: Linking Littoral, Benthic, and Pelagic Habitats. Journal of the North American Benthological Society **14**: 599–615.

Mercado, J. M., T. Ramírez, D. Cortés, M. Sebastián, A. Reul, and B. Bautista. 2006. Diurnal changes in the bio-optical properties of the phytoplankton in the Alborán Sea (Mediterranean Sea). Estuarine, Coastal and Shelf Science **69**: 459–470.

Mobley, C. D. 1994. Light and Water, Radiative Transfer in Natural Waters. Academic Press, San Diego, USA.

Moisan, J. R., T. A. H. Moisan, and M. a. Linkswiler. 2011. An inverse modeling approach to estimating phytoplankton pigment concentrations from phytoplankton absorption spectra. Journal of Geophysical Research **116**: C09018.

Morel, A. 1974. Optical properties of pure water and pure seawater, p. 1-24. *In* N.G. Jerlov and E. Steemann Nielsen [eds.], Optical Aspects of Oceanography. Academic Press, New York, USA.

Morel, A., and L. Prieur. 1977. Analysis of variations in ocean color. Limnology and Oceanography **22**: 709–722.

Olmanson, L. G., M. E. Bauer, and P. L. Brezonik. 2008. A 20-year Landsat water clarity census of Minnesota’s 10,000 lakes. Remote Sensing of Environment **112**: 4086–4097.

Pope, R. M., and E. S. Fry. 1997. Absorption spectrum (380-700 nm) of pure water. II. Integrating cavity measurements. Applied Optics **36**: 8710–8723.

Preisendorfer, R. W. 1976. Hydrologic Optics. U.S. Dept. of Commerce, National Oceanic and Atmospheric Administration, Environmental Research Laboratories, Pacific Marine Environmental Laboratory.

Remer, L. A., Y. J. Kaufman, D. Tanré, S. Mattoo, D. A. Chu, J. V. Martins, R.-R. Li, C. Ichoku, R. C. Levy, R. G. Kleidman, T. F. Eck, E. Vermote, and B. N. Holben. 2005. The MODIS Aerosol Algorithm, Products, and Validation. Journal of the Atmospheric Sciences **62**: 947–973.

Reynolds, C., V. Huszar, and C. Kruk. 2002. Towards a functional classification of the freshwater phytoplankton. Journal of Plankton **24**: 417–428.

Rudorff, C. M., E. M. L. M. Novo, and L. S. Galvão. 2006. Spectral mixture analysis for water quality assessment over the Amazon floodplain using Hyperion / EO-1 images. Revista Ambi-Agua **1**: 65–79.

Sathyendranath, S., L. Lazzara, and L. Prieur. 1987. Variations in the spectral values of specific absorption of phytoplankton. Limnology and Oceanography **32**: 403–415.

Sathyendranath, S., T. Platt, G. Cota, and V. Stuart. 2001. Remote sensing of phytoplankton pigments: A comparison of empirical and theoretical approaches. International Journal of Remote Sensing **22**: 249–273.

Spigel, R., C. Howard-Williams, M. Gibbs, S. Stephens, and B. Waugh. 2005. Field calibration of a formula for entrance mixing of river inflows to lakes: Lake Taupo, North Island, New Zealand. New Zealand Journal of Marine and Freshwater Research **39**: 785–802.

Stramski, D., A Bricaud, and A. Morel. 2001. Modeling the inherent optical properties of the ocean based on the detailed composition of the planktonic community. Applied Optics **40**: 2929–2945.

Utermöhl, H. 1931. Neue Wege in der quantitativen Erfassung des Planktons. Verhandlung Internationale Vereinigung de Limnologie **5**: 567–595.

Vidot, J., and R. Santer. 2005. Atmospheric correction for inland waters—application to SeaWiFS. International Journal of Remote Sensing **26**: 3663–3682.

Vincent, W. F. 1983. Phytoplankton production and winter mixing: contrasting effects in two oligotrophic lakes. Journal of Ecology **71**: 1–20.

Viner, A. B. 1988. Phosphorus on suspensoids from the Tongariro River (North Island, New-Zealand) and its potential availability for algal growth. Archiv für Hydrobiologie **111**: 481–489.

White, E., M. Downes, M. Gibbs, and L. Kemp. 1980. Aspects of the physics, chemistry, and phytoplankton biology of Lake Taupo. New Zealand Journal of Marine and Freshwater Research **14**: 139–148.

Wilson, T. A., A. Amirbahman, S. A. Norton, and M. A. Voytek. 2010. A record of phosphorus dynamics in oligotrophic lake sediment. Journal of Paleolimnology **44**: 279–294.

Xiaoyu, Z., Y. Dingtian, Z. Xiaofeng, W. Difeng, L. Shujing, and P. Delu. 2005. Pre-operational monitor system of large inland lake water quality with MODIS imagery. Proc. SPIE 5977.

6 Conclusions

6.1 Research summary

Human activities are increasingly impacting upon the quality and quantity of freshwaters across the globe. Management of freshwaters needs to be cost-effective, and in order for this to occur there must be emphasis on technological developments related to monitoring and modelling of water quality so that there is informed decision making. This thesis describes methods developed for remote sensing of water quality variables and temperature using empirical, semi-analytical and analytical algorithms, with synoptic estimations derived to allow comparisons with 3-D lake model simulations of water temperature and suspended minerals.

The high spatial resolution of Landsat and the freely available archive of data spanning more than 40 years have made Landsat the sensor of choice for monitoring inland water quality in small lakes. In order to efficiently make use of this resource for water quality monitoring, automation of image processing is required. In Chapter 2 an automated image processing method was derived to estimate chl *a* from Landsat imagery, using empirical models. The automation allowed processing of large numbers of images, and an evaluation of algorithm robustness over multiple images. For the estimation of chl *a* over a time series of images, the use of symbolic regression resulted in a significant improvement in the precision of chl *a* estimation compared with traditional approaches based on regression equations. Whilst Landsat remote sensing provides high spatial resolution, spectral resolution is low, which can result in opposing absorption and scattering features of optically active constituents that contribute to subsurface irradiance reflectance within individual bands. To investigate the potential sources of error of chl *a* using the symbolic regression algorithm, bio-optical modelling was used to estimate theoretical changes in Landsat subsurface irradiance reflectance from waters containing fixed chl *a* and varying coloured dissolved organic matter (CDOM) or tripton. Bio-optical modelling demonstrated that the presence of CDOM and tripton contributes to large changes in simulated Landsat B1-B3 subsurface irradiance reflectance. Therefore CDOM and tripton can perturb the symbolic regression relationship, and have the potential to cause moderate to large errors in chl *a* estimation in optically complex waters. However, in Chapter 2 it was demonstrated that Landsat-based empirical algorithms for remote sensing of chl *a* still provide a valuable method for mapping the distribution of phytoplankton at a landscape scale, providing synoptic 'snapshots' and a cost effective solution for examining temporal trends in water quality across a large number of lakes for which it may not be feasible to establish a routine ground-based monitoring programme in all lakes. Trends in satellite imagery acquisition and processing show that the spatial resolution and frequency of image capture are increasing and therefore remote sensing is likely to be increasingly used for detection of temporal and spatial trends in water quality within and between lakes.

Water temperature is fundamental in determining water circulation and mixing patterns, and for inducing spatial (horizontal and vertical) and temporal variations in phytoplankton biomass. Atmospheric correction (AC) is a crucial step in determining water temperature from satellite data, as differences between bulk water temperature and uncorrected satellite-derived water skin temperature can be as large. In Chapter 3 the accuracy of Landsat water surface temperature retrieval was investigated, including the influence of different sources of atmospheric profile data used in MODTRAN-based atmospheric correction. The highest accuracy of Landsat ETM+ temperature estimation in Lake Rotorua was with radiosonde data as an input into MODTRAN, which gave a root-mean-square-error (RMSE) of 0.37 ºC, followed by MODIS Level 2 (0.55 ºC), AIRS Level 3 (0.75 ºC), and NASA data (1.05 ºC). Of the globally available atmospheric profile data for atmospheric correction, MOD07 provided the most accurate water temperature retrieval, with an error comparable to that obtained from radiosonde data. Lake surface water temperature images were used to validate a 3-D hydrodynamic model of Lake Rotoehu. This validation proved satisfactory for using the hydrodynamic model to reproduce the dominant spatial variations in temperature in the lake, including the path of a geothermal inflow and basin-scale thermal distribution patterns. This study highlighted the ability of the 3-D hydrodynamic model ELCOM to accurately estimate physical properties of lakes such as temperature and the inferred circulation pattern, while demonstrating the applicability of using satellite imagery for 3-D model validations.

The temporal resolution of Landsat data (16 days) is such that in New Zealand there is limited access to cloud-free images. While the research using Landsat in Chapters 2 and 3 allowed for high spatial resolution snapshots of chl *a* concentration and water temperature, the temporal resolution was limited. In larger lakes, the use of ocean colour satellites such as MODIS offers the possibility of near real time monitoring of water quality. A semi-analytical algorithm was developed in Chapter 3, to determine spatial and temporal variations of tripton in a large, shallow lake (Ellesmere, South Island, New Zealand), from the Moderate Resolution Imaging Spectroradiometer (MODIS) subsurface remote sensing reflectance. These data were used to quantitatively validate simulations of suspended inorganic minerals derived from a 3-D hydrodynamic-ecological model, ELCOM-CAEDYM, using four different spatially-resolved statistical techniques. The statistical analysis showed that the model did not perform well in reproducing both basin-scale and fine-scale spatial variation in suspended minerals derived from MODIS satellite imagery. The spatially resolved statistical analysis of modelled and satellite estimated suspended minerals allowed a quantitative statistical comparison which would not otherwise have been possible with conventional regression methods. Application of the bio-optical over the lifetime of the MODIS sensor will greatly extend its spatial and temporal coverage for monitoring purposes, and provide a tool to validate the simulated suspended minerals from 1-D and 3-D models on a daily basis. The models developed in this study could be of value for management purposes, to provide a guide to assigning water levels that may reduce sediment resuspension and potentially allow re-establishment of an alternate clear-water state associated with the re-colonisation of macrophytes.

The empirical and semi-analytical approach adopted to estimate water quality parameters from remote sensing imagery in chapters 2 and 4 was not able to estimate with any accuracy multiple co-varying water quality parameters. Analytical algorithms were therefore developed in order to model the combined effects of all optically active substances on subsurface remote sensing reflectance. The model was optimised using in situ IOPs from the literature. Images were atmospherically corrected using 6sv. Two different chl *a*-specific absorption spectra were used, based on the seasonal dominance of phytoplankton phyla with differing absorption properties. The application of this model resulted in good agreement between estimated and in situ chl *a* concentrations (r^2=0.71, $p<0.01$). Highest concentrations were observed during winter when Bacillariophytes (diatoms) dominated the phytoplankton assemblage. On 4 and 5 March 2004 an unusually large turbidity current was observed originating from the Tongariro River inflow in the south-east of the lake. In order to resolve fine details of the plume, empirical relationships between MODIS band 1 reflectance (250-m resolution) and SS estimated from MODIS bio-optical features (1-km resolution) were used to estimate SS at 250-m resolution. Complex lake circulation patterns were observed including a large clockwise gyre. With the development of this bio-optical model MODIS can be used to remotely sense optically active constituents in near real time, and the relationship developed for SS estimation using band 1 can therefore be used to provide sufficient resolution to detect fine-scale features such as turbidity currents.

6.2 Final conclusions

Remote sensing of lake water temperature has been undertaken in a number of instances, however, my study identified that atmospheric correction is critical in the retrieval of accurate surface water temperature data. For the Landsat satellite, radiative transfer modelling of the atmosphere is the only accurate atmospheric correction option applicable to thermal imagery. Atmospheric profile data that is modelled or captured is an essential input to the radiative transfer model. My study has shown that the accuracy of this data has significant effects on the accuracy atmospheric correction and subsequent water surface temperature retrieval. Use of radiosonde atmospheric profile data to parameterise the radiative transfer model offered the highest accuracy of temperature retrieval, however, use of MODIS also resulted in high-accuracy temperature retrieval and has the advantage of being able to be applied globally.

For the remote sensing of optically active water constituents, there is no one definitive remote sensing solution for any lake or group of lakes, and the method needs to be tailored to the lake size and optical complexity of the system, and the spectral and spatial resolution of the remote sensor. Algorithms for remote sensing of optically active water constituents can be divided into analytical, semi-analytical or empirical methods. Empirical methods are applicable where there is a simple relationship between the optically active constituent of interest (e.g., chl *a*, or tripton). Empirical methods targeting specific water quality parameters are therefore usually limited to lakes where only one water quality variable dominates reflectance. This empirical approach requires in situ samples to be taken near the time of image capture for a few representative lakes (e.g., 10 – 15 as in my study) within the image. However, with atmospheric corrections applied to images, these estimations can be extended to other images without in situ samples, in a semi-quantitative fashion. Semi-analytical algorithms can often be applied in the place of empirical algorithms, and have a number of advantages. Semi-analytical algorithms can be developed independently of in situ samples, are applicable to multiple satellite sensors and have greater spatio-temporal applicability. Analytical algorithms are designed to determine more than one water quality parameter simultaneously, however, a suitable satellite sensor is required which has the spectral resolution to separate fine reflectance features. Such satellites include the low spatial resolution ocean colour satellites such as MODIS and MERIS. The disadvantages of low spatial resolution are offset, however, by the high temporal resolution (daily imagery in the case of MODIS) and spectral resolution. Most analytical methods do not require in situ data (except for validation), but do require parameterisation with in situ inherent optical properties.

Remote sensing remains the only method to quantitatively assess water quality over large areas simultaneously, and has the potential to allow monitoring of water quality globally. However, remote sensing should not be considered as a replacement for traditional monitoring techniques, but is complimentary, as it can only derive information on optically active water quality constituents. Thus information cannot be derived for variables such as nutrients or pollutants such as heavy metals. In addition, remote sensing does not capture variations of optically active components deeper in the water column, which means that relevant phenomena such as deep chlorophyll maxima are not included in assessments of biomass and productivity of aquatic systems.

The data derived from in situ grab-sampling, autonomous water quality monitoring sensors, remote sensing and 3-D modelling all have different spatial, temporal and water quality parameter characteristics. The analysis of data from each of these sources enables more effective water quality monitoring and management. Remote sensing provides the opportunity to calibrate, update, and validate 3-D models based on hindcast simulations. Modelling studies provide insights into complex water quality dynamics, describing observed spatial distributions which are critical to understanding ecosystem function. With increased development and deployment of autonomous water quality monitoring sensors, opportunities to calibrate and validate satellite remote sensing algorithms will increase in the future. In this study remote sensing and 3-D modelling data were synthesised to provide an example of unparalleled opportunity for cost effective and quantitative validation of modelling results.

6.3 Recommendations for future work

In Chapter 2, chl *a* explained most of the variation in retrieved Landsat water surface reflectance, however, in some of the shallow Rotorua lakes resuspended sediment may influence the accuracy of chl *a* retrieval. Further investigation is needed into satellite platforms that possess the spectral resolution to allow the application of water quality retrieval algorithms that account for multiple optically active constituents. For example, bio-optical algorithms have been used with medium-spectral resolution imaging spectrometer (MERIS) data for the remote sensing of turbid inland waters where both chl *a* and suspended minerals are responsible for significant portions of the reflectance measured by satellites. The precision of bio-optical models depends on their parameterization of inherent optical properties, of which very little is known regarding the Rotorua lakes. Future research should be focused on measuring there parameters, in conjunction with in situ radiometry.

As demonstrated in Chapter 3, the 3-D hydrodynamic model reproduced satellite-observed surface water temperature with considerable accuracy. At 30-m horizontal resolution, the model was suited for validation by 60-m resolution thermal satellite imagery, however, at 30-m the resolution was coarse considering the small area occupied by the geothermal plume zone. Increasing the resolution would cause the model to run too slowly for more intensive validation through time, but alternative grid structures with varying cell size could be investigated to at least partially circumvent this problem. Hydrodynamic models exist which use unstructured triangular cells, for example, and these may allow for higher resolution near the shoreline. Additionally, in situ data on current velocity/direction and temperature in the plume zone would provide model validation data that could more specifically target circulation patterns.

As demonstrated in Chapter 4 the 3-D model of Lake Ellesmere performed poorly in reproducing MODIS-estimated, basin-scale and fine-scale variations in suspended minerals. As identified in detail in the discussion in Chapter 4, there are a number of improvements which could be made to the modelling approach. These include investigation of horizontally varying grain size, and application of more advanced wave models to account for diffraction and refraction. Furthermore the inherent optical properties of Lake Ellesmere could be measured in order to validate the semi-analytical modelling approach used to estimate suspended sediment.

In Chapter 5, a radiative transfer model, 6sv, was used to atmospherically correct MODIS 1-km resolution satellite imagery. With automation the entire archive of MODIS imagery for Lake Taupo could be processed, which would further elucidate the validity and robustness of the seasonally parameterised bio-optical model. More investigation is needed on the absorption properties of phytoplankton in winter and spring, as at this time the largest uncertainty in chl *a* estimations was encountered, likely due to species composition changes and the associated changes in reflectance characteristics of the assemblage.

6.4 Future directions

Recent technological developments and remote sensing technology have allowed remote sensing to focus from deriving chl *a* in Case 1 oceanic waters to deriving chl *a*, coloured dissolved organic matter and tripton in optically complex Case 2 inland and coastal waters. Along with sensor technology, water quality retrieval algorithms have also become more sophisticated. The development of sensors with moderate spatial resolution and high spectral resolution, such as MODIS, has facilitated the continued development of bio-optical algorithms for remote sensing of Case 2 waters. The Visible Infrared Imaging Radiometer Suite (VIIRS) on-board the National Preparatory Project (NPP) satellite (launched 28 October 2011) is designed to improve upon the MODIS data record, with increased spatial resolution (750 m), whist maintaining similar spectral resolution.

The Landsat satellite offers the longest continuous optical record of the Earth’s surface, spanning more than 40 years. While it has limited spectral resolution and limited signal-to-noise ratio (which limits temporal stability), the sensor has proved exceedingly useful for many applications, including remote sensing of large and small lakes. Currently the Landsat 5 and Landsat 7 sensors are at the end of their functional life and the remote sensing community is eagerly awaiting their replacement with proposed new satellite launches. The Landsat Data Continuity Mission (LDCM), which supports the Operational Land Imager (OLI) on-board Landsat 8, has improved quantization and spectral resolution over past Landsat satellites. The combination of data from OLI and VIIRS sensors will improve water quality and remote sensing solutions for small and large lakes, ensuring further expansion of NASA-based remote sensing of water quality.

7 Appendix

7.1 ENVI IDL image processing routines written for Landsat image processing

```
PRO batch_subset_via_roi_landsat_rot

  ENVI, /RESTORE_BASE_SAVE_FILES
  ENVI_BATCH_INIT, LOG_FILE='batch.txt'
input_dir = 'C:\Users\mat\Documents\LANDSAT\rotsouthETM\'
input_dir_name_lenght=STRLEN(input_dir)
output_location = 'C:\Users\mat\Documents\LANDSAT\rotsouthETM\'
flist=FILE_SEARCH('C:\Users\mat\Documents\LANDSAT\rotsouthETM\*',
COUNT=count)

FOR h=0, count-1 Do Begin

        path_filename=flist[h]
        imagelist=FILE_SEARCH(path_filename+'\*.TIF')
        path_filename_lenght=STRLEN(path_filename)
        filename=STRMID(path_filename,input_dir_name_lenght)
;;;;;;;;;;;;;;;;;;;;;;;;;;;;;;;;;;;;;;;;;;;;;;;;;;;;;;;;;;;;;;;;;;;;;;;;;;;;;;;;;;;;;;;;;;;;;;;;;;;;
        envi_open_file, imagelist(0), r_fid=fid
        ENVI_FILE_QUERY,fid,DIMS=dims,NS=ns,NL=nl,NB=nb
        t_fid=LONARR(nb)+fid
        pos=LINDGEN(nb)

        ;open the EVF file
        evf_file = 'E:\LANDSAT_6stxts\clipS.evf'
        evf_id=ENVI_EVF_OPEN(evf_file)

        ;get the vector information

     ENVI_EVF_INFO,evf_id,NUM_RECS=num_recs,DATA_TYPE=data_type,P
     ROJECTION=projection,$
        LAYER_NAME=layer_name

        ;print information about each record
        PRINT, 'Number of records:',num_recs
        FOR i=0,num_recs-1 DO BEGIN
```

```
        record=ENVI_EVF_READ_RECORD(evf_id,i)
        PRINT, 'Number of nodes in Record
     '+STRTRIM(i+1,2)+':',N_ELEMENTS(record[0,*])
        PRINT, 'Record Info:'
        PRINT, record
        ENDFOR

          ; Get record info (assuming one record in EVF)
          record=ENVI_EVF_READ_RECORD(evf_id,0)

          ;  Result[0, *] contains the x values, and Result[1, *] contains the y values
          xMap=record[0,*]
          yMap=record[1,*]

          roi_id = ENVI_CREATE_ROI(COLOR=4, NAME='rotCLIP_roi', NS=ns,
     NL=nl)

          ; Define the roi
          ENVI_DEFINE_ROI, roi_id, /POLYGON, XPTS=xMap, YPTS=yMap
          ;roi_data = ENVI_GET_ROI_DATA(roi_id,POS=pos,FID=t_fid)

          ;Convert record to xy pixel coordinates of the image to be subsetted
          ENVI_CONVERT_FILE_COORDINATES,fid,xf,yf,xMap,yMap

          ;Prepare the subset dimensions
          dims[0]= ENVI_GET_ROI_DIMS_PTR(roi_id) ;-1L ; A Pointer to the
     ;Opened ROI
          dims[1]=min(xf)-1 ; The starting sample number, the first x pixel is 0
          dims[2]=max(xf)-1 ; The Ending sample number
          dims[3]=min(yf)-1 ; The starting line number, the first y pixel is 0
          dims[4]=max(yf)-1 ; The ending line number.

          ;Use copyfile_doit to copy input file with new dimensions

     ENVI_DOIT,'CF_DOIT',FID=t_fid,POS=pos,DIMS=dims,REMOVE=0,OUT_
     NAME=path_filename+'\'+filename+'_b1DN_rotS.img',R_FID=r_fid

          envi_file_mng, id=fid, /remove
          envi_file_mng, id=r_fid, /remove

;;;;;;;;;;;;;;;;;;;;;;;;;;;;;;;;;;;;;;;;;;;;;;;;;;;;;;;;;;;;;;;;;;;;;;;;;;;;;;;;;;;;;;;;;;;;;;;;;;;;;;

        envi_open_file, imagelist(1), r_fid=fid
        ENVI_FILE_QUERY,fid,DIMS=dims,NS=ns,NL=nl,NB=nb
        t_fid=LONARR(nb)+fid
        pos=LINDGEN(nb)

        ;open the EVF file
        evf_file = 'E:\LANDSAT_6stxts\clipS.evf'
```

```
   evf_id=ENVI_EVF_OPEN(evf_file)

   ;get the vector information

ENVI_EVF_INFO,evf_id,NUM_RECS=num_recs,DATA_TYPE=data_type,P
ROJECTION=projection,$
   LAYER_NAME=layer_name

   ;print information about each record
   PRINT, 'Number of records:',num_recs
   FOR i=0,num_recs-1 DO BEGIN
   record=ENVI_EVF_READ_RECORD(evf_id,i)
   PRINT, 'Number of nodes in Record
'+STRTRIM(i+1,2)+':',N_ELEMENTS(record[0,*])
   PRINT, 'Record Info:'
   PRINT, record
   ENDFOR

     ; Get record info (assuming one record in EVF)
     record=ENVI_EVF_READ_RECORD(evf_id,0)

     ;  Result[0, *] contains the x values, and Result[1, *] contains the y values
     xMap=record[0,*]
     yMap=record[1,*]

     roi_id = ENVI_CREATE_ROI(COLOR=4, NAME='rotCLIP_roi', NS=ns,
NL=nl)
     ; Define the roi
     ENVI_DEFINE_ROI, roi_id, /POLYGON, XPTS=xMap, YPTS=yMap
     ;roi_data = ENVI_GET_ROI_DATA(roi_id,POS=pos,FID=t_fid)

     ;Convert record to xy pixel coordinates of the image to be subsetted
     ENVI_CONVERT_FILE_COORDINATES,fid,xf,yf,xMap,yMap

     ;Prepare the subset dimensions
     dims[0]= ENVI_GET_ROI_DIMS_PTR(roi_id) ;-1L ; A Pointer to the
Opened ROI
     dims[1]=min(xf)-1 ; The starting sample number, the first x pixel is 0
     dims[2]=max(xf)-1 ; The Ending sample number
     dims[3]=min(yf)-1 ; The starting line number, the first y pixel is 0
     dims[4]=max(yf)-1 ; The ending line number.

     ;Use copyfile_doit to copy input file with new dimensions

ENVI_DOIT,'CF_DOIT',FID=t_fid,POS=pos,DIMS=dims,REMOVE=0,OUT_
NAME=path_filename+'\'+filename+'_b2DN_rotS.img',R_FID=r_fid

     envi_file_mng, id=fid, /remove
     envi_file_mng, id=r_fid, /remove
```

```
;;;;;;;;;;;;;;;;;;;;;;;;;;;;;;;;;;;;;;;;;;;;;;;;;;;;;;;;;;;;;;;;;;;;;;;;;;;;;;;;;;;;;;;;;;;;;;;;;;;;;;;;;;;;;;;;;;;;;;;;;;;;;;;;;;;;;;;;;;;
      envi_open_file, imagelist(2), r_fid=fid
      ENVI_FILE_QUERY,fid,DIMS=dims,NS=ns,NL=nl,NB=nb
      t_fid=LONARR(nb)+fid
      pos=LINDGEN(nb)

      ;open the EVF file
      evf_file = 'E:\LANDSAT_6stxts\clipS.evf'
      evf_id=ENVI_EVF_OPEN(evf_file)

      ;get the vector information

    ENVI_EVF_INFO,evf_id,NUM_RECS=num_recs,DATA_TYPE=data_type,P
    ROJECTION=projection,$
      LAYER_NAME=layer_name

      ;print information about each record
      PRINT, 'Number of records:',num_recs
      FOR i=0,num_recs-1 DO BEGIN
      record=ENVI_EVF_READ_RECORD(evf_id,i)
      PRINT, 'Number of nodes in Record
    '+STRTRIM(i+1,2)+':',N_ELEMENTS(record[0,*])
      PRINT, 'Record Info:'
      PRINT, record
      ENDFOR

       ; Get record info (assuming one record in EVF)
       record=ENVI_EVF_READ_RECORD(evf_id,0)

       ;  Result[0, *] contains the x values, and Result[1, *] contains the y values
       xMap=record[0,*]
       yMap=record[1,*]

       roi_id = ENVI_CREATE_ROI(COLOR=4, NAME='rotCLIP_roi', NS=ns,
    NL=nl)
       ; Define the roi
       ENVI_DEFINE_ROI, roi_id, /POLYGON, XPTS=xMap, YPTS=yMap
       ;roi_data = ENVI_GET_ROI_DATA(roi_id,POS=pos,FID=t_fid)

       ;Convert record to xy pixel coordinates of the image to be subsetted
       ENVI_CONVERT_FILE_COORDINATES,fid,xf,yf,xMap,yMap

       ;Prepare the subset dimensions
       dims[0]= ENVI_GET_ROI_DIMS_PTR(roi_id) ;-1L ; A Pointer to the
    Opened ROI
       dims[1]=min(xf)-1 ; The starting sample number, the first x pixel is 0
       dims[2]=max(xf)-1 ; The Ending sample number
       dims[3]=min(yf)-1 ; The starting line number, the first y pixel is 0
       dims[4]=max(yf)-1 ; The ending line number.
```

```
              ;Use copyfile_doit to copy input file with new dimensions

        ENVI_DOIT,'CF_DOIT',FID=t_fid,POS=pos,DIMS=dims,REMOVE=0,OUT_
        NAME=path_filename+'\'+filename+'_b3DN_rotS.img',R_FID=r_fid

              envi_file_mng, id=fid, /remove
              envi_file_mng, id=r_fid, /remove
;;;;;;;;;;;;;;;;;;;;;;;;;;;;;;;;;;;;;;;;;;;;;;;;;;;;;;;;;;;;;;;;;;;;;;;;;;;;;;;;;;;;;;;;;;;;;;;;;;;;;;;;;;;;;;;;;;;;;;;;;;;;;;;;;;;;;;;;;
            envi_open_file, imagelist(3), r_fid=fid
            ENVI_FILE_QUERY,fid,DIMS=dims,NS=ns,NL=nl,NB=nb
            t_fid=LONARR(nb)+fid
            pos=LINDGEN(nb)

            ;open the EVF file
            evf_file = 'E:\LANDSAT_6stxts\clipS.evf'
            evf_id=ENVI_EVF_OPEN(evf_file)

            ;get the vector information

        ENVI_EVF_INFO,evf_id,NUM_RECS=num_recs,DATA_TYPE=data_type,P
        ROJECTION=projection,$
            LAYER_NAME=layer_name

            ;print information about each record
            PRINT, 'Number of records:',num_recs
            FOR i=0,num_recs-1 DO BEGIN
            record=ENVI_EVF_READ_RECORD(evf_id,i)
            PRINT, 'Number of nodes in Record
        '+STRTRIM(i+1,2)+':',N_ELEMENTS(record[0,*])
            PRINT, 'Record Info:'
            PRINT, record
            ENDFOR

              ; Get record info (assuming one record in EVF)
              record=ENVI_EVF_READ_RECORD(evf_id,0)

              ;  Result[0, *] contains the x values, and Result[1, *] contains the y values
              xMap=record[0,*]
              yMap=record[1,*]

              roi_id = ENVI_CREATE_ROI(COLOR=4, NAME='rotCLIP_roi', NS=ns,
        NL=nl)
              ; Define the roi
              ENVI_DEFINE_ROI, roi_id, /POLYGON, XPTS=xMap, YPTS=yMap
              ;roi_data = ENVI_GET_ROI_DATA(roi_id,POS=pos,FID=t_fid)

              ;Convert record to xy pixel coordinates of the image to be subsetted
              ENVI_CONVERT_FILE_COORDINATES,fid,xf,yf,xMap,yMap
```

```
        ;Prepare the subset dimensions
        dims[0]= ENVI_GET_ROI_DIMS_PTR(roi_id) ;-1L ; A Pointer to the
    Opened ROI
        dims[1]=min(xf)-1 ; The starting sample number, the first x pixel is 0
        dims[2]=max(xf)-1 ; The Ending sample number
        dims[3]=min(yf)-1 ; The starting line number, the first y pixel is 0
        dims[4]=max(yf)-1 ; The ending line number.


        ;Use copyfile_doit to copy input file with new dimensions

    ENVI_DOIT,'CF_DOIT',FID=t_fid,POS=pos,DIMS=dims,REMOVE=0,OUT_
    NAME=path_filename+'\'+filename+'_b4DN_rotS.img',R_FID=r_fid

        envi_file_mng, id=fid, /remove
        envi_file_mng, id=r_fid, /remove
;;;;;;;;;;;;;;;;;;;;;;;;;;;;;;;;;;;;;;;;;;;;;;;;;;;;;;;;;;;;;;;;;;;;;;;;;;;;;;;;;;;;;;;;;;;;;;;;;;;;;;;;;;;;;;;;;;;;;;;;;;;;;;;;;;;;;;;;;;;
      envi_open_file, imagelist(4), r_fid=fid
      ENVI_FILE_QUERY,fid,DIMS=dims,NS=ns,NL=nl,NB=nb
      t_fid=LONARR(nb)+fid
      pos=LINDGEN(nb)

      ;open the EVF file
      evf_file = 'E:\LANDSAT_6stxts\clipS.evf'
      evf_id=ENVI_EVF_OPEN(evf_file)

      ;get the vector information

    ENVI_EVF_INFO,evf_id,NUM_RECS=num_recs,DATA_TYPE=data_type,P
    ROJECTION=projection,$
      LAYER_NAME=layer_name

      ;print information about each record
      PRINT, 'Number of records:',num_recs
      FOR i=0,num_recs-1 DO BEGIN
      record=ENVI_EVF_READ_RECORD(evf_id,i)
      PRINT, 'Number of nodes in Record
    '+STRTRIM(i+1,2)+':',N_ELEMENTS(record[0,*])
      PRINT, 'Record Info:'
      PRINT, record
      ENDFOR

        ; Get record info (assuming one record in EVF)
        record=ENVI_EVF_READ_RECORD(evf_id,0)

        ;  Result[0, *] contains the x values, and Result[1, *] contains the y values
        xMap=record[0,*]
        yMap=record[1,*]
```

```
    roi_id = ENVI_CREATE_ROI(COLOR=4, NAME='rotCLIP_roi', NS=ns,
NL=nl)
    ; Define the roi
    ENVI_DEFINE_ROI, roi_id, /POLYGON, XPTS=xMap, YPTS=yMap
    ;roi_data = ENVI_GET_ROI_DATA(roi_id,POS=pos,FID=t_fid)

    ;Convert record to xy pixel coordinates of the image to be subsetted
    ENVI_CONVERT_FILE_COORDINATES,fid,xf,yf,xMap,yMap

    ;Prepare the subset dimensions
    dims[0]= ENVI_GET_ROI_DIMS_PTR(roi_id) ;-1L ; A Pointer to the
Opened ROI
    dims[1]=min(xf)-1 ; The starting sample number, the first x pixel is 0
    dims[2]=max(xf)-1 ; The Ending sample number
    dims[3]=min(yf)-1 ; The starting line number, the first y pixel is 0
    dims[4]=max(yf)-1 ; The ending line number.


    ;Use copyfile_doit to copy input file with new dimensions

ENVI_DOIT,'CF_DOIT',FID=t_fid,POS=pos,DIMS=dims,REMOVE=0,OUT_
NAME=path_filename+'\'+filename+'_b5DN_rotS.img',R_FID=r_fid

    envi_file_mng, id=fid, /remove
    envi_file_mng, id=r_fid, /remove
;;;;;;;;;;;;;;;;;;;;;;;;;;;;;;;;;;;;;;;;;;;;;;;;;;;;;;;;;;;;;;;;;;;;;;;;;;;;;;;;;;;;;;;;;;;;;;;;;;;;;;;;;;;;;;;;;;;;;;;;;;;;;;;;;;;;;;;;;;;;;;;;;;;;;;;;;;;;;;;;;;;;;;;;;;;;;;;;;;;;;;;;;;;;;;;;;;;;;;;;;;;;;;;;;;;;;;;;;;;

  envi_open_file, imagelist(7), r_fid=fid
  ENVI_FILE_QUERY,fid,DIMS=dims,NS=ns,NL=nl,NB=nb
  t_fid=LONARR(nb)+fid
  pos=LINDGEN(nb)

  ;open the EVF file
  evf_file = 'E:\LANDSAT_6stxts\clipS.evf'
  evf_id=ENVI_EVF_OPEN(evf_file)

  ;get the vector information

ENVI_EVF_INFO,evf_id,NUM_RECS=num_recs,DATA_TYPE=data_type,P
ROJECTION=projection,$
  LAYER_NAME=layer_name

  ;print information about each record
  PRINT, 'Number of records:',num_recs
  FOR i=0,num_recs-1 DO BEGIN
  record=ENVI_EVF_READ_RECORD(evf_id,i)
  PRINT, 'Number of nodes in Record
'+STRTRIM(i+1,2)+':',N_ELEMENTS(record[0,*])
```

```
      PRINT, 'Record Info:'
      PRINT, record
      ENDFOR

       ; Get record info (assuming one record in EVF)
       record=ENVI_EVF_READ_RECORD(evf_id,0)

       ;  Result[0, *] contains the x values, and Result[1, *] contains the y values
       xMap=record[0,*]
       yMap=record[1,*]

       roi_id = ENVI_CREATE_ROI(COLOR=4, NAME='rotCLIP_roi', NS=ns,
    NL=nl)
       ; Define the roi
       ENVI_DEFINE_ROI, roi_id, /POLYGON, XPTS=xMap, YPTS=yMap
       ;roi_data = ENVI_GET_ROI_DATA(roi_id,POS=pos,FID=t_fid)

       ;Convert record to xy pixel coordinates of the image to be subsetted
       ENVI_CONVERT_FILE_COORDINATES,fid,xf,yf,xMap,yMap

       ;Prepare the subset dimensions
       dims[0]= ENVI_GET_ROI_DIMS_PTR(roi_id) ;-1L ; A Pointer to the
    Opened ROI
       dims[1]=min(xf)-1 ; The starting sample number, the first x pixel is 0
       dims[2]=max(xf)-1 ; The Ending sample number
       dims[3]=min(yf)-1 ; The starting line number, the first y pixel is 0
       dims[4]=max(yf)-1 ; The ending line number.

       ;Use copyfile_doit to copy input file with new dimensions

    ENVI_DOIT,'CF_DOIT',FID=t_fid,POS=pos,DIMS=dims,REMOVE=0,OUT_
    NAME=path_filename+'\'+filename+'_b7DN_rotS.img',R_FID=r_fid

       envi_file_mng, id=fid, /remove
       envi_file_mng, id=r_fid, /remove

       print,  filename

ENDFOR

  ; Exit Envi
  ENVI_BATCH_EXIT
END
```

PRO landsat_rad_sixsin_gen

```
ENVI, /RESTORE_BASE_SAVE_FILES
  ENVI_BATCH_INIT, LOG_FILE='batch.txt'
```

```
;pi=!DPI

input_dir = 'C:\Users\mat\Documents\LANDSAT\rotnorthETM\'
input_dir_name_lenght=STRLEN(input_dir)

flist=FILE_SEARCH('C:\Users\mat\Documents\LANDSAT\rotnorthETM\LE*',
      COUNT=count)

FOR h=0, count-1 Do Begin

        path_filename=flist[h]
        imagelist=FILE_SEARCH(path_filename+'\*DN_rot.img')
        mtlfile=FILE_SEARCH(path_filename+'\*MTL.txt')
        filename=STRMID(path_filename,input_dir_name_lenght)
        pathfilenamelength=STRLEN(path_filename)
        imagebasename=STRMID(imagelist(0),pathfilenamelength+1,21)

;***************************************************************
; Convert from DC to at-sensor radiances to TOA reflectances

openr, lun, mtlfile, /get_lun
   ;print, mtl_file
   nll=file_lines(mtlfile)
   data=strarr(nll)
   readf,lun,data
   ; String to find: LMIN_BAND2/3/4
   str1=strmatch(data, '*LMIN_BAND2*')  ;returns lmin_band2 and qcalmin_band2
   w1=where(str1 eq 1, c1)
   str1s=strsplit(data(w1[0]),/EXTRACT)
   lmin_b2=float(str1s[2])
   str1=strmatch(data, '*LMAX_BAND2*')  ;returns lmin_band2 and
     qcalmin_band2
   w1=where(str1 eq 1, c1)
   str1s=strsplit(data(w1[0]),/EXTRACT)
   lmax_b2=float(str1s[2])
   gain2=((lmax_b2-lmin_b2)/(254.))^(-1.)   ;units = (W/(m2 sr um))^-1 = (m2 sr
     um)/W
   ;--------------
   str1=strmatch(data, '*LMIN_BAND3*')  ;returns lmin_band2 and qcalmin_band2
   w1=where(str1 eq 1, c1)
   str1s=strsplit(data(w1[0]),/EXTRACT)
   lmin_b3=float(str1s[2])
   str1=strmatch(data, '*LMAX_BAND3*')  ;returns lmin_band2 and
     qcalmin_band2
   w1=where(str1 eq 1, c1)
   str1s=strsplit(data(w1[0]),/EXTRACT)
   lmax_b3=float(str1s[2])
   gain3=((lmax_b3-lmin_b3)/(254.))^(-1.)   ;units = (W/(m2 sr um))^-1 = (m2 sr
     um)/W
```

```
;--------------
str1=strmatch(data, '*LMIN_BAND4*')  ;returns lmin_band2 and qcalmin_band2
w1=where(str1 eq 1, c1)
str1s=strsplit(data(w1[0]),/EXTRACT)
lmin_b4=float(str1s[2])
str1=strmatch(data, '*LMAX_BAND4*')  ;returns lmin_band2 and
  qcalmin_band2
w1=where(str1 eq 1, c1)
str1s=strsplit(data(w1[0]),/EXTRACT)
lmax_b4=float(str1s[2])
gain4=((lmax_b4-lmin_b4)/(254.))^(-1.)   ;units = (W/(m2 sr um))^-1 = (m2 sr
  um)/W

;-----------------------------
;--------------
str1=strmatch(data, '*LMIN_BAND1*')  ;returns lmin_band2 and qcalmin_band2
w1=where(str1 eq 1, c1)
str1s=strsplit(data(w1[0]),/EXTRACT)
lmin_b1=float(str1s[2])
str1=strmatch(data, '*LMAX_BAND1*')  ;returns lmin_band2 and
  qcalmin_band2
w1=where(str1 eq 1, c1)
str1s=strsplit(data(w1[0]),/EXTRACT)
lmax_b1=float(str1s[2])
gain1=((lmax_b1-lmin_b1)/(254.))^(-1.)   ;units = (W/(m2 sr um))^-1 = (m2 sr
  um)/W
;--------------
str1=strmatch(data, '*LMIN_BAND5*')  ;returns lmin_band2 and qcalmin_band2
w1=where(str1 eq 1, c1)
str1s=strsplit(data(w1[0]),/EXTRACT)
lmin_b5=float(str1s[2])
str1=strmatch(data, '*LMAX_BAND5*')  ;returns lmin_band2 and
  qcalmin_band2
w1=where(str1 eq 1, c1)
str1s=strsplit(data(w1[0]),/EXTRACT)
lmax_b5=float(str1s[2])
gain5=((lmax_b5-lmin_b5)/(254.))^(-1.)   ;units = (W/(m2 sr um))^-1 = (m2 sr
  um)/W
;--------------
str1=strmatch(data, '*LMIN_BAND7*')
w1=where(str1 eq 1, c1)
str1s=strsplit(data(w1[0]),/EXTRACT)
lmin_b7=float(str1s[2])
str1=strmatch(data, '*LMAX_BAND7*')
w1=where(str1 eq 1, c1)
str1s=strsplit(data(w1[0]),/EXTRACT)
lmax_b7=float(str1s[2])
gain7=((lmax_b7-lmin_b7)/(254.))^(-1.)   ;units = (W/(m2 sr um))^-1 = (m2 sr
  um)/W
```

```
    ;--------------

envi_open_file, imagelist(0), r_fid=fid,NO_REALIZE=1
ENVI_FILE_QUERY,fid,DIMS=dims,NS=ns,NL=nl,NB=nb
map_info=envi_get_map_info(fid=fid)
b1    = ENVI_GET_DATA(FID=fid, dims=dims, pos=0)
envi_file_mng, id=fid, /remove
ns=n_elements(b1[*,0])
nl=n_elements(b1[0,*])
b1r=fltarr(ns,nl)
b1r = ((b1)-1.)/gain1 + lmin_b1
envi_write_envi_file, b1r, map_info=map_info,
        out_name=input_dir+filename+'\'+imagebasename+'_b1_rad.img', r_fid=fid
envi_file_mng, id=fid, /remove
b1    = 0
b1r = 0

envi_open_file, imagelist(1), r_fid=fid,NO_REALIZE=1
ENVI_FILE_QUERY,fid,DIMS=dims,NS=ns,NL=nl,NB=nb
map_info=envi_get_map_info(fid=fid)
b2    = ENVI_GET_DATA(FID=fid, dims=dims, pos=0)
envi_file_mng, id=fid, /remove
b2r=fltarr(ns,nl)
filename_lenght=STRLEN(imagelist(1))
output_rootname = STRMID(imagelist(1),0,filename_lenght-4)
b2r = ((b2)-1.)/gain2 + lmin_b2
envi_write_envi_file, b2r, map_info=map_info,
        out_name=input_dir+filename+'\'+imagebasename+'_b2_rad.img', r_fid=fid
envi_file_mng, id=fid, /remove
close,lun
free_lun, lun
b2    = 0
b2r    = 0

envi_open_file, imagelist(2), r_fid=fid,NO_REALIZE=1
ENVI_FILE_QUERY,fid,DIMS=dims,NS=ns,NL=nl,NB=nb
map_info=envi_get_map_info(fid=fid)
b3    = ENVI_GET_DATA(FID=fid, dims=dims, pos=0)
envi_file_mng, id=fid, /remove
b3r=fltarr(ns,nl)
filename_lenght=STRLEN(imagelist(2))
output_rootname = STRMID(imagelist(2),0,filename_lenght-4)
b3r = ((b3)-1.)/gain3 + lmin_b3
envi_write_envi_file, b3r,
        map_info=map_info,out_name=input_dir+filename+'\'+imagebasename+'_b3_r
        ad.img', r_fid=fid
envi_file_mng, id=fid, /remove
close,lun
free_lun, lun
```

```
b3    = 0
b3r    = 0

envi_open_file, imagelist(3), r_fid=fid,NO_REALIZE=1
ENVI_FILE_QUERY,fid,DIMS=dims,NS=ns,NL=nl,NB=nb
map_info=envi_get_map_info(fid=fid)
b4    = ENVI_GET_DATA(FID=fid, dims=dims, pos=0)
envi_file_mng, id=fid, /remove
b4r=fltarr(ns,nl)
filename_lenght=STRLEN(imagelist(3))
output_rootname = STRMID(imagelist(3),0,filename_lenght-4)
b4r = ((b4)-1.)/gain4 + lmin_b4
envi_write_envi_file, b4r, map_info=map_info,
        out_name=input_dir+filename+'\'+imagebasename+'_b4_rad.img', r_fid=fid
envi_file_mng, id=fid, /remove
b4    = 0
b4r    = 0

envi_open_file, imagelist(4), r_fid=fid,NO_REALIZE=1
ENVI_FILE_QUERY,fid,DIMS=dims,NS=ns,NL=nl,NB=nb
map_info=envi_get_map_info(fid=fid)
b5    = ENVI_GET_DATA(FID=fid, dims=dims, pos=0)
envi_file_mng, id=fid, /remove
b5r=fltarr(ns,nl)
filename_lenght=STRLEN(imagelist(4))
output_rootname = STRMID(imagelist(4),0,filename_lenght-4)
b5r = ((b5)-1.)/gain5 + lmin_b5
envi_write_envi_file, b5r, map_info=map_info,
        out_name=input_dir+filename+'\'+imagebasename+'_b5_rad.img', r_fid=fid
envi_file_mng, id=fid, /remove
b5=0
b5r=0

envi_open_file, imagelist(5), r_fid=fid,NO_REALIZE=1
ENVI_FILE_QUERY,fid,DIMS=dims,NS=ns,NL=nl,NB=nb
map_info=envi_get_map_info(fid=fid)
b7    = ENVI_GET_DATA(FID=fid, dims=dims, pos=0)
envi_file_mng, id=fid, /remove
b7r=fltarr(ns,nl)
filename_lenght=STRLEN(imagelist(5))
output_rootname = STRMID(imagelist(5),0,filename_lenght-4)
b7r = ((b7)-1.)/gain7 + lmin_b7
envi_write_envi_file, b7r, map_info=map_info,
        out_name=input_dir+filename+'\'+imagebasename+'_b7_rad.img', r_fid=fid
envi_file_mng, id=fid, /remove
b7=0
b7r=0

;wg=where(b1 ne 0 and b3 ne 0 and b4 ne 0 and b5 ne 0, $
```

```
;        cmask)  ; the gaps m
;
;b1(wg) = (b1(wg)-1.)/gain1 + lmin_b1
;b3(wg) = (b3(wg)-1.)/gain3 + lmin_b3
;b4(wg) = (b4(wg)-1.)/gain4 + lmin_b4
;b5(wg) = (b5(wg)-1.)/gain5 + lmin_b5

; Convert to TOA reflectances

; Get acquisition date (mm and day)
    str1=strmatch(data, '*ACQUISITION_DATE*')
    w1=where(str1 eq 1, c1)
    str1s=strsplit(data(w1[0]),/EXTRACT)
    mm_str=strmid(str1s[2],5,2)
    dd_str=strmid(str1s[2],8,2)
    yy_str=strmid(str1s[2],0,4)
    timem=strmatch(data, '*SCENE_CENTER_SCAN_TIME*')
    w1=where(timem eq 1, c1)
    timeex=strsplit(data(w1[0]),/EXTRACT)
    hr=strmid(timeex[2],0,2)
    min=strmid(timeex[2],6,2)
    sec=strmid(timeex[2],9,2)
    decsec=(float(sec)/60)/100
    decmin=float(min)/60
    decmin=decmin+decsec
    utcdechr=decmin+hr
    latlongm=strmatch(data, '*SCENE_CENTER_SCAN_TIME*')
    w1=where(timem eq 1, c1)
    timeex=strsplit(data(w1[0]),/EXTRACT)
    hr=strmid(timeex[2],0,2)

Convert_to_DOY, float(mm_str), float(dd_str), float(yy_str), DOY

YRDOY= float(yy_str)*1000+DOY

str1=strmatch(data, '*SUN_ELEVATION*')
    w1=where(str1 eq 1, c1)
    str1s=strsplit(data(w1[0]),/EXTRACT)
    selev=double(str1s[2])
    sza=90.-selev

; Earth-sun-distance
get_dist, doy, distv

;b1_toa=fltarr(ns,nl)
;b3_toa=fltarr(ns,nl)
;b4_toa=fltarr(ns,nl)
;b5_toa=fltarr(ns,nl)
;b1_toa(wg) = pi*b1(wg)*distv^(2.0)/(1997.*cos(sza*pi/180.))
```

```
;b3_toa(wg) = pi*b3(wg)*distv^(2.0)/(1533.*cos(sza*pi/180.))
;b4_toa(wg) = pi*b4(wg)*distv^(2.0)/(1039.*cos(sza*pi/180.))
;b5_toa(wg) = pi*b5(wg)*distv^(2.0)/(230.8*cos(sza*pi/180.))

;b1_toa = pi*b1*distv^(2.0)/(1997.*cos(sza*pi/180.))
;b3_toa = pi*b3*distv^(2.0)/(1533.*cos(sza*pi/180.))
;b4_toa = pi*b4*distv^(2.0)/(1039.*cos(sza*pi/180.))
;b5_toa = pi*b5*distv^(2.0)/(230.8*cos(sza*pi/180.))

;b1=0
;b3=0
;b4=0
;b5=0
output_rootname_i = STRMID(imagelist(0),34,21)

;yrdoy=STRMID(filename,7,7)
;           yr=STRMID(filename,7,4)
;           doy=STRMID(filename,11,3)
;           hr=STRMID(filename,15,2)
;           yrdoyR=double(yrdoy)
;           dom=date_conv_dayofmonth( yrdoyR,'F')
;           monthn=date_conv_month_n( yrdoyR,'F')

restore, 'C:\Users\mat\Documents\LANDSAT\AtcorParamsLandsatRot.sav'

at_dateindex=where(atdata.field1 EQ YRDOY)

print, atdata.field1(at_dateindex)

aod=atdata.field4(at_dateindex)

ozone=atdata.field3(at_dateindex)

wat_vap=atdata.field2(at_dateindex)

aods=string(aod)
ozones=string(ozone)
wat_vaps=string(wat_vap)

wo=wat_vaps + ozones

print, aod, ozone, wat_vap

sixsinfilepath='C:\Users\mat\Documents\LANDSAT\sixsin\'

fname_inb1 = sixsinfilepath+filename+'_b1_6sin.txt'

  OPENW,1,fname_inb1, width=300
```

```
PRINTF, 1, '7'
PRINTF, 1, mm_str,' ',dd_str,' ',utcdechr,' ','176.37 -38.90'
PRINTF, 1, '8 option for Water Vapor and Ozone'
PRINTF, 1, wo
PRINTF, 1, '2 cont Model'
PRINTF, 1, '0'
PRINTF, 1, aods
PRINTF, 1, '-0.3  (target level, negative value)'
PRINTF, 1, '-705 (sensor level)'
PRINTF, 1, '138 (chosen band)'
PRINTF, 1, '1 (Non homogeneous surface)'
PRINTF, 1, '4 1 5 (ro1 ro2 radius)'
PRINTF, 1, '1 BRDF'
PRINTF, 1, '50 radiance (positive value)'

CLOSE,1

fname_inb2 = sixsinfilepath+filename+'_b2_6sin.txt'

  OPENW,2,fname_inb2, width=300

PRINTF, 2, '7'
PRINTF, 2, mm_str,' ',dd_str,' ',utcdechr,' ','176.37 -38.90'
PRINTF, 2, '8 option for Water Vapor and Ozone'
PRINTF, 2, wo
PRINTF, 2, '2 cont Model'
PRINTF, 2, '0'
PRINTF, 2, aods
PRINTF, 2, '-0.3  (target level, negative value)'
PRINTF, 2, '-705 (sensor level)'
PRINTF, 2, '139 (chosen band)'
PRINTF, 2, '1 (Non homogeneous surface)'
PRINTF, 2, '4 1 5 (ro1 ro2 radius)'
PRINTF, 2, '1 BRDF'
PRINTF, 2, '50 radiance (positive value)'

CLOSE,2

fname_inb3 = sixsinfilepath+filename+'_b3_6sin.txt'

  OPENW,3,fname_inb3, width=300

PRINTF, 3, '7'
PRINTF, 3, mm_str,' ',dd_str,' ',utcdechr,' ','176.37 -38.90'
PRINTF, 3, '8 option for Water Vapor and Ozone'
PRINTF, 3, wo
PRINTF, 3, '2 cont Model'
PRINTF, 3, '0'
PRINTF, 3, aods
```

```
PRINTF, 3, '-0.3  (target level, negative value)'
PRINTF, 3, '-705 (sensor level)'
PRINTF, 3, '140 (chosen band)'
PRINTF, 3, '1 (Non homogeneous surface)'
PRINTF, 3, '4 1 5 (ro1 ro2 radius)'
PRINTF, 3, '1 BRDF'
PRINTF, 3, '50 radiance (positive value)'

CLOSE,3

fname_inb4 = sixsinfilepath+filename+'_b4_6sin.txt'

  OPENW,4,fname_inb4, width=300

PRINTF, 4, '7'
PRINTF, 4, mm_str,' ',dd_str,' ',utcdechr,' ','176.37 -38.90'
PRINTF, 4, '8 option for Water Vapor and Ozone'
PRINTF, 4, wo
PRINTF, 4, '2 cont Model'
PRINTF, 4, '0'
PRINTF, 4, aods
PRINTF, 4, '-0.3  (target level, negative value)'
PRINTF, 4, '-705 (sensor level)'
PRINTF, 4, '141 (chosen band)'
PRINTF, 4, '1 (Non homogeneous surface)'
PRINTF, 4, '4 1 5 (ro1 ro2 radius)'
PRINTF, 4, '1 BRDF'
PRINTF, 4, '50 radiance (positive value)'

CLOSE,4

fname_inb5 = sixsinfilepath+filename+'_b5_6sin.txt'

  OPENW,5,fname_inb5, width=300

PRINTF, 5, '7'
PRINTF, 5, mm_str,' ',dd_str,' ',utcdechr,' ','176.37 -38.90'
PRINTF, 5, '8 option for Water Vapor and Ozone'
PRINTF, 5, wo
PRINTF, 5, '2 cont Model'
PRINTF, 5, '0'
PRINTF, 5, aods
PRINTF, 5, '-0.3  (target level, negative value)'
PRINTF, 5, '-705 (sensor level)'
PRINTF, 5, '142 (chosen band)'
PRINTF, 5, '1 (Non homogeneous surface)'
PRINTF, 5, '4 1 5 (ro1 ro2 radius)'
PRINTF, 5, '1 BRDF'
PRINTF, 5, '50 radiance (positive value)'
```

```
CLOSE,5

fname_inb7 = sixsinfilepath+filename+'_b7_6sin.txt'

  OPENW,7,fname_inb7, width=300

PRINTF, 7, '7'
PRINTF, 7, mm_str,' ',dd_str,' ',utcdechr,' ','176.37 -38.90'
PRINTF, 7, '8 option for Water Vapor and Ozone'
PRINTF, 7, wo
PRINTF, 7, '2 cont Model'
PRINTF, 7, '0'
PRINTF, 7, aods
PRINTF, 7, '-0.3  (target level, negative value)'
PRINTF, 7, '-705 (sensor level)'
PRINTF, 7, '143 (chosen band)'
PRINTF, 7, '1 (Non homogeneous surface)'
PRINTF, 7, '4 1 5 (ro1 ro2 radius)'
PRINTF, 7, '1 BRDF'
PRINTF, 7, '50 radiance (positive value)'

CLOSE,7

ENDFOR
END
```

PRO sixsauto_landsat

```
ENVI, /RESTORE_BASE_SAVE_FILES

input_dir = 'C:\Users\mat\Documents\LANDSAT\rotnorthETM\'
input_dir_name_lenght=STRLEN(input_dir)
sixsinput_dir = 'C:\Users\mat\Documents\LANDSAT\LANDSAT_6stxts\sixsout\'
output_location = 'C:\Users\mat\Documents\LANDSAT\rotnorthETM\sixs_images\'
ENVI, /RESTORE_BASE_SAVE_FILES
  ENVI_BATCH_INIT, LOG_FILE='batch.txt'
;pi=!DPI

flist=FILE_SEARCH('C:\Users\mat\Documents\LANDSAT\rotnorthETM\LE*2002
      024*', COUNT=count)

FOR h=0, count-1 Do Begin

          path_filename=flist[h]
          imagelist=FILE_SEARCH(path_filename+'\*rotrad.img')
```

```
            path_filename_lenght=STRLEN(path_filename)
            filename=STRMID(path_filename,input_dir_name_lenght)
            filename_lenght=STRLEN(filename)
            fname_inb1 = sixsinput_dir+filename+'_b1_6sin.txtout'
            fname_inb2 = sixsinput_dir+filename+'_b2_6sin.txtout'
            fname_inb3 = sixsinput_dir+filename+'_b3_6sin.txtout'
            fname_inb4 = sixsinput_dir+filename+'_b4_6sin.txtout'
            fname_inb5 = sixsinput_dir+filename+'_b5_6sin.txtout'
            fname_inb7 = sixsinput_dir+filename+'_b7_6sin.txtout'

n_header_lines = 169

ssdatab1=read_ascii(fname_inb1, header=sixsjunk1, $
  data_start=n_header_lines, count=n_records)

  xa1 = ssdatab1.field01(6,0)
  xb1 = ssdatab1.field01(7,0)
  xc1 = ssdatab1.field01(8,0)

ssdatab2=read_ascii(fname_inb2, header=sixsjunk2, $
  data_start=n_header_lines, count=n_records)

  xa2 = ssdatab2.field01(6,0)
  xb2 = ssdatab2.field01(7,0)
  xc2 = ssdatab2.field01(8,0)

ssdatab3=read_ascii(fname_inb3, header=sixsjunk3, $
  data_start=n_header_lines, count=n_records)

  xa3 = ssdatab3.field01(6,0)
  xb3 = ssdatab3.field01(7,0)
  xc3 = ssdatab3.field01(8,0)

ssdatab4=read_ascii(fname_inb4, header=sixsjunk4, $
  data_start=n_header_lines, count=n_records)

  xa4 = ssdatab4.field01(6,0)
  xb4 = ssdatab4.field01(7,0)
  xc4 = ssdatab4.field01(8,0)

ssdatab5=read_ascii(fname_inb5, header=sixsjunk5, $
  data_start=n_header_lines, count=n_records)

  xa5 = ssdatab5.field01(6,0)
  xb5 = ssdatab5.field01(7,0)
  xc5 = ssdatab5.field01(8,0)

ssdatab7=read_ascii(fname_inb7, header=sixsjunk7, $
  data_start=n_header_lines, count=n_records)
```

```
  xa7 = ssdatab7.field01(6,0)
  xb7 = ssdatab7.field01(7,0)
  xc7 = ssdatab7.field01(8,0)

envi_open_file, imagelist(0), r_fid=fid

  ; query the file and define the output file variables
  ENVI_FILE_QUERY,fid,DIMS=dims,NS=ns,NL=nl,NB=nb,fname=fname
  pos=LINDGEN(nb)


num_cols=dims[2]-dims[1]+1     ;dims[1] is the starting column number (starts o),
        dims[2] is ending column number
num_rows=dims[4]-dims[3]+1     ;dims[3] is the starting row number, dims[4] is the
        ending row number
num_bands=n_elements(pos)      ;number of bands from the pos selected for
        processing
                               ;or n_elements(image) meaning number of pixles in the image

; Define a empty BSQ array
image=fltarr(num_cols, num_rows, 6)

image[*,*, 0]= envi_get_data(fid=fid, dims=dims, pos=pos)

envi_file_mng, id=fid, /remove

envi_open_file, imagelist(1), r_fid=fid
ENVI_FILE_QUERY,fid,DIMS=dims,NS=ns,NL=nl,NB=nb,fname=fname
pos=LINDGEN(nb)
image[*,*, 1]= envi_get_data(fid=fid, dims=dims, pos=pos)
envi_file_mng, id=fid, /remove

envi_open_file, imagelist(2), r_fid=fid
ENVI_FILE_QUERY,fid,DIMS=dims,NS=ns,NL=nl,NB=nb,fname=fname
pos=LINDGEN(nb)
image[*,*, 2]= envi_get_data(fid=fid, dims=dims, pos=pos)
envi_file_mng, id=fid, /remove

envi_open_file, imagelist(3), r_fid=fid
ENVI_FILE_QUERY,fid,DIMS=dims,NS=ns,NL=nl,NB=nb,fname=fname
pos=LINDGEN(nb)
image[*,*, 3]= envi_get_data(fid=fid, dims=dims, pos=pos)
envi_file_mng, id=fid, /remove

envi_open_file, imagelist(4), r_fid=fid
ENVI_FILE_QUERY,fid,DIMS=dims,NS=ns,NL=nl,NB=nb,fname=fname
pos=LINDGEN(nb)
image[*,*, 4]= envi_get_data(fid=fid, dims=dims, pos=pos)
```

```
envi_file_mng, id=fid, /remove

envi_open_file, imagelist(5), r_fid=fid
ENVI_FILE_QUERY,fid,DIMS=dims,NS=ns,NL=nl,NB=nb,fname=fname
pos=LINDGEN(nb)
image[*,*, 5]= envi_get_data(fid=fid, dims=dims, pos=pos)

; Replace with CF_doit?

ref=fltarr(num_cols, num_rows, 6)


  ref(*,*,0)= (xa1*image(*,*,0)-xb1)/(1+xc1*(image(*,*,0)*(xa1)-xb1))
  ref(*,*,1)= (xa2*image(*,*,1)-xb2)/(1+xc2*(image(*,*,1)*(xa2)-xb2))
  ref(*,*,2)= (xa3*image(*,*,2)-xb3)/(1+xc3*(image(*,*,2)*(xa3)-xb3))
  ref(*,*,3)= (xa4*image(*,*,3)-xb4)/(1+xc4*(image(*,*,3)*(xa4)-xb4))
  ref(*,*,4)= (xa5*image(*,*,4)-xb5)/(1+xc5*(image(*,*,4)*(xa5)-xb5))
  ref(*,*,5)= (xa7*image(*,*,5)-xb7)/(1+xc7*(image(*,*,5)*(xa7)-xb7))

map_info=envi_get_map_info(fid=fid)

envi_file_mng, id=fid, /remove

;envi_write_envi_file, ref(*,*,0:3), map_info=map_info,
        out_name=outpath+output_rootname+'ell_6s.img', r_fid=fid

envi_write_envi_file, ref(*,*,*), map_info=map_info,
        out_name=output_location+filename+'_rot_6s.img', r_fid=fid

ref=0
image=0

envi_file_mng, id=fid, /remove

ENDFOR

envi_batch_exit

END
```

PRO landsat_mask

```
ENVI, /RESTORE_BASE_SAVE_FILES
  ENVI_BATCH_INIT, LOG_FILE='batch.txt'

input_dir = 'C:\Users\mat\Documents\LANDSAT\qual\'
```

```
output_location = 'C:\Users\mat\Documents\LANDSAT\qual\'
maskfile= 'C:\Users\mat\Documents\LANDSAT\masktest\classwat.img'

input_dir_name_lenght=STRLEN(input_dir)

ENVI, /RESTORE_BASE_SAVE_FILES
ENVI_BATCH_INIT, LOG_FILE='batch.txt'

flist=FILE_SEARCH(input_dir+'*chlN.img', COUNT=count)

FOR h=0, count-1 Do Begin

        path_filename=flist[h]
        path_filename_lenght=STRLEN(path_filename)
        filename=STRMID(path_filename,input_dir_name_lenght)
        filenamelength=STRLEN(filename)
        out_name=STRMID(filename,0,filenamelength-13)
        out_nameR=output_location+out_name+'chl_M_N_NAN.img'
;;;;;;;;;;;;;;;;;;;;;;;;;;;;;;;;;;;;;;;;;;;;;;;;;;;;;;;;;;;;;;;;;;;;;;;;;;;;;;;;;;;;;;;;;;;;;;;;;;;;;;;;;;

        envi_open_file, flist(h), r_fid=ifid

  ; query the file and define the output file variables
ENVI_FILE_QUERY,ifid,DIMS=dims,NS=ns,NL=nl,NB=nb,fname=fname
pos=LINDGEN(nb)

num_cols=dims[2]-dims[1]+1     ;dims[1] is the starting column number (starts o),
     dims[2] is ending column number
num_rows=dims[4]-dims[3]+1     ;dims[3] is the starting row number, dims[4] is the
     ending row number
num_bands=n_elements(pos)      ;number of bands from the pos selected for
     processing
                    ;or n_elements(image) meaning number of pixles in the image

envi_open_file, maskfile, r_fid=m_fid

m_pos = [0]

ENVI_MASK_APPLY_DOIT, FID = ifid, POS = pos, DIMS = dims, $
  M_FID = m_fid, M_POS = m_pos, VALUE = 'NaN', OUT_NAME = out_nameR,
     $
  IN_MEMORY = 0, R_FID = r_fid

envi_file_mng, id=ifid, /remove
envi_file_mng, id=m_fid, /remove
envi_file_mng, id=r_fid, /remove
;
;print, out_bname
```

```
endfor

end



PRO replacebaddata

ENVI, /RESTORE_BASE_SAVE_FILES
  ENVI_BATCH_INIT, LOG_FILE='batch.txt'
input_dir = 'C:\Users\mat\Documents\LANDSAT\sixsimages_rotS\'
input_dir_name_lenght=STRLEN(input_dir)
output_location = 'C:\Users\mat\Documents\LANDSAT\sixsimages_rotS\'
ENVI, /RESTORE_BASE_SAVE_FILES
ENVI_BATCH_INIT, LOG_FILE='batch.txt'

flist=FILE_SEARCH('C:\Users\mat\Documents\LANDSAT\sixsimages_rotS\*6s.im
       g', COUNT=count)

FOR h=0, count-1 Do Begin

          path_filename=flist[h]
          path_filename_lenght=STRLEN(path_filename)
          filename=STRMID(path_filename,input_dir_name_lenght)
          filenamelength=STRLEN(filename)
          out_name=STRMID(filename,0,filenamelength-4)
;;;;;;;;;;;;;;;;;;;;;;;;;;;;;;;;;;;;;;;;;;;;;;;;;;;;;;;;;;;;;;;;;;;;;;;;;;;;;;;;;;;;;;;;;;;;;;;;;;;;
          envi_open_file, flist[h], r_fid=fid

          ENVI_FILE_QUERY,fid, dims=dims, nb=nb

          pos  = lindgen(nb)

out_name=output_location+out_name+'rbd.img'

bandn=['b1', 'b2', 'b3', 'b4', 'b5', 'b7']

ENVI_DOIT, 'DEM_BAD_DATA_DOIT', DIMS=dims, FID=fid,
       MAX_THRESH=-0.000001, MIN_THRESH=-100, $
OUT_BNAME=bandn, OUT_NAME=out_name, POS=pos, R_FID=r_fid

envi_file_mng, id=fid, /remove
envi_file_mng, id=r_fid, /remove

endfor

end
```